Chemical Kinetics Modelling Study of Naturally Aspirated and Boosted SI Engine Flame Propagation and Knock

by

Jiayi Gu

A Doctoral Thesis

submitted in partial fulfillment of the requirements for the award of

Degree of Doctor of Philosophy of Loughborough University

April 2014

Abstract

Modern spark ignition engines are downsized and boosted to meet stringent emission standards and growing customer demands on performance and fuel economy. They operate under high intake pressures and close to their limits to engine knock. As the intake pressure is increased knock becomes the major barrier that prevents further improvement on downsized boosted spark ignition engines. It is generally accepted that knock is caused by end gas autoignition ahead of the propagating flame. The propagating flame front has been identified as one of the most influential factors that promote the occurrence of autoignition.

Systematic understanding and numerical relation between the propagating flame front and the occurrence of knock are still lacking. Additionally, knock mitigation strategy that minimises compromise on engine performance needs further researching. Therefore the objectives of the current research consist of two steps: 1). study of turbulent flame propagation in both naturally aspirated SI engine. 2) study of the relationship between flame propagation and the occurrence of engine knock for downsized and boosted SI engine. The aim of the current research is, firstly, to find out how turbulent flames propagate in naturally aspirated and boosted S.I. engines, and their interaction with the occurrence of knock; secondly, to develop a mitigation method that depresses knock intensity at higher intake pressure.

Autoignition of hydrocarbon fuels as used in spark ignition engines is a complex chemical process involving large numbers of intermediate species and elementary reactions. Chemical kinetics models have been widely used to study combustion and autoignition of hydrocarbon fuels. Zero-dimensional multi-zone models provide an optimal compromise between computational accuracy and costs for engine simulation. Integration of reduced chemical kinetics model and zero-dimensional three-zone engine model is potentially a effective and efficient method to investigate the physical, chemical, thermodynamic and fluid dynamic processes involved in in-cylinder turbulence flame propagation and knock.

The major contributions of the current work are made to new knowledge of quantitative relations between intake pressure, turbulent flame speed, and knock onset timing and intensity. Additionally, contributions have also been made to the development of a knock mitigation strategy that effectively depresses knock intensity under higher intake pressure while minimises the compromise on cylinder pressure, which can be directive to future engine design.

Dedication

Upon finishing this thesis, I would like to thank a few special people for everything they have done in support of my PhD research work and the accomplishment of this thesis.

First and foremost, to my principle supervisor, the much respected professor Rui Chen at Loughborough University, for his exceptional care, support and guidance. I feel so fortunate to be under his supervision and I can never fully express my gratitude using any language.

My gratitude especially for my parents, Mr Hui Tao and Ms Jingwen Gu, for their continuous and unlimited support and encouragement during my eight years at Loughborough University. They are always the best parents in the world.

Special thanks to my wife, Yuanyuan Bao, for her care, faith and everything she did to make my life as easy and comfortable as it has always been. Also a big thanks and kiss to my daughter Mia Gu for the happiness she brought to us.

Last but not the least, lots of thanks to my extraordinary friends and family members, whose names are not listed here, for their support and believe. Their help will always be remembered and cherished.

List of Figures

List of Tables

Nomenclature

A	Area [m^2]
B	Cylinder Bore [mm]
c_p	Specific Heat Capacity at Constant Pressure [J/Kg/K]
c_v	Specific Heat Capacity at Constant Volume [J/Kg/K]
D	Diffusion coefficient
E	Activation Energy [J/mole]
h	Specific Enthalpy [J/Kg] / Heat Transfer Coefficient [W/m^{2}K]
k	Reaction Rate Coefficient
L	Markstein Length [mm]
l	Turbulence Integral Length Scale [m]
m	Mass [Kg]
M	Molecular Weight [Kg/mole]
N_u	Nusselt Number
P	Pressure [bar]
P_{cl}	Peclet Number
Q	Heat transferred [J]

r	Radius [m]
R	Universal Gas Constant [J/Kg K]
R_e	Reynolds Number
S_L	Laminar Flame Speed [m/s]
S_T	Turbulent Flame Speed [m/s]
T	Temperature [K]
u'	Turbulence Intensity [m/s]
u_L	Laminar Burning Velocity [m/s]
u_T	Turbulent Burning Velocity [m/s]
V	Volume [m^3]
W	Work [J]
X	Mass Fraction
Y	Mole Fraction
K	Stretch rate [s^{-1}]

Greek Symbols

Δ	Gradient/Difference
λ	Thermal Conductivity [W/m K]
μ	Dynamic Viscosity [kg/(m s)]
ρ	Density Ratio

ω	Molar Production Rate
Φ	Fuel-Air Equivalence Ratio

Subscripts

b	Burnt Zone
chem	Chemical Energy
f	Flame/Burning Zone
i	Elementary Reaction Index
j	Species Index
un	Unburnt Zone
wall	Cylinder Walls

Abbreviations

BMEP	Brake Mean Effective Pressure
BSFC	Brake Specific Fuel Consumption
CA	Crank Angle
NA	Naturally Aspirated
SI	Spark Ignition
WOT	Wide Open Throttle

Contents

Chapter Six: Simulation of Knock in Downsized Boosted SI Engine……….129

Chapter Seven: Mitigation of Knock in SI Engine …………………….. ……….142

Chapter One: Introduction

1.1 Background

In the past a few decades, the development of spark ignition (SI) internal combustion engines (ICEs) has been vastly driven by the emission standards which have become more and more stringent year on year and the increasing customers' environmental awareness. Although a number of emission-reduction technologies have been put into practice, some new strategies must be deployed to meet the upcoming tighter EURO VI standard. New powertrain technologies, such as fuel-electric hybrid, electric with range extender engine, fully electric, fuel cell, have been proposed and some are already commercialised. However the popularisation of these new technologies are restricted by a series of handles including costs, practicality, infrastructure and reliability issues (Walzer 2001).

In recent years car manufacturers have turned back to ICE to look for a more practical and cost-effective solutions in responding to the imperative for improved fuel economy and reduced emissions. Among all solutions, engine downsizing has been the most established one and almost all manufacturers are offering engines that are downsized to some degree or preparing to deliver them (Hancock et al. 2008), (Hadler 2009), (Friedfeldt et al. 2012).

1.1.1 Engine Downsizing

The term 'Engine Downsizing' refers to the concept of using a engine with smaller displacement to meet the performance targets while giving improved fuel economy and reduced emissions. The most common approach to achieve this is through turbocharging and/or supercharging the engine. Both techniques force more air to be inducted into the engine, allowing more fuel to be burnt and generate more power. The engine behaves as a normal small engine when not worked hard, delivering improved fuel economy and reduced emissions (Taylor 2008).

The engine load is controlled by a throttle which controls the amount of air that flows into the engine to vary the power output. Thus, the power output of an engine can only be increased by the increase of the engine’s displacement. However, delivering this power using a large displacement means that for the majority of time the engine only works at a fraction of its maximum designed power and is therefore very inefficient. Engines with smaller displacement is less throttled at the same loading conditions than engines with larger displacement, thus featuring less pumping loss and, consequently, a higher real compression ratio which leads to more efficient operation, as shown in ***Fig.1-1***. Additionally, smaller engines are more mechanically efficient as the power loss due to internal friction is reduced as the engine displacement becomes smaller (LAKE et al. 2004; Fraser et al. 2009), (Miller et al. 2013).

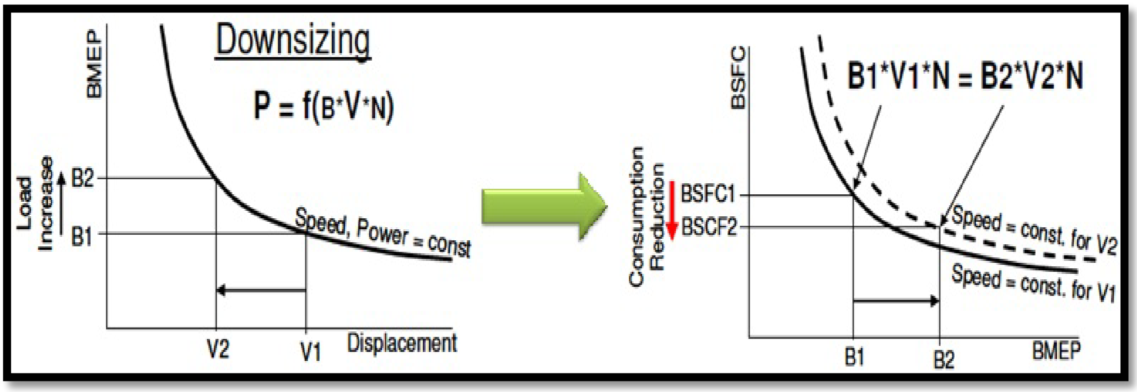

Fig. 1-1 The reduction in displacement pushes the engine to work at higher load (B.M.E.P.) and improves the fuel consumption (B.S.F.C.) (Miller et al. 2013).

1.1.2 Examples of downsized engines

Volkswagen 1.2 TFSI engine

The VW 1.2 TSI engine is the latest product under the manufacturer’s Downsizing design philosophy. This four-cylinder unit, which has been designed to replace the old 1.6 and 2.0 litre naturally aspirated M.P.I. engines, is equipped with direct injection, fuel stratified injection and turbocharging technologies. The combination provides high specific torque from much lower revs and it is maintained over a wide range of engine speed. This makes cars equipped with these engines more lively at lower engine speeds, which in turn makes them more economical and cleaner.

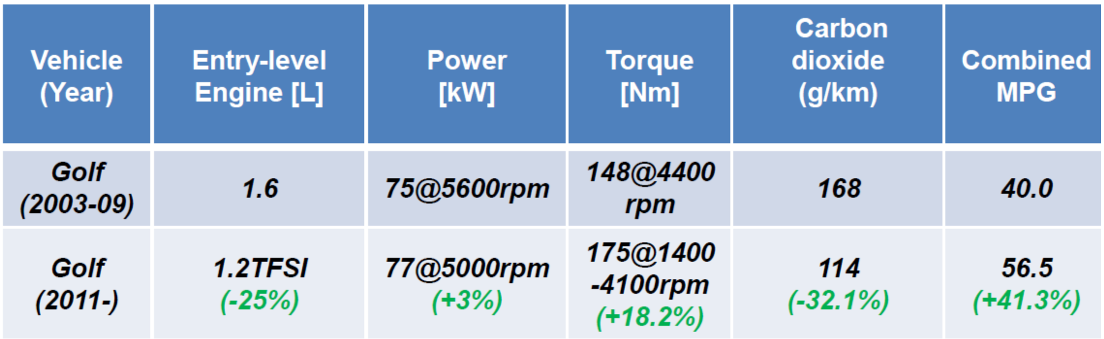

Vehicle (Year)	Entry-level Engine [L]	Power [kW]	Torque [Nm]	Carbon dioxide (g/km)	Combined MPG
Golf (2003-09)	*1.6*	*75@5600rpm*	*148@4400 rpm*	*168*	*40.0*
Golf (2011-)	*1.2TFSI* *(-25%)*	*77@5000rpm* *(+3%)*	*175@1400 -4100rpm* *(+18.2%)*	*114* *(-32.1%)*	*56.5* *(+41.3%)*

Fig. 1-2 Performance comparison of Volkswagen 1.6 M.P.I. engine and the downsized 1.2 TFSI engine on two generations of the Golf (Hadler 2009).

Ford 1.0 Ecoboost engine

This 1.0 litre turbocharged engine from the Ford’s Ecoboost family is a three-cylinder unit with direct injection, turbocharging and Ti-VCT technologies. The three-cylinder design significantly reduces the volume of the engine block which is of only the size of a A4 paper. Unbalanced flywheel has been employed to smooth out the natural vibration due to the three-cylinder design. The 1.0 litre Ecoboost unit has been designed to replace a series of small naturally aspirated M.P.I. engines.

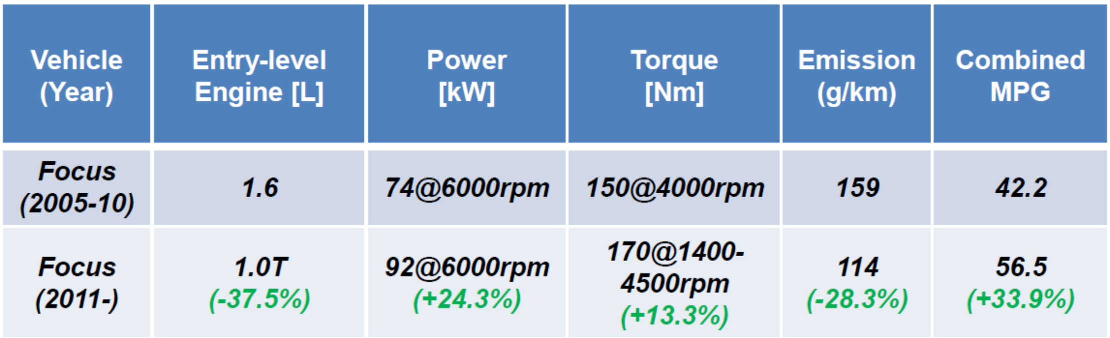

Vehicle (Year)	Entry-level Engine [L]	Power [kW]	Torque [Nm]	Emission (g/km)	Combined MPG
Focus (2005-10)	*1.6*	*74@6000rpm*	*150@4000rpm*	*159*	*42.2*
Focus (2011-)	*1.0T* *(-37.5%)*	*92@6000rpm* *(+24.3%)*	*170@1400-4500rpm* *(+13.3%)*	*114* *(-28.3%)*	*56.5* *(+33.9%)*

Fig. 1-3 Performance comparison of the Ford 1.6 M.P.I. engine and the downsized 1.0 Ecoboost engine on two generations of the Focus (Friedfeldt et al. 2012).

1.2 Motivation of the Current Research

To recover the power loss due to the displacement reduction, turbochargers and/or superchargers with boost pressures that are much higher than these on traditional turbocharged/supercharged engines are fitted to the downsized engines (Hancock et al. 2008). The increase in the boost pressures leads to significantly increased intake temperature and pressure. As a result, the propensity for unburnt mixture autoignition is higher than ever before (Attard et al. 2007).

The autoignition phenomenon in spark ignition engines was first recognized as early as in 1900's and identified as the major cause of the engine knock. Until the present time, the understanding of autoignition is still limited to its negative effect on spark ignition engine development (Liu 2010).

The undesirable contribution of the engine knock forces compromises to be made to the engines' operation strategies to deviate from operating at the optimal conditions, such as the compression ratio, EGR fraction and ignition timing (Zhen et al. 2013; Zhen et al. 2012). These compromises severely restrict the benefit of engine downsizing to be fully realized.

During the process of autoignition, the combustible mixture of fuel and oxidizer react in a self-accelerating manner and, eventually, ignite spontaneously leading to combustion. The autoignition process is kinetically-controlled by the chemical chain reactions between the fuel and the oxidizer molecules rather than any external ignition sources. The temperature of the mixture will gradually increase and accelerate when the energy released from chemical reactions exceeds the energy loss to the surroundings. At a temperature that is high enough to supply the activation energy, the reaction becomes a thermal explosion with large amount of energy being released in a very short period of time (Liu 2010).

In spark ignition engines, autoignition occurs within the unburnt mixture ahead of the propagating spherical flame front as a result of the piston motion and the propagating flame front. The compression work exerted by the piston and the flame front and the heat flux from the flame front act as external ignition sources that further raise the unburnt mixture temperature that accelerates the unburnt mixture autoignition process (Liu 2010). Thus it can be concluded that the temperature-sensitive autoignition phenomenon in spark ignition engines is significantly influenced by the flame speed and the thermal-chemical properties of the combustible mixture.

The combustion mode within spark ignition engines is turbulent premixed combustion with a wide range of temperature and pressure variations within one cycle and from one cycle to another (Heywood 1994). The key parameter for an accurate prediction of the unburnt mixture temperature and pressure (and therefore the autoignition of the unburnt mixture) is the knowledge of the turbulent flame speed throughout the combustion process. Though a lot of efforts have been dedicated into the studies of turbulent flame propagation in spark ignition engines, the understanding is still limited by its transient and unsteady nature. It has been a challenge to numerically simulate the turbulent flame speed in spark ignition engines due to the fact that it is the outcome of the interactions between the laminar flame speed and the turbulent quantities, the physicochemical quantities and the external disturbances (Byun 2011). Thus, successful calculation of the laminar flame speed is the first and the most important step in turbulent flame speed simulations.

Laminar flame speeds of spherical flames of a fuel or fuel blends are usually acquired experimentally using constant volume combustion bombs with sophisticated control system and temperature and pressure measurement devices. The bomb pressure history is used to obtained the laminar flame speed through thermodynamic analysis (Rahim et al. 2002; Metghalchi & Keck 1982; Bradley et al. 1996; Gu et al. 2000; Metghalchi & Keck 1980; Rozenchan et al. 2002; Kelley & Law 2009; Hu et al. 2009; Gülder 1982; Dowdy et al. 1991; Liu et al. 2013; Verhelst et al. 2005; Iijima & Takeno 1986; Saeed & Stone 2004; Milton & Keck 1984; Lewis & von Elbe 1934; Verhelst et al. 2011; Tang et al. 2008). The laminar flame speeds obtained in this way contain effects of ignition and flame stretch in the initial stage of flame propagation, where the flame radius is small. Also it includes effects of combustion bomb geometrical confinement (if the combustion bomb is non-spherical or the flame is not ignited centrally in a spherical combustion bomb) and flame instabilities in the later stages of its propagation, where the flame radius is large (Burke et al. 2009). Additionally, it is subject to relative thermal expansion all the way through the flame propagation process (Tang et al. 2008). Due to these effects, such laminar flame speed is not as simple as one of the fundamental properties of a specific fuel. Therefore, the propagation mechanism of a laminar flame and its interactions with these above-mentioned effects still need to be systematically described and numerically characterized. Therefore the modelling of laminar flame speed should be split into two parts. Firstly, the chemical part that deals with the combustion occurs within the reacting flame front which is closely linked with the thermo-chemical and transport properties of the mixture. Secondly, the part that describes the effects of flame stretch and instabilities.

The chemical part of laminar flame speed simulations is often ignored in available spark ignition engine models (Heywood 1994)(Liu & Chen 2009)(Stone 1987)(Ball et al. 1998)(Shayler et al. 1990)(Rakopoulos & Michos 2008). Instead, the combustion and flame propagation processes are replaced by mass fraction burnt functions such as the Wiebe functions. These models' capabilities of combustion chemistry simulation is limited or restricted to the use of chemical equilibrium calculations (Liu & Chen 2009). Thus, modelling laminar flame speed in relation with chemical kinetics provides a convenient tool for spark ignition engine simulation in terms of better understanding of the mechanism of turbulent flame propagation and the abnormal engine operations. Additionally, it provides the potentials of predicting the post-flame reactions and engine-out emissions.

Chemical kinetics of fuels used in spark ignition engines has been widely studied and can be generally interpreted as an oxidation process of fuel molecules involving a series of complex degenerate chain branching, carrying and terminating reactions with stable and intermediate radical species. Chemical kinetics mechanisms have been investigated and acknowledged as an important tool in the analysis of the rates of chemical processes and the factors that affect these rates. A chemical kinetics mechanism contains important elementary reactions and individual species and uses the best available rate parameters and thermo-chemical data. The size of such a model is decided by the numbers of reactions and species included in the model, which ranges from reduced models with only a few species and reaction steps to detailed models consisting of hundreds of chemical species and thousands of reactions.

The challenge arisen from using chemical kinetics in flame and engine simulations comes from the expansive computation cost. The computational power of modern computers has greatly advanced but is still not powerful enough to efficiently handle chemical kinetics calculation in cooperation with multidimensional modelling. In the simulation of combustion in spark ignition engine simulation, the integration of computational fluid dynamics (CFD) model with detailed chemical kinetics models, theoretically, provides unparalleled simulation accuracy and details in presenting combustion chamber geometries and combustion behaviour. However, numerical modelling of this scale requires substantial computer resources. The latest commercial IC engine simulation package that combines CFD and kinetics, the ***Chemkin Forté*** (Anon 2013), solves a complete HCCI cycle using a detailed mechanism and 10000 mesh cells in the magnitude of 10 hours.

1.3 Aim and Objectives

The aim of the current research is, firstly, to find out how turbulent flames propagate in naturally aspirated and boosted S.I. engines, and their interaction with the occurrence of knock; secondly, to develop a mitigation method that depresses knock intensity at higher intake pressure. The current study will fulfil the knowledge gap in existing SI engine combustion models and demonstrably predicts the flame propagation process and its relation to unburnt gas auto-ignition.

The major objectives of the current research are as follows:

1. To establish an understanding of the existing theories and modelling philosophies of SI engine combustion and the knock phenomenon.
2. To establish an understanding of chemical kinetics and the currently-available hydrogen- and gasoline-oxidation chemical kinetics mechanisms.
3. To formulate a transient laminar flame speed model in a constant volume combustion vessel to validate the philosophy of modelling transient laminar flame speed using chemical kinetics.

4. To establish a linkage between laminar and turbulent flame speeds using existing theories and numerically formulate and validate a model for turbulent flame speed a naturally aspirated SI engine.
5. Based on (4), to manipulate the input conditions and study the relation between turbulent flame speed and the knock phenomenon. Additionally, to develop a knock mitigation method that depresses knock while minimises compromises on engine performance.

1.4 Outline of the Thesis

Chapter 1: Introduction

The first chapter of the thesis provides background knowledge of modern downsized turbocharged spark ignition engines and discusses the aim, objectives and the outline of the thesis.

Chapter 2: Literature Review

The second chapter reviews the existing modelling philosophies of spark ignition engine combustion and the knocking phenomenon. Also included in this chapter are a brief introduction of chemical kinetics and review and discussion of available hydrogen- and gasoline-oxidation kinetics mechanisms.

Chapter 3: Instabilities of Spherical Hydrogen-air Flames

The third chapter introduces fundamental theories for cellular instabilities of outwardly propagating spherical flame. Based on experimental results, discuss the effects of temperature, pressure and equivalence ratio on the onset of cellular instabilities of spherical hydrogen-air flames

Chapter 4: Calculation of Transient Laminar Flame Speed

The forth chapter reports a transient laminar flame speed model which consists of a one-dimensional three-zone thermodynamics model and an in-house chemical kinetics solver which solves a reduced hydrogen-oxidation kinetics mechanism for the in-flame combustion simulation. The results obtained will be validated against experimental data.

Chapter 5: SI Engine Flame Propagation Simulation

This chapter will report the integration of the transient laminar flame speed, turbulent flame correlation and the engine geometry model developed in previous chapters. This integration will enable the study of flame propagation in a naturally aspirated SI engine. Detailed descriptions of the major components and the functionality of the numerical model will be presented. The results obtained will be validated against available data from open literature.

Chapter 6: Downsized Boosted SI Engine Knock Simulation

This chapter will describe and discuss the effects of downsizing and turbocharging on the flame propagation and its relation to the unburnt gas auto-ignition and, potentially, the knocking phenomenon.

Chapter 7: SI Engine Knock Mitigation

This chapter discuss a SI engine knock mitigation strategy that supress the knock while minimises the compromises on engine performance.

Chapter 8: Conclusions and Future Work

The final chapter of the thesis will discuss and conclude the achievements and the deficiencies of the current research work. Future work that can be done to improve the current work will be suggested.

Chapter Two: Literature Review

2.1 SI Engine Combustion

In S.I. engines with a conventional pan-shaped combustion chamber, the turbulence is mostly generated by the high shear flows during the induction process and modified during the compression. It is well established that the turbulence intensity as well as the mean flow increases almost in a linear fashion with increasing engine speed (Daneshyar & Hill 1987). The turbulence decays rapidly towards the end of the induction process and the characteristic dissipation time for the turbulent kinetic energy is smaller than the engine time scales. The turbulence during the induction exhibits a strong anisotropy, and the turbulence intensity as well as the mean velocity shows significant spatial variations. For disc shaped chambers, the turbulence when averaged over several cycles, displays a homogeneous and more isotropic structure towards the end of the compression stroke for both swirling and non-swirling flows (Gülder & Smallwood 2001).

As shown in ***Fig. 2-1***, it is widely accepted that the combustion regime in premixed SI engines falls into the wrinkled flame regime (Gülder & Smallwood 2001) and such conclusion is supported by extensive experimental results. By using molecular Rayleigh scattering, one researcher (Keck 1982) found that the flame front in spark ignition engines is made up of wrinkled laminar flames and islands of unburnt mixture may appear occasionally. For low-intensity large-scale turbulence, Damkohler (1947) proposed that $\boldsymbol{S_T/S_L}$, the ratio of the turbulent burning velocity ($\boldsymbol{S_T}$) to the laminar burning velocity ($\boldsymbol{S_L}$), is proportional to $\boldsymbol{A_w/A_o}$, the ratio of the wrinkled flame surface area ($\boldsymbol{A_w}$) to the flow cross section area ($\boldsymbol{A_o}$). For high-intensity, small- scale turbulence, combustion takes place in a distributed manner rather than a front propagation. Williams (1985) further claimed that, under the wrinkled turbulent combustion regimes, the process can be separated from the turbulence. Therefore, it is feasible to study the turbulent combustion process as a combination of two distinct phenomena: laminar flame propagation and turbulent flow field.

2.1.1 Regimes of SI Engine Combustion

In ***Fig. 2-1*** premixed turbulent combustion is classified into several regimes according to velocities, length scale and a number of dimensionless parameters (Peters 2000). Several scales can be defined in the study of turbulence. The integral time scale, τ_t, associated with energy dissipation of large eddies is defined as:

$$\tau_t = \frac{l_t}{u_t'} \qquad \textbf{(2-1)}$$

$$l_t = C_D \frac{{u_t'}^3}{\in} \qquad \textbf{(2-2)}$$

where l_t is the integral length scale of the large energy-containing eddies, u_t' is the r.m.s turbulent velocity and C_D is the turbulent length scale constant. The chemical time scale, τ_c, is defined as:

$$\tau_c = \frac{\alpha}{{S_L}^2};\ \alpha = \frac{k}{\rho C_p} \qquad \textbf{(2-3)}$$

where α is the thermal diffusivity and k is the thermal conductivity. The smallest eddies in a turbulent flow are characterized by the Kolmogorov time, velocity, and length scales:

$$\tau_\eta = \left(\frac{\upsilon}{\epsilon}\right)^{1/2};\ \nu_\eta = (\upsilon\epsilon)^{1/4};\ \eta = \left(\frac{\upsilon^3}{\epsilon}\right)^{1/4} \qquad \textbf{(2-4)}$$

Some dimensionless parameters can be defined from above-mentioned time and length scales. These parameters are used to distinguish different combustion regimes.

Turbulence Reynolds Number ($\boldsymbol{Re_t}$):

$$\boldsymbol{Re_t} = \frac{\mathbf{u_t'l_t}}{\boldsymbol{\nu}} \tag{2-5}$$

The turbulence Reynolds number characterises a turbulent flow in terms of the turbulence RMS velocity, $\mathbf{u_t'}$. It represents the ratio between the inertia force and the viscous force of the flow.

Damkohler Number ($\boldsymbol{Da}$):

$$\boldsymbol{Da} = \frac{\boldsymbol{\tau_t}}{\boldsymbol{\tau_c}} \tag{2-6}$$

The Damkohler number represents the ratio between the turbulence time scale and the chemical time scale. It indicates which one of these two effects is more dominant.

Karlovitz Number ($\boldsymbol{Ka}$):

$$\boldsymbol{Ka} = \frac{\boldsymbol{\tau_c}}{\boldsymbol{\tau_\eta}} \tag{2-7}$$

It defines the ratio of the chemical time scale and the Kolmogorov scale. When $\boldsymbol{K \ll 1}$ the chemical reactions occur much faster than all turbulent scales. Turbulence does not alter the flame structure and the chemical region is laminar.

Prandlt Number ($\boldsymbol{Pr}$):

$$\boldsymbol{Pr} = \frac{\boldsymbol{\nu}}{\boldsymbol{\alpha}} \tag{2-8}$$

The Prandlt number represents the ratio between the viscous force and the thermal diffusivity. It can related to the thickness of the thermal and velocity boundary layers.

Lewis Number ($\boldsymbol{Le}$):

$$\boldsymbol{Le} = \frac{\boldsymbol{\alpha}}{\boldsymbol{D}} \tag{2-9}$$

The Lewis number is the ratio between the thermal and molecular diffusivity of a species.

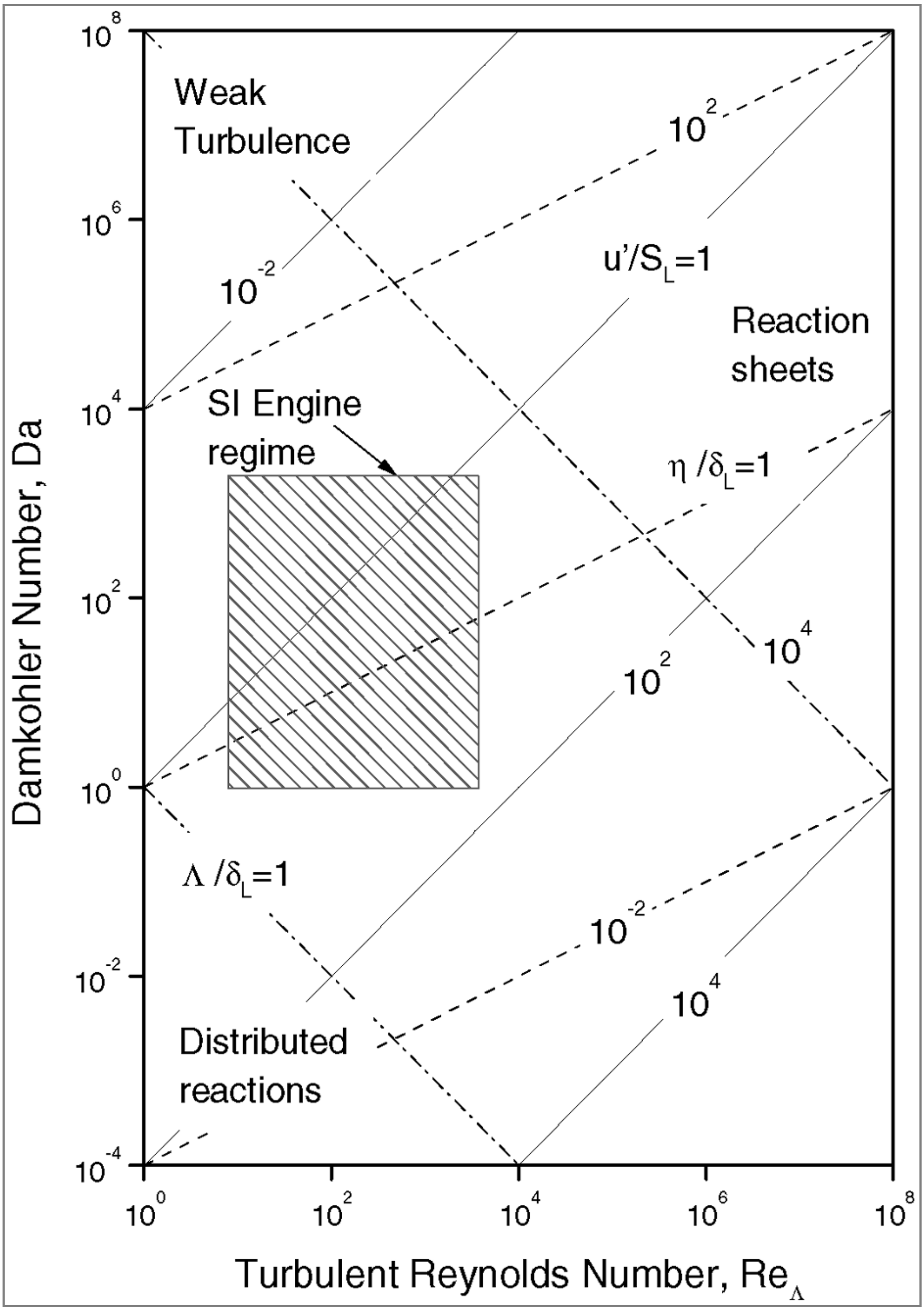

Fig. 2-1 Illustration of regimes of turbulent premixed combustion. The rectangle identifies the regimes of SI engines (Heywood 1988).

2.1.2 SI Engine Modelling

Multi-dimensional CFD models

Multidimensional modelling has been adopted as a powerful tool to investigate and analyse phenomena occurring in internal combustion engines, particularly with the rapid increase of computer power in recent years. Theoretically, a full-scale integration of CFD model of fine grid design with detailed chemical kinetics model provides unrivalled simulation accuracy and details of in-cylinder flow and combustion behaviours. However, a model at this numeric scale requires substantial CPU computing speed, large-scale storage and robust and fast numerical algorithm. Even with today's advanced high performance computers, the simulation time of such models is still measured in weeks or months.

Several solutions have been proposed trying to find the balance between the computational costs and the simulation accuracy. Reitz et al. (2006) adopted a 7-species chemical equilibrium model into his multi-dimensional engine model. The turbulent flame location, local temperature and pressure and the heat release rate are computed using KIVA-3V CFD codes with a mesh size in the range of 2-5mm. Burnt products are assumed to reach thermodynamic and chemical equilibrium states immediately behind the flame brush.

Other researchers proposed cost-reduction solution methods that either adopted a global or reduced chemical kinetics mechanism (Li et al. 2003; Kong & Reitz 1993; Ali et al. 2003) or a reduced CFD mesh to one- or two-dimensional (Iida et al. 2003; Iwashiro et al. 2002). These methods suffer from either degraded simulation accuracy or computational costs that are still relatively high.

Aceves et al. (2000) was among the first researchers who presented hybrid approach that formed a segregated sequential CFD multi-zone thermo-kinetic model. In the model, a detailed chemical kinetics model is implemented into a KIVA-2.1 CFD solver and a multi-zone thermodynamics model. The CFD model is responsible for solving the temperature and mixture formation process in the compression stroke until the ignition timing. The multi-zone model takes over from the ignition and simulates the combustion and expansion processes. These zones are defined by mass distribution and mixing between adjacent zones is disallowed. The model was validated against experimental results and showed good capability of predicting cylinder pressure and burn rate. The model also successfully reduced the computation time scale from weeks or months to hours or days. However, the model failed on the prediction of HC and CO emissions which are critical in modern engine design.

Quasi-dimensional multi-zone models

Quasi-dimensional models are used to simulate the ‘closed’ part of the S.I. engine cycle as they cannot properly predict the intake and exhaust strokes due to their dimensionless nature (Verhelst & Sheppard 2009). Quasi-dimensional models are distinguished from zero-dimensional models by the inclusion of certain geometrical parameters in the basic thermodynamic approach. This usually includes the radius of a thin flame front that separates the burnt and unburnt zones, creating a two-zone formation.

One advantage of these zero-dimensional models is the avoidance of the modelling of the in-cylinder process. Instead of considering the intake, mixture preparation, combustion and exhaust processes, a zero-dimensional model uses a pre-defined mass burning rate, also known as the Wiebe function (Liu & Chen 2009), to describe the combustion process. When the engine operating point stays the same Wiebe functions provide unrivalled simulation accuracy as it, in fact, works back from known experimental results. However as each Wiebe function is empirically defined as a specific engine operating point, extrapolation to other operating points is problematic.

Most quasi-dimensional S.I. engine models adopt a two-zone formation, assuming that the flame is a ultimately thin transition layer that transport mass and energy between the burnt and unburnt zones (Liu & Chen 2009). Additionally, the flame is assumed to be adiabatic and in chemical and thermodynamic equilibrium. The unburnt mass entrained into the flame is assumed to be consumed and transferred into burnt mass instantaneously. The burnt mixture composition is calculated using chemical equilibrium at a pre-defined combustion temperature and pressure. Typically, up to 12 species are considered in the equilibrium calculation: H_2O, H_2, OH, H, N_2, NO, N, CO_2, CO, O_2, O and Ar (Verhelst & Sheppard 2009). The actual number of species considered varies when the interests of the simulation shifts from just the combustion process. Reitz et al. (2006) used a 7-species chemical equilibrium system to determine the burnt mixture composition but an additional 10-species and 9-reaction kinetics model was adopted to predict the formation of NO and NO_2. Liu et al. (2009) proposed an zero-dimensional two-zone model to study the knock in S.I. engine. A chemical equilibrium containing 32 species was used in Liu’s model. The larger equilibrium system was chosen in order to keep accordance to the number of species included in the reduced chemical kinetics mechanism used to predict end gas autoignition.

In additional to the two-zone layout, some researchers developed a thermal boundary layer between the unburnt zone and the cylinder wall (Fiveland & Assanis 2001; Puzinauskas & Borgnakke 1991; Borgnakke et al. 1980), as shown in ***Fig. 2-2***. The addition of the boundary layer aids the fundamental understanding of the heat transfer process inside the cylinder.

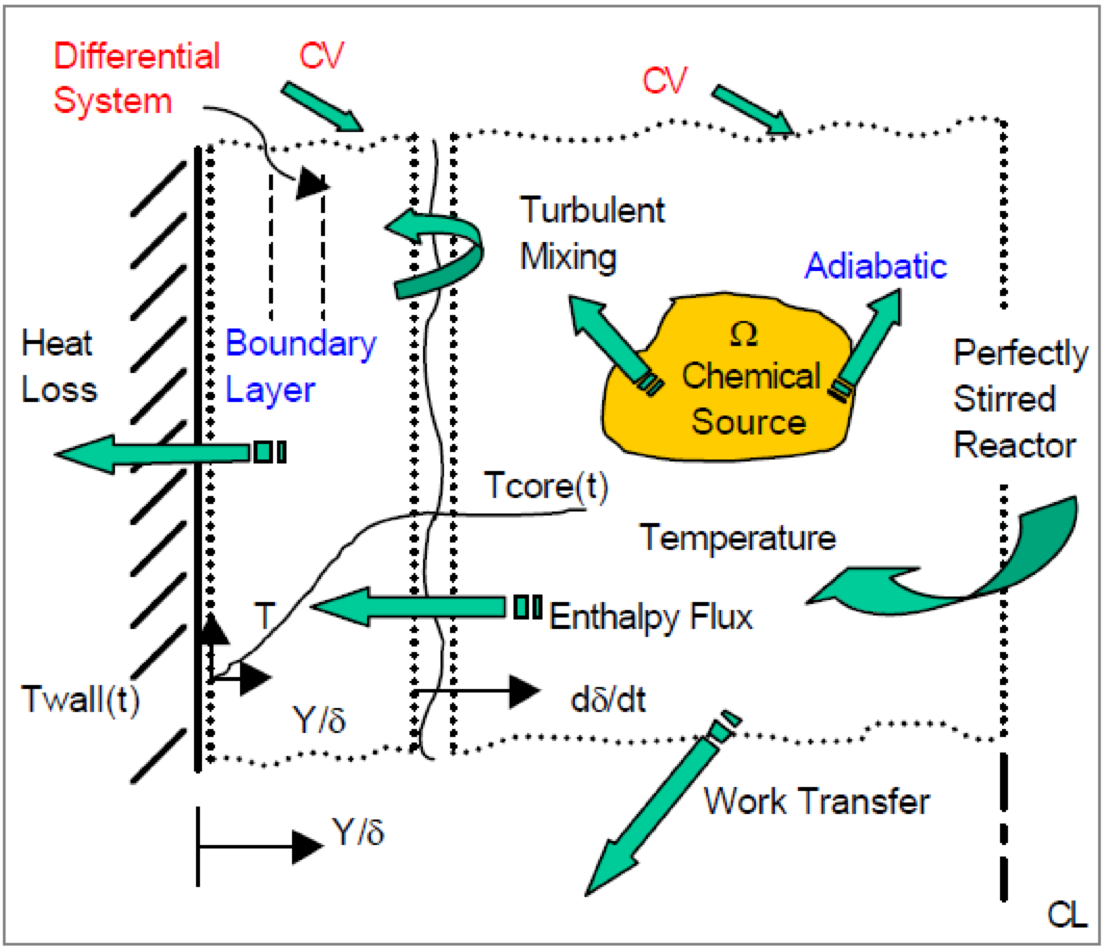

Fig. 2-2 Illustration of the interactions between the adiabatic core and the thermal boundary layer in a two-zone HCCI engine combustion model (Fiveland & Assanis 2001).

2.2 Engine Knock

Ideally, the spark-ignited flame should propagate steadily across the combustion chamber and consume the fresh charge. However abnormal combustion phenomena, such as the knock, are the major obstacles that prevent the improvements on engine thermal efficiency and specific power output. The causes of the engine knock include: engine design, operating parameters and combustion chamber deposits. The major causes of engine knock specifically occur in S.I. engines are categorised into two types: autoignition and surface ignition.

2.2.1 Autoignition

The combustion process in modern S.I. engines is precisely controlled by the spark ignition timing towards the end of the compression stroke. A flame kernel is formed a few milliseconds after the spark is fired. The flame kernel continues to grow outwardly and becomes a self-sustainable turbulent flame. The turbulent flame propagate across the combustion chamber to gradually consume the combustible fresh charge. As the flame propagates across combustion chamber the end gas is compressed by the flame front and the upward motion of the piston, causing pressure, temperature and density to increase. Some of the end gas fuel-air mixture may undergo slower pre-flame chemical reactions and start to release heat energy. This phenomenon is generally termed as ‘Autoignition’ (Heywood 1988). The autoignited end gases then burn very rapidly releasing energy at a rate 5 to 25 times higher in comparison to normal combustion. The occurrence of end gas autoignition depends on the competition between the consumption rate of the turbulent flame and the pre-flame chemical reactions ahead of the flame. If the end gas that has already autoignited is not consumed by the flame before the chemical reactions proceed to a critical level, sharp local temperature and pressure increase will occur (Liu 2010).

A sonic pressure wave is then created by the autoignition and it spreads across and resonates in the combustion chamber. This causes high frequency pressure oscillations inside the cylinder that produce sharp metallic noise and excessive vibration to the engine block. Such manifestations are termed as the ***knock***. Knock is undesirable as high pressure and local temperature can cause severe engine damage and is unpleasant to the driver and the passengers of the car. ***Fig. 2-3*** illustrates normal combustion and knocking combustion processes of S.I. engines. It has been acknowledged that knock is most likely to occur under high engine load at low engine speed. High engine load generates high cylinder temperature and pressure which triggers the end gas autoignition. Low engine speed allows the autoignition longer resident time to grow into a knocking combustion (Liu 2010).

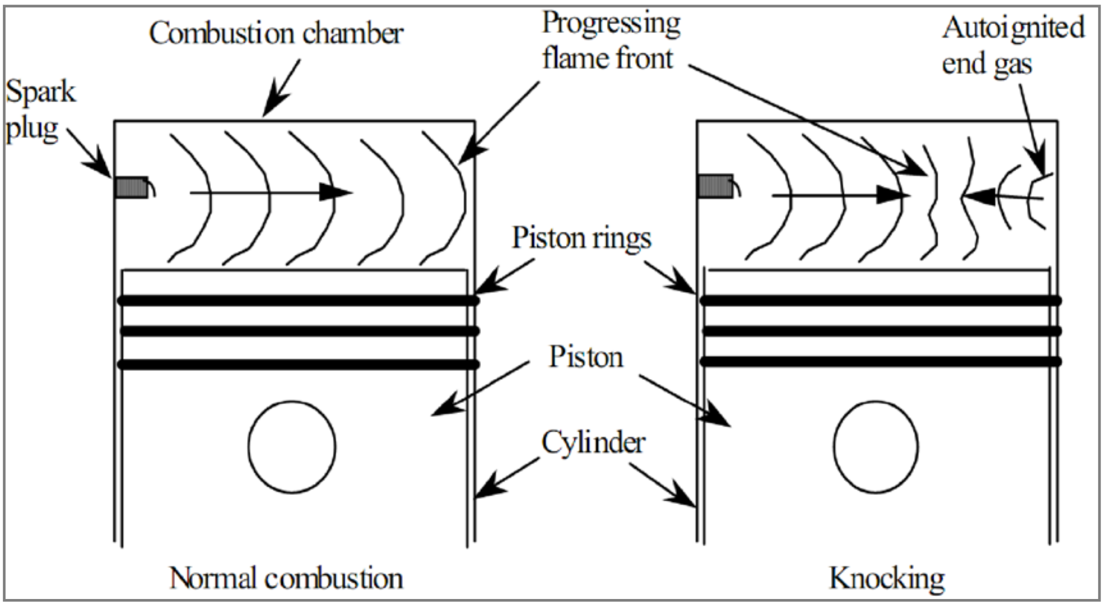

Fig. 2-3 Illustration of a normal combustion process and a knocking combustion process is S.I. engines (Zheng 2005).

The chemical kinetic reaction rates of the end gas are dependent on the local temperature, pressure and mixture strength. The following thermodynamic expression describes the P-T relationship for an adiabatic compression process:

$$T = T_i \cdot (P/P_i)^{\gamma-1/\gamma} \qquad \textbf{(2-10)}$$

where γ is the specific ratio of heat capacity. T_i and P_i represent the initial temperature and pressure at the start of the compression stroke, respectively. ***Eq. 2-10*** shows that the both temperature and pressure will increase if one of them is increased intentionally. Therefore, any factor that affects the mixture temperature and pressure will influence the occurrence of autoignition. There are several engine operating parameters that are considered to be important in the triggering of autoignition:

Spark Timing: Change of the ignition timings affects combustion phasing. Retarded ignition timings cause lower overall in-cylinder pressure because the combustion phasing is shifted away from the TDC position, which leads to the main combustion with major heat release occurs within a larger and faster expanding volume as the piston is moving downward. As a contrast, advanced spark timings causes earlier combustion that results in higher cylinder pressures. Knock occurrence is more subject to earlier spark timings because of the maximum end-gas temperature is increased.

Compression Ratio: With increased compression ratios, the volume swept by the piston during the compression and combustion phases becomes smaller. This leads to more intense compression on the end-gas and higher heat release from the mixture. As a result, a higher compression ratio increases the cylinder pressure and end gas temperatures.

Air-Fuel Ratio: At different AFRs, the in-cylinder mixture shows different combustion strength. Change of the mixture composition and thermodynamic properties affects combustion rates and the energy release, which in turn affects the cylinder pressure and the end-gas temperatures.

Intake Pressure: A higher intake pressure forces a larger amount of air-fuel mixture into the cylinder with higher initial pressure and volumetric efficiency cylinder, which consequently leads to higher overall in-cylinder pressure and combustion temperature.

Intake Temperature: It can be deduced from ***Eq. 2-1*** that mixture temperature in the compression process scales closely with initial temperature. Higher initial temperatures lead to higher overall mixture temperatures throughout the compression and combustion processes, which promote the rates of autoignition reactions.

EGR: Using EGR increases the total heat capacity of the end-gas and consequently reduces the temperature rise of the gas, which thermally diminishes knock tendency. However, the large number of reactive species present in the exhaust gas can also promote autoignition by chemical means.

<u>Engine Speed</u>: The chemical reactions of the end-gas takes time to proceed. At lower engine speeds, flame propagating speed become equivalent to or slower than the reaction characteristic time, so autoignition reactions is more likely to build up and advance.

Charge Preparation: The flow dynamic motion (turbulence, swirl, and tumble) affects the homogeneity of the mixture, which has a significant effect on combustion process. Local inhomogeneity of the mixture could lead to incomplete combustion or regionally high combustion temperature.

Combustion Chamber Geometry: The general shape of the combustion chamber, as well as spark plug location, affects the flame front area and the distance the flame front travels. Longer flame travel distance results in longer combustion duration and more time for autoignition chemistry to proceed.

2.2.2 Surface Ignition

Surface ignition describes the phenomena when the unburnt mixture is ignited by the overheated components in the cylinder or by glowing deposits. Those overheated components are typically the exhaust valves and the spark plug. Typical examples of glowing deposits can be carbon deposits and hot engine oil droplets (Dahnz et al. 2010). Surface ignition can occur before the spark ignition (pre-ignition) or after the spark ignition (post-ignition). Surface ignition creates one or multiple propagating flame fronts which interact with the main flame front to generate knocking combustion. The knock induced by surface ignition may be more intense than that induced by end gas autoignition. The reason being that multiple flame fronts can be ignited by the glowing deposits very early in the compression stroke and lead to more rapid heat release and rises of cylinder temperature and pressure (Heywood 1988). The knock originated from surface ignition cannot be controlled or mitigated effectively by the methods mentioned above.

2.2.3 The knock models

The modelling of end gas autoignition consists of two major categories: empirical correlations and chemical kinetics modelling (Heywood 1988). The experimental methods and empirical correlations are used to study end gas autoignition when the fundamental understanding of the chemistry involved were incomplete. Over the years, chemical kinetics modelling attracts more and more attention in the study of end gas autoignition, thanks to both improved understanding of autoignition chemistry and greatly advanced computational power. Numerical modelling provides a simple and cost-effective way of study end gas autoignition, compared to experimental methods.

Empirical correlations

The empirical expression for autoignition is derived by matching an Arrhenius function to measured data obtained from ignition delay time experiments. For a given fuel-oxidizer mixture under the conditions of $\boldsymbol{P}$ and $\boldsymbol{T}$, the ignition delay time is expressed as:

$$\boldsymbol{\tau} = \boldsymbol{A} \cdot \boldsymbol{P}^{-\boldsymbol{n}} \cdot \boldsymbol{EXP}(\boldsymbol{B}/\boldsymbol{T}) \qquad \textbf{(2-11)}$$

where $\boldsymbol{A}$ and $\boldsymbol{B}$ are fitting parameters dependent on fuel types and are obtained based on experimental results. A reaction progress coefficient, $\boldsymbol{c}$, is integrated to predict the occurrence of knock with temporal histories of temperature and pressure (Bray et al. 1994). Autoignition is deemed to occur when $\boldsymbol{\tau}$ exceeds a threshold value. Douaud and Eyzat (1978) proposed a correlation that has been extensively tested and widely accepted:

$$c = 17.68 \cdot (\frac{ON}{100})^{3.402} \cdot P^{-n} \cdot EXP(3800/T) \tag{2-12}$$

where τ is the induction time in milliseconds and ON is the octane number of the fuel. Empirical autoignition correlations in this form can be used in S.I. engine models. Although the correlations, by their own, are extensively tested, their ability of accurately predicting knock is still unclear in practice. Additionally, these correlations are too simple to prove any information on the reaction process.

Chemical kinetics modelling

The autoignition is a complex chemical process that involves hundreds of species and thousands of elementary reactions. Autoignition of simpler fuels, e.g. hydrogen, may include around 10 species and 20 reactions (O Conaire et al. 2004), while that of heavy hydrocarbon fuels, e.g. n-heptane, can contain more than 500 species and 3000 reactions (Curran et al. 1998).

In order to obtain complete predictions of any autoignition process, one should have all the reaction rate constants and elementary reaction steps in hand and powerful computational resource at acceptable cost. At the present time none of the above two requirement is fulfilled: the understanding of the elementary steps and rate constants is still lacking, the high performance computers are too costly to be widely used.

However, chemical kinetics modelling has still been greatly advanced in the past a few decades and is becoming an essential tool in the design and research of combustion systems. Westbrook and Dryer (1984) attributed the advancement of chemical kinetics modelling to the following factors:

1. Larger amount of elementary kinetic data becomes available.

2. Improvement in reaction rates estimation.

3. Development of faster and more reliable numeric algorithms.

4. Continuous advancement of computers

More information with regards to chemical kinetics and its applications in hydrogen and hydrocarbon oxidation studies is available in later chapters.

2.3 Laminar flames

Laminar flames are of great importance in the study of IC engine combustion. Premixed laminar flames can be adequately described by precise definitions of the following aspects: inner flame structures; flame thickness; dynamics of flame and flame stretch (Groot 2003).

2.3.1 Laminar flame structure

According to the temperature and species concentration gradients, a premixed flame can be considered to consist of three distinctive layers: the pre-heat layer, the inner layer and the oxidation layer, as shown in ***Fig. 2-4***. During combustion the flame acts as a conversion layer that lies between the unburnt zone, where a large amount of fuel and oxidiser present, and the burnt zone, whereas the amount is significantly reduced. In the detailed structure of a flame, the temperature increases smoothly from the initial in the pre-heat zone to its final state inside the oxidation layer. The concentrations of the intermediates and products will change in a similar manner, whereas the concentrations of fuel and oxidiser show a significant decrease.

The pre-flame layer refers to the unburnt mixtures that are immediately upstream of the inner layer. Chemical reactions within this layer proceed with very slow reaction rates and can be considered as chemically inert. The unburnt mixture is heated up by the heat flux from the reaction layer. In general, the pre-flame zone can be seen as a mixture preparation zone for the reaction layer.

The reaction zone is further divided into two sub-layers: the inner layer and the oxidation layer. In the inner layer, or often referred as fuel-consumption layer, fuel is consumed and converted into hydrogen and carbon monoxide, and active radicals are depleted by chain-breaking reactions. The inner layer makes most of the visible part of the flame and the visibility is due to those electronically-excited light-emitting species, such as CH, CN, C_2, and CHO, returning to their ground state. The inner layer is the thinnest compared to pre-flame layer and oxidation layer, typically by the order of one fifth to one tenth (Peters 1991). Majority of the energy is released within the inner layer and therefore the temperature gradient within the inner layer is the sharpest amongst the three layers. The combustion intermediates hydrogen and carbon monoxide reach their maximum concentrations within the inner layer.

The oxidation layer is located downstream of the reaction layer. Within the oxidation layer carbon monoxide and hydrogen are further oxidised into carbon dioxide and water. Thermodynamic equilibrium of all species is established in the oxidation layer rather than the inner layer as the residual time is not sufficient. Chemical reactions occur in the oxidation layer are often referred to as post-flame reactions and they play an important role in the products formation and the overall heat release of the combustion.

2.3.2 Laminar flame thickness

Flame thickness is an important scale parameter of any premixed laminar flames that it represents the depth of the reaction zone in which the fuel is consumed and bulk of heat is released. A classical definition of flame thickness $\boldsymbol{\delta_f}$ is based on a geometrical approach, as shown in ***Fig*. 2-5**. In this case, the thickness is defined as the interval of the steepest tangent to the temperature profile between the unburnt temperature and the adiabatic flame temperature (Heywood 1988):

$$\boldsymbol{\delta_f = \frac{T_{ad} - T_u}{(dT/ds)_{T_{il}}}} \qquad \textbf{(2-13)}$$

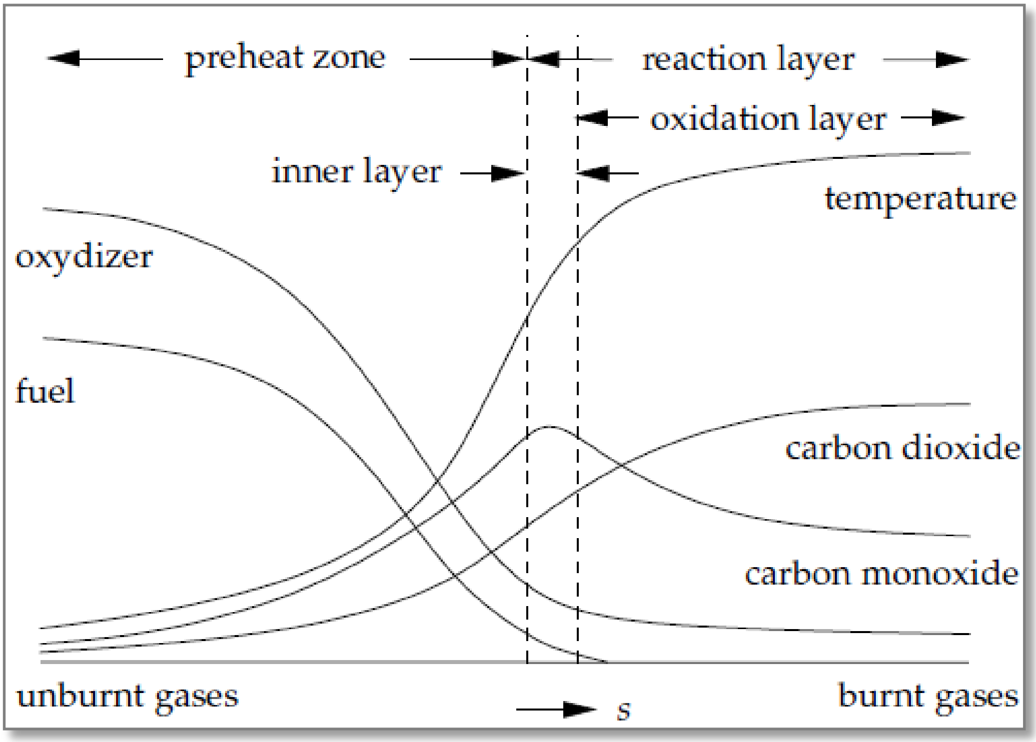

Fig. 2-4 Schematic illustration of a premixed flame structure with s represents the coordinate perpendicular to the flame surface (Gottgens J, Mauss F 1992).

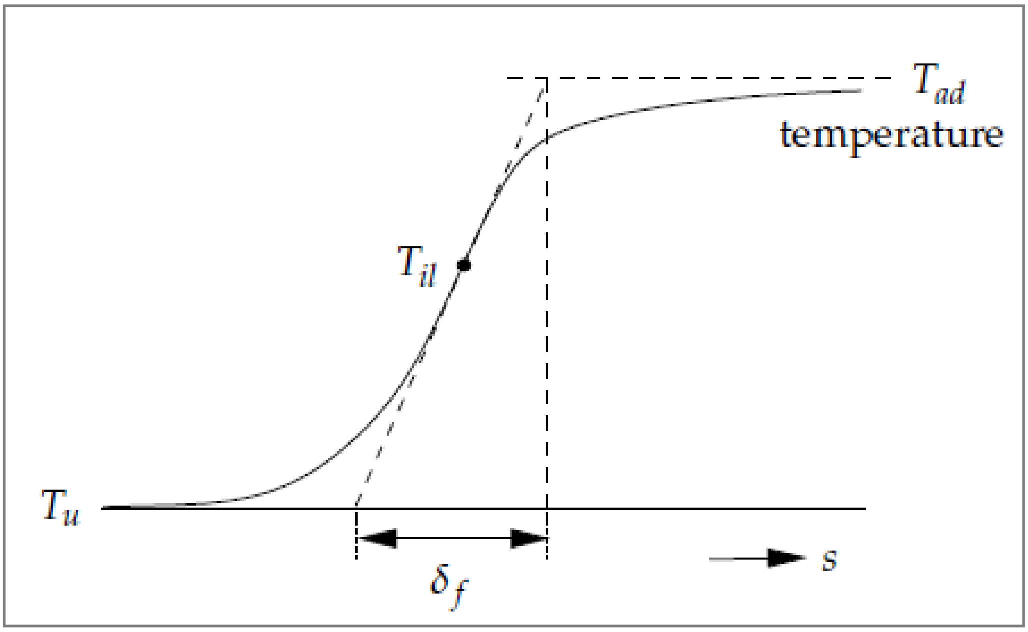

Fig. 2-5 Geometrical definition of premixed laminar flame thickness with s represents the coordinate perpendicular to the flame surface (Gottgens J, Mauss F 1992).

Flame thickness is crucial for the propagation and stability of the flame. The temperature and species concentration gradient are shaper across the flame front when the flame is thin. These shaper gradients provide stronger driving forces that enable the flame to be self-sustaining, i.e., fast and stable diffusion of heat and radical species from the reaction zone to preheat zone (Gottgens J, Mauss F 1992). The flame thickness itself in turn is a function of several other parameters. One of the most influential parameters is the equivalence ratio. Andrews and Bradley (1972b) found that the thickness of methane-air flames is at its thinnest when the mixture is slightly rich, which matches the observation that the laminar burning velocity is at its maximum in slightly rich mixtures.

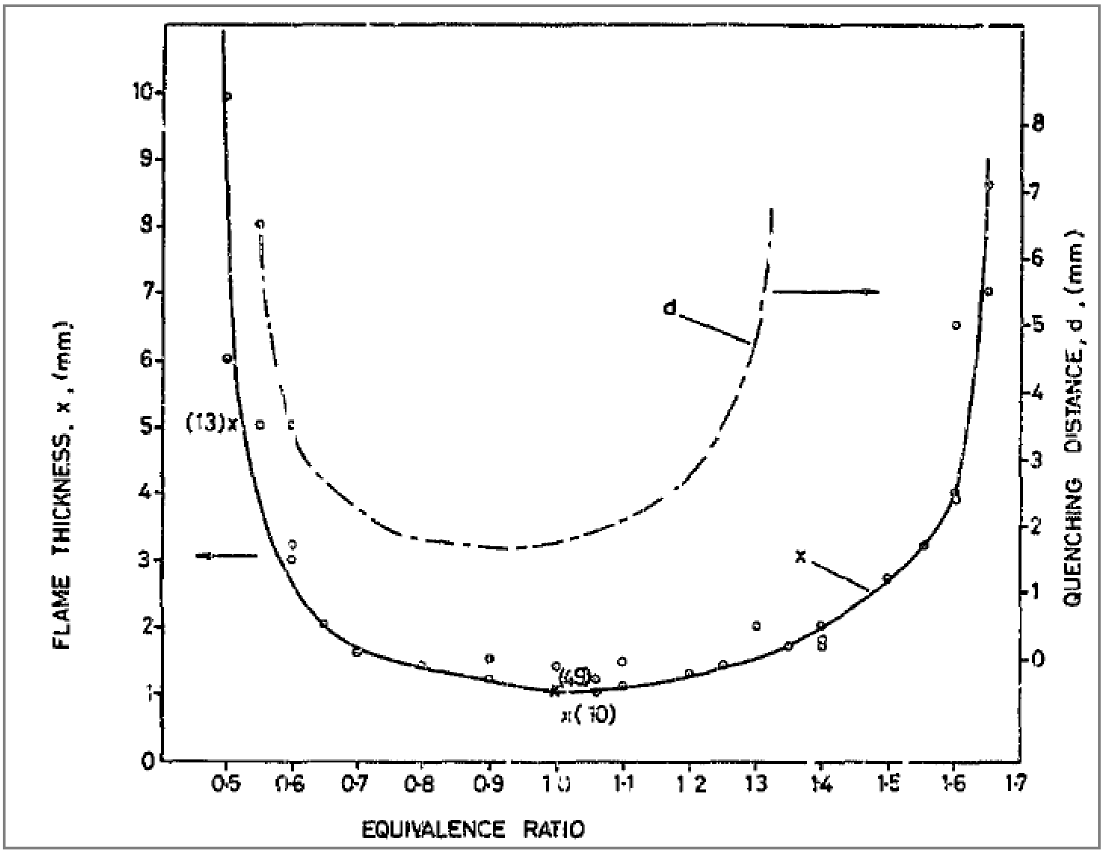

Fig. 2-6 Variation of flame thickness of premixed laminar methane-air flames at different fuel-air equivalence ratios (Andrews & Bradley 1972b).

2.3.3 Laminar burning velocity

The laminar burning velocity, denoted as $\boldsymbol{u_L}$, is one of the most fundamental and important properties of premixed flames. It can be defined as the velocity at which a flame front moves in the normal direction to its surface into the adjacent unburnt mixture due to chemical reactions and the diffusion of heat and mass (Groot 2003). Previous research on laminar burning velocities of various fuels revealed that there are a few dominating parameters that strongly influence the laminar burning velocity (Iijima & Takeno 1986; Liu et al. 2013; Metghalchi & Keck 1982; Bradley et al. 1996; Dowdy et al. 1991; Gu et al. 2000; Gülder 1982; Hu et al. 2009a; Metghalchi & Keck 1980; Milton & Keck 1984; Rahim et al. 2002):

Fuel-air equivalence ratio: the fuel-air equivalence ratio, denoted as $\boldsymbol{\Phi}$, determines the chemical composition the thermo-physical properties of the mixtures, and thus strongly affects the chemical reaction rates and combustion efficiency. Experimental studies show that laminar burning velocity reaches its maximum value under stoichiometric or slightly rich mixtures for hydrocarbon fuels and decreases rapidly if the mixtures are further diluted or enriched, as shown in ***Fig. 2-7***:

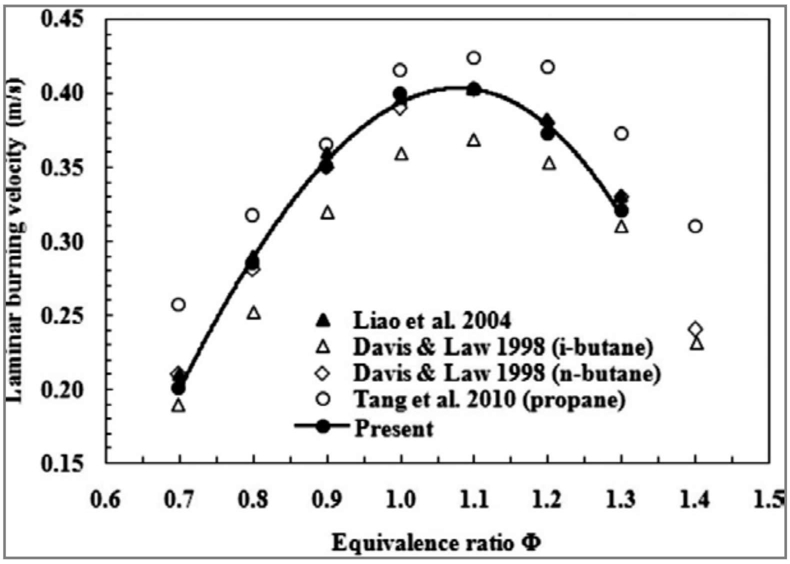

Fig. 2-7 Variations of laminar burning velocities of different hydrocarbon fuels (LPG, i-butane, n-butane and propane) (Akram et al. 2013).

Similar trends are found for other hydrocarbon fuels by Warnatz (1992) and the rapid decrease of laminar burning velocity in either side of stoichiometry has been attributed to the fact that it becomes more difficult for the flame to maintain its deflagrative wave and propagate forward.

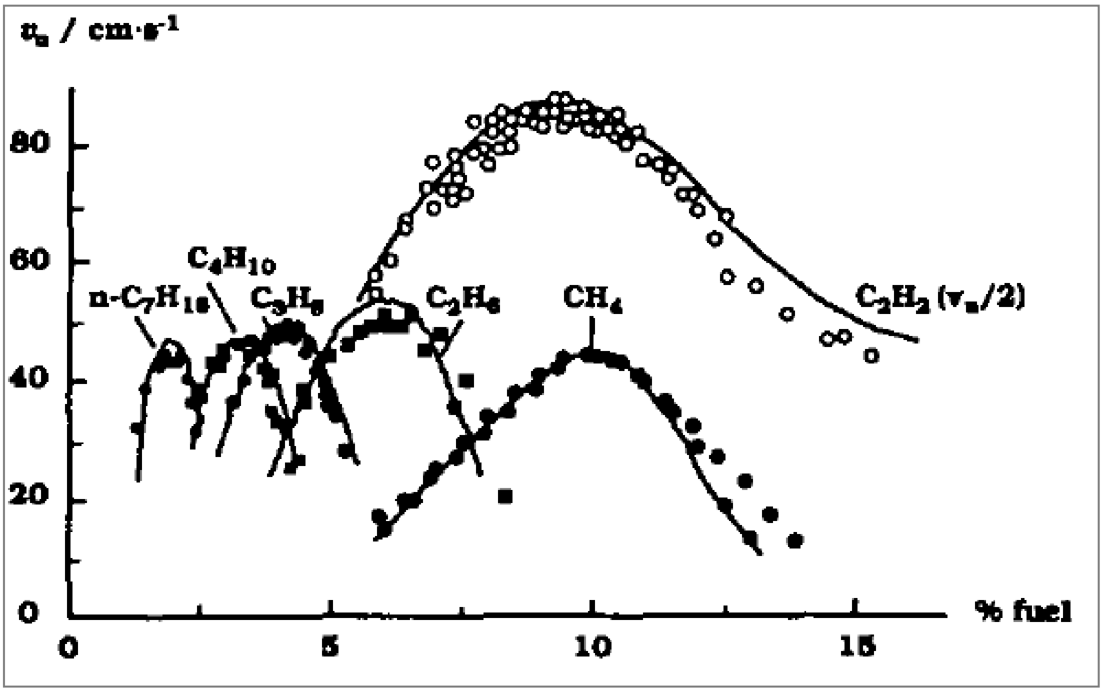

Fig. 2-8 Variations of laminar burning velocities of different hydrocarbon fuels (n-C_7H_{18}, C_4H_{10}, C_3H_8, C_2H_6, C_2H_2 and CH_4) against fuel-air equivalence ratio (Warnatz 1992).

However, research on non-hydrocarbon fuels showed a completely different trend of the laminar burning velocity. ***Fig. 2-9*** plots the laminar burning velocities of hydrogen-air flames obtained by different researchers against air-fuel equivalence ratio (λ<1 for rich mixtures). It's clearly shown that rich hydrogen-air flames attain maximum laminar burning velocity at approximately λ = 0.6, i.e., Φ = 1.7. The noticeable scatter in laminar burning velocities, particularly for very lean mixtures, is attributed to the effects of flame stretching and cellular instabilities on the flames, as some results shown (filled symbols) are stretch-free velocities that have been corrected for flame stretch while others (open symbols) are based on measurements that did not account for the flame stretching effect. The effects of both flame stretch and cellular instabilities will be reviewed and discussed in detail later in this chapter.

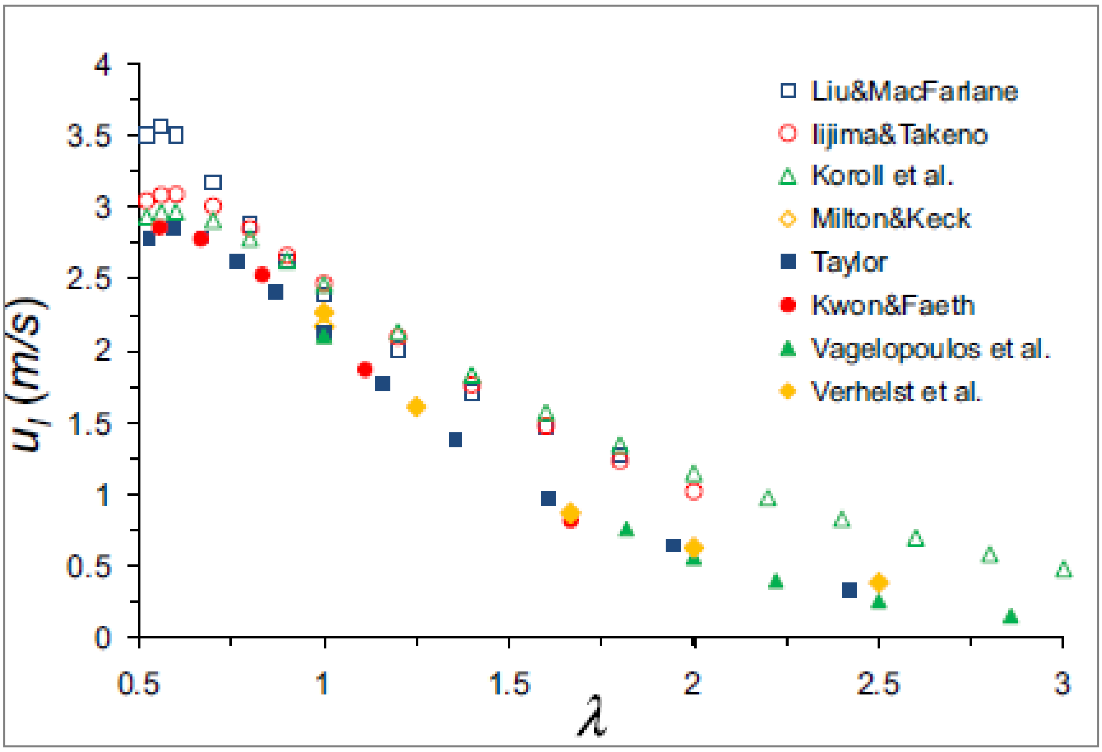

Fig. 2-9 Variations of laminar burning velocities of premixed hydrogen-air flames against air-fuel equivalence ratio (λ<1 for rich mixtures) at NTP (Verhelst et al. 2011).

Unburnt temperature: the unburnt temperature has great influence on the laminar burning velocity. Chemical reactions involved in oxidation of typical hydrocarbon fuels are extremely temperature sensitive as they are naturally kinetically-driven. Higher unburnt mixture will cause pre-heating effect on the mixture and results in higher chemical reactivity and therefore fast laminar burning velocity. Kuo (2005a) suggested a relationship between laminar burning velocity and unburnt temperature:

$$u_L \propto T_u^m \qquad \textbf{(2-14)}$$

where the exponent m ranges between 1.5 to 2 for different types of fuels.

Sensitivity analysis of key elementary reactions of methane oxidation mechanism performed by others (Hu et al. 2009a)(Hu et al. 2009b), as shown in ***Fig. 2-10***, reveal that the combustion of hydrocarbon and hydrogen is dominated by the competition of the key chain branching reaction which contributes to the production of highly active radicals:

$$\mathbf{H + O_2 \leftrightarrow O + OH}$$

and the key chain termination reactions which are responsible of the reduction of these highly active radicals:

$$\mathbf{H + O_2 + H_2O \leftrightarrow HO_2 + H_2O}$$

$$\mathbf{H + CH_3 + M \leftrightarrow CH_4 + H_2O}$$

The chain branching and termination reactions show high sensitivities to initial temperature changes but the sensitivities are reduced as the initial temperature is further increased, and such behaviour indicates that the reaction rates of these dominating reactions are more influential on the overall reaction under lower initial temperatures. ***Fig. 2-11*** and ***2-12*** illustrate the reaction rates and their change rates of the chain branching and termination reactions. Both reaction rates plotted in ***Fig. 2-11*** increase with the increment of initial temperature so it is difficult to conclude whether it’s the chain branching or the chain termination reaction that is more dominating in the scenario of increasing temperature. Therefore, it is necessary to investigate the change rates of the reaction rates of these two key reactions. In ***Fig. 2-9*** it can be clearly seen that the change rate of the chain branching reaction rate is higher than that of the chain termination reaction, such phenomenon results in concentration increases of highly reactive radicals in the mixture and enhance the laminar burning velocity.

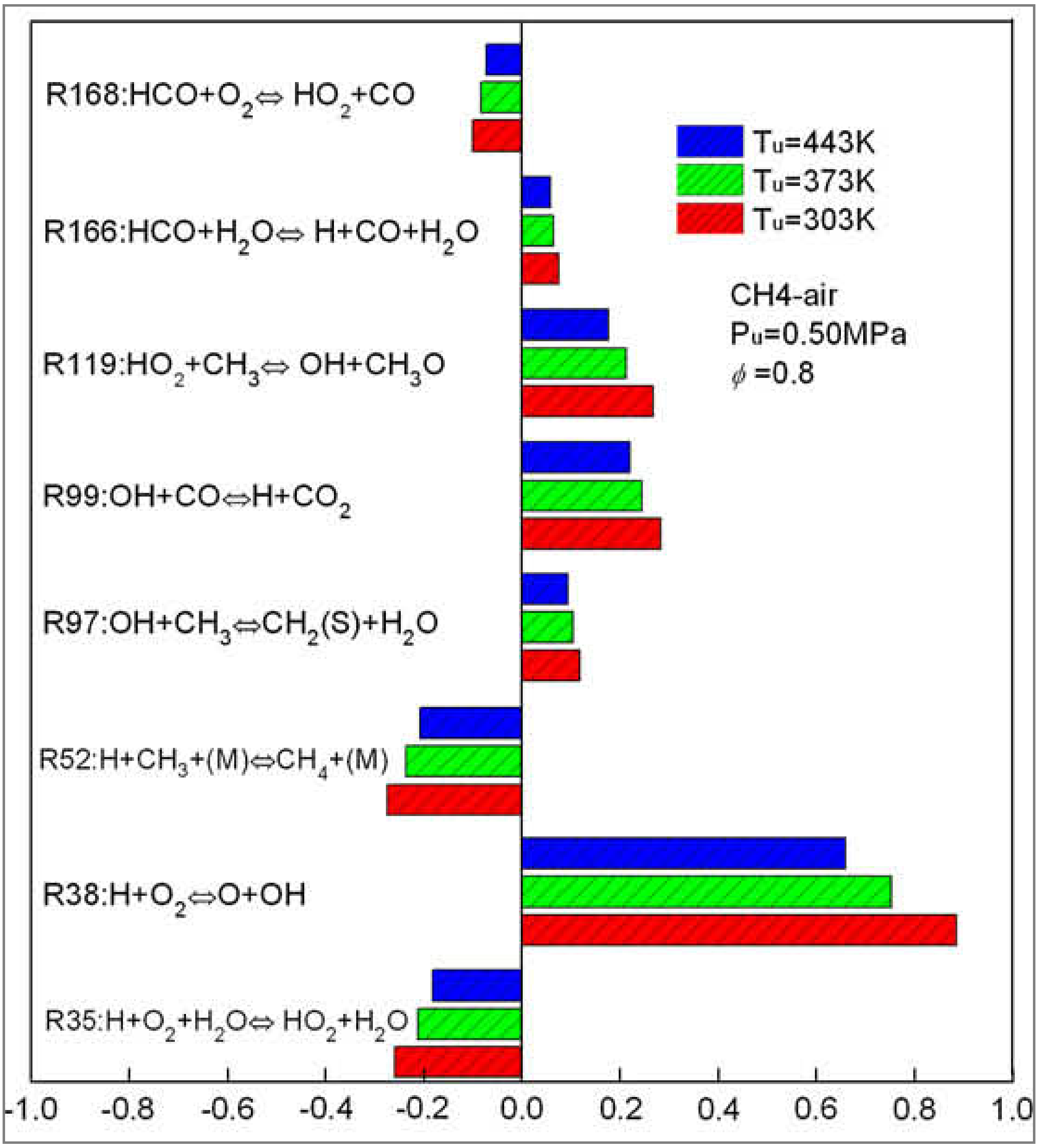

Fig. 2-10 Sensitivity factors of some key elementary reactions in methane oxidation mechanism under different initial temperatures (Hu et al. 2009b).

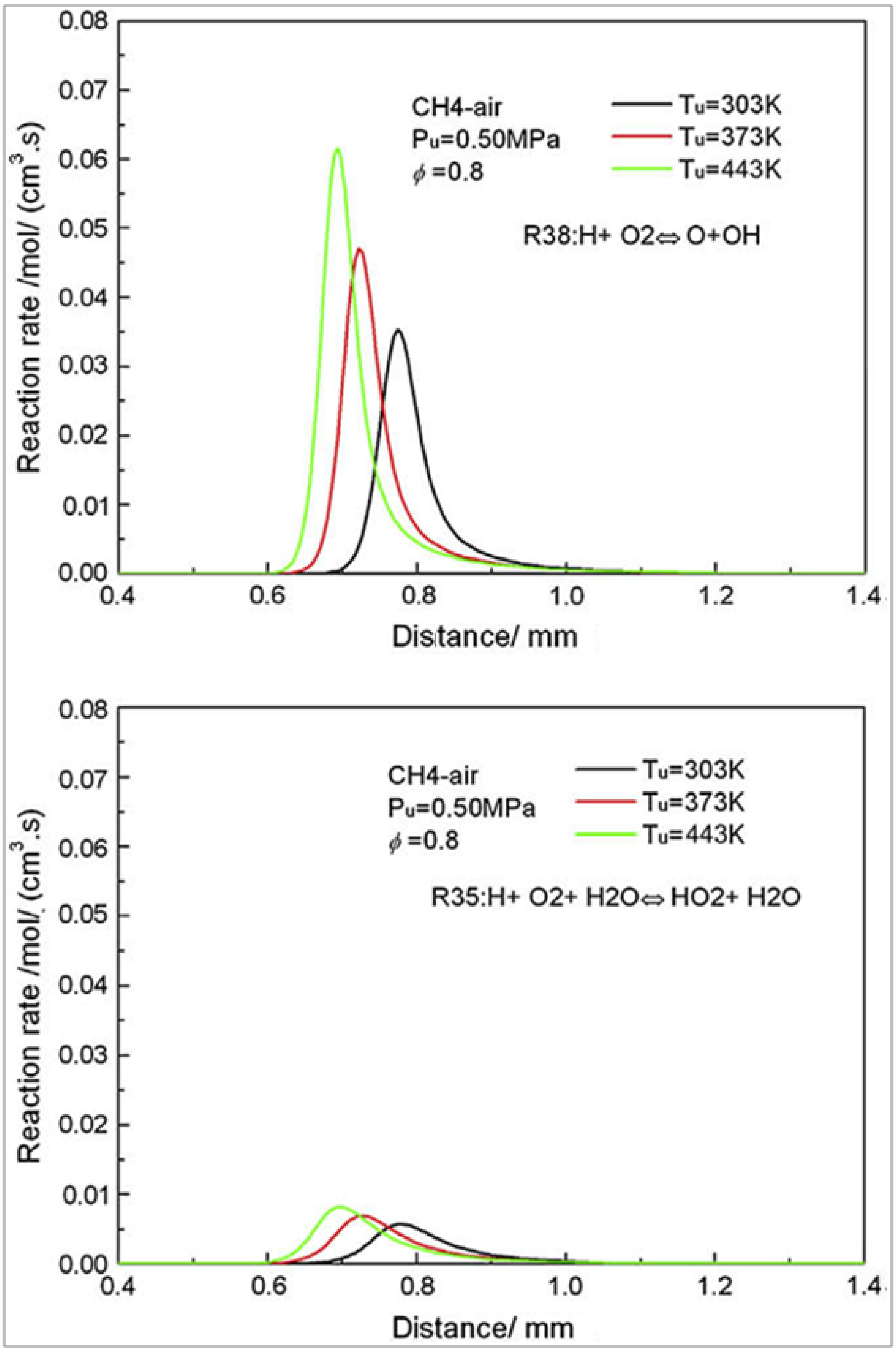

Fig. 2-11 Profiles of reaction rates of dominating chain branching (upper) and terminating (lower) reactions of methane oxidation mechanism under increasing initial temperature (Hu et al. 2009b).

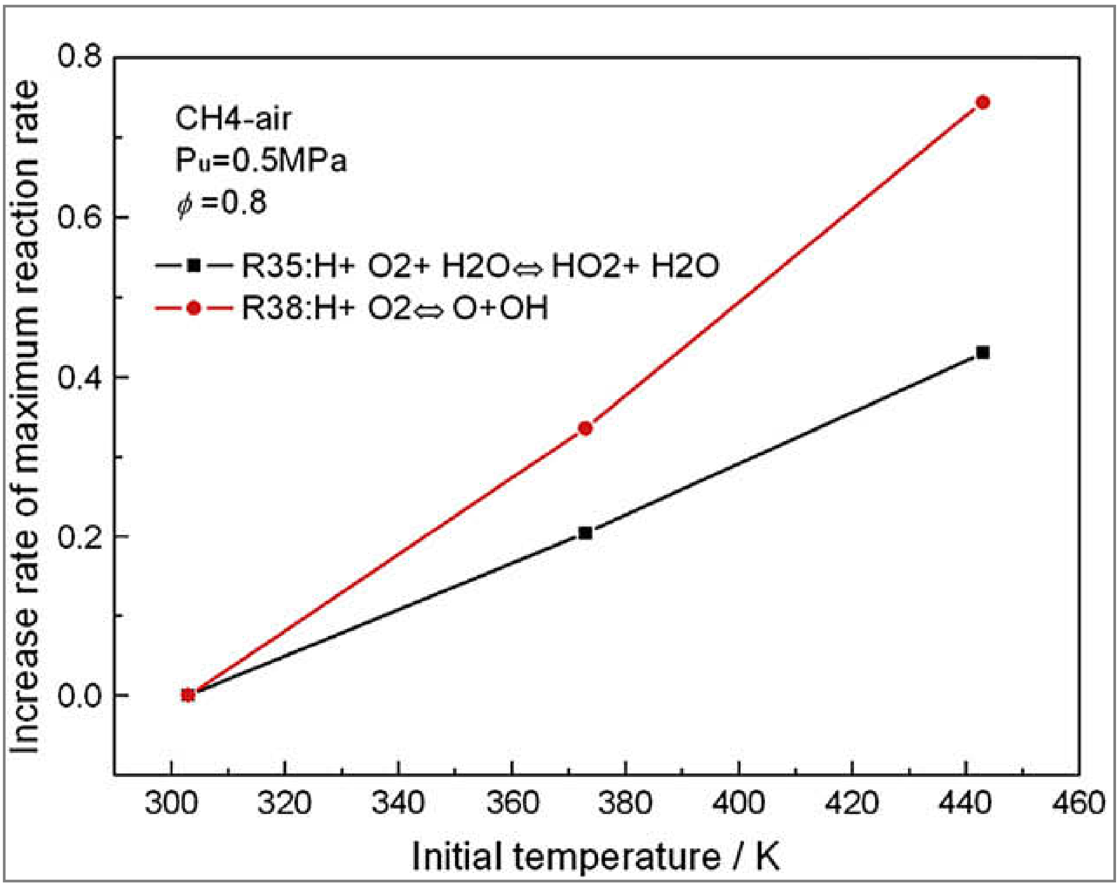

Fig. 2-12 Increase rates of reaction rates of dominating chain branching (R38) and terminating (R35) reactions of methane oxidation mechanism under increasing initial temperature (Hu et al. 2009b).

Unburnt pressure: the unburnt pressure is less influential than the unburnt temperature does but still has noticeable effect on the laminar burning velocity. Theoretically, increasing pressure will increase the collision rates of reacting molecules and thus increase the overall reaction rate (House. 2007), which should results in enhanced laminar burning velocities. However, previous research showed that laminar burning velocities of both non-diluted and diluted mixtures decrease exponentially with increasing pressure (Andrews & Bradley 1972b)(Verhelst et al. 2011)(Hu et al. 2009b)(Tang et al. 2008). Sensitivity analysis of key elementary reactions of methane oxidation mechanism performed by Hu et al., (2009a)(2009b), as shown in ***Fig. 2-14***, revealed that the combustion of hydrocarbon and hydrogen is dominated by the competition of the key chain branching reaction which contributes to the production of highly active radicals:

$$\mathbf{H + O_2 \leftrightarrow O + OH}$$

and the key chain termination reactions which are responsible of the reduction of these highly active radicals:

$$\mathbf{H + O_2 + H_2O \leftrightarrow HO_2 + H_2O}$$

$$\mathbf{H + CH_3 + M \leftrightarrow CH_4 + H_2O}$$

As the pressure is increased both reactions show significant sensitivity to the pressure change, indicating that both reactions have great influence on the laminar burning velocity. Further investigation on the sensitivity of reaction rates on pressure change of reactions $\mathbf{H + O_2 \leftrightarrow O + OH}$ and $\mathbf{H + O_2 + H_2O \leftrightarrow HO_2 + H_2O}$ reveal that the reaction rates of both chain branching and termination reactions are increased as the initial pressure is increased, as shown in ***Fig. 2-15***. However, ***Fig. 2-16*** shows that the increase rates of these two reaction rates are not identical. It can be clearly seen that with the increasing initial pressure the reaction rate of the chain termination reaction increases much faster than that of the chain branching reaction does. Such behaviours result in a rapid reduction in the concentrations of highly reactive radicals in the mixture. This reduction has been closely related to the retardation of the laminar burning velocity by other researchers (C.K. & F.L. 1981; Westbrook & Dryer 1980). Above discussions on the effects of temperature and pressure on the laminar burning velocity show that the laminar burning velocity is predominantly controlled by the concentration variations of the highly reactive radicals, which is vastly influenced by the highly temperature- and pressure-sensitive chain branching and termination reactions. The chain branching and termination reactions can be enhanced relative to each other by the variations of temperature and pressure, respectively, to increase and decrease the laminar burning velocity.

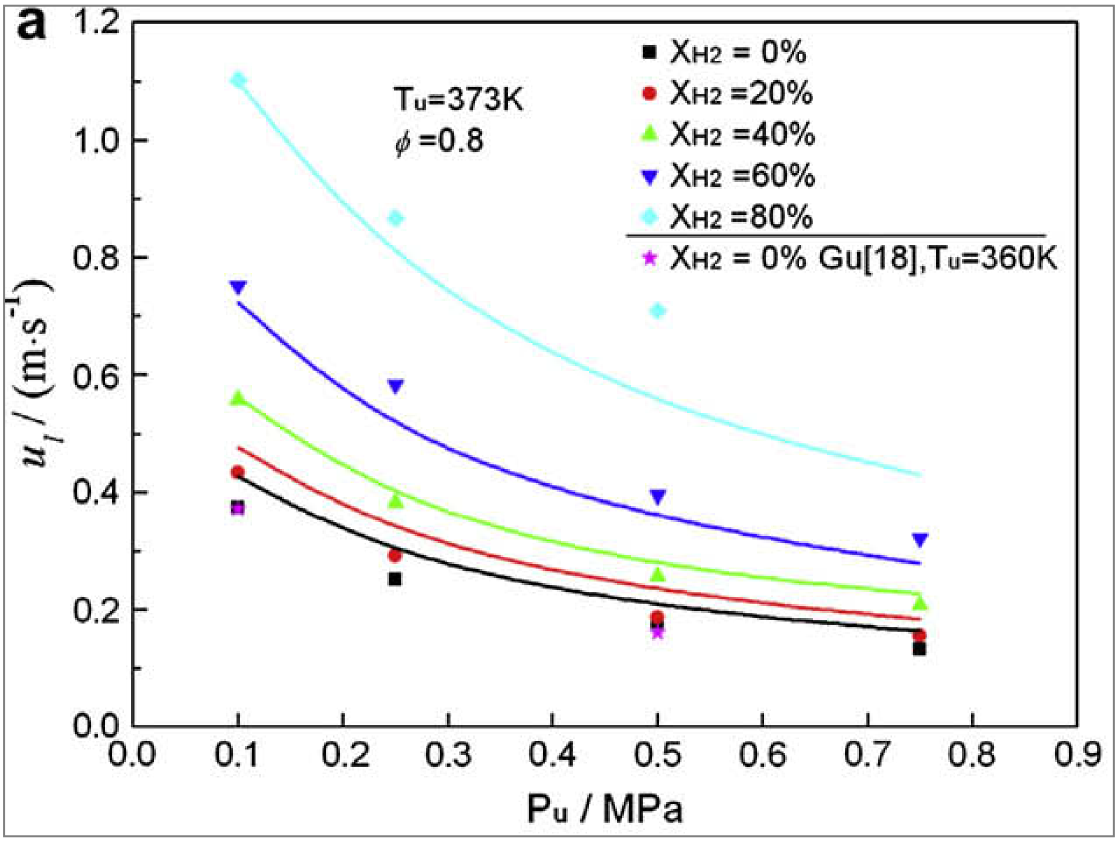

Fig. 2-13 Illustrations of experimental and numerical results of laminar burning velocities of methane-air mixtures at different temperatures, pressures and levels of hydrogen dilution (Hu et al. 2009b).

Residual gas fraction: in practical internal combustion engine usage, exhaust gas is often re-introduced into the combustion chamber in order to reduce emissions (Heywood 1988). The water vapour and CO_2 constituent within the exhaust gas are of high heat capacity and therefore can absorb larger amount of heat during the combustion and effectively reduce the peak cylinder temperature. Lowering the combustion temperature slows down the kinetically-driven chemical reactions and therefore reduces the laminar burning velocity. Ponnusamy et al. (2005) experimentally observed significant reduction in laminar burning velocity with increasing EGR fraction, as shown in **Fig. 2-17**. The 'simulated' exhaust gas used by

Ponnusamy et al. consists of 81.5% N_2 and 18.5% CO_2 as it is impractical to introduce liquid water or water vapour into the combustion chamber during the intake procedure.

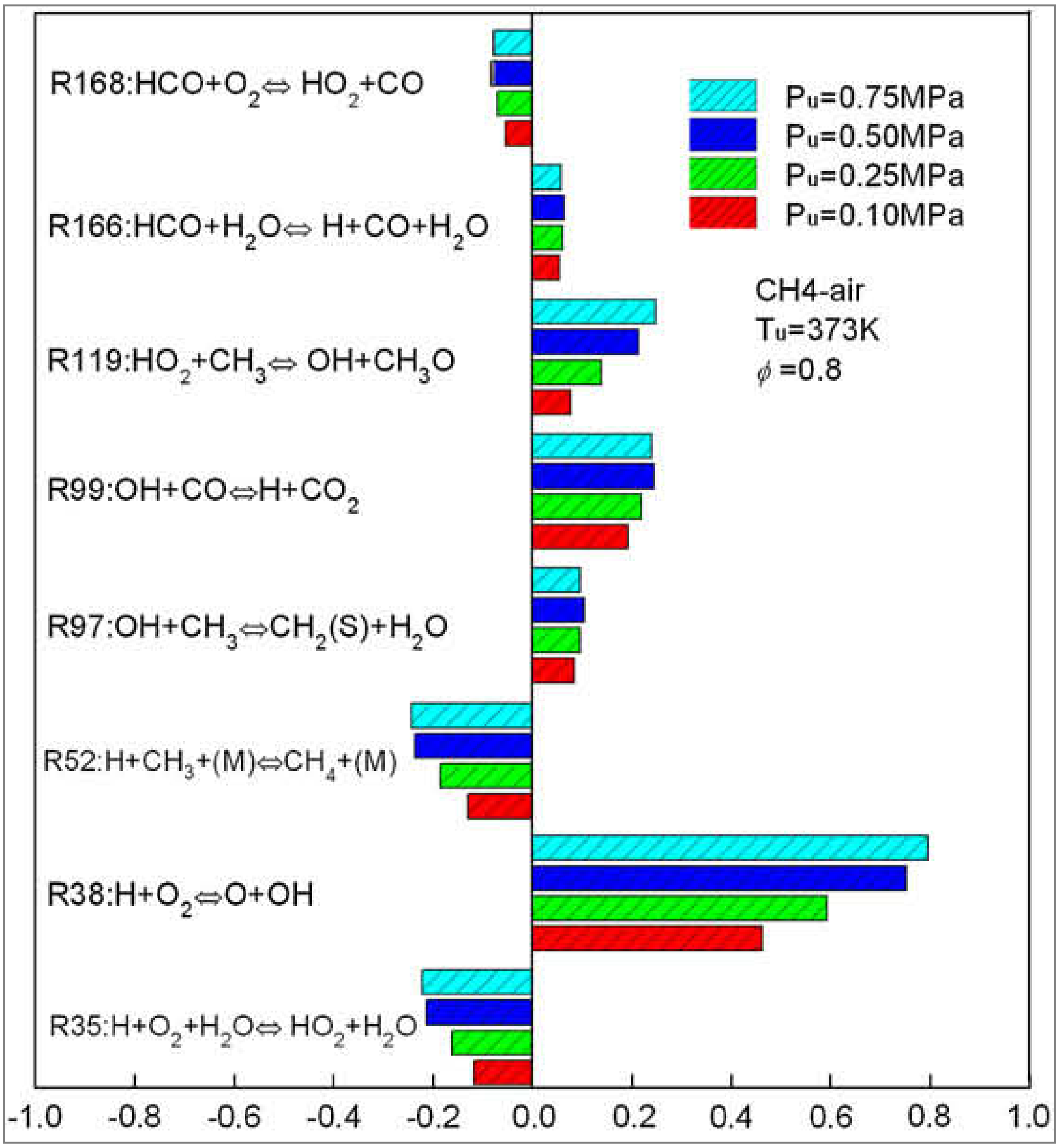

Fig. 2-14 Sensitivity factors of some key elementary reactions in methane oxidation mechanism under different initial pressures (Hu et al. 2009b).

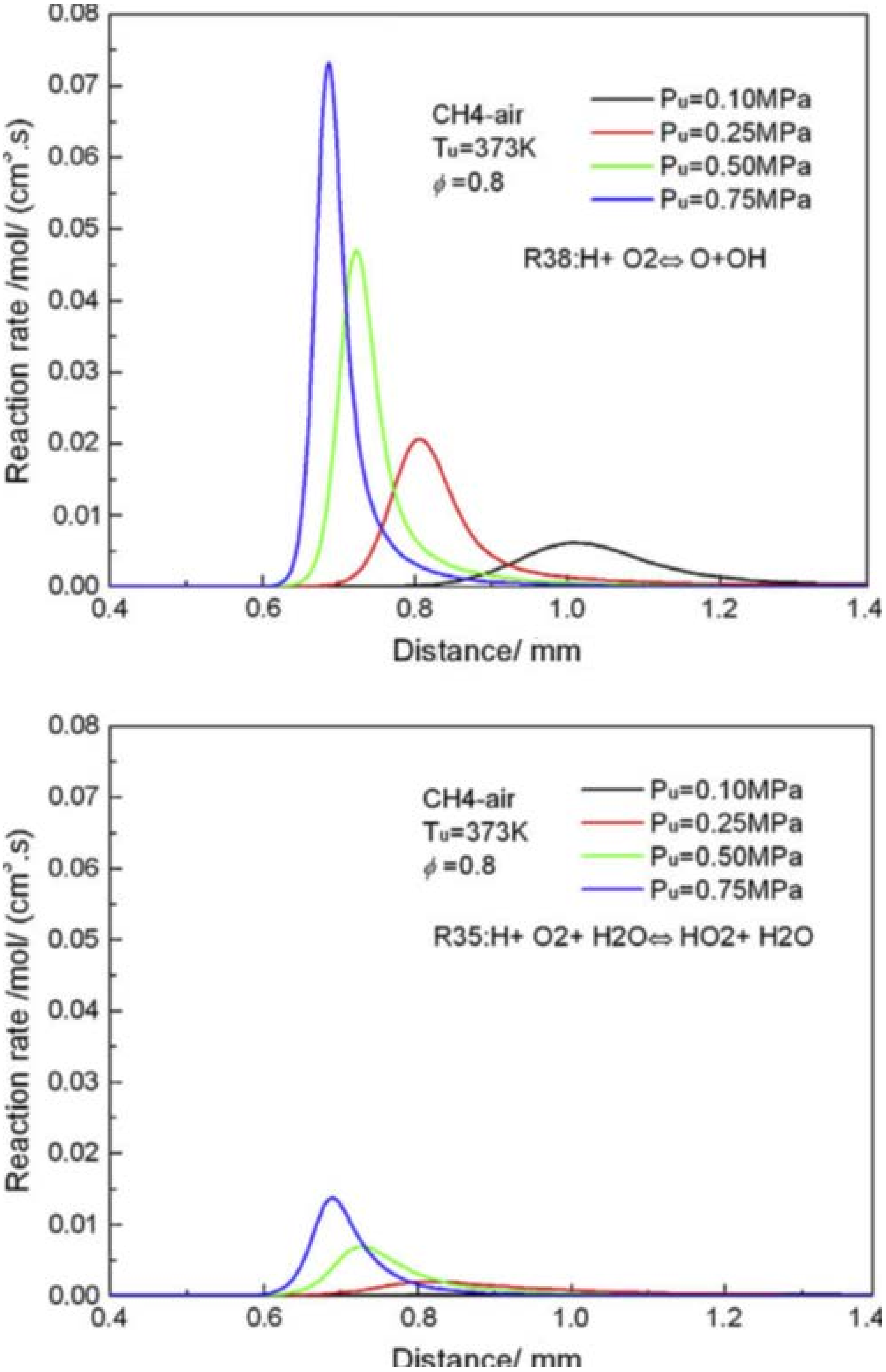

Fig. 2-15 Profiles of reaction rates of dominating chain branching (upper) and terminating (lower) reactions of methane oxidation mechanism under increasing initial pressure (Hu et al. 2009b).

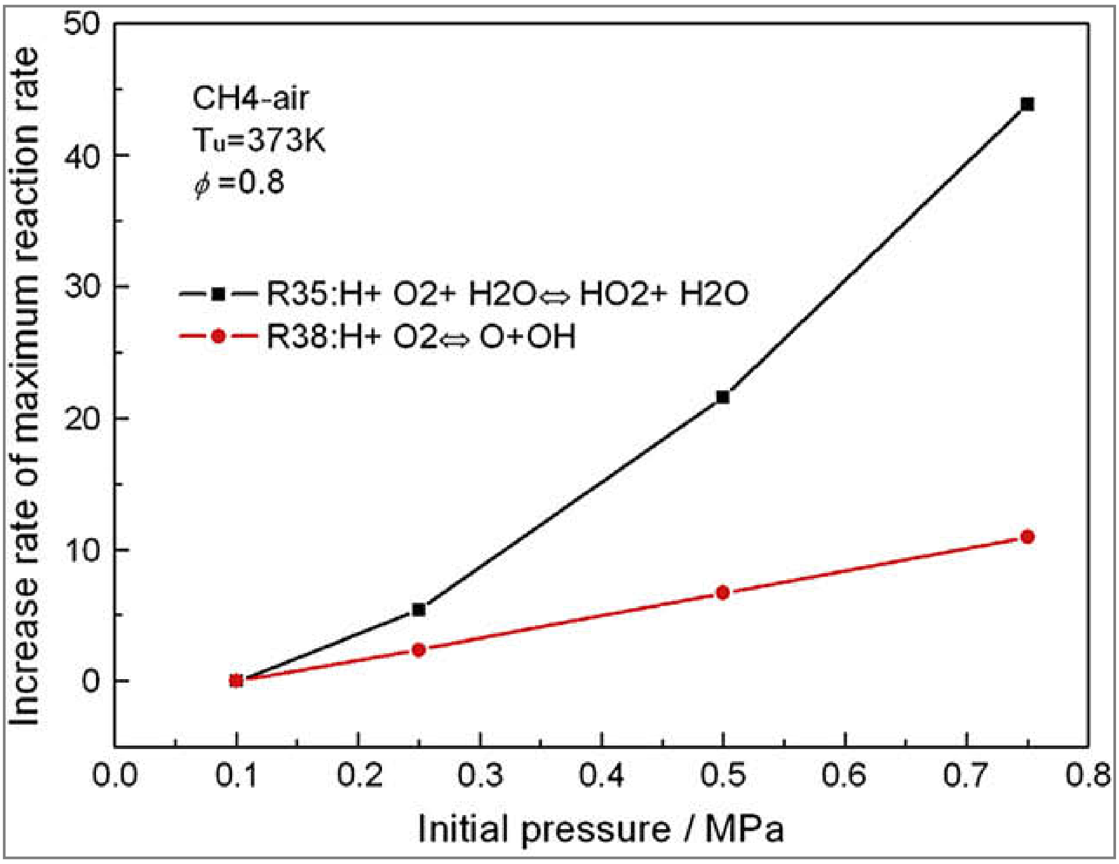

Fig. 2-16 Increase rates of reaction rates of dominating chain branching (R38) and terminating (R35) reactions of methane oxidation mechanism under increasing initial pressure (Hu et al. 2009b).

However the specific het capacity, denoted as c_p, of these 'simulated' exhaust gases is kept within 1% of that for realistic methane-air combustion products (Ponnusamy et al. 2005) and therefore reproduces the cooling effect of the EGR well.

A linear fit yields a reduction of 1.9m/s of laminar burning velocity for every additional percentage of EGR for stoichiometric methane-air flame. The reduction of laminar burning velocity is attributed to the increased c_p, resulted from the presence of the exhaust gases, that brings down the flame temperature.

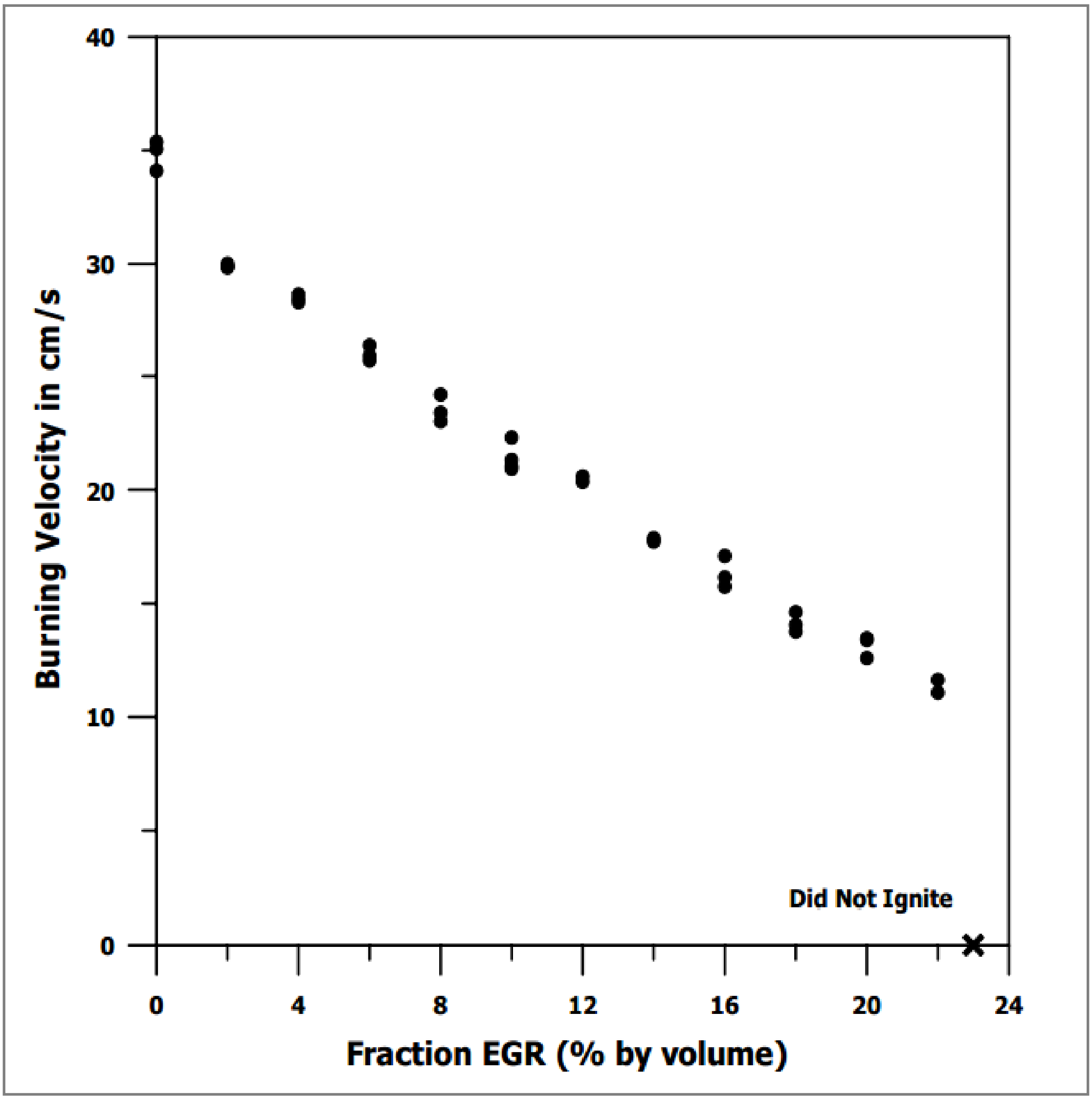

Fig. 2-17 Variation of the laminar burning velocity of stoichiometric methane-air flame against different volume fraction of EGR (Ponnusamy et al. 2005).

2.3.4 Flame stretch effect

Stretching of a flame can lead to variations of the fame behaviour compared to a flat flame with a purely one-dimensional flow and transport. Systematically understanding and numerically quantifying the effect of flame stretch are not only important for laminar flames but also for the study of turbulent flames. Karlovitz et al*.* (1953) was the first to introduce and develop the concept of flame stretch: 'if the flame surface is curved or it is non-stationary, as is commonly as a result of non-uniform flow and flame expansion, the flame surface suffers the effect of stretch'. The concept was originally developed to qualitatively account for the response of flames to the velocity gradients in the gas flow and to the curvature of the laminar flame surface. The generally accepted definition of the flame stretch rate, $\boldsymbol{K}$, is as follows:

$$\boldsymbol{K} = \frac{1}{A}\frac{dA}{dt} = \frac{2}{r_f}\frac{dr_f}{dt} \qquad \textbf{(2-15)}$$

It is a measure of the fractional rate of change of infinitesimal element of the flame surface area $\boldsymbol{A}$ that moves in the flame propagation speed. Matalon (1983) and subsequently Chung and Law (1984) derived a more manageable and concise expression for the flame stretch rate using the invariant formulation:

$$\boldsymbol{K} = \boldsymbol{\nabla} \cdot \boldsymbol{v^t} + (\boldsymbol{v_f} \cdot \boldsymbol{n_f})\, \boldsymbol{\nabla} \cdot \boldsymbol{n_f} \qquad \textbf{(2-16)}$$

where $\boldsymbol{v^t}$ is the flow velocity in the tangential direction of the flame surface and $\boldsymbol{n_f}$ represents the unit normal to the flame surface. The first term on the LHS of ***Eq. 2-16*** represents the contribution to flame stretch due to a non-uniform flow along the flame surface. A stagnation flame surface would be a typical example of a flame that experiences only the straining effect, $\boldsymbol{\nabla} \cdot \boldsymbol{v^t}$. The second term on the RHS represents the contribution due to the change in time of curvature of a flame surface. An example of a flame that only experiences the curvature effect, $(\boldsymbol{v_f} \cdot \boldsymbol{n_f})\, \boldsymbol{\nabla} \cdot \boldsymbol{n_f}$, is a perfect spherical outwardly expanding flame. That is to say the flame is not stretched if the flame front is stationary, i.e., $v_f = 0$, and meanwhile a gas flow in the perpendicular direction to the flame front, as in the case of a steady spherical flame or a flat flame with a uniform gas flow along the flame surface. Graphic illustration of above-mentioned cases are shown in ***Fig. 2-18***.

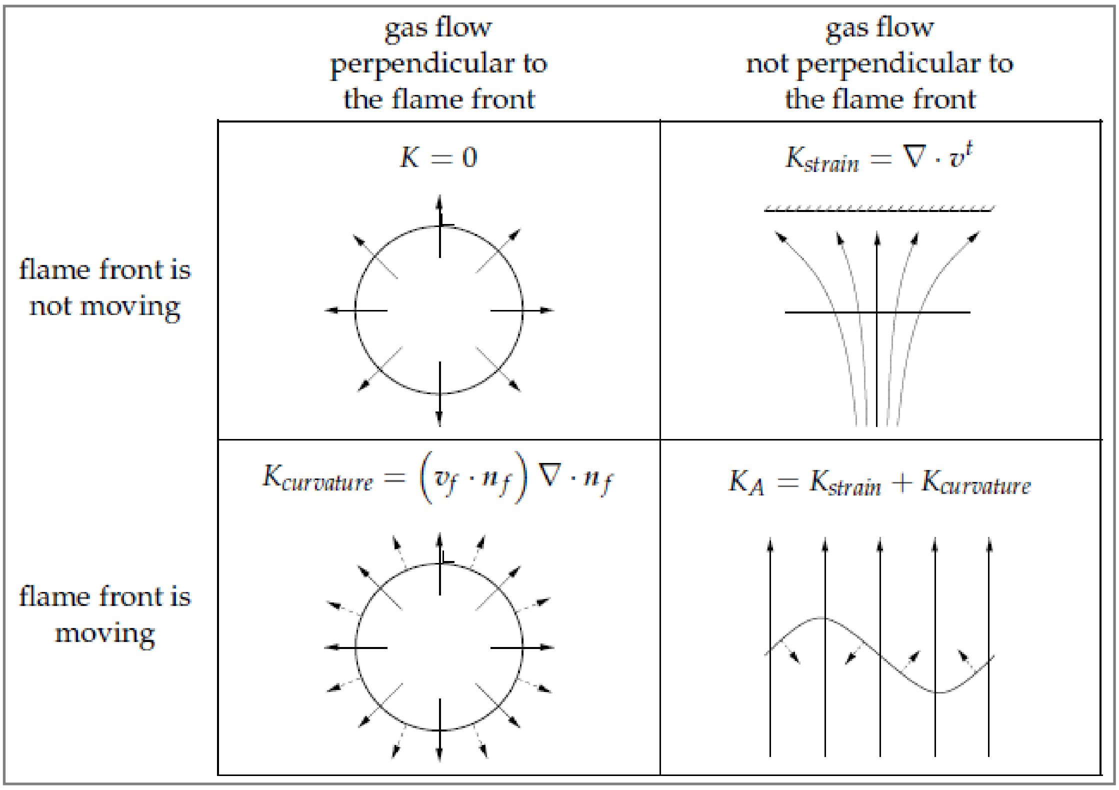

Fig. 2-18 An overview of different flame stretch effects on different types of flames. The continuous solid lines represent the flame surface. The continuous and the dashed arrows represent the velocity of the gas flow field and the flame front, respectively (Groot 2003).

Practically, the flame stretch rate of a spherical flame can be calculated using the instantaneous flame radius, r_f, and its rate of change, as shown in the RHS of ***Eq. 2-17***. Markstein (1964) further extended the flame stretch concept and claimed that the experimentally measured flame speeds are stretched flame speeds, S_n, and in order to calculate the unstretched flame speed, S_u, extrapolation procedures have to be conducted:

$$S_u - S_n = L_b K \tag{2-17}$$

where L_b is the Markstein Length of the unburnt mixture. S_u is obtained as the interception with the y-axis at K = 0. Value of L_b yields as the gradient of the line which represents the variation of measured flame speed, S_n, against K (Bradley et al. 1996; Bradley et al. 1998), as shown in ***Fig. 2-19***.

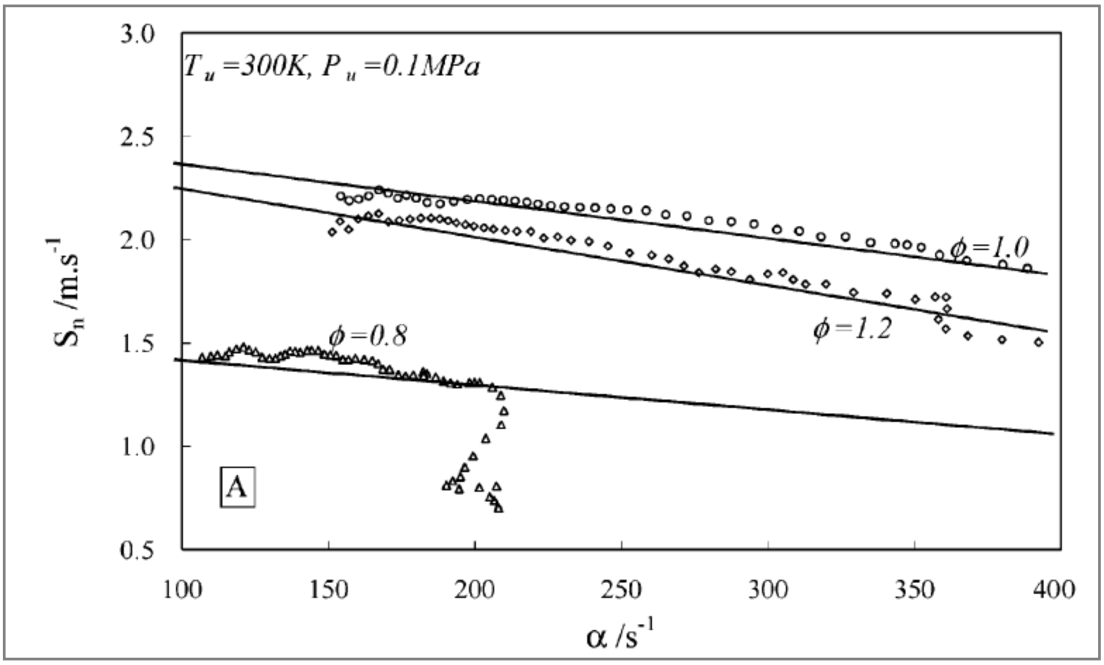

Fig. 2-19 Variations of stretched flame speeds under different equivalence ratios against flame stretch rate. The flame stretch rate is denoted as α in this case *(Andrews & Bradley 1996)* .

Bradley et al. (1972a) proposed a phenomenological law to account for two separate flame stretch effects that are respectively attributed to 1). Curvature at the cold front of a spherically outwardly propagating flame, 2). Flow field aerodynamic strain, and ***Eq. 2-17*** becomes:

$$S_u - S_n = L_c K_c + L_s K_s \tag{2-18}$$

L_c and L_c are Markstein Lengths associated with flame front curvature and the aerodynamic strain, respectively. K_c and K_s are the corresponding stretch rates.

Detailed methodology of deriving $\boldsymbol{S_u}$, $\boldsymbol{L_c}$ and $\boldsymbol{L_s}$ are stated by Bradley et al. (1972a). The two separate Markstein Lengths are usually combined into one single Markstein Length in practice, as proposed by Bechtold et al. (2001):

$$\boldsymbol{L = \delta[\alpha - (\sigma - 1)\gamma_1/\sigma]} \tag{2-19}$$

For the sake of convenience, the Markstein Length is often normalised by the flame thickness, $\boldsymbol{\delta_f}$, to give a dimensionless parameter Markstein Number, $\boldsymbol{Ma}$:

$$\boldsymbol{Ma = L/\delta_f} \tag{2-20}$$

The Markstein Number is very sensitive to fuel type, mixture strength and system pressure. Bechtold et al. (2001) measured the Markstein Number for different types of fuels at different equivalence ratios, as shown in ***Fig. 2-20***. The number of carbon contents in the fuel molecules have a dominant effect on Markstein Number. Fuels with higher carbon contents have higher Markstein Number and the Markstein Number decreases with increasing equivalence ratio, in a manner such that the higher the carbon contents the faster the Markstein Number decreases. However, simple hydrocarbon fuels such as Methane with only one carbon atom and non-hydrocarbon fuels such as Hydrogen show the opposite behaviour. Lean hydrogen-air mixtures also show negative Markstein Number which indicates the existence of negative flame stretch that is not found in hydrocarbon fuels.

The Markstein Number is also found to decrease with increasing pressure for stoichiometric and lean iso-octane/ air mixture (Bechtold & Matalon 2001). This phenomenon indicates a decreasing influence of the flame stretch on the laminar burning velocity at higher pressures. Increasing the temperature can partially restore the effectiveness of the flame stretch only at pressures higher than 2.5bar, and would otherwise worsen the effect of the flame stretch.

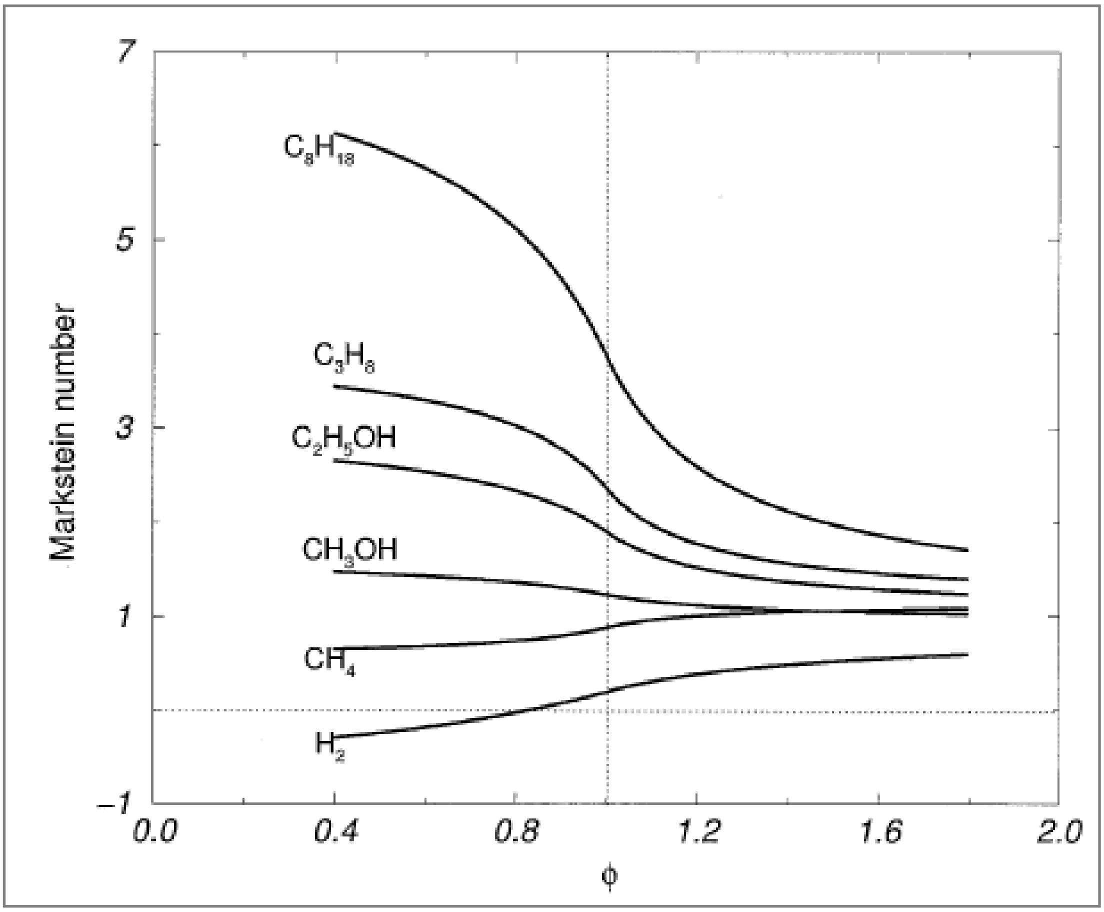

Fig. 2-20 Markstein Number of different types of fuel-air mixtures under different equivalence ratios (Bechtold & Matalon 2001).

Markstein Number has also been proven to have important influence on flame instabilities (Kwon & Faeth 2001). Although in S.I. engines the spark ignited flame will eventually become unstable and flame instabilities can enhance the burn rate, early destabilization is not favoured. Flames have higher Markstein Number, i.e., higher flame stretch rate, in the early stages of their growth and therefore it helps to stabilise the flames against hydrodynamic instabilities through the flame-stretch-induced thermo-diffusive effects. The larger the Markstein Number the greater the stabilization effect. As the flame grows the flame stretch decreases because of the reduction in surface curvature, so as the stabilization effect. Therefore the flame is more vulnerable to surface cellularity which eventually leads to self-turbulising. Early self-turbulising of flame can result in total distortion of flame surface and flame extinction and thus should be avoided. Negative Markstein Number is also found to be responsible for preferential-diffusion instability (Kwon & Faeth 2001).

Lewis Number is another key parameter in the studies of flame stretch. In one-step reaction mechanisms with large activation energies, Lewis Number is the differential diffusion of heat and deficient reactant (Kwon & Faeth 2001):

$$\boldsymbol{Le} = \frac{\boldsymbol{\lambda}}{\boldsymbol{\rho C_p D}} \qquad \textbf{(2-21)}$$

where the term $\boldsymbol{\lambda/\rho C_p}$ represents the thermal diffusivity of the mixture and the term $\boldsymbol{D}$ is the mass diffusivity of the deficient reactant. It has been long proven that cellular flames tend to form in mixtures that are deficient in the light reactants, such as in rich heavy hydrocarbon-air mixtures (n-heptane, iso-octane, etc) and lean light hydrocarbon-air mixtures (methane, hydrogen etc). The formation of cellular surface is partially due to thermo-diffusive instabilities, which is originally caused by competing effects of heat conduction from, and reactant diffusion into, the flame front. Smooth flame surface can be unstable when the mass diffusivity of the deficient reactant is greater than the heat diffusivity of the mixture, i.e., when $\boldsymbol{Le} < 1$ (Bechtold & Matalon 1987). Flames suffers thermo-diffusive instability can be unstable from the initial stage of propagation. Some researchers (Peters 2000) concluded that cellular patterns will form for $\boldsymbol{Le} < 1$ because the initial perturbation of the flame front is enhanced, while the $\boldsymbol{Le} > 1$ case is stabilizing. However in some research works (Groff 1982)(Simon & Wong 1953), instable flame surfaces are observed for mixtures with $\boldsymbol{Le} > 1$. Bechtold et al. (1987) conclude that this is a result of the hydrodynamic instability, which arise from thermal expansion generated by interaction between flame and the hydrodynamic disturbances. Various experimental observations showed that hydrodynamic instability occurs only when the flame reaches a critical value. Bechtold et al. (1987) proposed a critical value for Lewis Number:

$$\boldsymbol{Le^*} = \boldsymbol{1} - \frac{\boldsymbol{\sigma^2 Q_1}}{\boldsymbol{Q_2 E}} \qquad \textbf{(2-22)}$$

where $\boldsymbol{Q_1}$ and $\boldsymbol{Q_2}$ are empirical coefficients, derived in (Aung et al. 1997). It is also found that in most cases the critical Lewis Number is less than unity, which indicates that the rate of heat loss from the flame front has to be, by some margin, less than the rate of deficient mass flow into the flame front in order to maintain a stable flame.

Influences of chemistry and heat loss have been widely analysed. Under the assumption of one-step chemistry mechanism with large activation energy, non-unity Lewis Number induces a temperature change in the thin reaction layer, to which the burning velocity is very sensitive (Libby & Williams 1982; Libby & Williams 1983). Lewis Number larger than one causes excessive heat losses and promotes flame extinction, which can be retarded by density effect. By applying two-step reaction mechanism, Tam et al. (1984) found that, asymptotically, in weak flame stretch conditions reaction intermediate products are effective in retarding flame extinction, if the activation energy of the first reaction is large. Other researchers concluded as well that these intermediates influence the flame’s response to stretch (Peters & Smooke 1985).

In situations where the Lewis Number deviates significantly from unity, its effect is amplified. Peters et al. (1985) tested stretched lean ($\boldsymbol{\Phi}$=0.6) and rich ($\boldsymbol{\Phi}$=1.4) hydrogen-air flames with elementary kinetics. Due to the large diffusivity of hydrogen the Lewis Number is 0.31 for the lean mixture and due to large thermal diffusivity it is 3.02 in the rich case. The results show that in both cases, the effect of Lewis Number is dominating over the details of chemical kinetics. Extinction is observed for positive stretch in rich Hydrogen flames ($\boldsymbol{Le > 1}$).

2.4 Turbulent flames

When a laminar flame is entering a turbulent flow field the combustion regime of the flame is then replaced by one where the turbulence and the flame interact. Turbulent combustion results from the two-way interaction of chemistry and turbulence. When a flame interacts with a turbulence flow, turbulence is modified because of the strong accelerations through the flame front induced by heat release and of the large change in kinematic viscosity associated with temperature change. On the other hand, turbulence alters the structure of the flame and influence the reaction rates, in extreme cases, inhibit the flame completely leading to flame quenching (Aditya 2010).

It's been well known by experimentalists that by changing the turbulence level before initiating combustion in a vessel the combustion duration would vary significantly. The combustion rate, which is deduced from the turbulent burning velocity, is seen to increase with increasing turbulence level.

Unlike laminar burning velocity, $\boldsymbol{S_L}$, which is a physico-chemical constant that only depends on the mixture strength, temperature and pressure, the turbulent flame speed, $\boldsymbol{S_T}$, is also dependent on some turbulent parameters. The complexity of turbulent flame speed makes it more difficult to be properly defined and calculated (Aditya 2010). One common focus is in this field is the determination of the ratio $\boldsymbol{S_T/S_L}$ as a function of $\boldsymbol{S_L}$, and other turbulence parameters. However, there still lacks general consensus in this field except that turbulence enhances the ratio $\boldsymbol{S_T/S_L}$ in a limited range. There are still important questions to be answered e.g., the dependence of the turbulence Reynolds's number on $\boldsymbol{S_T/S_L}$, limits of enhancement on $\boldsymbol{S_T}$, etc.

The purpose of this section is to carry out a selective review on some well-established turbulent flame speed correlations. The relative strengths and weaknesses of these correlations will be discussed. A correlation that suits the purpose of being integrated with the laminar flame speed model and used for turbulent flame speed prediction in later S.I. engine simulation will be chosen.

It is not the author's intention to either judge and criticise any of the reviewed correlations or fulfil any drawbacks they may have. These correlations are reviewed solely in order to select the best-suited one for the application in later S.I. engine simulation.

2.4.1 Correlations of Turbulent Flame Speed

In the past, many experimental studies have been performed with different configurations and measurement techniques to obtain turbulent flame speed correlations. Many of these correlations are derived for specific fuels or limited range of conditions.

Anand-Pope's correlation

Anand et al. (1987) studied an idealised premixed turbulent flame which is statistically stationary and one-dimensional, and propagates through high-Reynolds-number turbulence which is non-decaying, homogeneous and isotropic upstream of the flame. The flame is studied with density ratio as a parameter. A one-step global chemistry is combined with the Bray-Moss-Libby model and the instantaneous thermo-chemical state is related to the reaction progress variable $\boldsymbol{c}$, as introduced in ***chapter 2.2.3***. The change of $\boldsymbol{c}$ is described by a probability density function (PDF) that is not pre-assumed. A linear correlation is obtained:

$$\frac{S_T}{S_L} = \mathbf{1.5} \cdot (\frac{u'}{S_L}) \qquad \textbf{(2-23)}$$

The model results showed that the turbulent flame speed, $\boldsymbol{S_T}$, decreased with increasing density ratio and attained an asymptotic value at $\boldsymbol{\rho_u}/\boldsymbol{\rho_b} = 4$.

The correlation proposed by Anand and co-workers is not fuel-specific, i.e. the model can take input of properties of different fuel properties. Due to its linear nature, the computational time required is modest. Anand claimed a 20 minutes computation time on IBM desktop.

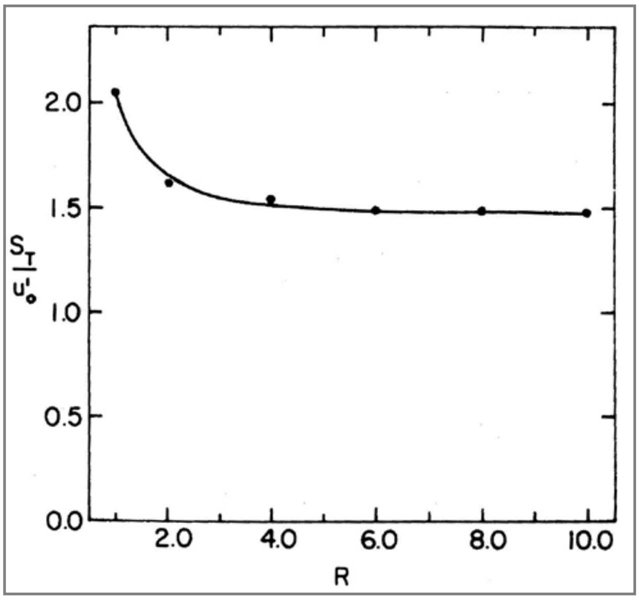

Fig. 2-21 Normalised turbulent flame speed against density ratio (Anand & Pope 1987).

Wirth-Peters' correlation

Wirth and Peters (1992) measured turbulent flame speeds for propane-air flames using a VW transparent engine. The engine is a four-cylinder, 1.6L unit with bore/stroke ratio of 79.5/80mm and a compression ratio of 8.5. The optical access is provided by via elongated crankcase and pistons with quartz window in the piston crown of about 58mm in diameter. Three additional square windows, 20 by 20mm, are placed into the cylinder wall beneath the cylinder head to provide three-dimensional optical access. Experiments were carried out using laser tomographic technique with Nd:YAG laser pulse. Experimental results revealed a decreasing trend of turbulence structure size.

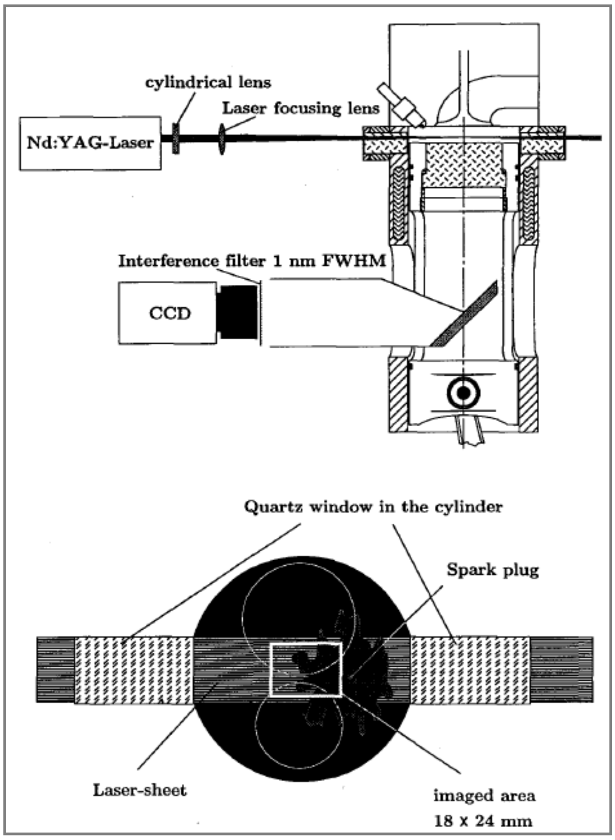

Fig. 2-22 Schematic of the VW transparent engine, optical layout and imaged area in the combustion chamber (Wirth & Peters 1992).

Wirth and Peters derived a flamelet formation for premixed turbulent flames based on a scalar field equation that describes the instantaneous flame front location in the turbulent flow field. The differential equation derived represents the local kinematic balance between fluid flow velocity, burning velocity and flame propagation velocity. A spectral closure of the problem was performed on the basis of a two-point correlation:

$$\frac{S_T}{S_L} = 1 + 0.8\left(\frac{u_t'}{S_L}\right)^{0.5} + 1.5\left(\frac{u_t'}{S_L}\right) \tag{2-24}$$

This correlation also includes the effects of flame stretch, which is seen as the sum of tangential strain and flame front curvature. Two key assumption made in the derivation are that the response of flame to a train field is instantaneous and time-varying strains only influence the flame at the mean property level. By applying these assumption, the derived correlation is only valid for turbulence flames in which the chemistry is sufficiently fast.

Gulder’s correlation

Gulder (1991) developed a turbulent flame speed correlation for the wrinkled flamelet combustion regime that is in similar formation of that derived by previous researchers (Wirth & Peters 1992):

$$\frac{S_T}{S_L} = 1 + 0.62\left(\frac{u_t'}{S_L}\right)^{0.5} \cdot {Re_L}^{0.25} \qquad \textbf{(2-25)}$$

The wrinkled flamelet regime was defined by the area bounded by $R_\eta \geq 1.5\,u'/S_L$ and $Re_L \leq 3200$. ***Eq. 2-25*** was validated against experimental data obtained on various types of fuels, as shown in ***Fig. 2-23***.

Gulder considered two different turbulent combustion regimes: The wrinkled flamelet regime where the turbulent Reynolds number based on the Kolmogorov length scale, η, is larger than the ratio u'/S_L; The distributed reaction regime where the ratio between the laminar flame thickness, δ_L and η is significantly larger than unity and the mixing is rapid compared to the chemistry. Additionally, Gulder claimed that there existed a transition regime where η is in the same magnitude of δ_L and the flame front no longer consists of then wrinkled reacting sheets and it gets thicker. Pockets of unburnt gas and burnt gas start to appear in the burnt zone and the unburnt zone, respectively. The turbulent flame speed correlation under this regime is expressed as:

$$\frac{S_T}{S_L} = Re^{0.25} \cdot EXP\left[a\left(\frac{u'}{S_L}\right)^{0.5}\right] \qquad \textbf{(2-26)}$$

Where a is a constant comparable to the slope of ***Eq. 2-25.***

Gulder’s correlation is relatively simple but works well in all three combustion regimes considered, with manipulations of equations and constants. It also has good flexibility as it’s been validated against a number of fuels.

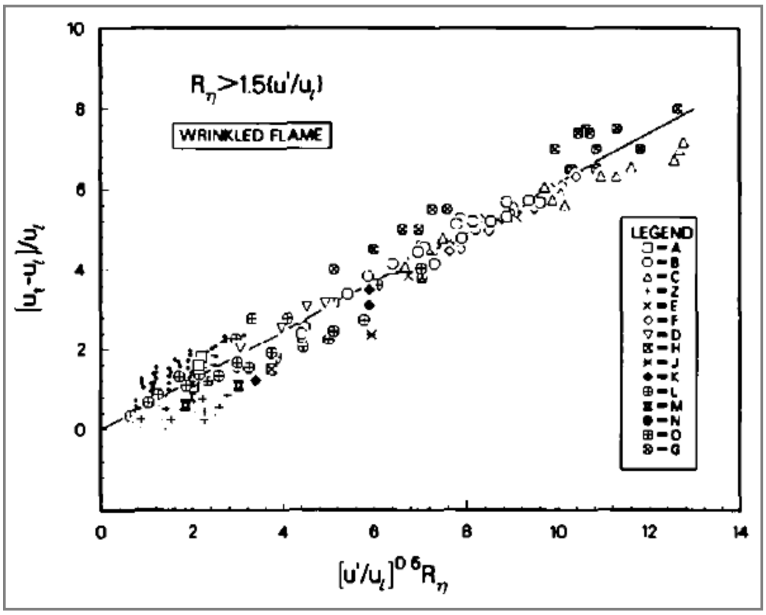

Fig. 2-23 Comparison of Eq. 2-25 and experimental results obtained using different fuels, including Hydrogen, Methane, Propane, Ethyne, Benzene and Natural Gas (Gülder 1991).

Bradley’s correlation

Abdel-Gayed and Bradley (1981) derived a correlation based on experimental data of stretched Methane-air flames:

$$\frac{S_T}{S_L} = 1 + 1.446\left(\frac{u_t'}{S_L}\right)^{0.4} \cdot {Re_L}^{0.15} \qquad \textbf{(2-27)}$$

The two-eddy theory of burning expresses the eddy decay and dissipation rates in terms of both eddy decay and chemical reaction for two groups of eddies within the turbulent spectrum: the large and the dissipative eddies. The large eddies are of a size given by the integral length scale, with a life time of u'/l_T. The dissipative eddies of a size, η, a lifetime, t_η, given by the Kolmogorov length and time scales, respectively. The rate of burning of each eddy size, is expressed by the product of the rate of eddy decay and the amount of mixture chemically reacted during the eddy lifetime.

Compared to previous correlations, Abdel-Gayed and Bradley's correlation showed exceptional accuracy in terms of predicting $\boldsymbol{S_T/S_L}$ under high level of turbulence, i.e., $\boldsymbol{Re_L = u'l_T/\nu}$ is large. However, the performance degraded when $\boldsymbol{Re_L}$ is reduced, as shown in ***Fig. 2-24***. The performance degradation was attributed to not only the incomplete understanding of physical/chemical nature of turbulent combustion, but also the uncertainties arisen in the two-eddy theory about the chemical lifetime in a dissipative eddy and the fractional volume occupied by such eddies (Abdel-Gayed & Bradley 1981).

Zimont's correlation

An efficient computational model was proposed by Zimont et al. (1998) with turbulent combustion at high Reynolds number in mind. Zimont and co-workers took into account of a series of physico-chemical phenomena in the determination of the correlation. These include: influence of fuel composition and concentration and the combustion pressure; thickening and distortion of the flame front by small- and large-scale eddies at high Reynolds number; effect of flame stretch; preferential diffusion effect. The derivation of the correlation started with the transport equation for the progress variable and its closure proposed by Moss et al. (1977). The closure is then completed by the turbulent flame speed model. Finally a flame stretch extension is added to the model. An expression for $\boldsymbol{S_T}$ is derived for both wrinkled and thickened flamelets in terms of physico-chemical characteristics of the combustible mixture:

$$\boldsymbol{S_T = A \cdot u'^{3/4} \cdot S_L{}^{1/2} \cdot \chi_u^{-1/4} \cdot l_T^{1/4}} \qquad \textbf{(2-28)}$$

where $\chi_u^{-1/4}$ is a term accounting for the molecular heat transfer coefficient of the unburnt mixture. The correlation was validated against multiple fuels including CH_4, C_2H_6, C_3H_8 and H_2 with estimated turbulent Reynolds number in the order of 1000, which is higher than typically reached in laboratory experiments.

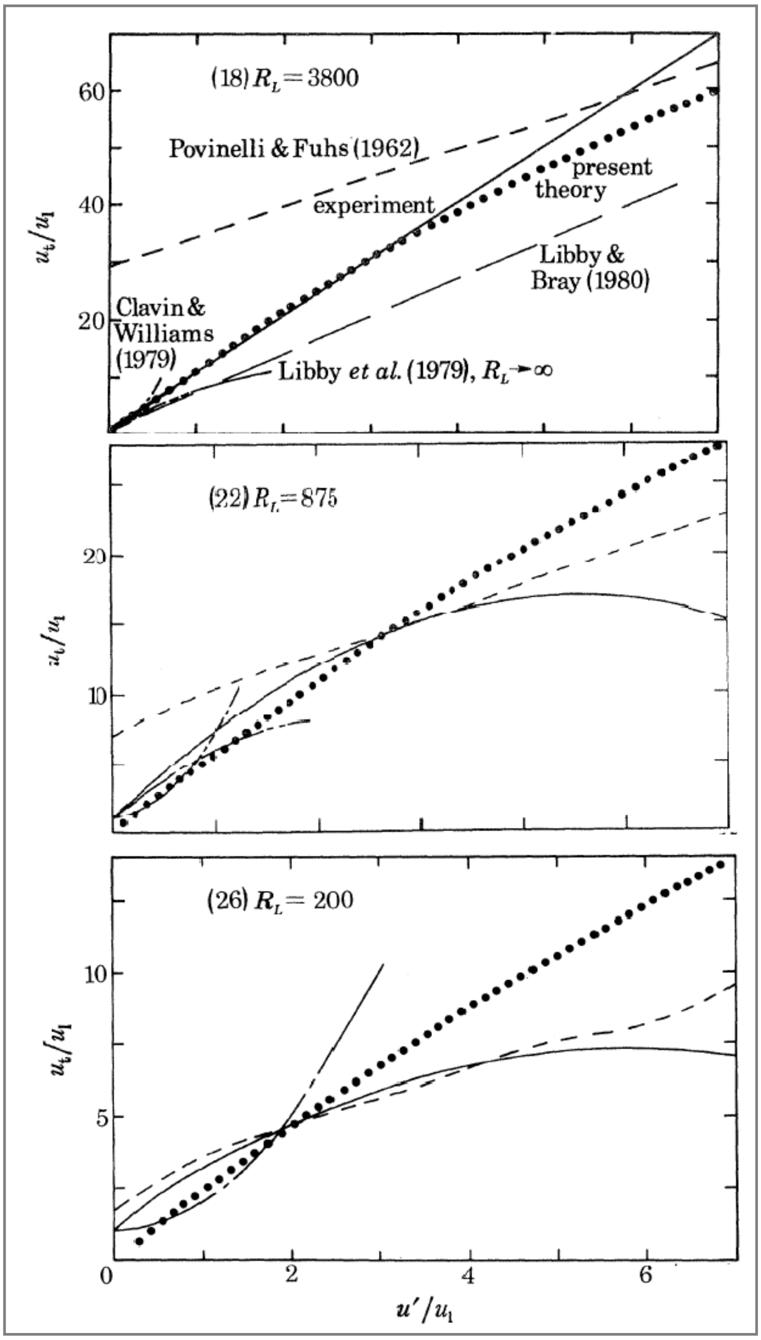

Fig. 2-24 Comparisons of experimental and theoretical values of S_T/S_L with different values of Re_L (Zimont et al. 1998).

2.4.2 Comparisons of correlations

The above-reviewed correlations are summarized in ***Table 2-1*** below. Besides the mathematical expressions of these correlations, ***Table 2-1*** also focuses on other characters of these correlations such as: whether the effect of flame stretch has been taken into account, and, the range of fuels used for the validation of the correlation. These additional information is important as they aid the selection of a best-suit correlation for future S.I. engine simulation application. In order to reveal the difference in between these correlations, their simulation results have been plotted in ***Fig.2-25***. The turbulent Reynolds number used in Gulder's, Bradley's and Zimont's correlations is 1000 which is purposely chosen to be higher than typical values achieved in fan-stirred vessels. Additionally, in Zimont's correlation, S_L is chosen as , the laminar burning velocity of stoichiometric Methane-air mixture at NTP, i.e. 0.45m/s (Bradley et al. 1996). A, l_T and u' are 0.52, 0.005m and 10m/s respectively, as recommended by Zimont. The value of χ_u is obtained in literature (Kuo,K 2005b).

Fig. 2-25 showed that there is a large scatter of data sets for turbulent flame speed correlations. The only agreement between reviewed correlations is that S_T increases noticeably with increasing u'. Such scatter indicates that substantial research is still needed in correlating S_T and u'. A universal turbulent flame speed is not yet existent. Each correlation proposed is developed based on different turbulence and combustion theories and the author's personal opinions, therefore they are all only reliable for a limited range of applications. All the correlations reviewed are derived within the wrinkled flamelet combustion regime. This is because the correlation that is chosen at the end of this chapter will be used in S.I. engine simulation.

Author	***Correlation***	***Regime***	***Stretch Effect***	***Validation Fuel***
Anand et al. (1987)	$\frac{S_T}{S_L} = 1.5 \cdot (\frac{u'}{S_L})$	***Wrinkled Flamelet***	***No***	CH_4
Wirth et al. (1992)	$\frac{S_T}{S_L} = 1 + 0.8(\frac{u'_t}{S_L})^{0.5} + 1.5(\frac{u'_t}{S_L})$	***Wrinkled Flamelet***	***No***	C_3H_8
Gulder (1991)	$\frac{S_T}{S_L} = 1 + 0.62(\frac{u'_t}{S_L})^{0.5} \cdot {Re_L}^{0.25}$	***Wrinkled Flamelet*** ***Corrugated Flamelet***	***Yes***	***Multiple***
Bradley et al. (1981)	$\frac{S_T}{S_L} = 1 + 1.446(\frac{u'_t}{S_L})^{0.4} \cdot {Re_L}^{0.15}$	***Wrinkled Flamelet***	***Yes***	***Multiple***[1]
Zimont et al. (1998)	$S_T = A \cdot {u'}^{3/4} \cdot {S_L}^{1/2} \cdot \chi_u^{-1/4} \cdot l_T^{1/4}$	***Wrinkled Corrugated Flamelet***	***Yes***	***Multiple***

Table 2-1 Summary of reviewed turbulent flame speed correlations proposed by different researchers.

---

[1] Bradley and co-worker validated the model by experimenting Methane-air flames. They also compared their model results with others' experimental results obtained from different fuels.

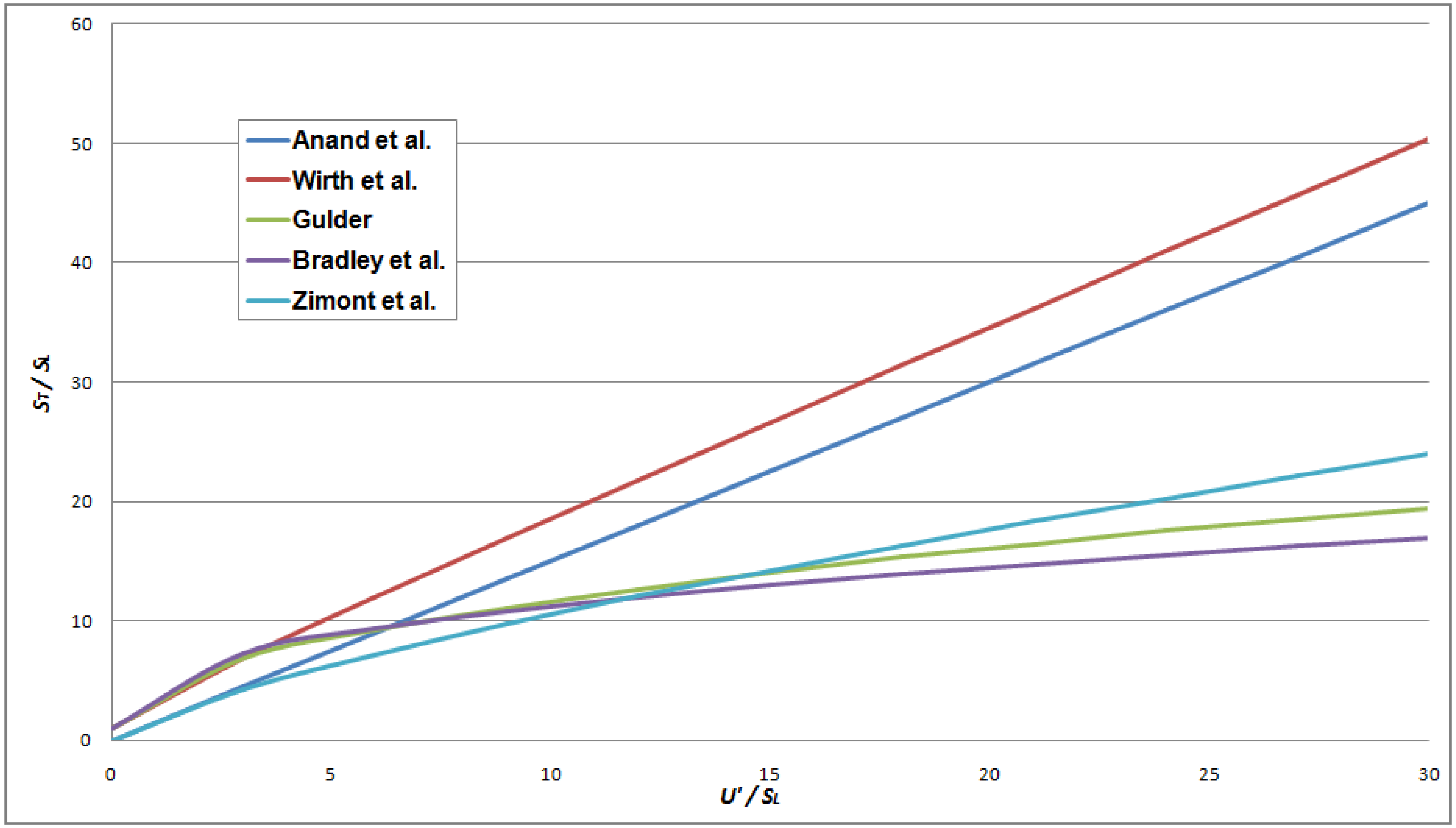

Fig. 2-25 Comparison of reviewed turbulent flame speed correlations proposed by different researchers.

2.4.3 Discussion on reviewed correlations

Anand and co-workers followed the original relation between $\boldsymbol{S_T}$ and $\boldsymbol{S_L}$ proposed by Damkohler (1947) and derived a linear correlation between $\boldsymbol{S_T}$ and $\boldsymbol{S_L}$. However, more recent experimental investigations of premixed turbulent flames, even at high ratios $\boldsymbol{u'/S_L}$ in the flamelet regime, showed that the relation between $\boldsymbol{S_T/S_L}$ and $\boldsymbol{u'/S_L}$ is not linear and depends on fuel type. Some local influences are found to be responsible for this effect (Wirth & Peters 1992).
Wirth and Peter developed a non-linear correlation using the G-equation concept. the correlation has been validated on a near-production S.I. engine, which is favourable for the current research. However, this correlation does not take into account of the effect of flame stretch. Flame stretch has been found to be particularly influential under lean-burn operating conditions, and have considerable impact on the mean turbulent heat release intensity (Zimont & Polifke 1998). Besides, Wirth and Peter's correlation has only been validated against one type of fuel which may make one to doubt its flexibility when some other available correlations are validated against multiple fuels.

Zimont's correlation has more solid and detailed theoretical background and is claimed to be more robust and computationally efficient. This makes it favourable for multi-dimensional simulations in complex geometries, e.g. internal combustion engines. Zimont's correlation has actually been adopted in the well-known commercial CFD package ***FLUENT 6.3*** for turbulent flames speed prediction, a proof that it is sufficiently accurate and efficient. The only drawback of this correlation, from the current author's point of view, is the inclusion of the empirical constant $\boldsymbol{A}$. On the plus side, such inclusion makes the correlation very flexible, i.e. $\boldsymbol{A}$ can be tuned to suit different fuels or operating conditions. But there is not implication that the variation of A is related to either the combustion process or the properties of the turbulence. This makes it difficult for an end-user to use values of A other than those recommended by Zimont and co-workers, with a sound theoretical ground.

The correlations proposed by Gulder and Bradley have very similar formation as they both include the effect of turbulent Reynolds number. Flame stretch is considered in both correlations and they have all been validated against multiple types of fuels. The only difference, from the current author’s perspective, is that they are biased towards different applications. Gulder’s correlation is applicable for three turbulent combustion regimes, making it a very flexible tool for a wide range of turbulent combustion. Bradley’s correlation, on the other hand, is based on the two-eddy theory and therefore is focused on the wrinkled flamelet regime. Bradley claimed that, by comparing to different theories of turbulent combustion, the two-eddy theory is more satisfactory for combustion in higher levels of turbulence.

2.5 Chemical Kinetics

The equilibrium composition of a reactive mixture can be predicted by the application of thermodynamic laws, In the case of that the chemical processes are much faster compared with the other processes like diffusion, heat transfer, flow etc. the thermodynamics alone allow the description of the system locally. In most cases, though, chemical reactions occur on timescales comparable with those of the flow and of the molecular transport processes. Therefore, information is needed about the rates at which the chemical reactions proceed. For this purpose, chemical kinetics has been investigated to study the rates of chemical processes in an effort to understand the factors that influence these rates and to develop theories that can be used to predict chemical processes.

In the research of internal combustion engines, chemical kinetics fulfils the needs for compact numerical models to represent hydrocarbon combustion and enables the establishment and development of numerical models for the design and prediction of practical engine systems. In general, chemical kinetics forms a link between experimental observation and numerical interpretations of the combustion processes in internal combustion engines.

2.5.1 Rate laws and rate constants

In this section, three types of reactions that are global, elementary and chain reactions and the terms, equations and basic laws applied to describe each reaction type are introduced.

Global reactions

The chemistry in fuel oxidation can be expressed by a global reaction mechanism. Assuming that a mole of fuel reacts with combustion products, it yields:

$$\mathbf{1}\boldsymbol{Fuel} + \boldsymbol{\alpha}\,\boldsymbol{Oxidizer} \rightarrow \boldsymbol{b}\,\boldsymbol{Products} \qquad \textbf{(2-29)}$$

The fuel consumption rate can be expressed by:

$$\frac{\boldsymbol{d[X_{Fuel}]}}{\boldsymbol{dt}} = \boldsymbol{k_G(T)} \cdot [\boldsymbol{X_{Fuel}}]^{\boldsymbol{n}} \cdot [\boldsymbol{X_{Oxidizer}}]^{\boldsymbol{m}} \qquad \textbf{(2-30)}$$

where $[\boldsymbol{X_i}]$ denotes the molar concentration of the $\boldsymbol{i}^{th}$ species in the mixture. $\boldsymbol{k_G(T)}$ is the global rate coefficient and is a strong function of temperature. The minus sign indicates that fuel concentration decreases with time. The exponent n and m relate to the reaction order.

Use of global reactions to express a chemical reaction system is frequently a ‘black box’ approach by providing the input-to-out perspective to the chemical process, which is not capable of providing a basis for understanding what is actually happening chemically in a system. The chemical equation ***Eq. 2-29*** indicates that the oxidation process of the fuel is a one-step and instantaneous process. In reality, it is however a much more complex and sequential process. This process involves the breaking and formation of chemical bonds and production and destruction of intermediate species. A global equation consequently is not adequate to describe a chemical process in details, so a collection of elementary reactions has to be used to depict a chemical process, which will be considered in the following section.

Elementary reactions

Elementary reactions express how actual molecules or ions react with each other. The equation in an elementary reaction represents the reaction at the molecular level rather than at a global point of view. Based on the number s of the molecules involved, elementary reactions are categorised into three types: unimolecular reactions, bimolecular reactions and trimolecular reactions (Liu 2010):

Unimolecular reactions

Unimolecular reactions describe the process that a molecule or ion decomposes itself. They are always first order reactions and can be expressed in the following form:

$$\boldsymbol{A \rightarrow products} \qquad \textbf{(2-31)}$$

The reaction rate of above reaction is directly proportional to the concentration of the reactant, $\boldsymbol{A}$:

$$\frac{d[A]}{dt} = -k \cdot [A] \quad \textbf{(2-32)}$$

where $\boldsymbol{k}$ represents the rate coefficient.

Bimolecular reactions

Most elementary reactions involved in combustion are bimolecular. In a bimolecular reaction two molecules collide and react with each other and form two different molecules:

$$aA + bB \rightarrow cC + dD \quad \textbf{(2-33)}$$

where $\boldsymbol{a}$, $\boldsymbol{b}$, $\boldsymbol{c}$ and $\boldsymbol{d}$ are stoichiometric coefficients. The reaction rate of this reaction is calculated by multiplying the reaction rate constants by the concentration of each of the reactants:

$$\frac{1}{a}\frac{d[A]}{dt} = \frac{1}{b}\frac{d[B]}{dt} = -\frac{1}{c}\frac{d[C]}{dt} = -\frac{1}{d}\frac{d[D]}{dt} = -k \cdot [A] \cdot [B] \quad \textbf{(2-34)}$$

The negative reaction rates indicate that the species are being consumed.

Trimolecular reactions

A trimolecular reaction involves the collisions amongst three molecules. The general form of a trimolecular reaction is:

$$A + B + M \rightarrow C + M \quad \textbf{(2-35)}$$

and the its reaction rate is expressed as:

$$\frac{d[A]}{dt} = -k \cdot [A] \cdot [B] \cdot [M] \tag{2-36}$$

where M can be any molecule and is often referred to as the third body.

Reaction rates of elementary reactions

It has been observed from both kinetic theories of gases and experiments that the rate constant, k, for an elementary reaction is an exponential function of temperature and is in the form of the Arrhenius equation:

$$k(T) = A \cdot T^{b} \cdot exp\left(-\frac{E_A}{R_u T}\right) \tag{2-37}$$

where A is the pre-exponential factor and E_A is the activation energy of the reaction which represents the energy level required to activate the chemical bonds break-up and rearrangement processes. These two constants are determined experimentally.

Chain reactions

Most gas-phase chemical reactions are initiated at low concentrations by the formation of an extremely reactive species that sets off a series of reactions leading to a self-amplifying and self-sustaining chain of chemical events. Such process is referred to as a chain reaction. Chain reactions occur after a short induction period that allows the formation and accumulation of the reactive species.

The sequence of a reaction chain can be typically divided into four stages:

Initiation: A highly reactive intermediates is formed usually through the action of an agent such as light, heat or a catalyst. These intermediates can be in the form of an atom, an ion or a neutral molecular fragment.

Chain branching: highly reactive intermediates react with the initial reactants to produce stable products and another intermediates. The newly formed intermediate reacts with the initial reactants as before to create a repetitive cycle during which more radicals are created than destroyed.

Chain propagation: the number of radicals remain more or less the same but different types of radicals are being produced in a stable manner.

Chain termination: opposite to the chain branching stage, more radicals are destroyed than produced in this stage.

A typical example of combustion chain reaction can be illustrated by the following generic reaction set:

Initiation $S \underset{k_{r1}}{\overset{k_{f1}}{\Leftrightarrow}} R_1^\bullet$

Branching $R_1^\bullet + S \underset{k_{r2}}{\overset{k_{f2}}{\Leftrightarrow}} R_2^\bullet + R_3^\bullet$

Propagating $R_2^\bullet + R_3^\bullet \underset{k_{r3}}{\overset{k_{f3}}{\Leftrightarrow}} \alpha \cdot R_4^\bullet$

Termination $R_1^\bullet + R_2^\bullet + R_3^\bullet + R_4^\bullet \underset{k_{r3}}{\overset{k_{f3}}{\Leftrightarrow}} \beta \cdot P$

where $\boldsymbol{S}$ represents the fuel molecules, $\dot{\boldsymbol{R}}_\mathbf{1}$, $\dot{\boldsymbol{R}}_\mathbf{2}$, $\dot{\boldsymbol{R}}_\mathbf{3}$ and $\dot{\boldsymbol{R}}_\mathbf{4}$ are the intermediates and $\boldsymbol{P}$ is the product. $\boldsymbol{k_f}$ and $\boldsymbol{k_r}$ represent the forward and reverse reaction rates, respectively.

Reaction rates of chain reactions

Based on the elementary reaction rates expressed using ***Eq. 2-35***, ***2-36*** and ***2-37***, the net production or destruction rates of any species involved in a series of chain reaction can mathematically expressed. The net production rate of $\dot{R}_1$ is the sum of all elementary rates producing $\dot{R}_1$ minus the sum of all elementary rates destroying $\dot{R}_1$:

$$\frac{d[\dot{R}_1]}{dt} = k_{f1}[S] + k_{f2}[\dot{R}_2][\dot{R}_3] + k_{f4}[P]^{\beta} - k_{r1}[\dot{R}_1] - k_{r2}[\dot{R}_1][S] - k_{f4}[\dot{R}_1][\dot{R}_2][\dot{R}_3][\dot{R}_4] \quad \textbf{(2-38)}$$

The same applies to $\dot{R}_2$, $\dot{R}_3$ and $\dot{R}_4$ and after obtaining expressions for each species it yields a system of first-order ordinary differential equation that describes the evolution of the chemical system:

$$\frac{d[X_i](t)}{dt} = f\,([X_1](t), [X_2](t), \dots, [X_n](t)) \quad \textbf{(2-39)}$$

With known initial conditions:

$$[X_i](t = 0) = [X_i]_0 \quad \textbf{(2-40)}$$

Together with the conservation equations of mass and energy the set of equations can be numerically integrated using computerized methods. It should be noted that such chemical system has an important feature of being stiff, which means some of the variables are changing rapidly while some are changing very slowly. The character of stiffness of a system of ODEs requires more complex numerical integration methods, i.e., Backward Euler method, to achieve reliable results.

2.5.2 Chemical kinetic combustion models

Chemical kinetics mechanisms are very useful tools in the prediction of autoignition in the study of both S.I. and H.C.C.I. engines, i.e., the autoignition timing, energy release rates, reaction intermediates and combustion products. There has been continuous interests in the development of better hydrocarbon- or hydrogen-oxidation mechanisms in order to increase combustion efficiency and reduce emissions (O Conaire et al. 2004). According to the numbers of species and elementary reactions involved, chemical kinetics mechanisms that are widely used in combustion simulations can be divided into three categories: detailed, reduced, and global:

Category	***Description***	***Species***	***Reactions***
Detailed (O Conaire et al. 2004; Konnov 2008; Li et al. 2004; Strohle & Myhrvold 2007)	A comprehensive reaction set	≈ 11	≈ 20 to 21
Reduced (Smooke & Williams 1995; Vlachos 1996; Boivin et al. 2011)	A simpler set by reduction of a detailed mechanism.	≈ 5	≈ 4 to 7
Global (Fernández-Galisteo et al. 2009)	Utilization of one-step global reaction for simplicity.	3	1

Table 2-2 Kinetics mechanisms used in the studies of hydrogen-oxidation.

Detailed chemical kinetics models

A detailed chemical kinetics model is a model that attempts to describe at molecular level the chemical process which occurs during combustion and which is essential for trace species predictions. The actual numbers of species or elementary reactions considered are subject to debate as different models have different focuses (Simmie 2003). Many researchers use truncated or skeletal mechanisms that completely neglect some intermediates or do not differentiate between various quantum state of one compound.

For decades, the study and development of chemical kinetics mechanisms have been concentrated on single sets of experimental data obtained from shock tubes, flow reactors or rapid compression machines (O Conaire et al. 2004). Schott and Kinsey (1958) studied the formation of OH radicals in hydrogen-air combustion under 1atm and a wide temperature range between 1085-2700K in a shock tube. Five chain branching reactions from a detailed mechanism were shown to have significant influence on the oxidation of hydrogen and its ignition delay. Skinner and Ringrose (Konnov 2008) performed measurements in shock tube with extended pressure up to 5atm and found similar results. Chen et al. (1984) and Slack (1977) measured the ignition delay of hydrogen-air mixture under similar temperature and pressure range but different levels of dilution using inert gas Argon. However, the reliance on just one set of experimental data is criticized recently (Smith 2002) who asserts uncertainty limits on individual reaction rate constants produce a parameter space for imprecise predictions of key combustion properties such as the flame speed and the ignition delay. Following Smith’s critics some researchers started to develop and validate their chemical kinetics mechanism against a wider range of experimental results that were obtained by various experimental techniques.

Several detailed hydrogen oxidation mechanisms have been proposed over the years. The motivation of such continuous development is the substantial progress made in accurate measurement of the elementary reaction rates and thermodynamic properties as well as in measurement of the integral combustion characteristics such as burning velocities, ignition delays, and product formation during slow oxidation (Konnov 2008). Others (Mueller et al. 1999) proposed a detailed hydrogen oxidation mechanism using only a flow reactor over the temperature range of 850-1040K, at equivalence ratio between 0.3 and 1.0 and pressures between 0.3 to 17.5atm. By taking advantages of a expanded database and improved rate constants of **$H + O_2$ (+ N_2) = HO_2 (+ N_2)**, **$HO_2 + OH = H_2O + O_2$**, and **$HO_2 + HO_2 = H_2O_2 + O_2$**, the proposed mechanism was in better agreement with experimental results. Similarly, Davies et al. (2003) improved the detailed H_2/CO mechanism they proposed previously by adopting new rate constants for the important reaction $H + O_2 + M = HO_2 + M$ and new thermodynamic data for OH radicals. Based previous works of (Konnov 2008),(Hughes et al. n.d.) and the GRI-mech (Smith et al. n.d.), Conaire (2004) developed a detailed hydrogen oxidation mechanism which was validated against experimental results obtained from multiple sources including shock tube, flow reactor, freely propagating flames and burner-stabilized flames. With increased attention paid to the suitability to simulations under high pressure, i.e. internal combustion engines, Conaire validated the mechanism over the range of 298-2700K, 0.05-87atm and Φ = 0.2-6. By applying a pressure-dependent rate constant for **$H + OH + M = H_2O + M$** Conaire's mechanism achieved better overall agreement to a wide range of physical conditions and greater consistency over existing hydrogen oxidation mechanism.

Reduced chemical kinetics models

As the numbers of species and reactions required to describe a chemical reaction system in details increases, the demand on computational power becomes the major huddle that prevents detailed chemical kinetics models to be adopted in the simulation of practical combustion applications, i.e. internal combustion engines. The situation gets even worse when detailed chemical kinetics models are coupled with multi-dimensional CFD calculations (Ra & Reitz 2008). Recent detailed *n*-heptane oxidation mechanism developed by Curran et al. (1998) contains 560 species and 2539 elementary reaction. An iso-octane oxidation mechanism by the same author later (Curran et al. 2002) contains 857 species and 3606 elementary reactions. It is still too expensive to use detailed chemical kinetics mechanisms in engine simulation with multidimensional CFD codes, even with modern high-performance super computers. Therefore methods of simplification on detailed chemical kinetics models are required. The simplified mechanisms are often referred to as reduced chemical kinetics mechanisms. The reduced mechanisms should retain all the critical fuel chemistry predicted by detailed mechanisms, but with much improve computational efficiency. The extent of comprehensiveness of the reduced mechanisms depends on the available computational resources and the information required from the simulation.

Various theoretical methods of simplification have been proposed. Maas et al. (2000) proposed a reduction method based on the Intrinsic Low-Dimensional Manifolds (ILMDs). The dynamical behaviours of the chemical systems are well reproduced, independent on the fuel type considered. Simpler reaction mechanisms of Syngas, methane, iso-octane, n-dodecane are achieved. By analysing the reaction rates, Law et al. (1998) developed a reduced methane oxidation mechanism that consists of 16 species and 12 lumped steps. The reduction was carried out on GRI-Mech 1.2 which consists of 31 species and 175 elementary reactions. The reduced mechanism retained the capabilities of predicting a wide range of combustion phenomena with extensive thermo-dynamical parametric variations.

In terms of applications in engine combustion simulations, Reitz et al. (2008) proposed a reduced oxidation mechanism by combing reduced n-heptane and iso-octane oxidation mechanisms. By adopting the reduced mechanism into a multi-dimensional CFD H.C.C.I. engine model and D.I. diesel engine model, the mechanism was proven to produce reliable predictions on engine combustion as well as improved computational efficiency over detailed mechanism. Tanaka et al. (2003) have developed a reduced oxidation mechanism for gasoline, as a mixture of *n*-heptane and iso-octane, as shown in ***Fig. 2-26***. The mechanism which consists of 32 species and 55 elementary reactions takes into account of the effects of wall heat transfer on the adiabatic core gas temperature by adding then displacement volume of the laminar boundary layer to the cylinder volume. Chemical interactions between n-heptane and iso-octane are also included. Tanaka's mechanism successfully predicts the two-stage heat release of heavy hydrocarbons which involves low and high temperature cycles followed by a chain explosion.

Global chemical kinetics models

Global chemical kinetics mechanisms describe the chemistry in terms of a few of the principle reactants and products in one or more function steps (Zheng 2005). The motivation of developing a global chemical kinetics mechanism is the application in combustion simulations that required considerable computational resource, i.e. multi-dimensional engine simulation.

The chain reaction theory still applies in the construction of global mechanisms. In general, the high temperature chemistry is described by one or two reaction steps and the other reactions are used to represent the low and intermediate temperature chemistry (Liu 2010). The drawback of global mechanisms is its inability of predicting the post-ignition reactions and the combustion intermediates. Therefore, the usage of global mechanisms is limited to the prediction of pre-ignition behaviours, e.g. ignition delay.

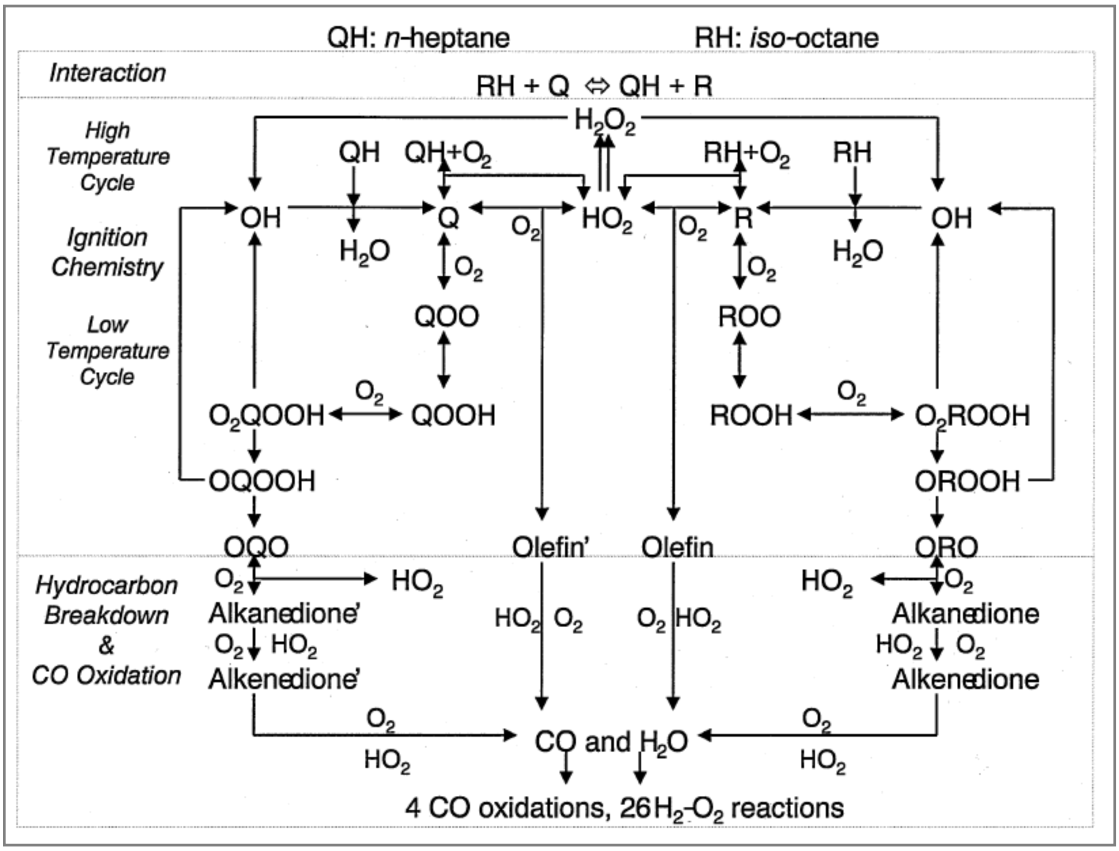

Fig. 2-26 Illustration of the reduced chemistry of the mixture of n-heptane and iso-octane as developed by Tanaka et al. (Tanaka et al. 2003).

Westbrook et al. (1996) developed a one-step global mechanism of hydrogen oxidation:

$$\mathbf{H_2 + 1/2\ O_2 = H_2O}$$

where the overall reaction rate is expressed as:

$$\boldsymbol{k = 1.8\, x\, 10^{13}\ \cdot EXP\left(-\frac{17614K}{T}\right) \cdot\ [H_2]^{1.0}\ \cdot\ [O_2]^{0.5}} \qquad \textbf{(2-41)}$$

In laminar flame speed simulations, the global mechanism was only reliable in a limited range of equivalence ratio between 0.55 and 1.1. Predictions outside this range was considered poor and unreliable. The poor prediction was attributed to the chemical and thermal structure changes in the flame as the stoichiometry varies which could not be properly accounted for in the global mechanism.

Chapter Three: Hydrogen-Air Spherical Flame Instabilities

This chapter focuses on the systematic studies of the onset of hydrogen-air spherical flame instabilities which is defined by the critical radius, and its relationships with equivalence ratio, temperature and pressure. The aim of the current chapter's research is to:

(1) Experimentally identify the critical radius for the onset of instabilities of hydrogen-air flames, and,

(2) Systematically examine the effects of temperature, pressure and fuel-air equivalence ratio on the variation of the critical radius.

3.1 Cellular flame instabilities

According to the mechanism that triggers the instabilities of laminar flames two main kinds of instabilities are defined and studied: unequal diffusion instability and hydrodynamic instability (Bradley et al. 1996; Tang et al. 2009; Aung et al. 1998; Hu et al. 2009; Aung et al. 1997; Kwon & Faeth 2001; Bradley et al. 1998; Sun et al. 2012; Bradley & Harper 1994). A third category, buoyant instability, caused by gravitational effect, can also be found in previous research (Vu et al. 2011). It is often neglected as its effect on rapidly propagating flames is minor compared to the other two categories of instabilities.

3.1.1 Unequal diffusion instabilities

The unequal diffusion instability is sometimes referred to as thermal-diffusive instability. During the flame propagation process, both mass and thermal diffusions exist across the flame surface. The energy ratio of the two kinds of diffusion is expressed by the Lewis Number, $\boldsymbol{Le}$:

$$\boldsymbol{Le} = \frac{\boldsymbol{D_T}}{\boldsymbol{D_{iM}}} \tag{3-1}$$

Where $\boldsymbol{D_T}$ is the thermal diffusivity of the unburnt mixture:

$$\boldsymbol{D_T} = \frac{\boldsymbol{\lambda}}{\boldsymbol{\rho_u C_p}} \tag{3-2}$$

Where $\boldsymbol{\lambda}$ is the unburnt gas thermal conductivity, $\boldsymbol{\rho_u}$ is unburnt gas density and $\boldsymbol{C_p}$ is specific heat at constant pressure. And, $\boldsymbol{D_{iM}}$ is the mass diffusivity of the deficient reactant (e.g. fuel in lean flames, oxygen in rich flames):

$$\boldsymbol{D_{iM}} = \left(\sum_{\substack{j=1 \\ j\neq i}}^{n} \boldsymbol{V_j}/\boldsymbol{D_{ij}}\right)^{-1} \tag{3-3}$$

Where $\boldsymbol{i}$ indicates the limiting reactant, $\boldsymbol{V_j}$ is the volume fraction of species $\boldsymbol{j}$ and $\boldsymbol{D_{ij}}$ is the mass diffusivity of the deficient reactant relative to the species $\boldsymbol{j}$.

When $\boldsymbol{Le} > 1$, the energy of thermal diffusion exceeds the mass diffusion and the swelling parts lose heat energy more rapidly than the mass diffusion of the deficient reactant can compensate for. Therefore the net energy flow would be negative. As a result, the flame temperature gradually falls below the adiabatic temperature and the burning velocity reduces. The concave parts, on the contrary, gain positive net energy due to stronger mass diffusion of the deficient reactant than the energy loss by thermal diffusion. Consequently, flame temperature and burning velocity both increase. In general, the decelerating and accelerating effects induced, respectively, in the swelling and concave parts cancel each other out, and the flame surface maintains its smoothness and stability. On the other hand, when $\boldsymbol{Le} < 1$, both the swelling and concave parts will be enhanced, and therefore the flame rapidly loses its surface smoothness . Such instability often occurs in the early stage of flame propagation when $\boldsymbol{Le} < 1$ and can be identified by irregular distortions of the flame surface, as shown in ***Fig. 3-1***.

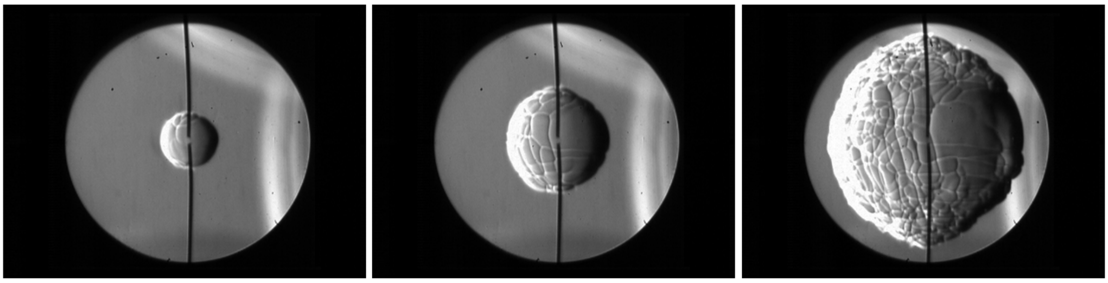

Fig. 3-1 Evolution of the unequal diffusion instability on hydrogen-air flame at 298 K, 1 bar and Φ=0.2. Measured at 1.324ms, 2.654ms and 5.314ms after ignition.

3.1.2 Hydrodynamic instabilities

In some occasions, although the flame can maintain $Le > 1$ it still undergoes cellular instability in the later stage of its propagation. This instability was first studied by Darrieus and Landau (2001). In their research the flame is seen as a density discontinuity and mechanism of such instability is described as the interactions between the hydrodynamic disturbances generated by the flame and the flame itself. Additionally, hydrodynamic instability is also responsible for flame surface wrinkling (Vu et al. 2011). Such instability can be distinguished when the flame radius is large enough and the diffusion stability cannot offset its effect. It can be identified by regular cellular distortions of the flame surface, as illustrated in ***Fig. 3-2***.

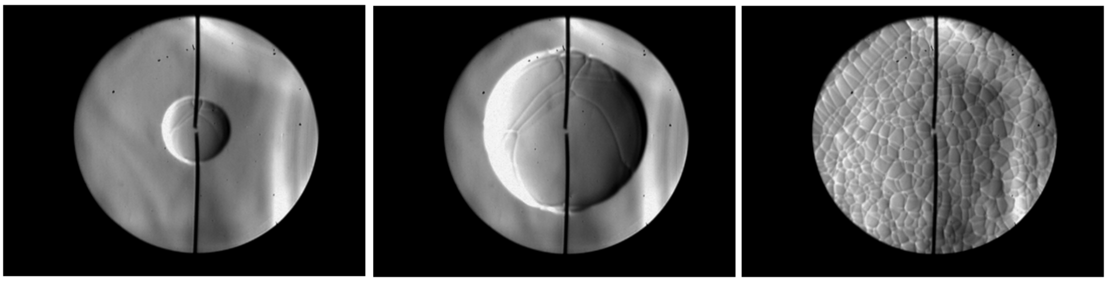

Fig. 3-2 Evolution of the hydrodynamic instability on hydrogen-air flame at 298 K, 1 bar and Φ=1.0. Measured at 0.707ms, 1.704ms and 4.032ms after ignition.

Hydrodynamic instability occurs in all flame propagation processes and its intensity is directly proportional to density ratio, σ, of burned and unburnt gas, and inversely proportional to flame thickness δ.

$$\sigma = \frac{\rho_u}{\rho_b} \quad \textbf{(3-4)}$$

$$\delta = \frac{v}{u_l} \quad \textbf{(3-5)}$$

Where v is unburnt gas kinematic viscosity; u_l is unstretched laminar burning velocity.

3.1.3 Buoyant instabilities

The buoyant instability is caused by the body force in the presence of density gradient. For relatively fast-burning mixtures the flames have a spherically symmetric structure and the fast flame speeds leave the buoyant effect not enough time to operate. For weaker mixtures, the flames can retain a spherical structure initially but begin to rise in the later stage of combustion. This phenomenon is due to the gravitational acceleration (buoyancy forces) preferentially accelerates the less-dense burnt mixtures contained in the spherical flame kernel and such acceleration destabilises the flame. The buoyant instability occurs in relatively weak mixtures and near-flammability limit scenarios. Experimental studies on hydrogen-air flame instabilities showed that for the buoyant instability to make noticeable effect on the flame the fuel-air equivalence ratio has to be approximately 0.3 or leaner (Aung et al. 1998).

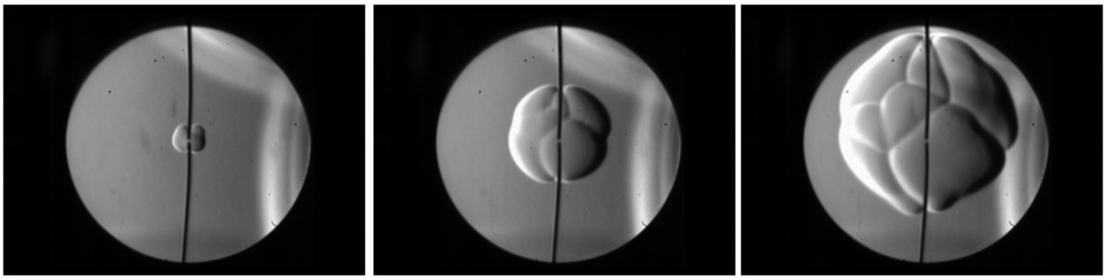

Fig. 3-3 Evolution of the buoyant instability on hydrogen-air flame at 298 K, 0.5 bar and Φ=0.3. Measured at 3.373ms, 19.998ms and 46.598ms after ignition.

3.2 Experimental results

3.2.1 Experimental apparatus

A spherical stainless steel combustion bomb with 400mm inner diameter which is capable of withstanding the temperature and pressure generated by combustion with initial conditions up to 1.5MPa and 650K, as shown in ***Fig.3-4***, has been employed. The bomb has extensive optical access through a pair of orthogonal quartz windows of 100mm diameter. The optical system is arranged into a Z-shaped, the two primary mirrors have diameter of 100mm and focal length of 100cm.The slit has an adjustment range of 0-3mm and the blade can be adjusted in the range of 0-10mm. There are two intake routes, one for air, the other for hydrogen. Low-pressure sensor is used to accurately measure partial pressure of gas with the precision of 0.001bar. The combustible mixture is spark ignited at centre of the chamber using electrodes extending from the top and the bottom. One electrode is fixed while the other could be moved for adjusting the ignition gap. After the induction of fuel and air is completed sufficient time is allowed for the mixture motion to decay. The bomb is flushed with dry air when combustion is finished to ensure minimum amount of residuals are left before subsequent combustion is initiated. Following the ignition, gas temperature inside the bomb is obtained from two chrome–alumel thermocouples. Pressure is measured during the explosion with a Kistler pressure transducer. Flame images are recorded by a TRI Phantom v7.3 camera which is capable of a maximum speed of 200,000 frames per second.

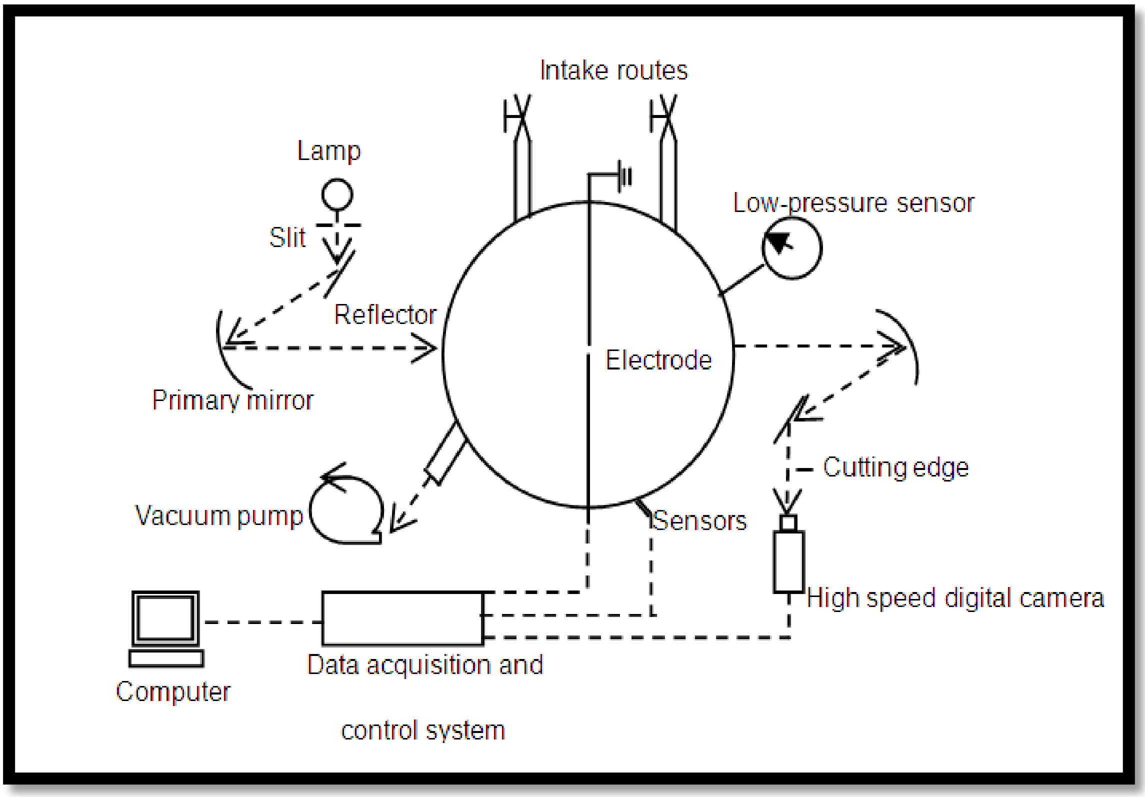

Fig. 3-4 Schematic illustration of the experimental apparatus.

3.2.2 Experimental data processing

The flame images are then post-processed by imaging analysis software, and the flame radius is tracked. In some measurements the spherical flame front becomes un-recognisable in the later stage of flame propagation due to flame instabilities and the self-tubulisation phenomenon, therefore only those images in which a clear and sphere-like flame front can be identified have been processed

In most flame propagation processes, two distinctive instants at which flame surfaces lose initial smoothness can be found:

- Large cracks on the flame surface begin to branch and the formation of cracks in new directions, as illustrated by the 3rd images of ***Fig. 3-4***. The reason for the formation of these cracks can be unequal diffusion instability, un-even distribution of spark energy and local unburnt mixture inhomogeneity.

- Sudden and spontaneous appearance of a large number of small cells over the entire flame surface (the 4th image of ***Fig. 3-5***). The characteristic length scale of such cells is significantly smaller than that of those large cracks. The appearance of these small cells is caused by hydrodynamic instability.

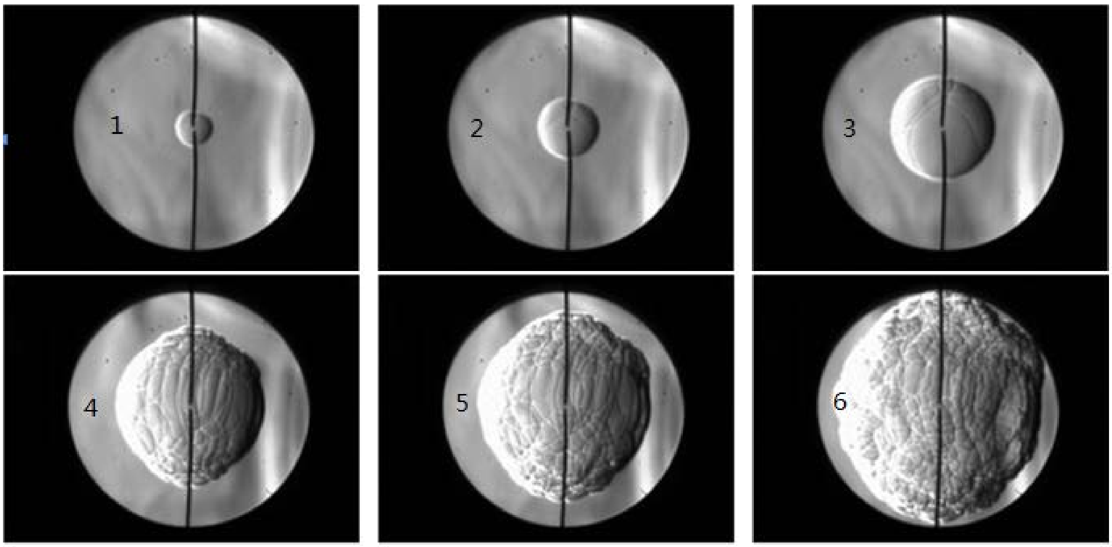

Fig. 3-5 Serial images of propagation process of hydrogen-air flame at 298 K, 1 bar, Φ=0.8. Measurement times are (from top left to bottom right): 0.382ms, 0.771ms, 1.50ms, 3.01ms, 3.48ms and 4.56ms.

In the analysis below, the second instant will be used primarily as the onset of flame instability, unless significant unequal diffusion instability can be identified earlier. The reason being: firstly, unlike the unequal diffusion instability, hydrodynamic instability occurs in almost all flame propagations. Secondly, compared to the growth and branching of large cracks, hydrodynamic instability occurs with very high intensity, i.e. small cells grow across the entire flame surface spontaneously, making it relatively easier to accurately identify the exact onset timing. Additionally, values of $\boldsymbol{Le}$, $\boldsymbol{\sigma}$ and $\boldsymbol{\delta}$ are calculated based on initial temperature, pressure and equivalence ratio prior to ignition.

.

3.3 Results and discussion

In order to systematically understand the parameters that influence the onset timing of cellular flame instabilities, the effects of fuel-air equivalence ratio, temperature, and pressure have been measured, categorised and discussed. In order to eliminate the effect of difference in bomb size, the onset timing of instabilities is represented by ‘normalised critical flame radius’ which is defined as the ratio of critical flame radius and the bomb radius: R_f/R_{bomb}.

3.3.1 Effects of fuel-air equivalence ratio

Fig. 3-6 to ***Fig. 3-8*** show the effects of the fuel-air equivalence ratio on onset timing of flame instabilities. A common characteristic found in all three figures is that, despite the increase in initial temperature, the flame tends to lose stability earlier under leaner conditions and becomes progressively more stable as the equivalence ratio moves towards stoichiometry. Such behaviours are expected as lean and stoichiometric/rich hydrogen-air flames, respectively, are naturally unequal diffusion instable ($\boldsymbol{Le} > 1$) and stable ($\boldsymbol{Le} < 1$).

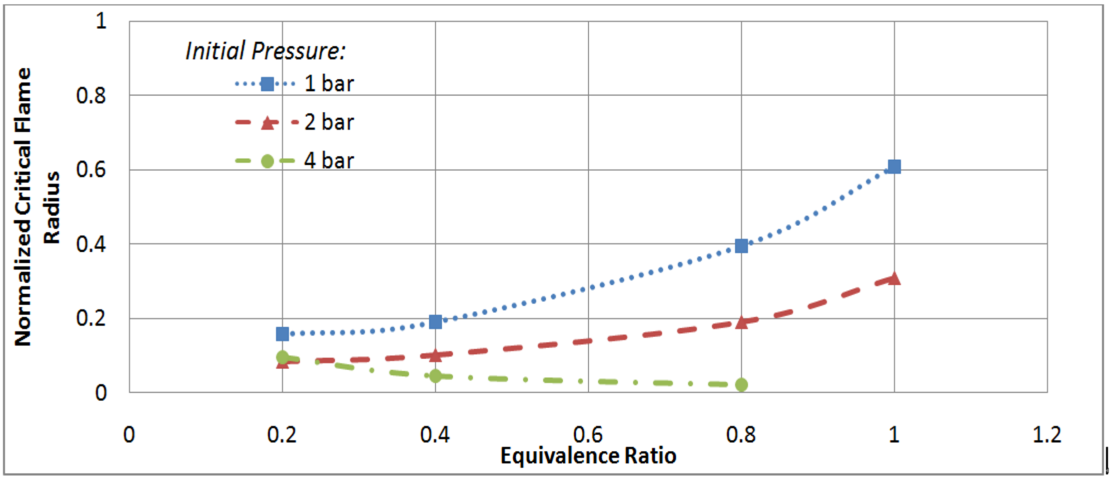

Fig. 3-6 The variations of the normalized critical flame radius under different equivalence ratios at an initial temperature of 298 K and initial pressure of 1, 2 and 4bar.

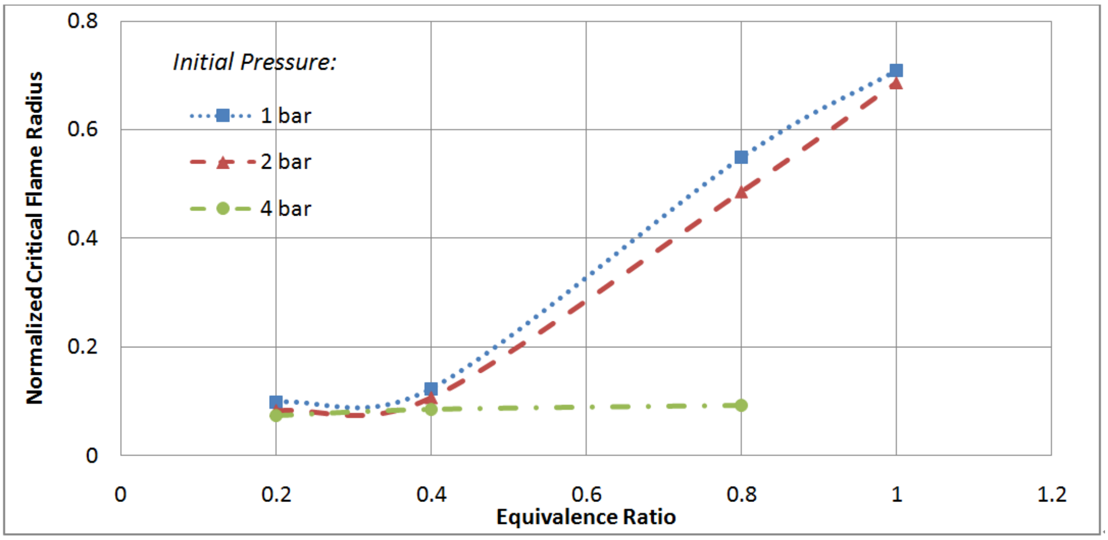

Fig. 3-7 The variations of the normalized critical flame radius under different equivalence ratios at an initial temperature of 343 K and initial pressure of 1, 2 and 4bar.

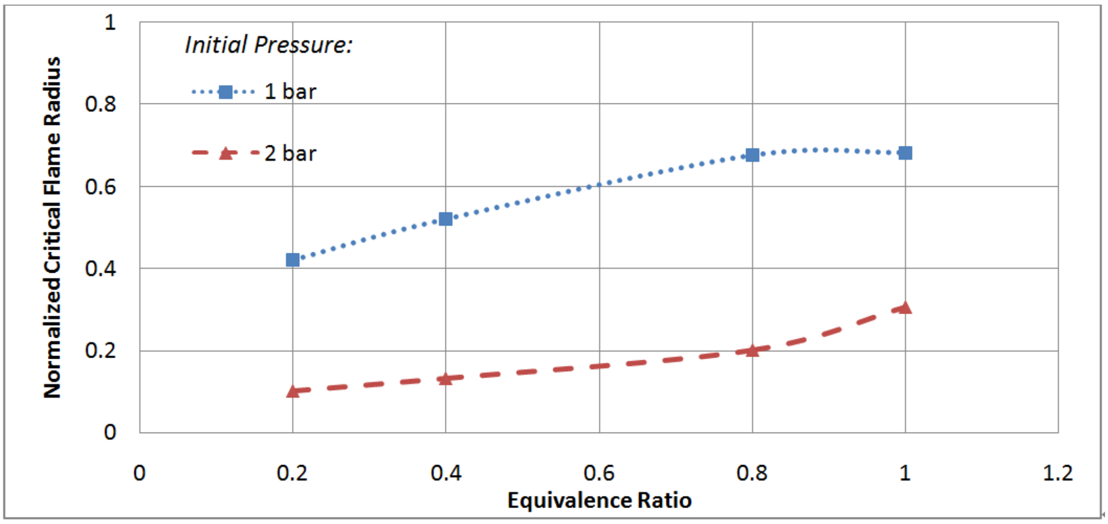

Fig. 3-8 The variations of the normalized critical flame radius under different equivalence ratios at an initial temperature of 423 K and initial pressure of 1 and 2bar.

Fig. 3-9 shows the variation of the Lewis number, calculated using ***Eq. 3-1***, under different equivalence ratios, temperatures and pressures. Lean hydrogen-air mixtures have low Lewis numbers and therefore are prone to unequal diffusion instability, especially when $\Phi = 0.2$ that the propensity to destabilize is so strong such that the flame stretch effect cannot offset the destabilization to stabilize the flame; the flame surface loses uniformity at a very early stage as shown in ***Fig. 3-2***.

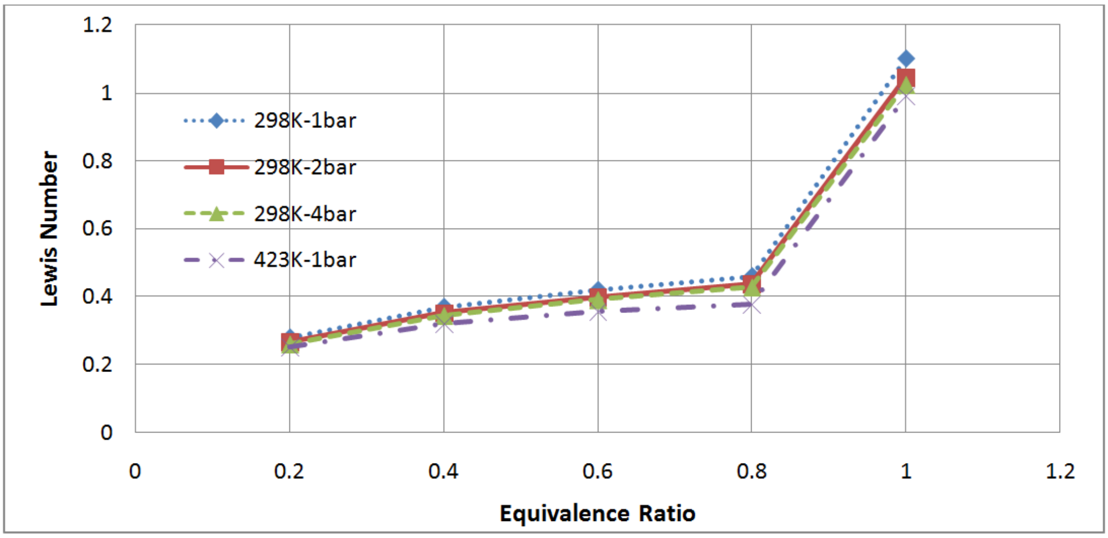

Fig. 3-9 Calculated Lewis Number under different equivalence ratios, temperatures and pressures.

The fuel-air equivalence ratio affects the flame instabilities primarily by reducing and enhancing the propensity to unequal diffusion instability. For lean hydrogen-air flames unequal diffusion instability occurs in the initial stage of flame propagation before any signs of hydrodynamic instability can be observed. On the other hand, stoichiometric and rich hydrogen-air flames naturally have Lewis numbers that are greater than 1 and thus have higher resistance to unequal diffusion instability. In experimental observations, these flames can maintain uniformity to a later stage of propagation before hydrodynamic instability is triggered. In general, equivalence ratio affects flame instability under lean-burn conditions and at the early stage of flame propagation. Flame stability becomes less sensitive to equivalence ratio when Φ gradually moves towards stoichiometry.

3.3.2 Effects of temperature

The effects of temperature on the flame instabilities are illustrated in ***Fig. 3-10*** and ***Fig. 3-11***. Graphically these effects can be split into two categories: effect on lean flames ($\boldsymbol{\Phi} = 0.2, 0.4$) and effect on near-stoichiometric to stoichiometric flames ($\boldsymbol{\Phi} = 0.8, 1.0$). For lean flames, increased temperature can, especially under lower pressure, delay the occurrence of unequal diffusion instability. The reason could be that very lean flames ($\boldsymbol{\Phi} = 0.2, 0.4$) always suffer from slow burning speed. Such slow propagation gives cracks that are formed by either initial spark defects and local inhomogeneity or unequal diffusion effect plenty of time to grow and branch. By increasing the temperature the combustion is greatly intensified, so is the burning speed. This increase in burning speed is particularly significant in very lean flames. It greatly reduces the time for the cracks to form and grow. Therefore the flames retain their relative smoothness for a longer time ('relative' means that very lean flames are often 'born' with large cracks due to unequal diffusion instability).

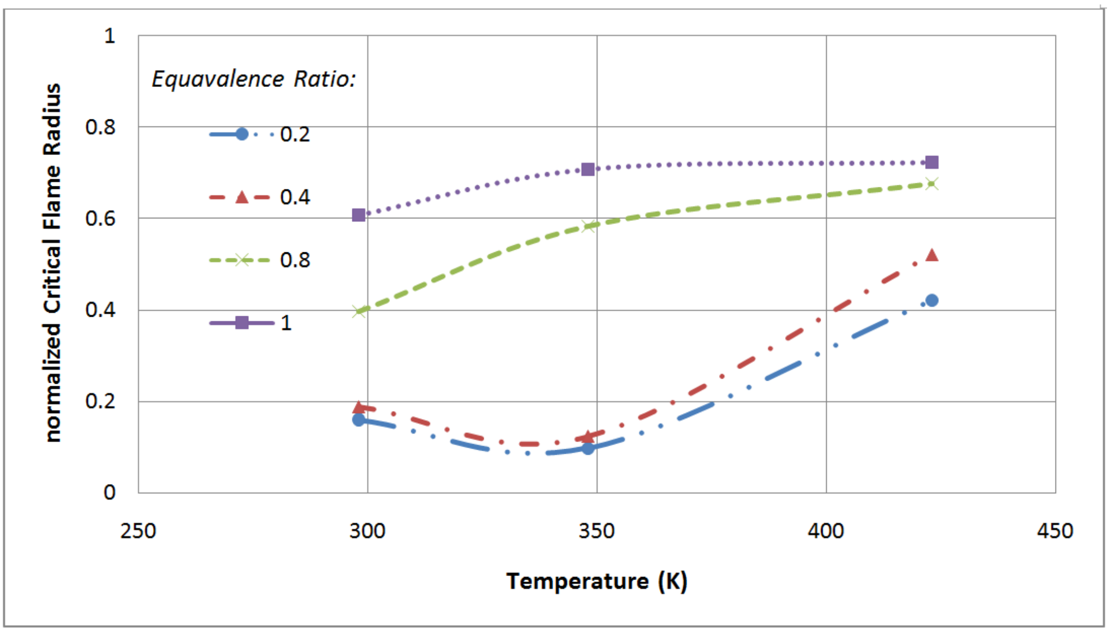

Fig. 3-10 The variations of the normalized critical flame radius under different temperatures at an initial pressure of 1bar and fuel-air equivalence ratio of 0.2 to 1.0.

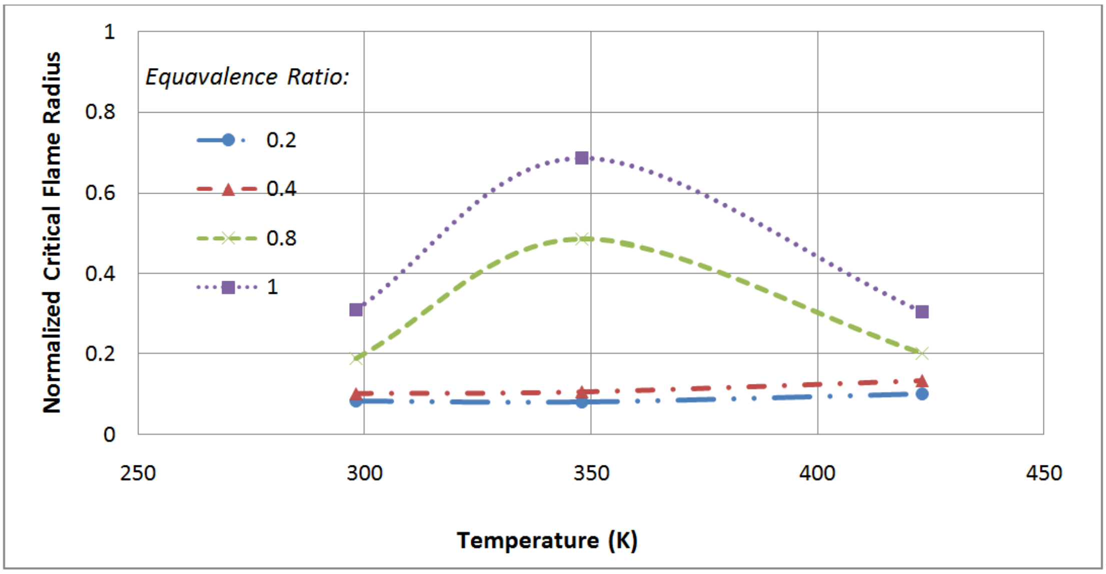

Fig. 3-11 The variations of the normalized critical flame radius under different temperatures at an initial pressure of 2bar and fuel-air equivalence ratio of 0.2 to 1.0.

For stoichiometric and near-stoichiometric flames ($\boldsymbol{\Phi} = 0.8, 1.0$) the above-mentioned delaying effect of increasing temperature is also noticeable. These flames are either naturally unequal diffusionally stable or have much stronger resistance to unequal diffusion instability compared to leaner flames, therefore, it is logical to conclude that increased temperature stabilizes flames from hydrodynamic instability.

Calculated density ratio, $\boldsymbol{\sigma}$, using ***Eq. 3-4*** and shown in ***Fig. 3-12***, revealed that $\boldsymbol{\sigma}$ is inversely proportional to temperature, which means that propensity to hydrodynamic instability is reduced as the temperature is increased. Contradictorily, when the combustion is initiated in a higher pressure environment the delaying effect is completely levelled off for very lean flames or even reversed for stoichiometric and near-stoichiometric flames. It suggests that temperature is not the dominant factor for the onset of flame instabilities.

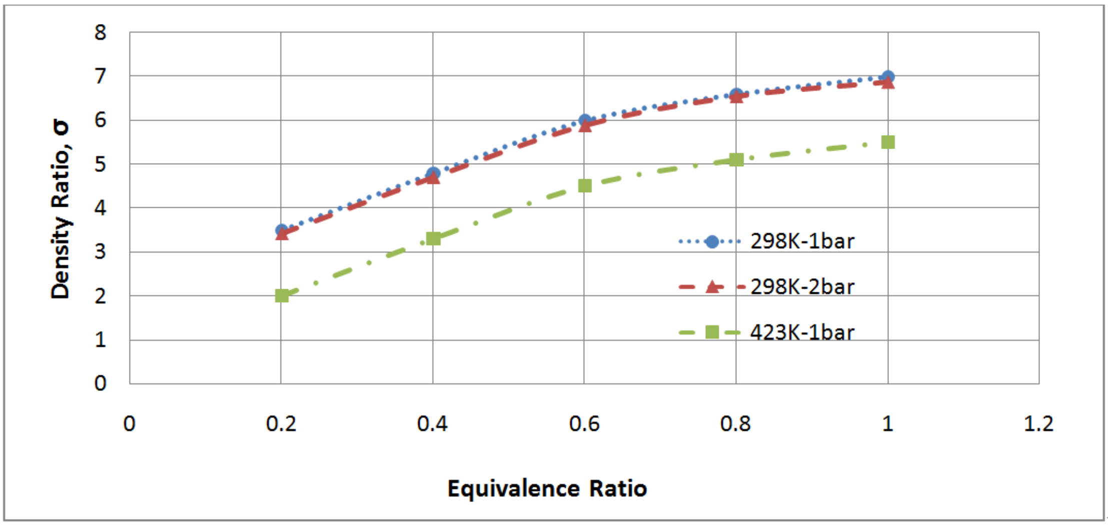

Fig. 3-12 Calculated density ratio under different equivalence ratios, temperatures and pressures.

3.3.3 Effects of pressure

Under lower pressure (i.e., 1bar), flames under different equivalence ratios show good consistence in terms of unequal diffusion instability i.e., lean hydrogen flames ($\boldsymbol{\Phi} = 0.2, 0.4$) lose stability very early; when the mixture is enriched to $\boldsymbol{\Phi} = 0.8$ the flame shows much better resistance to unequal diffusion instability, but still loses surface smoothness much sooner than stoichiometric flame which is naturally unequal diffusionally stable and eventually breaks up due to hydrodynamic destabilization, as shown in ***Fig. 3-13***.

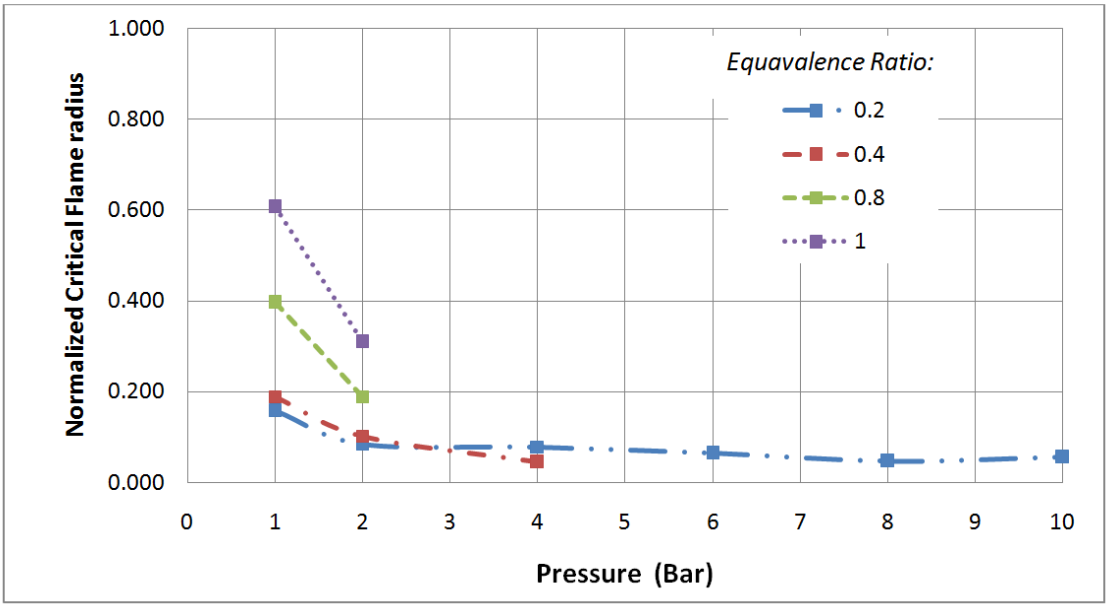

Fig. 3-13 The variations of the normalized critical flame radius under different pressures at an initial temperature of 298K and fuel-air equivalence ratio of 0.2 to 1.0.

As the pressure is increased all flames exhibit much earlier destabilization, particularly the stoichiometric and near-stoichiometric flames. Very lean flames ($\boldsymbol{\Phi} = 0.2, 0.4$) experiences relatively less advance in destabilization. That is to say, it is the hydrodynamic instability rather than the unequal diffusion instability that has been more significantly enhanced. However, since the Lewis number, $\boldsymbol{Le}$, and density ratio, $\boldsymbol{\sigma}$, are almost unchanged with pressure variation (shown in ***Fig. 3-9*** and ***Fig. 3-12*** respectively), neither unequal diffusion nor hydrodynamic instability, in theory, should be enhanced by the increase of pressure. Therefore another parameter must be responsible for the advance in destabilization. ***Fig. 3-14*** shows the calculated flame thickness, $\boldsymbol{\delta}$, obtained using ***Eq. 3-5***. It can be clearly seen that $\boldsymbol{\delta}$ is stable against temperature change but is more sensitive to pressure increase i.e., the flame becomes thinner as the pressure is increased. A thinner flame usually indicates intensified combustion and faster flame speed but it also results in lower tolerance to both internal and external disturbances, making the flame more vulnerable to destabilization.

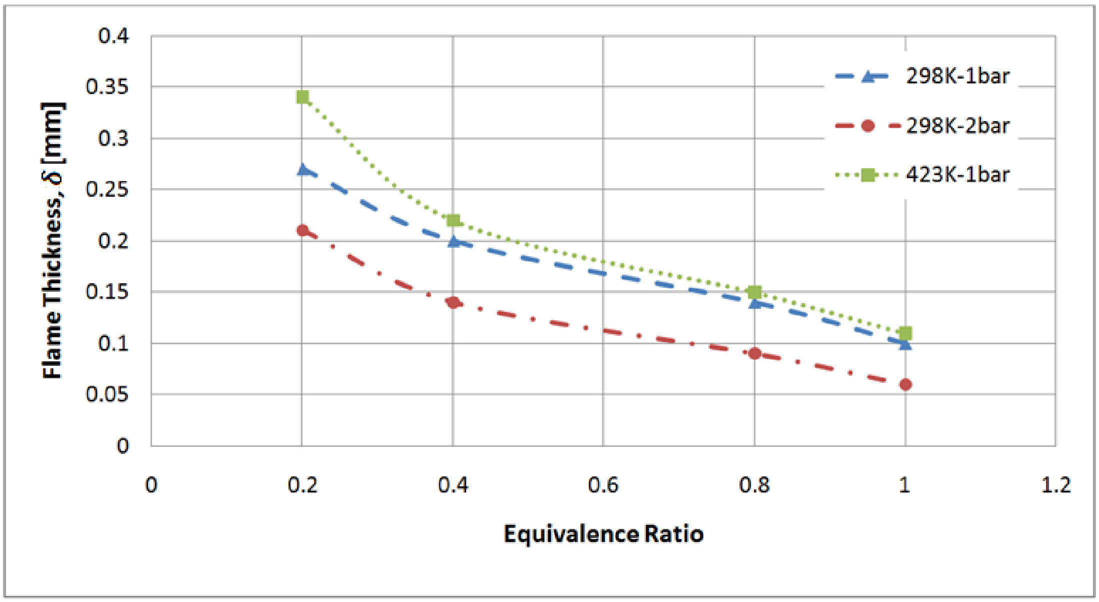

Fig. 3-14 Calculated flame thickness under different equivalence ratios, temperatures and pressures.

The same characteristic was also found and summarized in the work by Law (2004). Therefore it is logical to conclude that thinner flames tend to promote early hydrodynamic instability, as shown in ***Fig. 3-15***. Also found from ***Fig. 3-15*** is that as the flame front becomes thinner the number of cells increases and the average size of cells decreases.

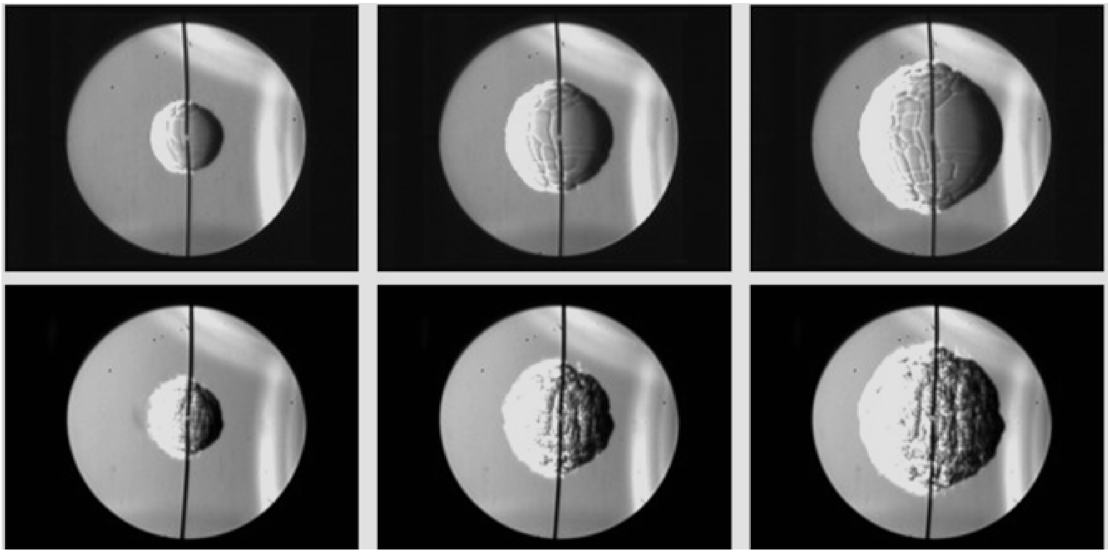

Fig. 3-15 Serial images of propagation process of hydrogen-air flame at 298 K, Φ=0.8 and 1bar (upper row) and 2bar (lower row). Respective flame thicknesses are calculated to be 0.03 and 0.016mm.

3.4 Summary

The onset of flame instabilities of laminar hydrogen-air spherical premixed flames has been studied in a constant volume combustion bomb using high-speed Schlieren and Shadow photography techniques. The effects of equivalence ratio, temperature and pressure were identified and analysed. The following conclusions can be drawn based on the analysis of experimental results:

- Outwardly propagating spherical flames experience two categories of instabilities: unequal diffusion instability caused by unequal mass and thermal diffusion, and hydrodynamic instability caused by interactions between the flame and external disturbances.
- Unequal diffusion instability can be visually identified by the gradual growth and branching of large cracks. Its appearance is governed by the Lewis number. Stoichiometric hydrogen flames are naturally stable to unequal diffusion instability.
- Hydrodynamic instability can be visually identified by sudden and spontaneous appearance of small cells across the entire flame surface. Changes to certain parameters can only delay its appearance but not totally eliminate it.
- The onset of flame instabilities is identified by the means of measuring critical flame radius. The critical radius is proven to be under the influences of equivalence ratio, temperature and pressure.
- Equivalence ratio governs the value of the Lewis number, $\boldsymbol{Le}$, and therefore decides whether the flame is naturally stable or instable to unequal diffusion instability. When $\boldsymbol{Le} < 1$, cells induced by unequal diffusion effect grow instantaneously at the beginning of flame kernel formation.
- Increased temperature has a strong delaying effect on the appearance of unequal diffusion cells, particularly for very lean flame. The reason could be enhanced combustion rate and flame speed that allow less time for the cells to appear and grow. For stoichiometric flames, temperature increase reduces the density ratio, $\boldsymbol{\sigma}$, and therefore weakens the hydrodynamic instability.

- Experimental results revealed that pressure is the most dominant of the three parameters under investigation in terms of the onset of flame instability. Although pressure variation barely affects either $\boldsymbol{Le}$ or $\boldsymbol{\sigma}$ which means it doesn’t enhance unequal diffusion and hydrodynamic instabilities, but it affects the flame in a more direct manner: by changing the flame thickness. Increased pressure significantly weakens the flame front making it more vulnerable to destabilization. Higher pressure also induces a larger number of cells of smaller average size.

Chapter Four: Calculation of Transient Stretched Laminar Flame Speed

4.1 Introduction

The calculation of the laminar burning velocities is one of the fundamental components in modelling a variety of combustion systems, such as internal combustion (IC) engines. Some studies were conducted in constant volume combustion experiments and the laminar burning velocity was express as function of bomb pressure history, $\boldsymbol{u_l} = \left(\frac{\boldsymbol{1}}{\boldsymbol{F_1 P}}\right)\left(\frac{\boldsymbol{r_c}}{\boldsymbol{P}}\right)\left(\frac{\boldsymbol{dP}}{\boldsymbol{dt}}\right)$ (Iijima & Takeno 1986). Others using semi-empirical equations in the form of: $\boldsymbol{u_l} = \boldsymbol{u_l^0}\left(\frac{\boldsymbol{T_u}}{\boldsymbol{T_0}}\right)^{\boldsymbol{a}}\left(\frac{\boldsymbol{P_u}}{\boldsymbol{P_0}}\right)^{\boldsymbol{b}}$, where $\boldsymbol{u_l^0}$ is the reference laminar burning velocity at known mixture strength, temperature and pressure, $\boldsymbol{a}$ and $\boldsymbol{b}$ are dependents determined experimentally (Lewis & von Elbe 1934). More recently, Dowdy (1991) and Rahim (2002) developed methods, either linear or non-linear, for extrapolating expressions of the mass fraction burnt and the instantaneous flame speed using bomb pressure history. The authors claimed that these models were reliable when the flame size was relatively small and the bomb pressure increase is not significant. This is due to the fact that the relationship between the mass fraction burnt and the bomb pressure becomes non-linear as the flame size exceeds approximately 10% of the size of the combustion bomb (Dowdy et al. 1991; Rahim et al. 2002). In order to make above-mentioned calculations work, full sets of experimental data, i.e. the exponents $\boldsymbol{a}$ and $\boldsymbol{b}$ and the bomb pressure history, is a prerequisite. The accuracy of a and b depends on the range of the experiments conducted. Numerous experiments with small increments of temperature and pressure have to be conducted in order to maintain high fidelity, making it an expensive and time consuming process (Lewis & von Elbe 1934; Metghalchi & Keck 1982; Metghalchi & Keck 1980). Furthermore, it is difficult to integrate combustion chemistry into such calculations, when prediction of combustion products has become increasingly important in IC engine simulations. Some commercial packages, such as the **Chemkin Forté** (Anon 2013), integrate three-dimensional fluid dynamics and chemical kinetics to study the flame propagation and emission formation processes in IC engines. These packages are capable of providing simulation results of high complexity and accuracy, but at the costs of computational time at the magnitude of hours. It would be a necessity to have a cost-effective one-dimensional laminar burning velocity model that is integrated with combustion chemistry.

The aim of this study is to develop a one-dimensional transient laminar burning velocity model that eliminates the need for priori experiments and with the capability of solving combustion chemistry. The model developed is based on a one-dimensional three-zone thermodynamic model that calculates the mass transfer and diffusion and the heat transfer between zones. The chemical processes involved in the combustion are solved using an in-house chemical kinetics solver with an established reduced hydrogen-oxidation mechanism from literature. The model has the potential to be adopted into future IC engine models for the purpose of cost-effective combustion and emission formation studies.

4.2 Model Development

The propagation of a spherical flame front divides the combustion bomb into three distinctive zones: burnt zone, burning zone and unburnt zone, as illustrated by ***Fig.4-1***. The flame front consumes the unburnt gas at the rate of the stretched laminar flame speed i.e. $\boldsymbol{S_f = d_{r_f}/dt}$, which can be seen as the result of the combination of three factors: the laminar burning velocity, the relative thermal expansion and the flame stretch effects. The model development starts with calculation of the laminar burning velocity and the effects of relative thermal expansion and flame stretch will be added later.

The mode has a layered structure where the unburnt zone is divided into a number of thin sub-layers, which is denoted by $\boldsymbol{n}$. The flame propagation process is seen as the consecutive consumption of these thin unburnt layers. After the ignition, the flame will first consume the innermost layer and this unburnt layer has become the burning zone. During the consumption, the temperature and pressure will increase in the burning zone, thereby compressing and heating up the rest of the unburnt zone. After a short period of time, $\vartriangle \boldsymbol{t_{flame}}$, the consumption of the current burning layer completes and the flame then moves into the adjacent unburnt layer (the second innermost one). The laminar burning velocity at the $\boldsymbol{n^{th}}$ layer is calculated as:

$$\boldsymbol{u_{l,n}} = \frac{(\boldsymbol{r_{bomb}} - \boldsymbol{r_{kernel}})/\boldsymbol{n}}{\Delta \boldsymbol{t_{flame,n}}} \tag{4-1}$$

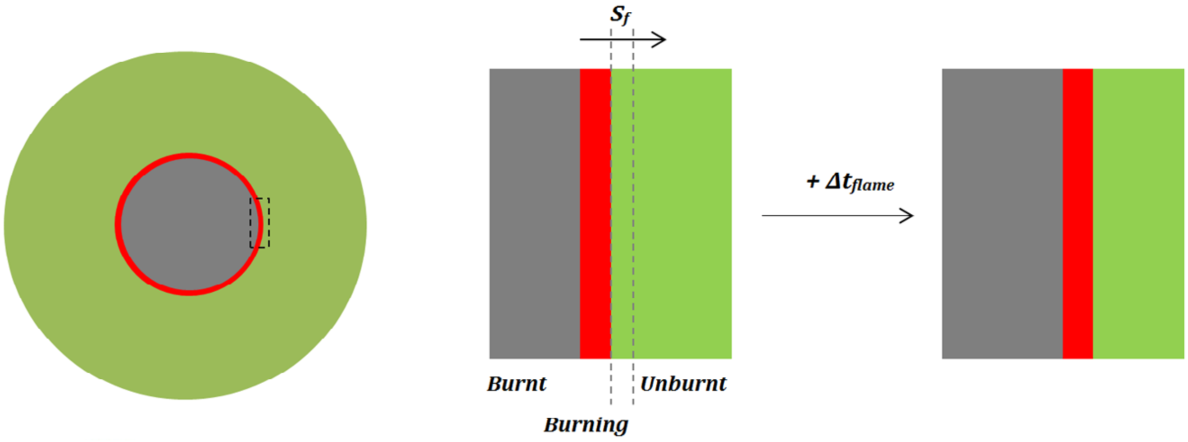

Fig.4-1. Schematic of the three-zone layout and the flame propagation process.

One advantage of the 'layered' structure is avoidance of flame thickness calculation. In practice, a flame consumes unburnt mixture entrained within the flame thickness at each propagation step. Flame thickness of a laminar flame has been well-studied and is a function of local temperature, pressure and mixture strength (M Metghalchi & Keck 1980)(Milton & Keck 1984). However, proper calculation of thickness of turbulent flames, which are commonly seen in IC engines, is still lacking (Liu & Chen 2009). This can be a potential problem in the future when the current laminar burning velocity model is adopted into IC engine models. In the 'layered' structure, each layer can contain multiple flame propagation steps, i.e. multiple flame thicknesses. Therefore, the laminar burning velocity obtained using **Eq.4-1** can be interpreted as the average laminar burning velocity through the thickness of each sub-layers.

4.2.1 Modelling assumptions

The following widely-used assumptions in combustion and flame simulations have been applied in the current modelling:

- both burnt and unburnt gases act as perfect gas;
- flow motion within the bomb is neglected throughout combustion;
- pressure across the bomb is uniform during the combustion process;
- flame maintains its spherical shape and laminar flame speed is uniform across the flame front;
- unburnt mixture is compressed isentropically by the flame and is in a chemical-frozen status.
- combustion starts at an ignition kernel, $\boldsymbol{r_{kernel}}$, of 2mm;

4.2.2 Governing equations

The unstretched laminar burning velocity is a fundamental combustion parameter and depends only on temperature, pressure and equivalence ratio. Thus it is possible to calculate the unstretched laminar burning velocity with thermodynamics and chemical kinetics models. The thermodynamics model calculates the unburnt temperature, pressure and mixture composition at each flame position as the flame propagates, and the chemical kinetics model solves the combustion chemistry.

The principles of energy and mass conservation are applied to all three zones to describe the energy flow within the combustion bomb.

Unburnt Zone: Temperature and pressure of the unburnt zone are influenced by two major factors: the heat transfer from the flame and the compression work exerted by the flame. These are described in **Eq.4-2**:

$$\left(\boldsymbol{m_u} - \boldsymbol{m_f}\right) \cdot \boldsymbol{C_{p,u}} \cdot \frac{\boldsymbol{dT_u}}{\boldsymbol{dt}} = \dot{\boldsymbol{Q}}_{\boldsymbol{f,u}} + \dot{\boldsymbol{W}}_{\boldsymbol{f}} + \dot{\boldsymbol{Q}}_{\boldsymbol{f,d}} - \boldsymbol{m_f} \cdot \boldsymbol{H_u} \qquad (4\text{-}2)$$

where $\boldsymbol{m_f}$ represents the mass entrained by the burning zone, $\dot{\boldsymbol{Q}}_{\boldsymbol{f,u}}$ represents the convective heat transfer from the flame to the unburnt zone and $\dot{\boldsymbol{W}}_{\boldsymbol{f}}$ is the compression work done by the volume change. $\boldsymbol{H_u}$ represents the mean specific enthalpy of burning mixture at $\boldsymbol{T_u}$.

$$\dot{\boldsymbol{Q}}_{\boldsymbol{f,u}} = \boldsymbol{h_f} \cdot \boldsymbol{A_f} \cdot (\boldsymbol{T_f} - \boldsymbol{T_u}) \qquad (4\text{-}3)$$

$$\dot{\boldsymbol{W}}_{\boldsymbol{f}} = \mathrm{P}_{\boldsymbol{u}} \cdot \frac{\boldsymbol{d}\mathrm{V_u}}{\boldsymbol{dt}} \qquad (4\text{-}4)$$

where $\boldsymbol{h_f}$ is the heat transfer coefficient, $\boldsymbol{A_f}$ is the surface area of the flame, $\boldsymbol{T_f}$ and $\boldsymbol{T_u}$ are the temperature of the flame and the unburnt zone respectively, $\boldsymbol{V_u}$ represents the instantaneous volume of the unburnt zone and $\boldsymbol{P_u}$ is the unburnt pressure.

The heat transfer coefficient, $\boldsymbol{h_f}$, for flame propagation inside internal combustion engines is estimated as (Liu & Chen 2009):

$$\boldsymbol{h_f} = \boldsymbol{C_h} \cdot \boldsymbol{B}^{-0.2} \cdot \boldsymbol{P}^{0.8} \cdot \boldsymbol{w}^{0.8} \cdot \boldsymbol{T_f}^{0.53} \qquad (4\text{-}5)$$

where $\boldsymbol{C_h}$is the heat transfer rate constant, $\boldsymbol{B}$ is cylinder diameter, $\boldsymbol{w}$ is the characteristic speed within the cylinder. The term $\boldsymbol{B}$ will be set as the diameter of the bomb, instead of that of an engine cylinder.

Burnt Zone: All burnt mixtures are assumed to be in chemical equilibrium state (Daneshyar & Hill 1987). The energy conservation of the burnt zone is in a similar manner to that of the unburnt zone, except that the energy addition by mass transfer from the previous calculation step has to be taken into account:

$$(m_b + m_f)\cdot C_{p,b}\cdot\frac{dT_b}{dt} = \dot{Q}_{f,b} + V_b\cdot\frac{dP}{dt} + m_f\cdot H_f \tag{4-6}$$

where m_f represents the burnt mass transferred from the burning zone into the burnt zone. H_f represents the mean specific enthalpy of burning mixture at T_f.

Burning Zone: The energy flow within the burning zone is described by **Eq. 7**.

$$m_f\cdot C_{p,f}\cdot\frac{dT_f}{dt} = \dot{Q}_{chem} + \dot{Q}_{f,u} + \dot{Q}_{f,b} - \dot{Q}_{f,d} \tag{4-7}$$

where $\dot{Q}_{chem}$ represents the primary heat release from chemical reactions and the kinetic equations that describe the reactions within this layer are formulated as an ODE set (Liang et al. 2009):

$$\dot{Q}_{chem} = -\sum_{k=1}^{K}\frac{dY_k}{dt}\frac{(\Delta h_f^0)_k}{W_k} \tag{4-8}$$

$$\frac{dY_k}{dt} = \frac{\dot{\omega}_k}{\rho}W_k \quad k = 1,\ldots,K \tag{4-9}$$

where $(\Delta h_f^0)_k$ is the enthalpy of formation of the k^{th} species, ρ represents the density of the reacting mixture, $\dot{\omega}_k$ and W_k are the molar production rate and molecular weight of the species, respectively. In previous work (Saeed & Stone 2004; Byun 2011), the heat transfer from the flame front to the bomb walls has been found to be negligible and is therefore not included in the model.

The term $\dot{Q}_{f,d}$ takes into account of the energy transfer due to the diffusion effect of burning mixtures to the unburnt zone. It is evaluated using the mixture-averaged method introduced in the TRANSPORT library in the CHEMKIN-III package (Kee et al. 1996):

$$\dot{Q}_{f,d} = \frac{H_f}{c_p}\sum_{k=1}^{K}\rho\cdot\frac{dY_k}{dt}\cdot V_k\cdot c_{p,k} \tag{4-10}$$

where $V_k$and $c_{p,k}$ are, respectively, the diffusion velocity and constant pressure and the heat capacity of the k^{th} species.

4.2.3 Chemical kinetics mechanism

The accuracy of unstretched laminar burning velocity calculation depends on the realism of the kinetics mechanism and the accuracy of the reaction rates. Hydrogen combustion kinetics has been widely studied (Mueller et al. 1999)(Vlachos 1996)(Law et al. 2003)(O Conaire et al. 2004)(Li et al. 2004)(Konnov 2008)(Hu et al. 2009). The hydrogen combustion kinetics mechanism used in the current research is the mechanism consists of 11 species and 19 reversible elementary reactions (Burke et al. 2011). The major improvements of this mechanism over previous mechanism include: clarification of uncertainties in the temperature and pressure dependence of rate constants for HO_2 formation/consumption reactions; demonstration of the pressure dependence of $H+O_2=OH+O$ and the temperature dependence of the $H+HO_2$ channels. The thermo-chemical data for the species involved are computed using the CHEMKIN-III package. An in-house chemical kinetics solver (Liu & Chen 2009) will be used in the burning zone to calculate the reaction rates of each elementary reaction and concentration variations of each reactants.

4.2.4 Defining of the end of in-flame reactions

In order to calculate the in-flame reaction duration, $\triangle \boldsymbol{t_{flame}}$, needed in **Eq.4-1**, one parameter that defines the end of the in-flame reaction need to be defined. The end of the in-flame reactions is not necessarily the end of the overall reactions occurs between the fuel and oxidant entrained into the flame. Together with intermediate products, a tiny amount of unburnt fuel and oxidant will continue reacting after being transferred into the burnt zone, this is commonly known as post-flame reactions .

In-flame reactions are characterized as high reaction rate and rapid energy release while post-flame reactions are relatively slow and release less energy. Therefore, reaction rates of some active intermediate products would be a sensible indication of the transit from in-flame to post-flame reactions. The H radical is known to be a very important intermediate product in hydrogen and hydrocarbon oxidations (Li et al. 2004)(Burke et al. 2011). It provides critical channels for $H+O_2$ and $H+HO_2$ reactions. As shown in ***Fig.4-2***, the change in the concentration of the H radical is closely related to consumptions of fuel and oxidant and the temperature increase (energy release). ***Fig.4-3*** shows the variations of H radical mole fraction and its change rate, $\dot{\boldsymbol{Y}}_{\boldsymbol{H}}$.

$$\dot{\boldsymbol{Y}}_{\boldsymbol{H}} = (\boldsymbol{Y}_{\boldsymbol{H}} - \boldsymbol{Y}'_{\boldsymbol{H}})/\Delta\mathbf{t} \tag{4-11}$$

where $Y_H$and Y_H' are the mole fraction of H radical in current and previous calculation time steps. $\Delta \mathbf{t}$ is the calculation time interval which is 10^{-6} second. In order to plot both curves on the same graph, $\dot{Y_H}$ has been divided by 10^5.

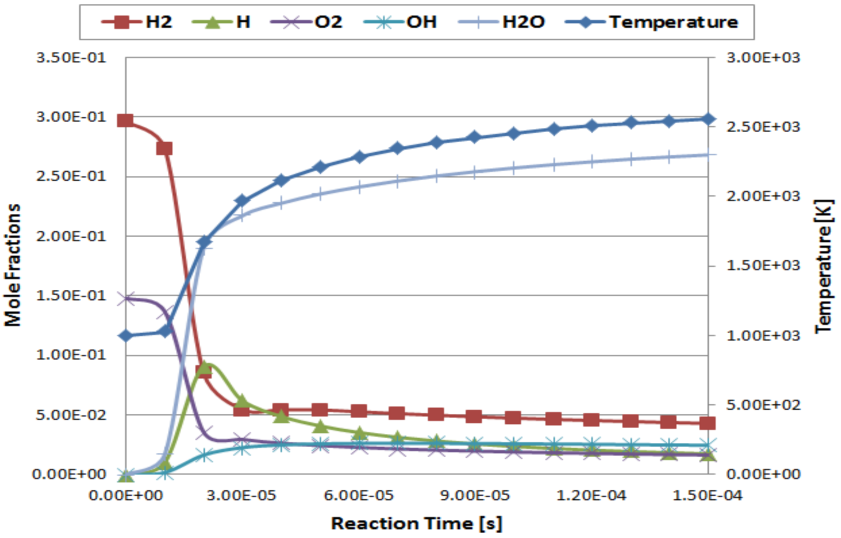

Fig.4-2. Variations of the mole fractions of reactants and the burning zone temperature during H_2-Air combustion at Φ=1.0, 1000K and 1bar.

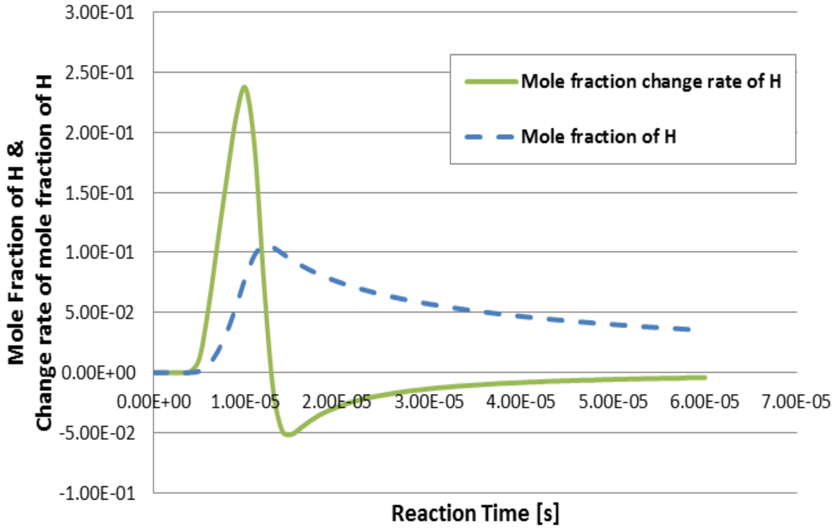

Fig.4-3. Variations of the mole fraction of H radical and its change rate.

Initial shape increase of $\dot{Y_H}$ indicates a period of fast production of H radicals that overwhelms the consumption; after reaching its positive maxima $\dot{Y_H}$ starts to drop showing that the consumption rate increases rapidly and eventually overwhelms the production rate when $\dot{Y_H}$ becomes negative; the negative minima of $\dot{Y_H}$ indicates the period of fastest consumption, after which both the production and consumption of H radicals start to cease as $\dot{Y_H}$ increases towards a constant value close to zero, which indicates the end of fast chemical reactions. In the current study, the end of in-flame reactions is defined as the point when $(\dot{Y_H} - \dot{Y_H}')/\dot{Y_H} \leqq 10^{-3}$. The value of the unstretched laminar burning velocity is then calculated using **Eq.4-1**. The choice of $\boldsymbol{n}$ in **Eq.4-1** is largely dependent on the size of the bomb. For the bomb used in the current study ($\boldsymbol{r_{bomb}}$=200mm), the value of $\boldsymbol{n}$ is chosen to be 400 to achieve best balance between convergence and computational time.

4.3 Unstretched laminar flame speed

Regarding to the characterization of a spherical expanding laminar flame, two categories of velocities have to be distinguished (Byun 2011; Gerke 2007): one is the velocity at which the laminar flame front propagates into the unburnt mixtures at a fixed reference spatial frame, i.e. $\boldsymbol{d_{r_f}/dt}$, also known as the laminar flame speed; the other is the corresponding burning velocity which differ from the laminar flame speed by the amount of burnt gases expansion velocity.

The unstretched laminar flame speed can be obtained by adding the burnt gases expansion velocity, $\boldsymbol{S_b}$, to the unstretched laminar burning velocity (Byun 2011):

$$\boldsymbol{S_u = u_l + S_b = u_l \cdot \kappa_{exp}} \tag{4-12}$$

$$\boldsymbol{\kappa_{exp} = \frac{\rho_u/\rho_b}{((\rho_u/\rho_b)-1)X_b+1}} \tag{4-13}$$

where $\boldsymbol{S_u}$ represents the unstretched laminar flame speed, $\boldsymbol{\kappa_{exp}}$ is the expansion coefficient, $\boldsymbol{\rho_u}$ and $\boldsymbol{\rho_b}$ are densities of the unburnt and the burnt mixtures and $\boldsymbol{X_b}$ is the mass fraction burnt. **Fig.4-4** shows the calculated density ratios, $\boldsymbol{\rho_u/\rho_b}$, at different temperatures and pressure. Both the equivalence ratio and initial temperature have great effects on the density ratio and the initial pressure only influences the value slightly.

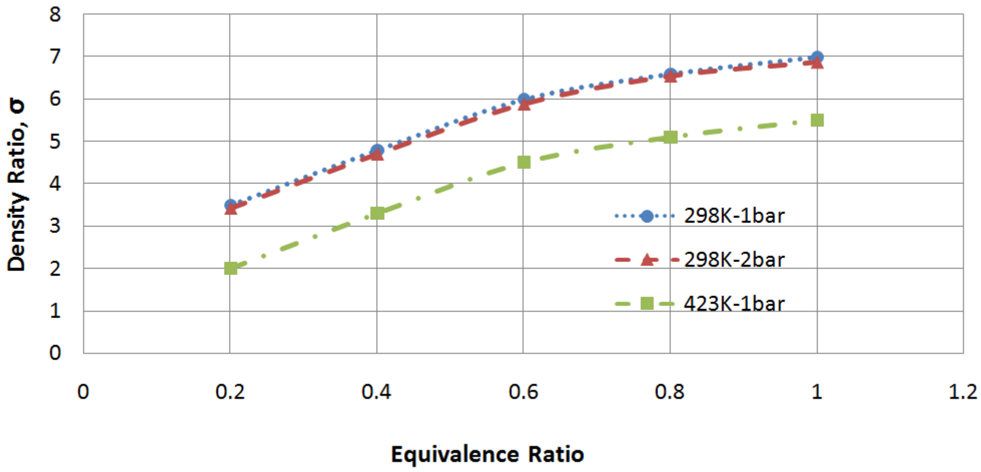

Fig.4-4. Calculated density ratio of unburnt and burnt Hydrogen-Air mixtures at different initial temperatures, pressures and equivalence ratio.

4.4 Stretched laminar flame speed

The relationship between the unstretched laminar flame speed, $\boldsymbol{S_u}$, the stretched laminar flame speed, $\boldsymbol{S_f}$, is described as (Bradley et al. 1996):

$$\boldsymbol{S_f = S_u - L_b \kappa} \tag{4-14}$$

$$\boldsymbol{\kappa} = 2\frac{S_f}{r_f} \tag{4-15}$$

where $\boldsymbol{\kappa}$ is the total stretch rate of a stable outwardly propagating spherical flame, $\boldsymbol{L_b}$ is the Markstein length of the burnt mixture. One limitation of **Eq.4-14** is that, as the response of the flame speed to the stretch is not always monotonic, when the flame becomes unstable it accelerates due to the cellular structure on the surface and the linear relationship is violated. Some researchers (Bradley et al. 1996)(Verhelst et al. 2005) adopted a methodology that only extrapolates the linear part in the flame speed vs. flame stretch plot to zero stretch. Such methodology ignores the non-linear response of the flame speed but is widely accepted and used. The onset of the cellular structure is represented by the critical *Peclet Number*, $\boldsymbol{P_{cl}} = \boldsymbol{r_{cl}/\delta_l}$, where $\boldsymbol{r_{cl}}$ is the radius that the flame starts to accelerate due to cellularity and $\boldsymbol{\delta_l}$ is the laminar flame thickness. Since there is few computation methods that reproduce the non-linear behaviour of $\boldsymbol{L_b}$ without priori experimental measurements the author has to use the proposed values of $\boldsymbol{L_b}$ obtained based on the linear extrapolation of $\boldsymbol{S_f}$ vs. $\boldsymbol{\kappa}$ curves, although this might result in underestimation of flame speed when the flame radius is relatively large. Several methods of extrapolating $\boldsymbol{L_b}$ of hydrogen-air mixtures have been reported at normal temperature and pressure (NTP) (Aung et al. 1997). $\boldsymbol{L_b}$ tends to increase monotonically with equivalence ratio and change sign around $\boldsymbol{\Phi}$ = 0.8, which implies that lean mixtures experience an earlier transition to unstable cellular structure. Verhelst (Verhelst et al. 2005) proposed values of $\boldsymbol{L_b}$ for higher temperature and pressure by using the regression methodology developed by Bradley (Bradley et al. 1996). These values will be used in the current study.

Finally, based on Eq. 1and 12-15 and the relationship between stretched and unstretched laminar flame speed, $\boldsymbol{S_f}$ can be obtained as:

$$\boldsymbol{S_f = u_l \cdot \frac{\rho_u/\rho_b}{((\rho_u/\rho_b)-1)X_b+1} - L_b \frac{2 \cdot S_f}{r_f}} \tag{4-16}$$

In the RHS of **Eq.4-16**, the stretched laminar flame speed is represented as a combination of the unstretched laminar burning velocity, the relative thermal expansion, and the flame stretch effect.

4.5. Model Validation

4.5.1 Experimental apparatus

A spherical stainless steel combustion bomb with 400mm inner diameter which is capable of withstanding the temperature and pressure generated by combustion with initial conditions up to 1.5MPa and 650K, as shown in **Fig.3-4** in Chapter Three, has been employed. The bomb has extensive optical access through a pair of orthogonal quartz windows of 100mm diameter. The optical system is arranged into a Z-shaped, the two primary mirrors have diameter of 100mm and focal length of 100cm.The slit has an adjustment range of 0-3mm and the blade can be adjusted in the range of 0-10mm. There are two intake routes, one for air, and the other for hydrogen. Low-pressure sensor is used to accurately measure partial pressure of gas with the precision of 0.001bar.The combustible mixture is spark ignited at centre of the chamber using electrodes extending from the top and the bottom. One electrode is fixed while the other could be moved for adjusting the ignition gap. After the induction of fuel and air is completed sufficient time is allowed for the mixture motion to decay. The bomb is flushed with dry air when combustion is finished to ensure minimum amount of residuals are left before subsequent combustion is initiated. Following the ignition, gas temperature inside the bomb is obtained from two chrome–alumel thermocouples. Pressure is measured during the explosion with a Kistler pressure transducer. Flame images are recorded by a TRI Phantom v7.3 camera which is capable of a maximum speed of 200,000 frames per second. Additional information on the experimental apparatus can be found in literature (Liu et al. 2011).

Three measurements are performed for each initial condition and the deviations are less than 7%. The flame images are then post-processed by imaging analysis software, and the flame radius is tracked. In some measurements, the spherical flame front becomes un-recognisable in the later stage of flame propagation due to flame instabilities and the self-tubulisation phenomenon, as shown in ***Fig.4-5***, therefore only those images in which a clear and sphere-like flame front can be identified have been processed. The instantaneous flame speed is calculated as: $\boldsymbol{S_f} = \boldsymbol{\Delta r_f / dt_{camera}}$, where $\boldsymbol{\Delta r_f}$ is the flame radius increase between two consecutive flame images and $\boldsymbol{dt_{camera}}$ is the time interval between two images.

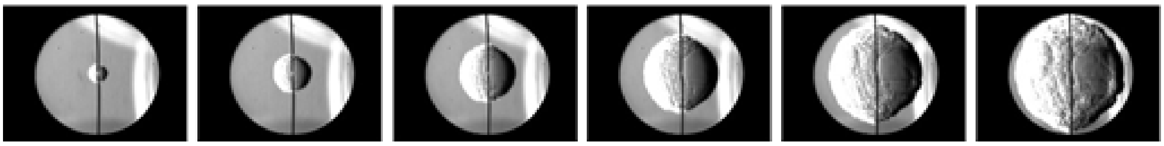

Fig.4-5. Experimental images in the sequence of propagation. Measured flame radiuses are: 5.8, 12.1, 17.8, 23.9, 30.0 and 35.0mm. H_2-Air mixture at 298K, 1bar and Φ=0.6.

4.5.2 Validation of unstretched laminar burning velocity

Fig.4-6 shows the unstretched laminar burning velocities at various equivalence ratios. In all three cases, the burning velocities increase with increasing temperature and become more sensitive to temperature increase at higher temperature region. These phenomena are expected as the unstretched laminar burning velocities are kinetically-controlled. These values are also compared with results obtained from a correlation (Iijima & Takeno 1986). The maximum differences in three cases are: 6.6% for Φ=1.0, 6.3% for Φ=0.8 and 7.0% for Φ=0.6, these values are all below the recommended deviation suggested by the authors.

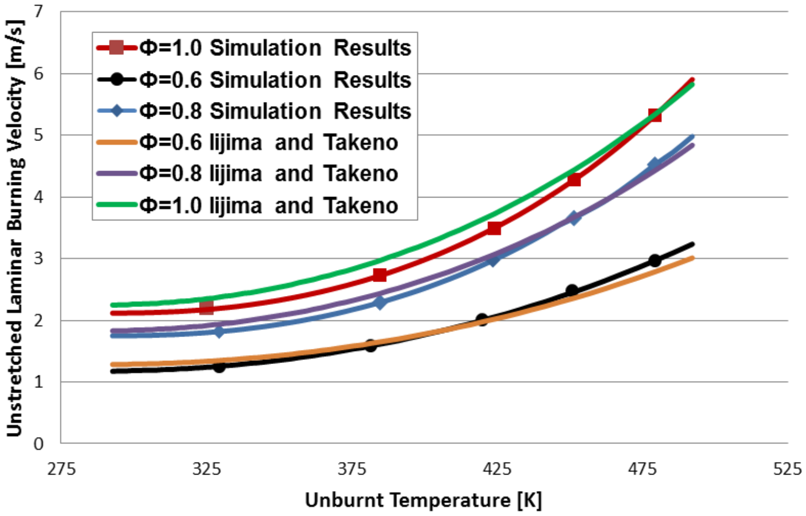

Fig.4-6. Comparisons of simulated unstretched laminar burning velocities of hydrogen-air mixtures and numerical correlations (Iijima & Takeno 1986).

4.5.3 Validation of stretched laminar flame speed

Fig.4-7 shows the comparisons of the calculated transient stretched laminar flame speeds, using **Eq.4-16**, and the experimental results. In order to clearly demonstrate the variations of flame speed at different stages of its propagation, the flame radius is normalised by the bomb radius to give a dimensionless parameter normalised flame radius: $\boldsymbol{r_n = r_f / r_{bomb}}$. Such normalisation also enables the comparisons to experimental data obtained in spherical bomb of different sizes. The moment when the flame surface becomes cellular is marked by the open symbols in ***Fig.4-7.*** Leaner flames tend to destabilize earlier as they have a Lewis number that is less than unity and are therefore less resistant to destabilization.

The calculated flame speeds match the measured flame speeds well in most of the flame propagation processes and the effects of flame stretching is discussed in section 3.5. Fluctuations of flame speed are noticeable. These fluctuations are due to flame surface cellularity which causes variations of flame speed and the inconsistence in the defining of the flame front during the post-process of experimental images, particularly when the flame surface is completely cellular. The flame speed of very lean mixture ($\boldsymbol{\Phi}$=0.6) maintains an almost constant value throughout the combustion with a large initial speed reduction due to large stretching rates. It has been reported that the rapid decay of the ignition energy also contributes to the flame speed reduction (Verhelst et al. 2005). In contrast, stoichiometric hydrogen-air flame experiences a rapid initial flame speed increase as a result of decaying flame stretch and strengthening combustion. Following the initial increase the flame speed maintains a nearly constant value from 20% to 55% bomb radius. The flame surface becomes completely cellular when the flame radius reaches the size of about 60% bomb radius and a steep increase in flame speed is triggered by the cellular structures.

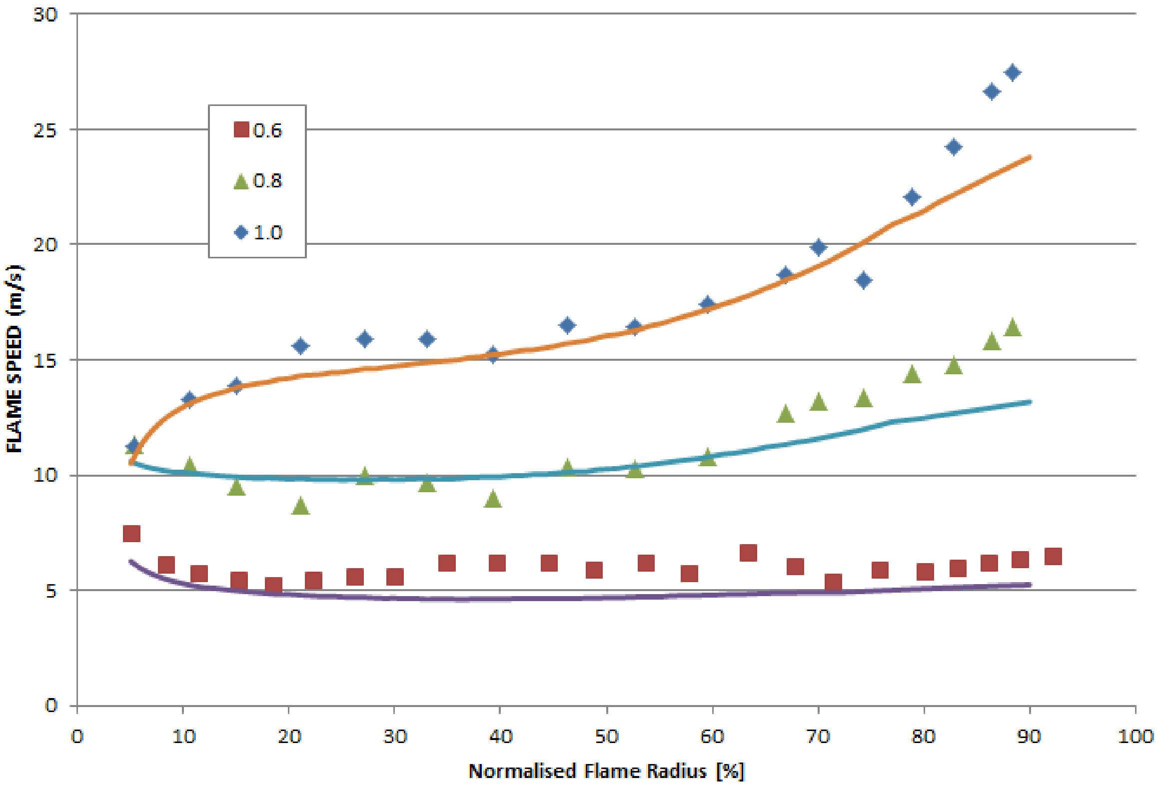

Fig.4-7. Comparison of the transient stretched hydrogen-air laminar flame speeds. Solid lines represent simulation results and markers represent experimental results. Initial temperature 298K and initial pressure 1 bar.

4.6 Summary

i. A transient unstretched laminar burning velocity model based on three-zone thermodynamic model and reduced chemical kinetics has been developed. The model achieved similar level of accuracy as traditional numerical correlations, while being independent on bomb pressure history or priori determination of reference laminar burning velocities. Thus the model has been more predictive, rather than simply reproduce what has happened in the experiments.

ii. The employment of chemical kinetics in the burning zone enables the model to calculate flame-out burnt products and gives the model the potential of predicting post-flame reactions and ultimately the emission formation when integrated into IC engine models.

iii. Based on the unstretched laminar burning velocity model, stretched flame speed model has been developed using established theories and experimental data. The model reproduced the effect of flame stretch well. The predicted flame speed has been validated against experimental results and good agreement has been achieved.

Flame speed has been found to increase with increased fuel-air equivalence ratio (from 0.6 to 1.0), temperature and pressure.

iv. The timing of the end of in-flame reactions has not been thoroughly studied and clearly defined in the literature. The choice of using the change rate of the concentration of H radical to define the end of the in-flame reactions is based on the literature study of hydrogen oxidation mechanisms, where the H radical has been identified as one of the most active intermediate products and is directly related to the consumptions of the fuel and the energy release rate.

v. Since a method that predicts the non-linear behaviour of Markstein length, particularly after the flame surface is cellular, is not yet available, the authors have to adopt the linear Markstein length, this results in underestimation of laminar flame speed when the flame front is cellular. Future improvement of the model should be focused in this area.

vi. The developed model requires less computational power and completes calculation for flame speeds in a combustion bomb of 200mm inner radius in the magnitude of fifteen seconds. The computational costs are expected to be in the magnitude of a few minutes when the developed model is integrated into IC engine simulations, which represents a noticeable saving on computational costs.

Chapter Five: Simulation of Flame Propagation in SI Engine

5.1 Introduction

Turbulent flame propagation within the combustion chamber is inherently unsteady (Heywood 1988) and is of great importance to spark ignition engine operation. Firstly, the unburnt charge, theoretically, is to be consumed by the propagating flame front in a sequential manner, therefore, the flame is responsible for combustion efficiency and cycle-to-cycle variations; Secondly, the propagating flame front is widely accepted as one of the major factors that contributes to the end gas autoignition. The key parameter for systematic understand of accurate prediction of combustion process is knowledge of the burning rate of the flame propagating through the charge (Liu et al. 2013). Due to the unsteady and transient nature of turbulent flames, extrapolation of experimental results obtain in laboratory conditions, i.e. NTP, is very difficult because of high in-cylinder temperature and pressure (Liu et al. 2013; Aleiferis & Rosati 2012; Peterson et al. 2014; Dahms et al. 2011).

In recent decades, numerical engine combustion simulation is becoming a powerful and cost-effective (when compared to engine testing) tool in the research and design of spark ignition engines. There are different levels of spark ignition engine combustion models. Computation fluid dynamics (CFD) modelling coupled with detailed (Long & Reitz n.d.), reduced (Blunsdon & Dent 1994; Eckert et al. 2003; Kong et al. 1995) and global (Liu et al. 2006) chemical kinetics showed a potential of replicate the turbulent flame propagation and predict abnormal combustion phenomenon, e.g. knock, in spark ignition engines. The chemical kinetics mechanism is applied to account for the temporal and spatial variance of the properties of unburnt mixture. The actual turbulent flame speed is calculated using a turbulent flame speed closure and an empirical correlation of laminar flame speed (Zimont & Polifke 1998). The combination of CFD thermodynamics model and chemical kinetics model provides sufficient accuracy but it comes with massive computational costs. Additionally, because empirical laminar flame speed correlations are fuel specific and only reliable in a limited range of operating conditions, the flexibility of the model is affected. Simpler spark ignition models have been developed using zero-dimensional modelling technique. These models use chemical equilibrium combustion models to determine the thermo-chemical state of the burnt products at a predefined flame temperature. These models are computationally efficient, and provide a handy tool in engine design and operating strategy testing. However, the turbulent flame propagation process is completely neglected and replace by a function of burnt mass fraction, i.e. Wiebe function (Shayler et al. 1990; Stone 1987; Rakopoulos & Michos 2008; Shudo et al. 2001; Ball et al. 1998; Rousseau et al. 1999; Ghojel 2010). The use of chemical equilibrium makes these models functionally unable to predict end gas autoignition. Liu (Liu & Chen 2009) greatly improved models of this kind by having a three-zone formation and adopting a reduced gasoline chemical kinetics mechanism into the unburnt zone to not only the combustion but also the onset of knock. Liu’s work has broadened the usage of models based on zero-dimensional thermodynamics and chemical kinetics for spark ignition engine research.

The current research has been vastly motivated by Liu’s work. The purpose of current research is to implement the developed chemical kinetic laminar flame speed model (introduced in chapter four), together with an ‘out-of-box’ turbulent flame speed correlation, into a zero-dimensional multi-zone thermodynamics model to simulate the turbulent flame propagation process within the combustion chamber.

5.2 Overview of the model

The model developed by the current study is a zero-dimensional SI engine combustion model which has a three-zone formation. It consists of, moving away from the spark plug, a burnt zone, a burning zone and a unburnt zone. The division of the zone is based on their different thermodynamic and chemical states, as shown in ***Fig. 5-1*** below.

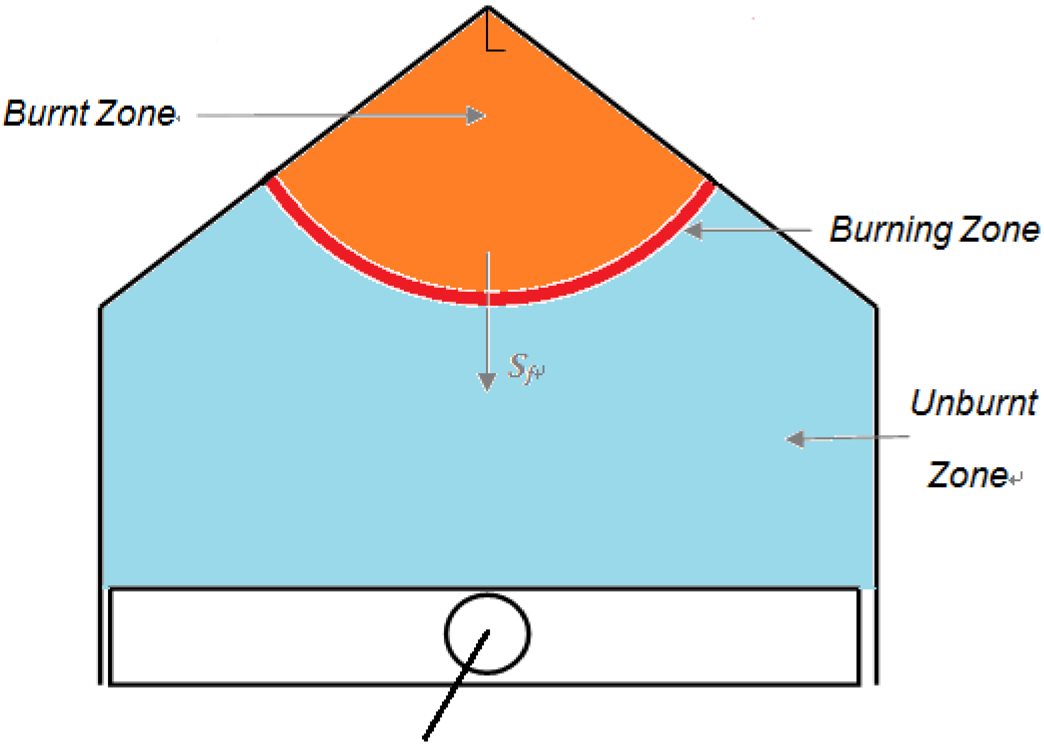

Fig. 5-1 Schematic illustration of the three-zone combustion chamber layout.

The burnt zone contains the burnt products and trace of intermediates that are not fully reacted, and is assumed to be in a thermodynamic and chemical equilibrium state. The burning zone represents the reaction layer of the flame front. It is where the unburnt mixture is consumed by violet chemical chain reactions and heat energy is released. The unburnt zone is made of unburnt fuel and air mixture upstream of the propagating flame front. The unburnt zone, unlike the burnt zone, is not assumed to be in a thermodynamic and chemical equilibrium state. The temperature and pressure in this zone is allowed to vary as a result of piston motion, flame propagation and heat transfer.

A modified version of Tanaka's chemical kinetics mechanism (Tanaka et al. 2003) is applied to both the burning and the unburnt zone in order to:

- Study the combustion process ***within*** the flame front by calculating a number of parameters including: flame temperature, species concentration evolution and combustion duration.
- Predict autoignition of unburnt mixture and onset timing of knock.

The modification was carried out by Liu et al. (2009) in order to adapt the mechanism into spark ignition engine combustion simulation, as the original mechanism was developed for HCCI combustion.

The simulation model consists of five major components:

- A engine cylinder model
- A flame geometry model
- A zero-dimensional thermodynamics model
- An in-cylinder turbulence model
- A chemical kinetics model (applied in two zones)

These components will be introduced in the following sections.

5.2.1 Model assumptions

The proposed model is a mathematical model of the compression and combustion (BDC-TDC-BDC) processes in a premixed naturally aspirated spark ignition engine. Some assumptions are applied in the development of the model:

1. Throughout these processes, the cylinder is treated as a variable volume plenum chamber, spatially uniform in pressure (Filipi & Assanis 1991).
2. Gas properties are calculated based on the ideal gas law. The in-cylinder mixture is assumed to be homogeneous and in a chemical-frozen state prior to ignition. Unburnt mixture is compressed isentropically. Autoignition is neglected at this stage of simulation to concentrate on flame propagation simulation.
3. The ignition process is neglected and a flame kernel is assumed to exist after the breakdown period. The kernel initially propagates at the rate of laminar flame speed under thermodynamic conditions at ignition. Pressure is assumed to be uniform on both sides of kernel (Tan & Reitz 2003). Herweg and Marly (1992) suggested values for kernel size and breakdown period to be 1mm radius and 200μs respectively.
4. The combustion regime in SI engines is assumed to fall into the wrinkled flame regime, as discussed in Chapter Two, where a turbulent flame is seen as thin laminar flamelets embedded in a turbulent flow. The advantage of the regime is that the calculation of chemical reactions and turbulent flow can be separated (Tan & Reitz 2003).
5. The turbulent flame front is assumed to have a spherical shape and such shape is maintained throughout the combustion process. The instantaneous turbulent flame front is arbitrarily wrinkled by the small eddies in the turbulent flow. A mean flame front centre line is introduced to simplify the flame geometry, as depicted in ***Fig. 5-2***. The red solid line and grey dashed curves represent the instantaneous and the mean centre line of the flame front respectively. Two solid black curves represents the mean flame front based on the mean flame front centre line. The mean flame front has the same thickness as the instantaneous flame front, which is denoted as δ_T.

6. The turbulent intensity within the combustion chamber is assumed to be spatially uniform. Additionally, the turbulence intensity is assumed to be a function of crank angle and its reference value at TDC, at a given engine speed.

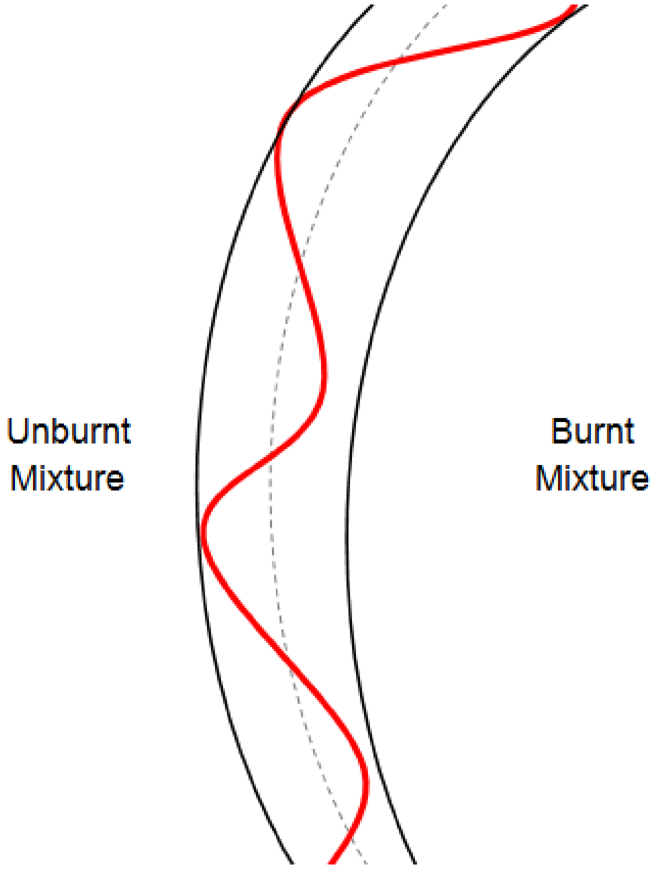

Fig. 5-2 Schematic diagram showing the mean instantaneous centre line of the flame front, mean centre line of the flame front and the mean flame front.

5.3 The engine cylinder model

The engine cylinder model calculates the following parameters as a function of the crank angle:

- Combustion chamber volume variation due to piston motion.
- Combustion chamber height variation due to piston motion.

- Cylinder area variation due to piston motion.
- Unburnt mixture temperature and pressure variations due to piston motion and convective heat transfer from/to the walls.

5.3.1 In-cylinder volume derivation

The volume of the cylinder and its derivative are calculated as a function of crank angle from the compression ratio, stroke, bore and connecting rod length (Shaver & Gerdes 2003).

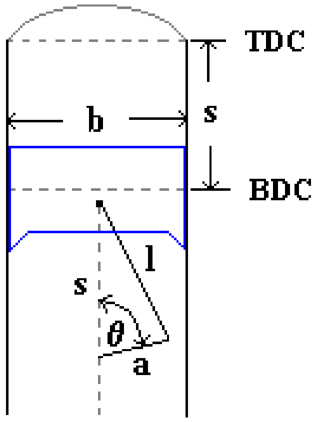

Fig. 5-3 Illustration of a typical piston-crank-cylinder assembly.

In ***Fig. 5-3*** $\boldsymbol{b}$ is cylinder bore, $\boldsymbol{s}$ is stroke of the engine, ***l*** is the connecting rod length and ***a*** is the crank radius. The volume of the combustion chamber when piston is at TDC is referred as the clearance volume, $\boldsymbol{V_c}$, the volume when piston is at BDC is the maximum volume of the cylinder, $\boldsymbol{V_{max}}$. the volume in between $\boldsymbol{V_{max}}$ and $\boldsymbol{V_c}$ is known as the displacement volume, $\boldsymbol{V_d}$.

$$\boldsymbol{V_d = \frac{\pi}{4} \cdot b^2 \cdot s} \tag{5-1}$$

At a given crank angle, the instantaneous chamber volume is expressed as:

$$\boldsymbol{V = \frac{\pi}{4} \cdot b^2 \cdot H + V_c} \tag{5-2}$$

where $\boldsymbol{H}$ is the instantaneous chamber height:

$$\boldsymbol{H = a + l -} [\left(\boldsymbol{l^2 - a^2 Sin^2\theta}\right)^{\mathbf{0.5}} + \boldsymbol{a\cos\theta}] \qquad \textbf{(5-3)}$$

The compression ratio is defined as r =$\boldsymbol{V_{max}/\ V_c}$ and therefore r =1+$\boldsymbol{V_d/\ V_c}$. Solving for $\boldsymbol{V_c}$ yields:

$$\boldsymbol{V_c} = \frac{\boldsymbol{V_d}}{\boldsymbol{r-1}} \qquad \textbf{(5-4)}$$

Substituting ***Eq. 5-4*** and ***5-4*** into ***Eq. 5-2***:

$$\boldsymbol{V} = \frac{\boldsymbol{V_d}}{\boldsymbol{r-1}} + \frac{\boldsymbol{V_d}}{2}[\mathbf{1} + \boldsymbol{R - \cos\theta} - (\boldsymbol{R}^2 - \boldsymbol{Sin^2\theta})^{0.5}] \qquad \textbf{(5-5)}$$

The predicted instantaneous combustion chamber height and volume are shown in ***Fig. 5-4***.

5.3.2 Surface area derivation

In order to study the heat transfer between the flame and the cylinder walls, $\boldsymbol{A_W}$, cylinder head, $\boldsymbol{A_H}$, and the piston head, $\boldsymbol{A_P}$, the instantaneous surface area of the cylinder, $\boldsymbol{A}$, has been evaluated:

$$\boldsymbol{A = A_W + A_H + A_P = \pi bx} + \mathbf{12} * \frac{\boldsymbol{V_c}}{\boldsymbol{b}} + \frac{\boldsymbol{\pi}}{\mathbf{4}} \cdot \boldsymbol{b}^2 \qquad \textbf{(5-6)}$$

The predicted instantaneous cylinder area is shown in ***Fig.5-4***

5.4 The flame geometry model

The flame is assumed to be initiated at the cone tip of the combustion chamber and propagates downwards to the piston. Due to relative motion and positions of the flame front and the piston, a number of possible flame front geometries may occur during its propagation by comparing the cone radius, $\boldsymbol{R_{cone}}$ and the instantaneous chamber height, $\boldsymbol{H}$. The resultant flame geometries are illustrated in ***Fig. 5-5*** and ***Table 5-1*** below.

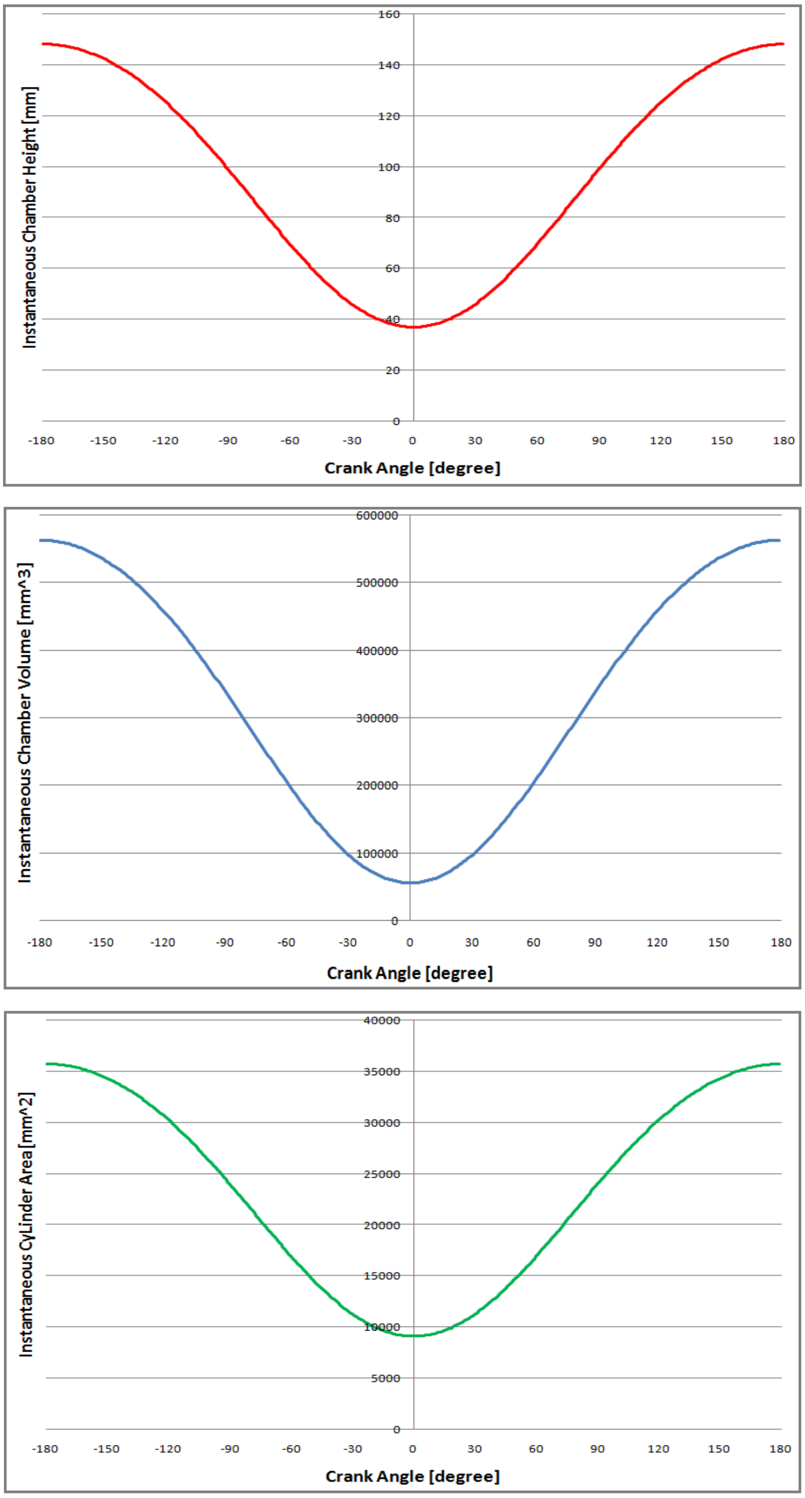

Fig. 5-4 Illustration of calculated instantaneous combustion chamber height (upper), instantaneous combustion chamber volume (mid) and instantaneous cylinder area (lower).

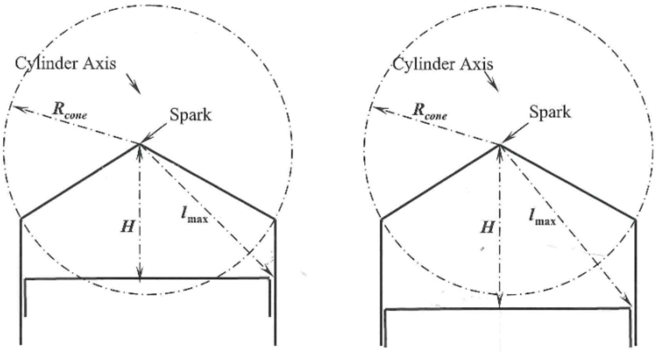

Fig. 5-5 Illustration of two possible flame geometries due to position of the piston position. Case 1 (left) represents situations where $R_{cone} > H$ and case 2 (right) represents situations where $R_{cone} < H$.

IF $H < R_{cone}$, AND	*Flame volume + Burnt volume*	IF $H > R_{cone}$, AND
$R_K < H$	$V = \frac{\pi}{3} R_K{}^3 (1 - \cos\theta_{cone})$	$R_K < R_{cone}$
$H \le R_K < R_{cone}$	$V = \pi R_K^3 \left(\cos\alpha_{end} - \frac{1}{3}\cos^3 a_{end} - \frac{2}{3}\cos\theta_{cone} \right)$	
$R_{cone} \le R_K < l_{\max}$	$V = V_{tdc} + \frac{\pi B^2}{4}(R_K \cos\alpha_{cy} - h_{tdc}) + \pi b^2 \left(\frac{1}{3}\cos^3\alpha_{cy} - \frac{1}{3}\cos^3\alpha_{end} + \cos\alpha_{cy} - \cos\alpha_{end} \right)$	$H \le R_K < l_{\max}$
	$V = V_{tdc} + \frac{\pi B^2}{4}(R_K \cos\alpha_{cy} - h_{tdc}) + \pi B^2 \left(\frac{2}{3} - \frac{1}{3}\cos^3\alpha_{cy} - \cos\alpha_{cy} \right)$	$H \ge R_K > R_{cone}$
$R_K \ge l_{\max}$		$R_K \ge l_{\max}$

Where H =the distance between ignition point and the piston top.
R_{cone} = the coning radius
R_K =the radius of the spherical flame
$l_{\max}$ =the distance from the ignition point to the corner point of piston top and the cylinder wall
B = the cylinder bore
h_{tdc} =the height from ignition point to the piston top at TDC
V_{tdc} =the cylinder volume at TDC
$V_{cylinder}$ = the cylinder volume at any given piston position
$\alpha_{cy} = \arccos(B/2/R_K)$
$\alpha_{end} = \arccos(H/R_K)$

Table 5-1 Illustration of the volume of flame and burnt zone as a function of flame radius.

5.5 The thermodynamics model

5.5.1 Volume of combustion chamber

The combustion chamber volume varies as a function of crank angle and as a result of piston motion. Nevertheless, the instantaneous chamber volume at any given crank angle is conserved:

$$\boldsymbol{V = V_b + V_f + V_u} \tag{5-7}$$

where $\boldsymbol{V_b}$, $\boldsymbol{V_f}$, $\boldsymbol{V_u}$ are volumes at the beginning of each calculation step.

5.5.2 Conservation of mass and species:

The total mass at the start of compression stroke (BDC) is conserved throughout compression and combustion stroke:

$$\boldsymbol{m = m_b + m_f + m_u} \tag{5-8}$$

where $\boldsymbol{m_b}$, $\boldsymbol{m_f}$, $\boldsymbol{m_u}$ are mass at the beginning of each calculation step.

$$\boldsymbol{m_u = m_u{}' - m_f} \tag{5-9}$$

$$\boldsymbol{m_b = m_b' + m_f{}'} \tag{5-10}$$

where $\boldsymbol{m_u{}'}$, $\boldsymbol{m_f{}'}$ and $\boldsymbol{m_b'}$ are mass of the previous calculation step.

The species in three zones are also conserved. The concentrations of any species in unburnt and burning zones are expressed as:

$$\boldsymbol{\frac{dX_{i,j}}{dt} = \frac{M_i \cdot \dot{\omega}_\iota}{\rho_j}} \tag{5-11}$$

where $\boldsymbol{X}$ represents the mass fraction of a species. Subscripts $\boldsymbol{i}$ and $\boldsymbol{j}$ denote the species and zones considered. $\boldsymbol{M_i}$ and $\boldsymbol{\omega_i}$ represents the molecular weight and molar production rate of species $\boldsymbol{i}$ respectively. Similar expression for the burnt zone can also be obtained:

$$\frac{dX_{i,b}}{dt} = \frac{1}{m_b}\frac{dm_b}{dt} \cdot \left(X_{i,f} - X_{i,b}\right) + \frac{M_i \cdot \dot{\omega}_i}{\rho_b} \qquad \textbf{(5-12)}$$

5.5.3 Conservation of energy

The energy conservation equations for burnt, burning and unburnt zone are described in Section 4.2 in Chapter Four in details. The same set of equations is used here.

5.6 The chemical kinetics model

The chemical kinetics model used in the current research is a modified version of Tanaka mechanism (Tanaka et al. 2003). The mechanism was originally developed for mixtures of n-heptane and iso-octane in HCCI combustion mode and modified by Liu (Liu & Chen 2009) to suit SI combustion simulation.

The modification process is briefly introduced below. Sensitivity analysis on the Tanaka mechanism showed that R6 and R18 (generally expressed as RH + OH = R +H_2O) were the most influential on both the ignition delay and the burn rate. The enhancement of their pre-exponential constants of the rate constants leads to a shorter ignition delay and a higher burn-rate. This phenomenon is attributed to the role of alkyl radical formation reactions in the oxidation chemistry, where both reactions represent the attack of the active radical OH to abstract the atom H from fuel molecules. The pre-exponential constants were enhanced by a factor of 1 to 10, and the modified mechanism was put into the model to investigate its effect on knock onset, knock intensity, combustion duration and peak cylinder pressure. The results show that the increase of the enhance factors from 1 to 6 leads to knock position being advanced by about 23%, the peak pressure being increased by around 16%, and knock intensity being raised by about 100%. Further increasing the enhance factors from 6.0 to 10.0 can only affect these three parameters by about 3%, 2%, and 15%, respectively. Thus, it was concluded the enhance factor of the value of 6.0 was the turning point and has been employed. The modified mechanism is listed in ***Appendix A***.

5.7 The turbulence flame speed correlation

Based on the discussion in Section 2.4.3 in Chapter Two, the correlation proposed by Bradley and co-workers (1981) has been chosen to be used for turbulent flame speed calculations. The choice is based on:

- The correlation does not contain empirical constant, therefore end users don't have to tune the correlation to make it fit its purpose for different applications.
- The correlation is comprehensively validated against a number of fuels and takes into account of effects of flame stretch and the turbulent Reynolds number.
- The two-eddy theory, which the correlation is based on, is particularly suitable for combustion with higher turbulence levels, e.g. modern internal combustion engines with higher compression ratios and boosted engines.

In order adopt this correlation, calculations of a number of parameters are required, including the turbulence Reynolds number, integral length scale and turbulence intensity. The Rapid Distortion Theory developed by Wong and Hoult (1979) is widely used for this purpose. Wong and Hoult claimed that the instantaneous integral length scale and turbulence intensity can be calculated as a function of a reference value and the instantaneous mixture density, based on the conservation of angular momentum for large eddies:

$$\boldsymbol{l_T = l_T' \cdot (\frac{\rho_{u,0}}{\rho_u})^{1/3}} \tag{5-21}$$

$$\boldsymbol{u' = u_0' \cdot (\frac{\rho_u}{\rho_{u,0}})^{1/3}} \tag{5-22}$$

where $\boldsymbol{\rho_{u,0}}$ is the unburnt density at the time of spark ignition. The theory has been adopted by a number of researchers for spark ignition engine simulation (Filipi & Assanis 1991)(Assanis & Heywood 1986)(Prucka et al. 2010). Heywood et al. and Filip et al. suggested $\boldsymbol{l'_T}$ to be the combustion chamber height at TDC. Prucka et al. (Prucka et al. 2010) extended the theory and concluded that $\boldsymbol{l'_T}$ equals to instantaneous chamber height at a given crank angle and ***Eq. 5-21*** becomes:

$$\boldsymbol{l_T = H \cdot (\frac{\rho_{u,0}}{\rho_u})^{1/3}} \qquad \textbf{(5-23)}$$

Eq. 5-23 provides a convenient dimensionless method to estimate the instantaneous integral length scale which is a critical parameter in the model.

It’s been clearly shown in ***Eq. 5-22*** that, in order to calculate turbulent flame speed, a reference or initial value of turbulent intensity is still required. In-cylinder turbulence intensity is inherently unsteady and experiences significant cycle-to-cycle variation. A lot of efforts (Hall & Bracco 1987) have been dedicated into the measurement of in-cylinder turbulence intensity and resolving for turbulence intensity at TDC. Kim et al. (Kim et al. 1992) measured turbulence intensity at TDC on a Subaru engine that has very similar operating conditions to the test engine used for the current study. The turbulence intensity has been found to increase linearly against engine speed.

5.8 Model validation

In order to validate the engine combustion and flame propagation model, the calculated results are compared to experimental data obtained from engine tests.

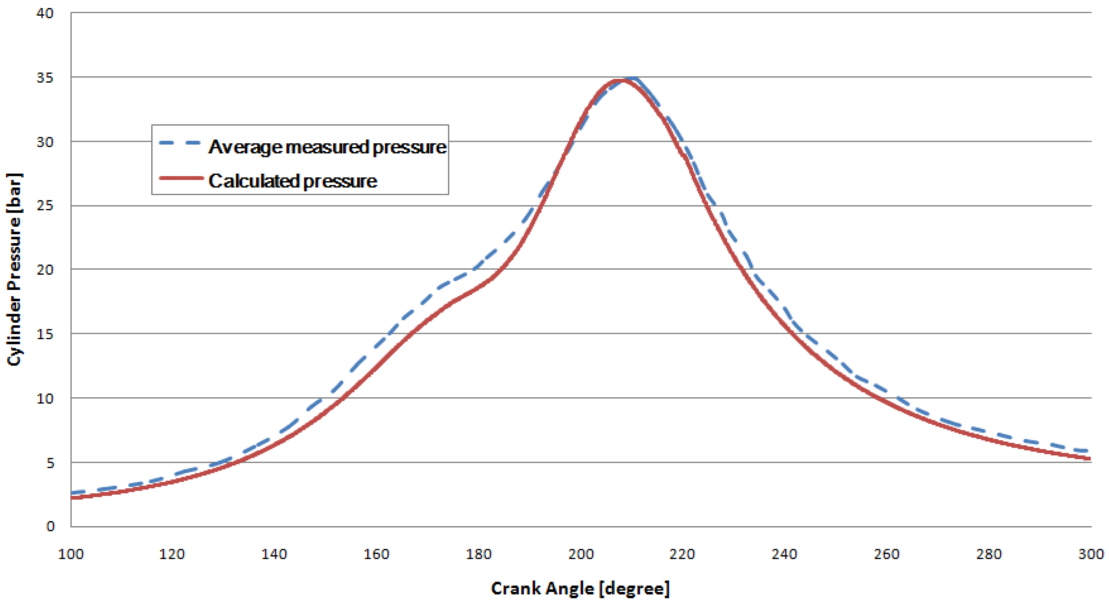

Fig. 5-6 Comparison between experimental data (dashed) and calculated results (solid). Initial temperature, pressure, equivalence ratio are 300K, 1bar and 0.7. Ignition at 9° BTDC.

Liu et al. (2009) measured engine performances using a single cylinder, 4-stroke Ricardo E6 research SI engine. The engine specifications are listed in ***Table 5-2***. The engine was equipped with a pressure transducer and the data was recorded at an interval of one-tenth of a crank angle degree. A Lab-View based engine data acquisition system was used to record 50 consecutive engine cycle data. ***Fig. 5-6*** shows the comparison between measured and calculated cylinder pressure. The measured pressure shown is the averaged pressure based on 50 cycles under WOT position, 1500RPM and ignition timing of 9° BTDC.

Stroke	**111.2 mm**
Bore	76.2 mm
Con-rod length	240.5 mm
Compression ratio	10
IVO	9° BTDC
IVC	37° ABDC
EVO	41° BBDC
EVC	10° ATDC

Table 5-2 Test engine specifications

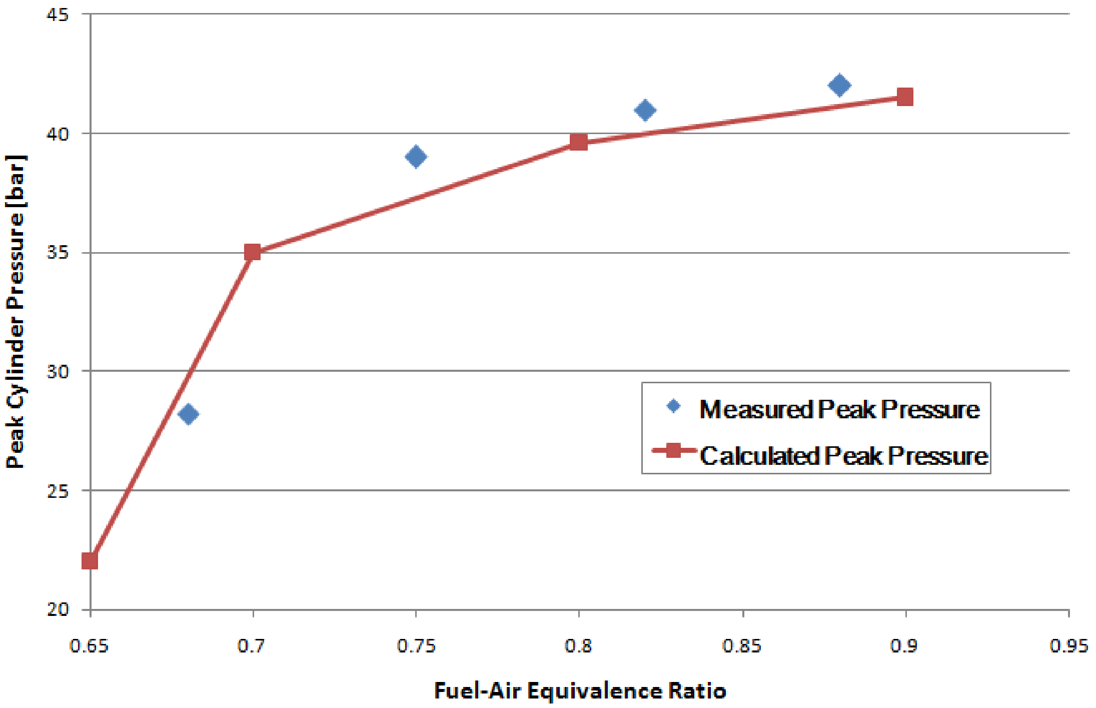

Fig. 5-7 Comparison of measured and calculated peak cylinder pressure.

It can be seen from ***Fig. 5-6*** that the calculated cylinder pressure matches experimental results well. The calculated pressure under-estimates the pressure by approximately 2bar between the end of compression stroke and the initial stage of combustion. It can be attributed to the assumption of a constant cylinder wall temperature of 420K. The unburnt mixture temperature increases and exceeds the assumed 420K wall temperature towards the end of compression stroke and starts to loss heat energy to the wall. Such loss reduces the cylinder temperature and pressure. Shortly into the combustion phase, the cylinder pressure variation becomes to be dominated by the propagating turbulent flame front. Therefore the over-estimated heat loss to the wall is not significant from this point and onwards.

Fig. 5-7 illustrates the measured and calculated peak cylinder pressure with various fuel-air equivalence ratio. The peak cylinder pressure increases with increasing equivalence ratio. The increase is attributed to faster laminar flame speed which leads to faster turbulent flame speed in the model. The calculated peak cylinder pressure is, in general, slightly underestimated and the matching with measured data gets better as equivalence ratio increases. The underestimation may be due to the use of a spherical mean flame front, as described in Section 5.2.1. The assumed mean flame front has a smaller surface area than the actual wrinkled flame front does, and therefore the heat transfer to the unburnt zone, which is proportion to the flame surface area, is reduced and less heat energy is transferred into the unburnt zone. The match with measured data gets better with increasing equivalence ratio may be because leaner combustion is less stable and experiences greater cyclic variation. Richer combustion is more stable and repeatable, therefore produces more reliable experimental data.

Fig. 5-8 illustrates the maximum flame temperature achieved during flame propagation at various equivalence ratios. The maximum flame temperature is relatively low for lean mixtures and increases rapidly as the mixture is strengthened

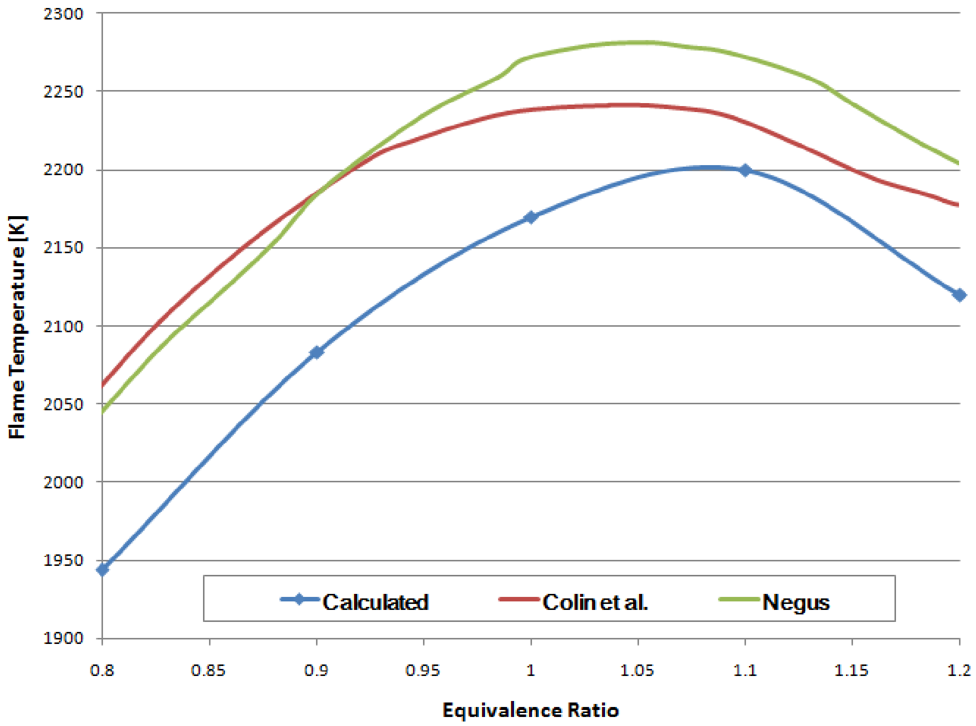

Fig. 5-8 Comparison of flame temperature variations against equivalence ratios. Initial temperature and pressure are 300K and 1bar. Ignition at 9° BTDC.

towards stoichiometry. Slightly rich mixture, i.e. Φ is approximately 1.05, has the highest flame temperature. Also shown in ***Fig. 5-8*** is the comparisons with adiabatic flame temperatures at the same initial conditions obtained by different researchers (Ferguson & Kirkpatrick 2001)(Negus 1997). The calculated flame temperatures are lower than the adiabatic flame temperatures, which is expected as heat transfer is neglected in the calculation adiabatic flame temperatures. The difference between the calculated and adiabatic flame temperatures is not constant, i.e. about 100K for leaner mixtures and 30-70K for stoichiometric and richer mixtures. This may be attributed to the difference in the accumulative heat loss. Leaner mixtures have lower flame speeds and therefore allows longer time for accumulative heat energy loss to the unburnt zone and cylinder walls, if the whole combustion process is considered. On the contrary, although richer mixtures combust at higher flame temperatures which increase temperature gradient and the rate of heat loss, they have faster flame speeds and allows less time for heat energy loss to accumulate. Therefore, richer flames combust at temperatures that is closer to the ‘ideal’ adiabatic flame temperatures.

5.9 Model Results and Discussion

This section presents some results obtained by the engine combustion model, these include: engine cylinder pressure, laminar burning velocity, turbulent flame speed and the ratio of turbulent and laminar flame speed.

Fig. 5-9 shows the cylinder pressure histories of various equivalence ratios at 1500RPM and ignition at 9° BTDC. The cylinder pressure is roughly the same until approximately 20° after TDC. The small pressure difference may be attributed to different heat transfer coefficients caused by different mixture compositions. After that the cylinder pressure starts to vary with an increasing trend as the mixture is strengthened form lean to slightly rich, i.e. Φ=1.1. This is expected as richer mixtures contain more chemical energy and combust at a higher efficiency. However, the cylinder pressure starts to decrease when the mixture is further strengthened from Φ=1.1 and onwards, as a result of excessive fuel and lower combustion efficiency.

Fig. 5-10 shows the instantaneous laminar burning velocities during flame propagation process at various equivalence ratios. Laminar burning velocities increase with crank angle during the combustion phase as a result of increased unburnt zone temperature. the rate of increase reaches maximum between approximately 30 to 35° after TDC when the unburnt zone is compressed to a small fraction of its original volume and obtains very high temperature. The rate of increase start to decrease towards the end of the flame propagation process. Such decrease occurs immediately after the peak cylinder pressure is achieved. This phenomenon indicates that the decrease is pressure-related and is caused by the enhancements to pressure-sensitive chain termination reactions.

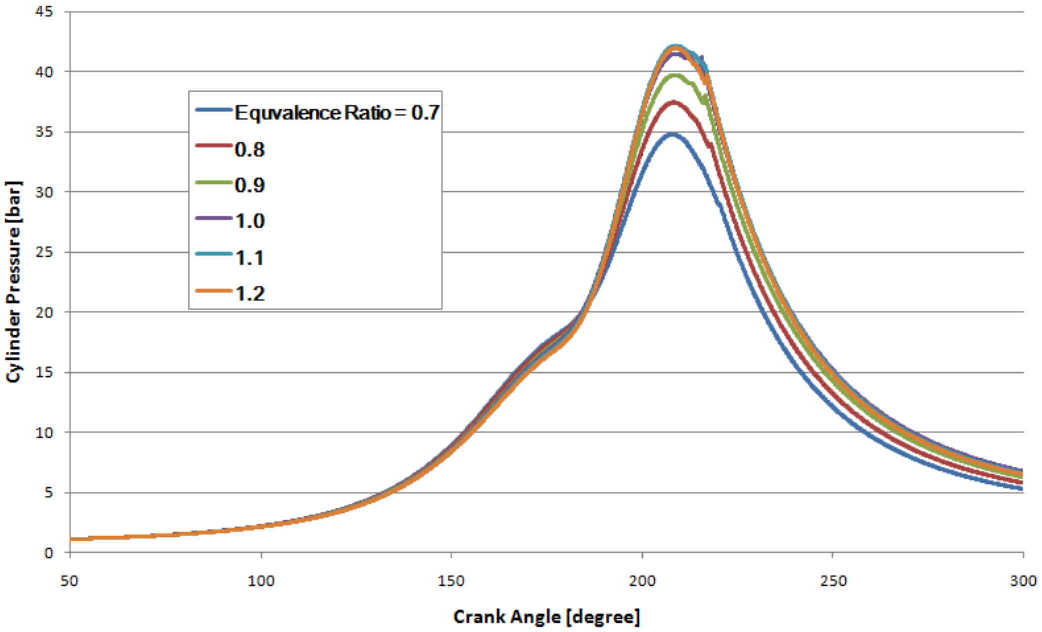

Fig. 5-9 Calculated cylinder pressure at various equivalence ratios. Initial temperature and pressure are 300K and 1bar. Ignition at 9° BTDC.

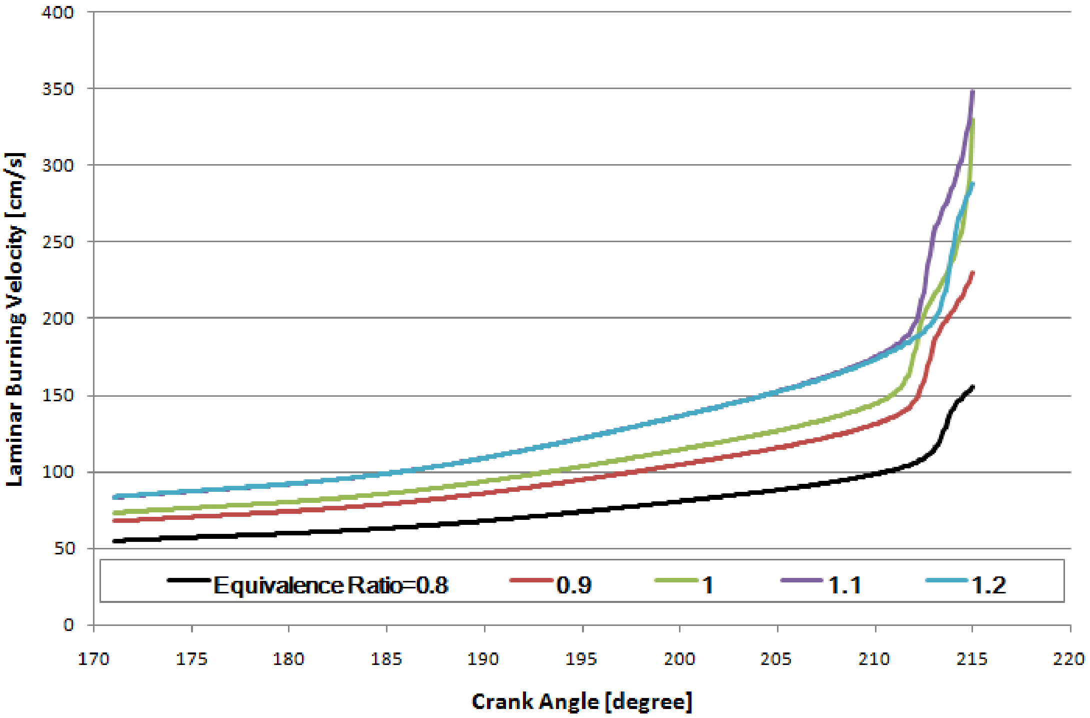

Fig. 5-10 Calculated laminar burning velocity during the combustion phase at various equivalence ratios. Initial temperature and pressure are 300K and 1bar. Ignition at 9°BTDC.

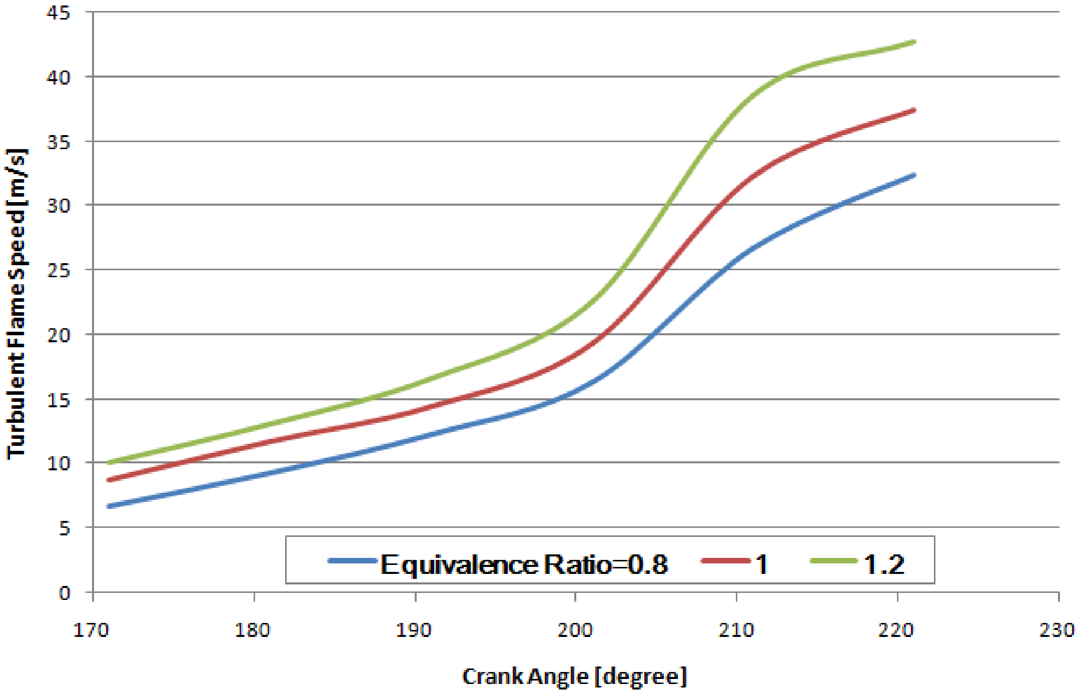

Fig. 5-11 Calculated turbulent flame speeds during the combustion phase at various equivalence ratios. Initial temperature and pressure are 300K and 1bar. Ignition at 9°BTDC.

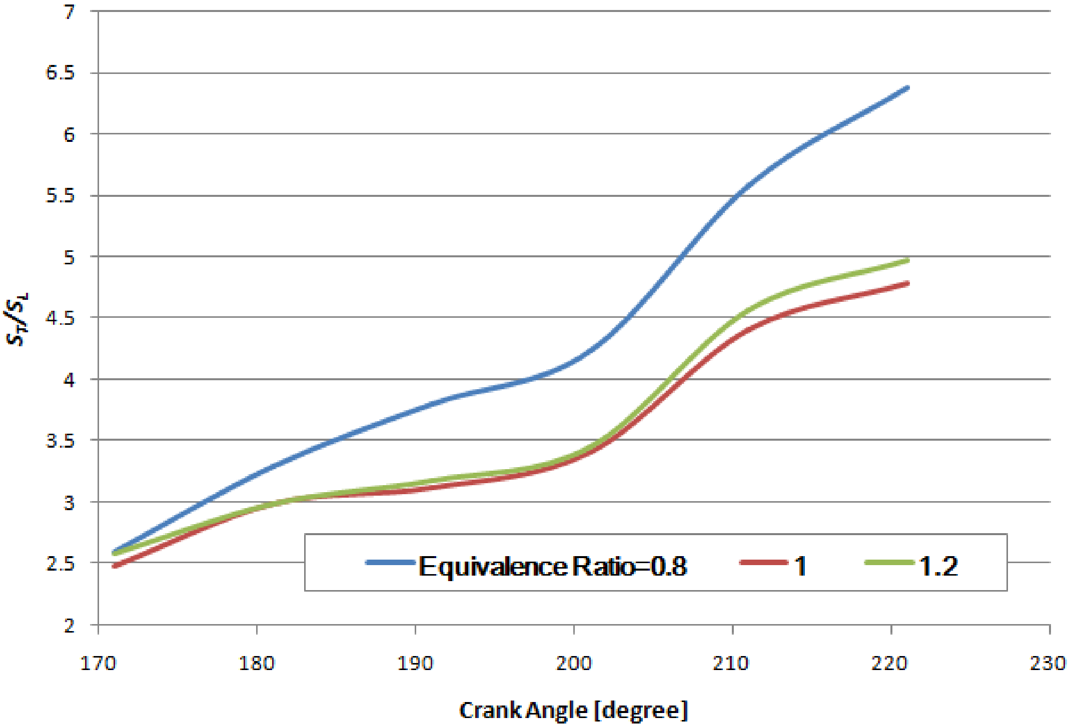

Fig. 5-12 Calculated ratios between turbulent and laminar flame speeds during the combustion phase at various equivalence ratios. Initial temperature and pressure are 300K and 1bar. Ignition at 9°BTDC.

Fig. 5-11 shows the calculated turbulent flame speeds during the flame propagation processes at different equivalence ratios. Similar to the calculated laminar burning velocities in ***Fig. 5-10***, turbulent flame speed increases against crank angles and richer mixtures combust at higher speeds. The increase with increase equivalence ratio is expected as turbulent flame speed is vastly dependent on laminar burning velocity, as shown in Chapter Four. The calculated turbulent flame speeds have much higher rate of increase, compared to the calculated laminar burning velocities. This is attributed to the influence of turbulence intensity which is illustrated by ***Eq. 2-17***. Turbulence intensity affects the laminar flamelets by stretching and wrinkling the flame surface and thus enhances the burn rate (Gülder 1991). Also seen in ***Fig. 5-11*** is that the calculated turbulent flame speeds accelerate earlier than the calculated laminar burning velocities do, but with lower rate of increase, indicating that other factors are influential in the variation of turbulent flame speeds.

Fig. 5-12 reveals the variation of $\boldsymbol{S_T/S_L}$ during the combustion phase at various equivalence ratios. The ratio can be considered as the effect of the turbulent flow on the laminar flamelets. $\boldsymbol{S_T/S_L}$ increases steadily during the early stage of flame propagation with a decreasing rate of increase, which is attributed to decay of the turbulence induced during the intake stroke. However the rate of increase raises rapidly from around 200° crank angle. Such sudden increase is caused by the turbulence amplification due to the rapid distortion resulting from unburnt mixture compression exerted by the propagating flame front (Assanis & Heywood 1986). The sudden increase also coincides with rapid increase of calculated turbulent flame speeds seen in ***Fig.5-11***. In addition, it can be clearly seen that in-cylinder turbulence has more significant effect on leaner flames, e.g. $\boldsymbol{\Phi}$=0.8, than it does on stoichiometric and rich flames. This may be because of leaner flames propagates at lower speeds and allow more time for the turbulence to take effect. Previous studies (Tseng et al. 1993) on hydrocarbon –air flames concluded that leaner flames are thinner, and therefore can be affected by a wider range of eddies in the turbulence spectrum.

5.10 Summary

Turbulent flame propagation process plays an important role in spark ignition combustion. It has dominating effect on combustion efficiency and cyclic variations. In this chapter, a simulation model has been developed to study turbulent flame propagation in spark ignition engines. The model is based on the zero-dimensional approach and consists of three zones, i.e. burnt, burning and unburnt. A modified chemical kinetics mechanism, originally developed by Tanaka and co-workers, has been applied in the burning zone to simulate the in-flame combustion. The calculated results have been validated against available experimental data for cylinder pressure history, maximum cylinder pressure and maximum flame temperature.

The model has shown the ability of calculating instantaneous turbulent flame speeds based on the wrinkled flamelet combustion regime where the combustion and the turbulence are predicted separately. Both laminar burning velocities and turbulent flame speeds are found to increase with increasing equivalence ratios from lean to slightly rich conditions. The effects of the turbulence intensity are plotted and discussed. It has been revealed that turbulence flow has more significant effects on leaner flames which travel at lower flame speeds and are influenced by a wider range of eddies in the turbulence spectrum.

The model also shows potential of being modified to study abnormal combustion phenomenon, i.e. knock, in spark ignition engines, due to the zonal formation of the model and the available gasoline combustion chemical kinetics mechanism. In the next chapter, the model will be modified and used to study the knock phenomenon.

Chapter Six: Downsized Boosted SI Engine Knock Simulation

6.1 Introduction

Design of modern spark ignition engines are significantly influenced by stringent emission regulations and growing customers' demand for lower running costs. Downsizing and intake boosting have become the short-to-medium term solution for major car manufacturers. By downsizing an engine, it is pushed to operate at higher engine load and therefore has higher efficiency. The power and torque losses due to reduction of wept volume is compensated by intake boosting, e.g. turbocharging and supercharging. With these new engine designs, has come a growing concern for the understanding, control and avoidance of end gas autoignition and the resultant knock (Blunsdon & Dent 1994).

It is widely accepted that the propagating flame front is one of the most important factors that contribute to the occurrence of end gas autoignition and knock. The propagating flame front influence end gas autoignition and knock by increasing unburnt mixture temperature and pressure by compression and heat convection. Rapid compression and excessive heat convection to the unburnt mixture and easily trigger autoignition and the resultant knock with high intensity. However, due to its complexity and extremely transient nature, the relation and interaction between flame propagation and knock are still not thoroughly understood.

In previous chapter, a spark ignition engine turbulent flame propagation model has been developed and validated. The model is capable of predicting turbulent flame propagation process within the combustion chamber with reasonable accuracy. The objective of this chapter is to further develop the model to enable the capability of predicting end gas autoignition and the resultant knock.

6.1.1 Model assumptions

The model assumptions are largely carried over from corresponding section in Chapter Five with some minor changes:

1. the unburnt mixture is no longer assumed to be in a chemically-frozen status. Chemical reactions are allowed but only after ignition. Pre-ignition prior to ignition is neglected.
2. Autoignition is assumed to occur in one bulk gas and not in a distributed manner. And in one calculation step, the total mass fraction burnt consists of contributions of flame, $\boldsymbol{X_f}$, and autoignition, $\boldsymbol{X_{auto}}$, i.e.:

$$\boldsymbol{X_{burnt} = X_f + X_{auto}} \quad \textbf{(6-1)}$$

3. The variation of unburnt zone temperature is influenced by the addition of chemical energy released from autoignition, and **Eq. 4-2** becomes:

$$\boldsymbol{\left(m_u - m_f - m_{auto}\right) \cdot C_{p,u} \cdot \frac{dT_u}{dt} = \dot{Q}_{auto} + \dot{Q}_{f,u} + \dot{W}_f - \left(m_f + m_{auto}\right) \cdot H_u} \quad \textbf{(6-2)}$$

where $\boldsymbol{m_{auto}}$ represents the mass consumed by autoignition and $\boldsymbol{Q_{auto}}$ is the energy released by autoignition.

6.2 Knock Detection

Identification of knock during spark ignition engine cycles has been widely researched. A number of different methods of identifying the onset and the intensity of knock have been proposed (Blunsdon & Dent 1994; Inoue et al. 2012; Blunsdon & Dent 1994; Lee et al. 1998; Worret et al. n.d.; Attard et al. 2010). Cylinder pressure histories have been proven to be a very indicative parameter in the study of knock. Pressure history of a typical knocking cycle can be characterized by two distinctive features: random pressure oscillation and sudden shape pressure increase (Arrigoni & Cornetti 1974). The onset timing and intensity of knock can be determined by either of these two parameters.

Due to the inability of predicting cylinder pressure oscillation, the onset timing and intensity are calculated based on the cylinder pressure history in the current research. Liu et al. (2009) proposed a method that used a threshold value of cylinder pressure gradient change rate to identify the onset timing of knock:

$$\boldsymbol{K = \frac{(P_n/P_{n-1})/\Delta\theta + (P_{n+1}/P_n)/\Delta\theta}{\Delta\theta}} \tag{6-3}$$

This method is illustrated in ***Fig. 6-1***. A threshold value for $\boldsymbol{K}$ is recommended by Liu and co-workers to be 30bar/CA^2 by matching pressure histories and occurrence of knock over 50 consecutive non-knocking and knocking cycles. In the present study, cycles with the value of $\boldsymbol{K}$ greater than the threshold are considered as knocking cycles. The crank angle where this threshold value is first exceeded is identified as the onset timing of knock. The level of knock is represented by knock intensity which can be defined as the maximum pressure increase rate, $\boldsymbol{(dP/d\theta)_{max}}$.

7.3 Model Validation

The engine used for the knock model validation is the same Ricardo E6 single cylinder 4-stroke test engine as introduced in Chapter Five. Due to large cyclic variations under knocking combustion, 50 consecutive cycles have been measured. The knock onset timing and intensity are then calculated by averaging the experimental data obtained from the knocking cycles of the 50 measured cycles. This process is illustrated in ***Fig. 6-2*** and ***6-3*** below.

The test conditions are 1500RPM, 373K, 1bar and $\boldsymbol{\Phi}$=0.9 at 9°BTDC ignition. Big scarce of experimental data can be found in both figures and are attributed to significant cyclic variations under knocking combustion cycles. Out of these 50

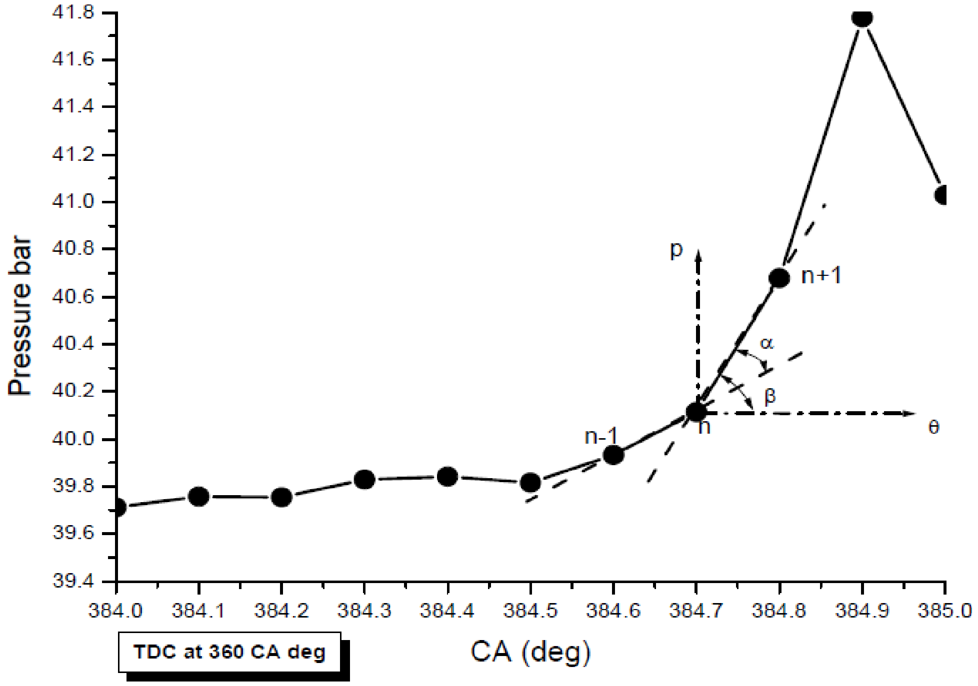

Fig. 6-1 Schematic illustration of the method used to identify knock onset timing and intensity (Liu & Chen 2009).

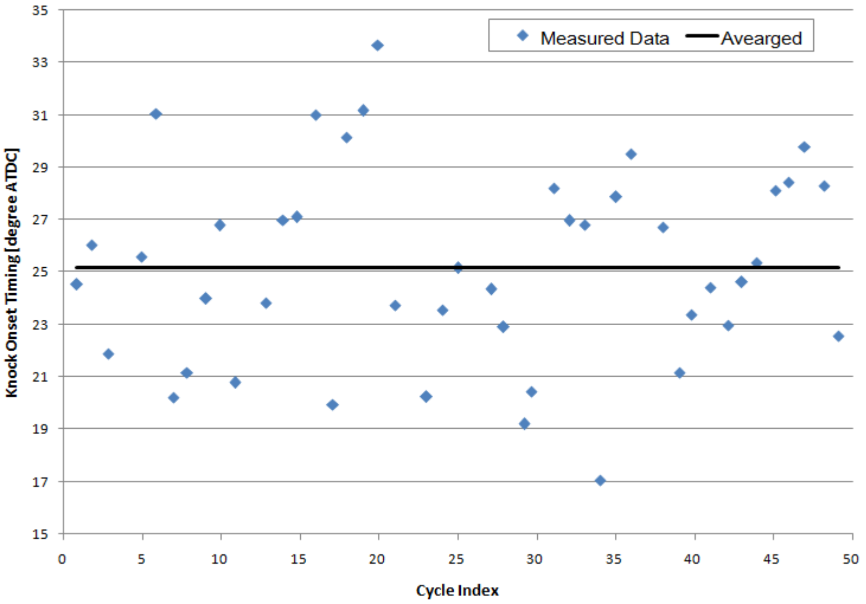

Fig. 6-2 Illustration of experimental data process method applied to knock onset timing measurements. Based on 49 knocking cycles out of 50 measured.

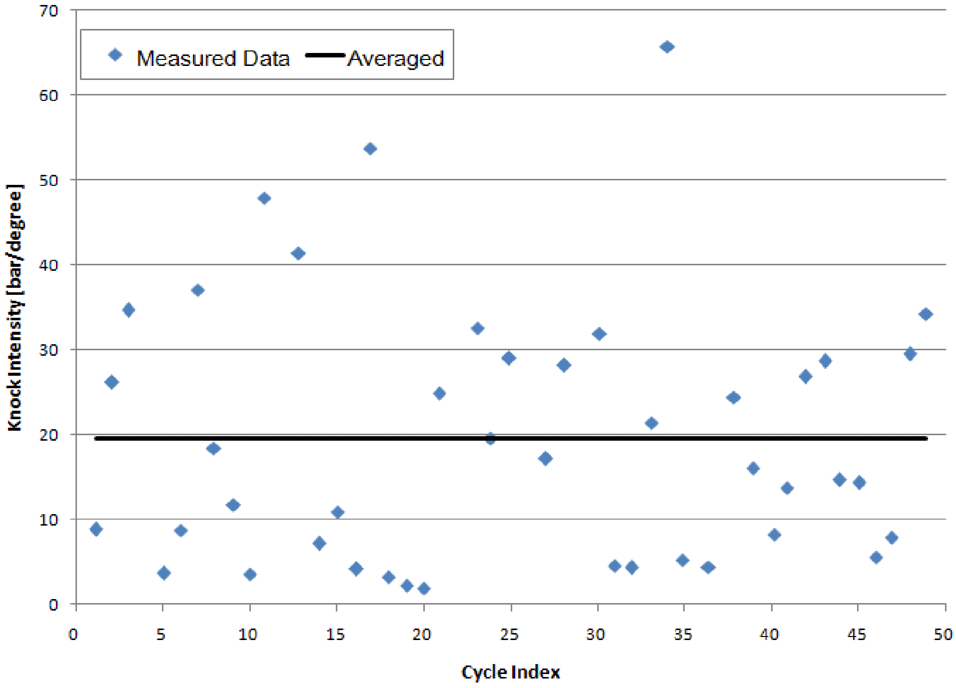

Fig. 6-3 Illustration of experimental data process method applied to knock intensity measurements. Based on 49 knocking cycles out of 50 measured.

measured cycles, 49 are knocking cycles and 1 is considered to be knock-free. The averaged values are obtained by adding measured data and dividing the number of knocking cycles.

Fig. 6-4 shows the comparisons of calculated and measured knock onset timing and intensity at different engine speeds. It can be clearly seen that as the engine speed is increased, knock onset timing is delayed and knock intensity is reduced, both in a almost linear manner. Engine speed determines the time available for the combustion phase. Due to its kinetically-controlled and time-dependent nature, knock (end gas autoignition) is logically delayed as engine speed increases. The reduction in knock intensity may be attributed to the fact that the compression exerted by the propagating flame front on unburnt mixture is growingly offset by the faster downward motion of piston during the expansion stroke, as the engine speed is increased. The match with measured results is acceptable and the model has been proven to be able to simulate spark ignition engine autoignition and knock.

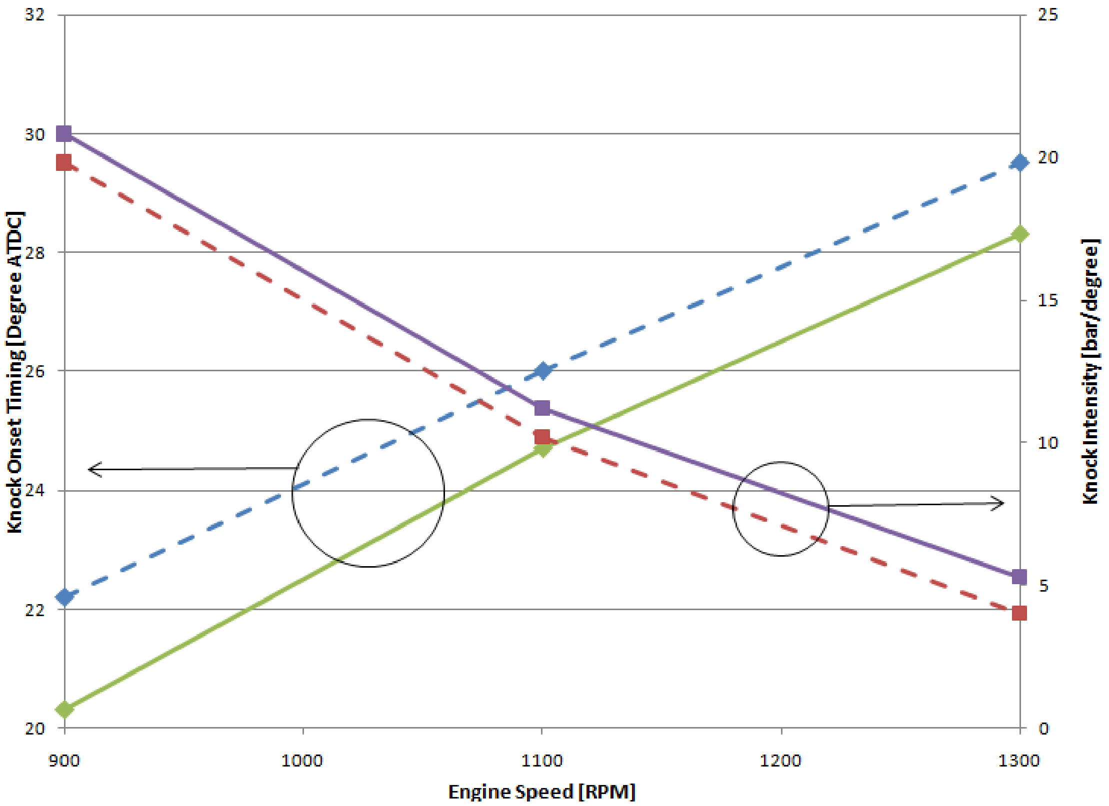

Fig. 6-4 Comparisons of calculated (solid lines) and measured (dashed lines) knock onset timing and intensity at different engine speeds.

6.4 Model Results and Discussion

6.4.1 Effect of intake pressure

Fig.6-5 illustrates the effect of intake pressure on cylinder pressure history. It can be seen that the cylinder pressures of all three cases increased isentropically during the compression stroke prior ignition. Intake pressure takes effect shortly after TDC when the cylinder pressure of the case with 3bar intake pressure increases with the highest increase rate. Before reaching its peak cylinder pressure, there has been a period when the cylinder pressure increases almost vertically, indicating that a large amount of heat energy is released in short time. Cylinder pressure history of combustion with 2bar intake pressure has a similar increase rate but has much lower peak cylinder pressure. Additionally, the cylinder pressure curve is smoother compared to 3bar intake pressure scenario. That means the autoignition occurs in a less aggressive manner and the heat release is more gradual and regulated.

Fig. 6-6 shows the corresponding knock onset timing and intensity. A conclusion can be drawn that as intake pressures is increased, knock occurs earlier during the combustion phase and with higher intensity. This is attributed to increased unburnt temperature as a result of the increase in intake pressure. ***Fig. 6-7*** depicts the unburnt zone temperature at the crank angle when knock intensity is defined in the three cases discussed. This temperature increases with increase intake pressure in almost the same manner as the knock intensity does in ***Fig.6-6***. Autoignition is extremely sensitive to temperature change due to its kinetically-controlled nature. Chemical reaction rates are significantly amplified when temperature is high. Additionally, higher intake pressure means more fuel and air mixture is inducted into the combustion chamber and therefore more energy can be released, by either flame combustion or autoignition, creating higher cylinder pressure.

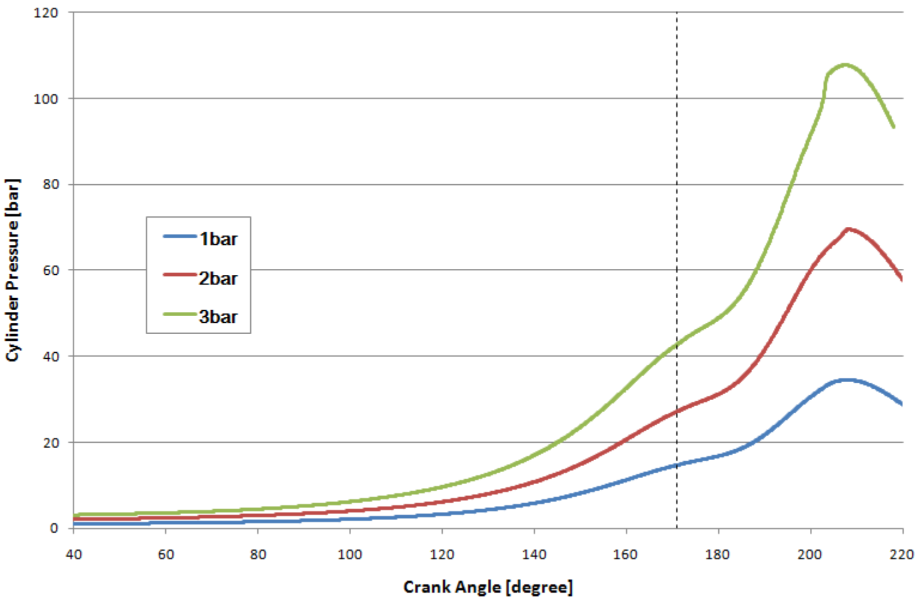

Fig. 6-5 Calculated cylinder pressure histories with different initial pressures. Other initial conditions are 1500RPM, 373K, Φ=1.0 and ignition at 9°BTDC.

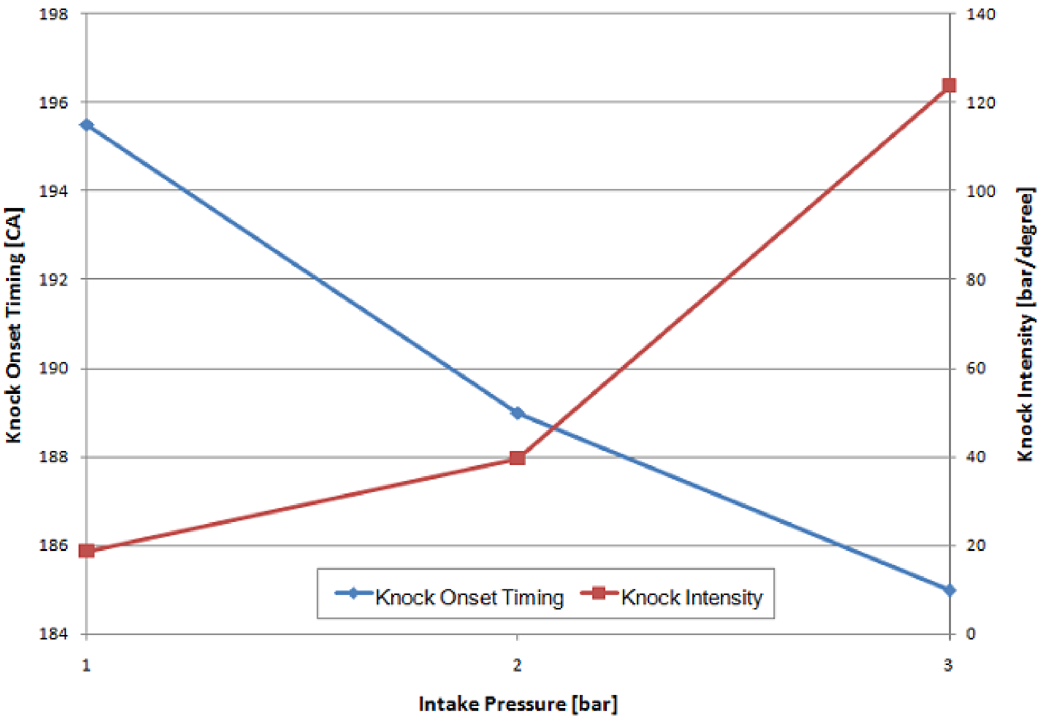

Fig. 6-6 Calculated knock onset timing and intensity at different intake pressures. Other initial conditions are 1500RPM, 373K, Φ=1.0 and ignition at 9°BTDC.

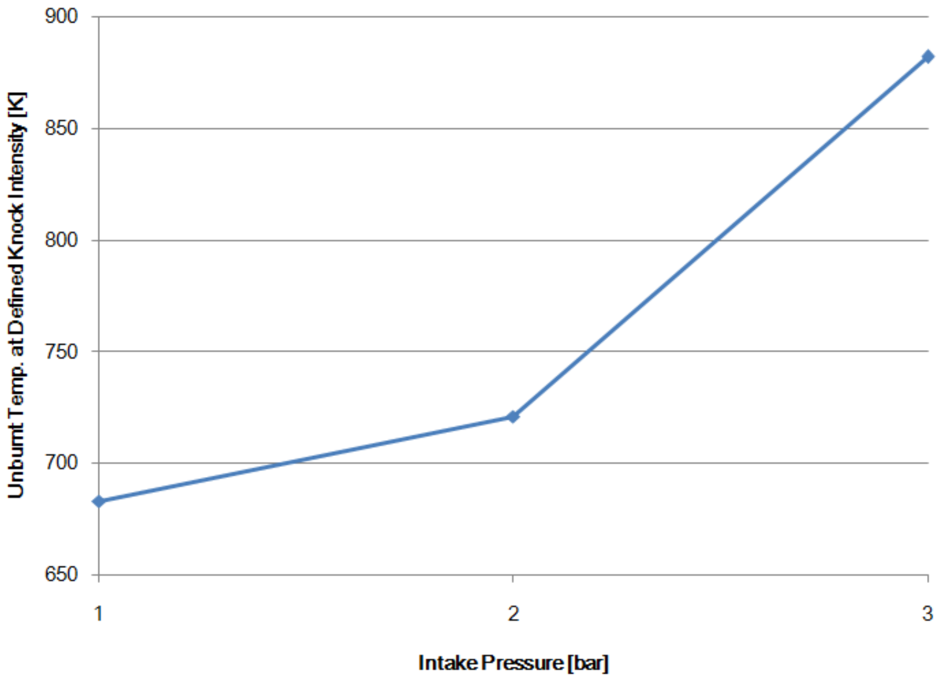

Fig. 6-7 Unburnt temperature at CA where knock intensity is defined.

7.4.2 Mass fraction burnt

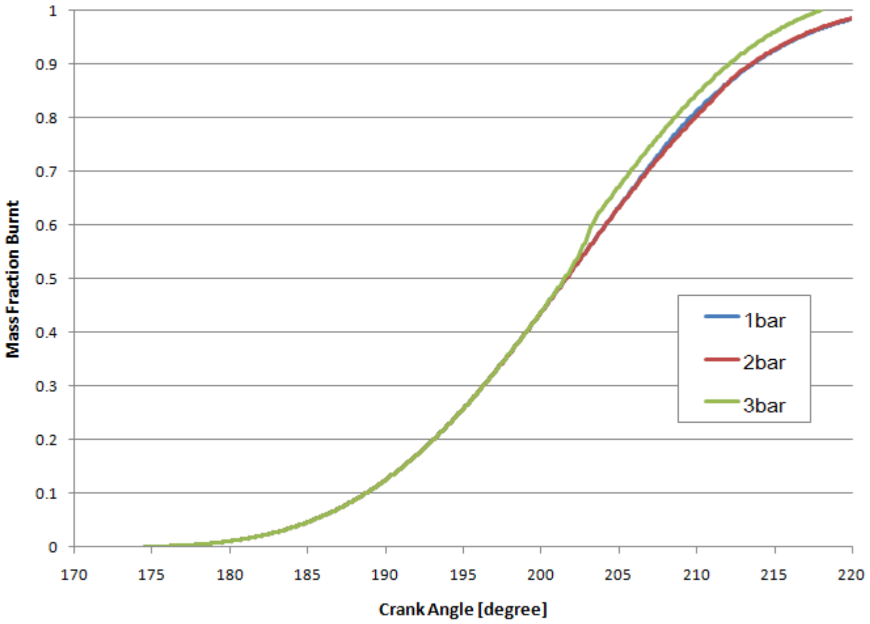

Fig. 6-8 Comparison of mass fraction burnt histories at different intake pressures. Other initial conditions are 1500RPM, 373K, *Φ*=1.0 and ignition at 9°BTDC.

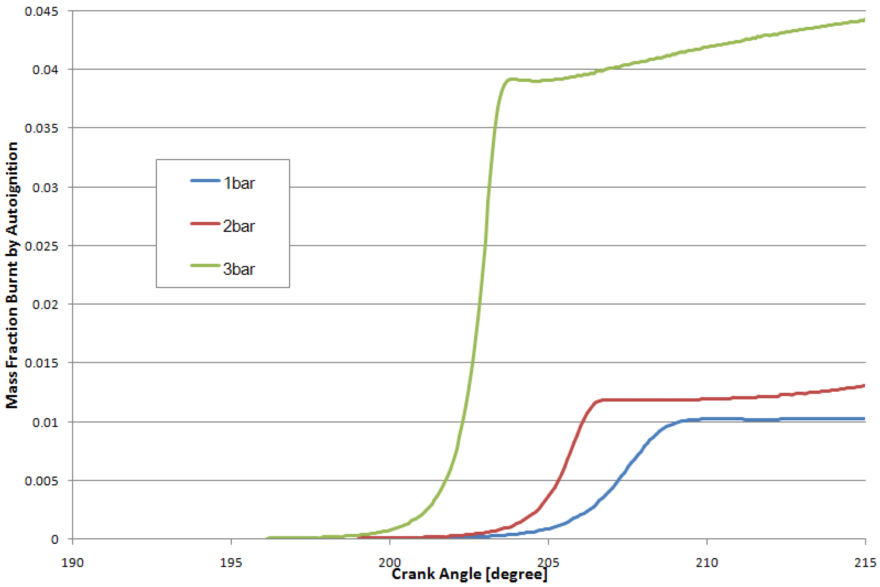

Fig. 6-9 Comparisons of mass fraction burnt by autoignition at different intake pressures. Other initial conditions are 1500RPM, 373K, *Φ*=1.0 and ignition at 9°BTDC.

Mass fraction burnt histories of the three cases being discussed are shown in ***Fig. 6-8***. The characteristics of the curves for 1bar and 2bar combustion scenarios generally follows the typical SI engine combustion process described by Wiebe Functions that it consists of three stages: an initial slow burning stage where the flame develops and accelerates; a fast burning period when 80% of combustible mixture is consumed; finally a finishing stage when the burning rate reduces significantly due to flame quenching and extinguishing (Rousseau et al. 1999). However, when intake pressure is increased to 3bar the mass fraction burnt curve shows noticeable additional acceleration at approximately 20° after TDC, when approximately 50% of initial mass has been burnt. In order to investigate the cause of such additional acceleration, the histories of mass fraction burnt by autoignition at all three intake pressures are depicted in ***Fig. 6-9***. It can be clearly seen that mass fraction burnt by autoignition increases as intake pressure is raised. At lower intake pressures, i.e. 1 and 2bar, the mass fraction burnt by autoignition shows much longer build-up period but only consumes 1% and 1.4% of total initial mass, respectively. When intake pressure is increased to 3bar, the characteristics of mass fraction burnt by autoignition changes dramatically. The build-up period is almost halved with much greater rate of increase and ultimately consumes 4.4% of total initial mass, which is three times more than combustion at 2bar intake pressure. This rapid burning period by autoignition corresponds to the sudden acceleration of total mass fraction burnt curve in ***Fig. 6-8***. Clearly, the occurrence of autoignition significantly shortens the overall combustion duration. Such changes in overall combustion duration cannot be well described using typical Wiebe Functions alone.

6.4.3 Effect of flame speed

As previously mentioned the engine speed determines the time available for combustion and end gas autoignition. When the engine speed is fixed, then the flame

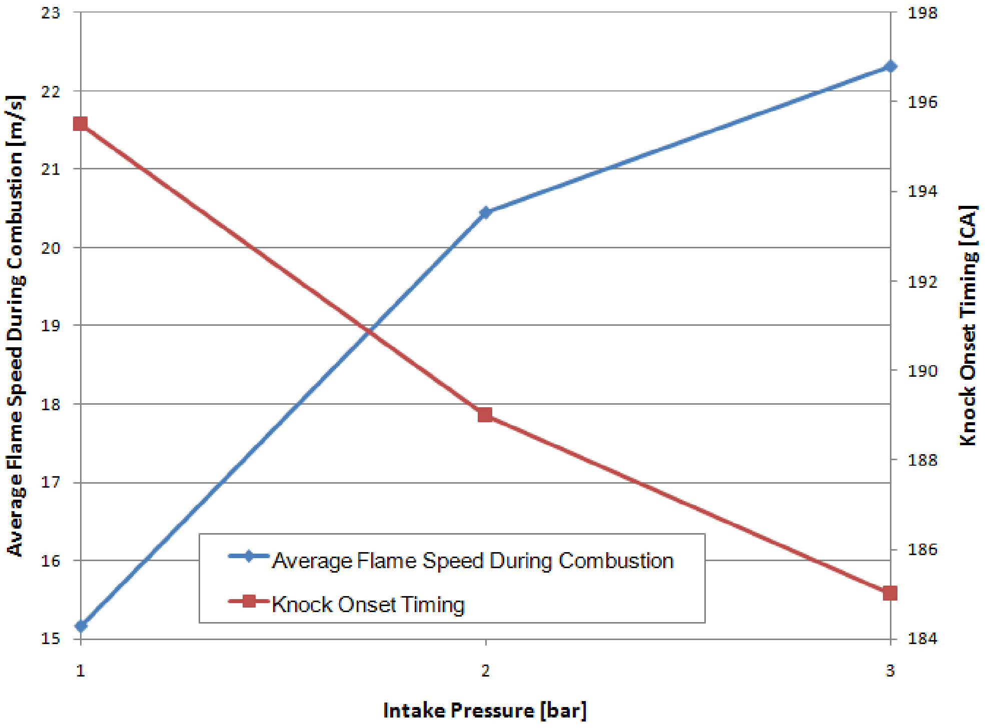

Fig. 6-10 Illustration of relation between average flame speed during combustion and knock onset timing.

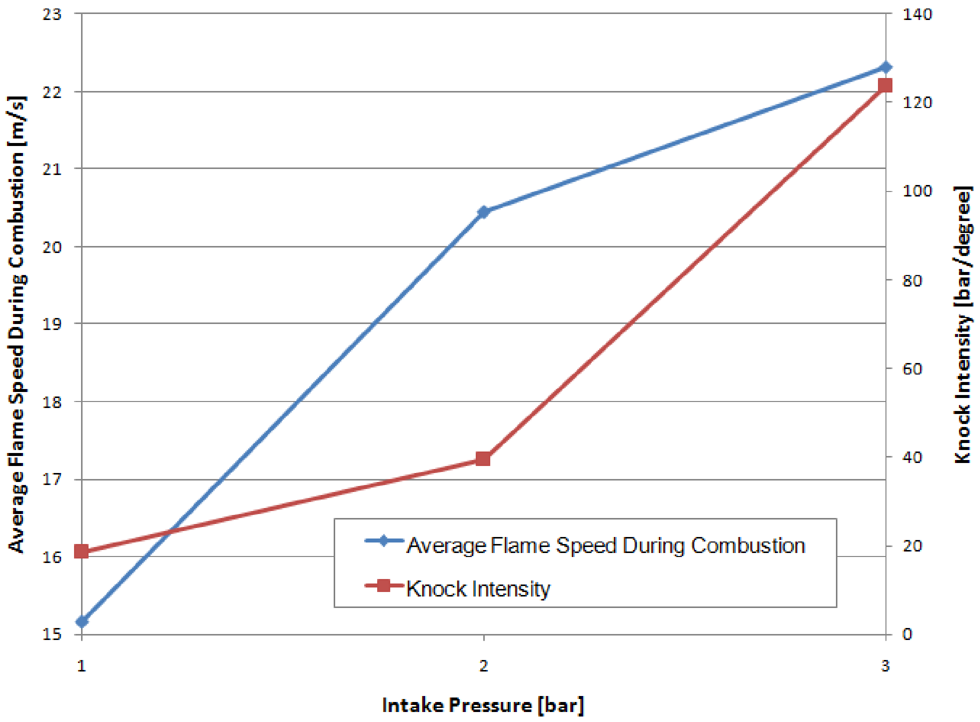

Fig. 6-11 Illustration of relation between average flame speed during combustion and knock intensity.

speed becomes the dominating time scale for combustion and end gas autoignition. It is necessary to investigate the relation between flame propagation and knock. ***Fig. 6-10*** and ***6-11*** show the relations between average flame speed and knock onset timing, and knock intensity, respectively. Initial conditions are 373K, stoichiometric mixture and ignition at 9° BTDC. The average flame speed is obtained by adding calculated turbulent flame speed at each crank angle and divide the sum by number of crank angles of the combustion phase. Average flame speed has been chosen over peak flame speed because it is more indicative when being used as indication of time availability for autoignition.

6.5 Summary

It can be clearly seen that average flame speed increases with increasing intake pressure. This is mainly attributed to the correspondent temperature increase resultant from the intake pressure change. As described in Chapter Five, the calculated turbulent flame speed consists of a chemical-kinetics-based laminar flame speed and a laminar-to-turbulent flame speed correlation. Therefore, as the unburnt temperature raises the laminar flame speed is increased, and so does the turbulent flame speed. However such increase of turbulent flame speed is not linear against intake pressure variation, i.e. 35.9% increase in average flame speed is achieved by increasing intake pressure from 1bar to 2bar, but only 9% has been achieved when it’s been further increased to 3bar. This may be because when intake pressure is raised to 3bar, cylinder pressure during later stage of combustion is sufficiently high for pressure-sensitive chain termination reactions to become dominant over temperature-sensitive chain branching reactions, and thus reduces the laminar flame speed. Additionally, the turbulence intensity is assumed to be a function of only its reference value and crank angle, i.e. independent of temperature and pressure change. Therefore the increase rate of average flame speed is lowering as intake pressure is increased.

Also shown in ***Fig. 6-10*** and ***6-11*** is that, as average flame speed is increased, knock onset timing is advanced and knock intensity is amplified. Theoretically, faster average flame speed should allow less time for autoignition to build up and develop into knock, or reduce knock intensity if it does develop into a knocking cycle. However, such phenomenon has not been replicated in the simulation results. This finding indicates that, in practical application, increasing intake pressure without optimisation of other engine operating parameters will increase flame speed and cylinder pressure and, therefore, improve engine performance, but also induce severe knock problem, making such operating strategy unfeasible. An optimized operating strategy that allows higher intake pressures to improve engine performance but also, at the meantime, keeps the knock in a controlled level should be further investigated.

Chapter Seven: Mitigation of Knock in SI Engine

7.1 Introduction

A key strategy for knock prevention and mitigation is shortening the combustion duration and allowing less time for autoignition to develop (Towers & Hoekstra, 1998). Increasing average flame speed during combustion phase is one of the most effective ways for shortening the combustion duration. So far, the methods used to increase flame speed is by the use of increased cylinder pressure and temperature. These methods have been proven to be effective but also to promote the occurrence of knock. Therefore, an operating strategy that increases average flame speed but does not affect the occurrence of knock needs further development.

The turbulent flame speed in the current study is calculated as a combination of laminar flame speed and effect of turbulence intensity. Increase of turbulence flame speed can be achieved by manipulations of either laminar flame speed or turbulence intensity. Increase of laminar flame speed is always accompanied by higher propensity of knock, and is therefore unfeasible. In this section of the chapter, the effect of increasing turbulence intensity on occurrence of knock will be investigated.

7.2 Effect of Turbulence Intensity on Combustion

According to ***Eq. 4-2***, increase of turbulence intensity, $\boldsymbol{u'}$, has a direct effect on turbulent flame speed. ***Fig. 7-1 to 7-3*** show the effect of enhancing turbulence intensity on average flame speed during the combustion phase of three intake pressures (1, 2 and 3bar). The turbulence intensity is artificially increased by multiplying by an enhancing factor, i.e. 2, 4 and 6. The resultant increased average flame speeds under three intake pressures have been enhanced by factors of approximately 1.31, 1.65 and 2.18, respectively. This has proven that turbulence intensity enhancement is a very effective method for increasing flame speeds. Also shown in these three figures are the corresponding changes in combustion durations in these three scenarios. A similar trend can be found for all three scenarios, that is as turbulence intensity is increased, average flame speed decreases and combustion duration shortens. This is logical as majority of combustible charge inducted into the combustion chamber is consumed by flame propagation. More rapid flame speed means less time required to burn a given amount of combustible charge. The reduction in combustion duration, however, is not uniform in all three scenarios. Reduction under lower intake pressures, i.e. 1 and 2bar, is more significant than it is under higher intake pressure, i.e. 3bar. This may be attributed to the fact that when flame propagates very rapidly it impinges piston head earlier and loses surface area and heat energy (Chander & Ray, 2005). The loss of flame surface area reduces overall burning rate of the flame. Increased heat transfer lowers flame temperature and reduces combustion efficiency. Under higher intake pressures, average flame speed is indeed increased by turbulence intensity enhancement, but such increase is partially offset by the earlier impingement of piston head. Therefore less reduction in combustion duration is achieved as intake pressure is increased.

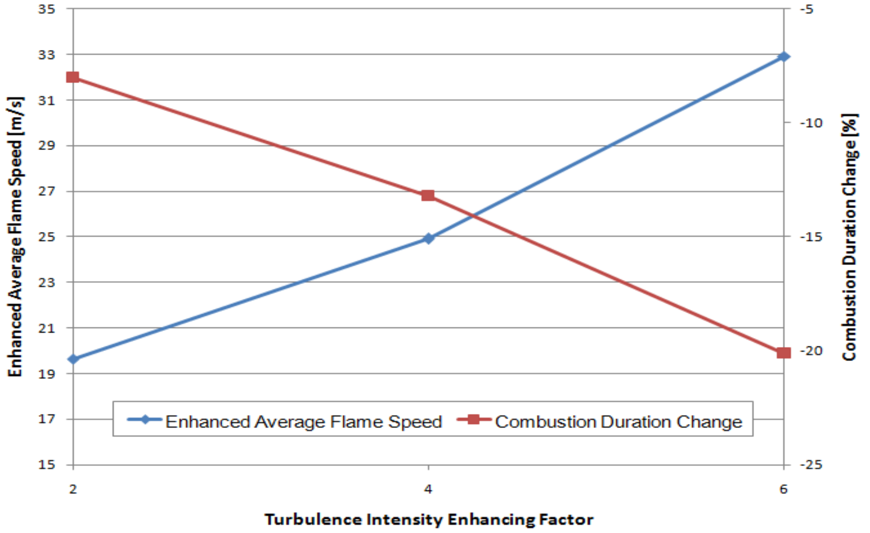

Fig. 7-1 Effects of turbulence intensity enhancement on combustion. Initial conditions are 1bar, 373K, stoichiometric mixture and ignition at 9° BTDC.

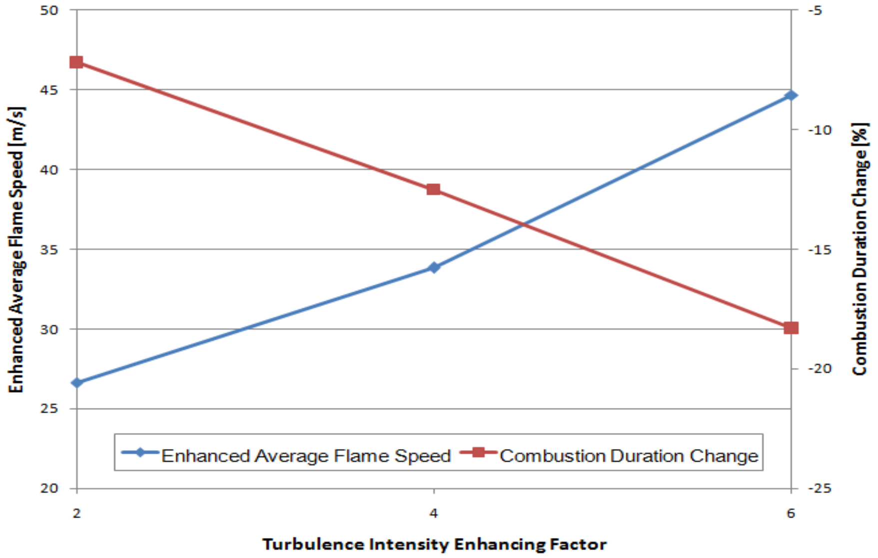

Fig. 7-2 Effects of turbulence intensity enhancement on combustion. Initial conditions are 2bar, 373K, stoichiometric mixture and ignition at 9° BTDC.

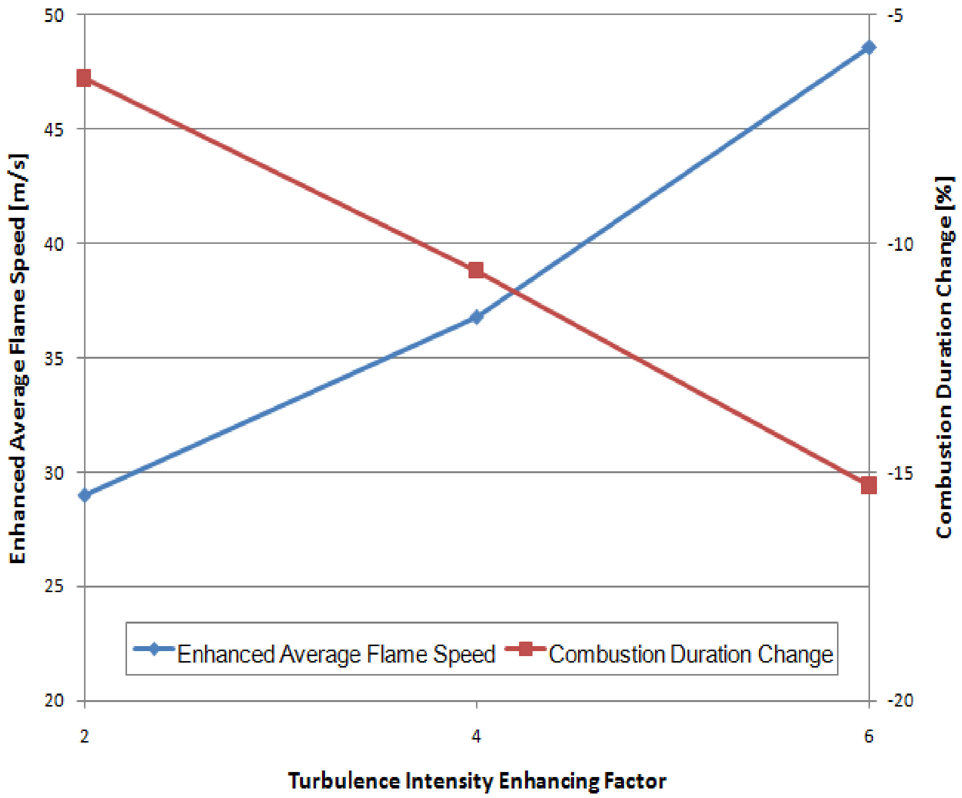

Fig. 7-3 Effects of turbulence intensity enhancement on combustion. Initial conditions are 3bar, 373K, stoichiometric mixture and ignition at 9° BTDC.

7.3 Effect of Turbulence Intensity on Engine Knock

Nevertheless, the enhancement of turbulence intensity can potentially be a mitigation method for knock, especially under higher intake pressures. As previously mentioned, enhanced turbulence intensity increases average flame speed and shortens combustion duration, thus allows less time for time-dependent autoignition to develop into knock or retards the onset timing of knock to reduce its intensity. ***Fig. 7-4 to 7-6*** show the effects of turbulence intensity enhancement on knock onset timing, knock intensity and mass fraction burnt by autoignition. It can be clearly seen that as turbulence intensity is enhanced, knock onset timing is slightly advanced towards TDC, indicating an increase in unburnt mixture temperature. This is attributed to increased flame speeds causing faster compression on unburnt mixture. Both knock intensity and mass fraction burnt by autoignition have been reduced by turbulence intensity enhancement. As the flame propagates faster more combustible charge is consumed by flame combustion and less is burnt by slower-reacting time-dependent autoignition combustion. Because less charge is burnt in unburnt zone by autoignition, less energy is released and therefore lowering knock intensity significantly.

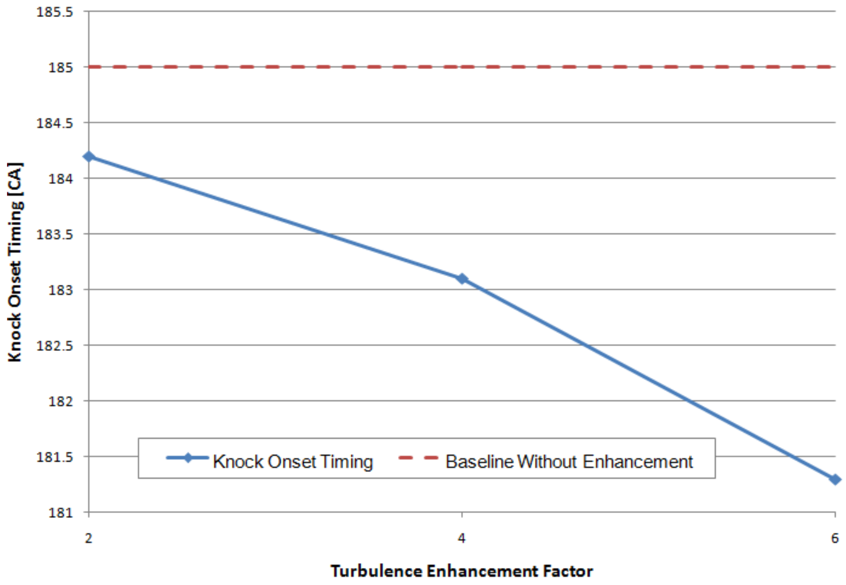

Fig. 7-4 Effects of turbulence intensity enhancement on knock onset. Initial conditions are 373K, 3bar, stoichiometric mixture and ignition at 9° BTDC.

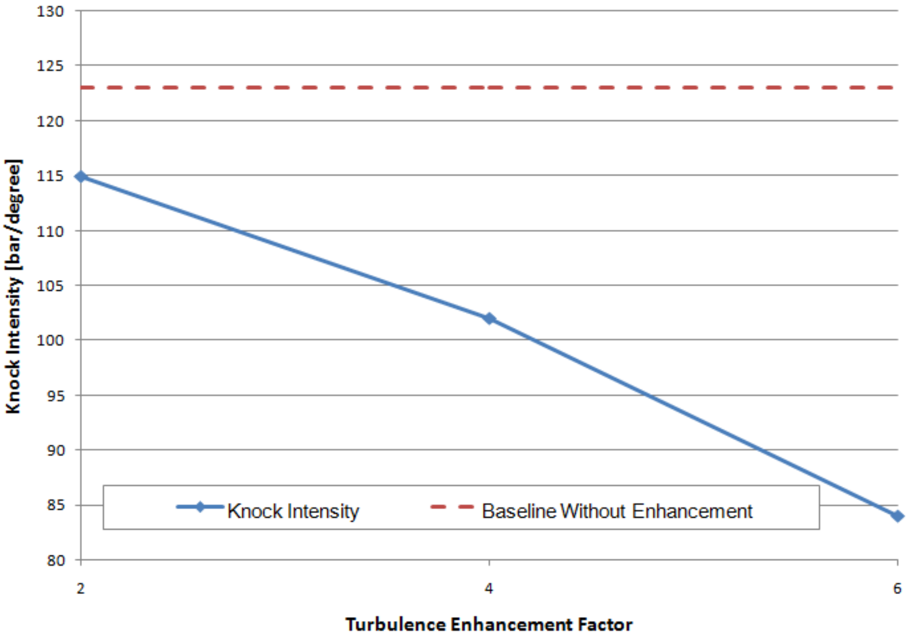

Fig. 7-5 Effects of turbulence intensity enhancement on knock intensity. Initial conditions are 373K, 3bar, stoichiometric mixture and ignition at 9° BTDC.

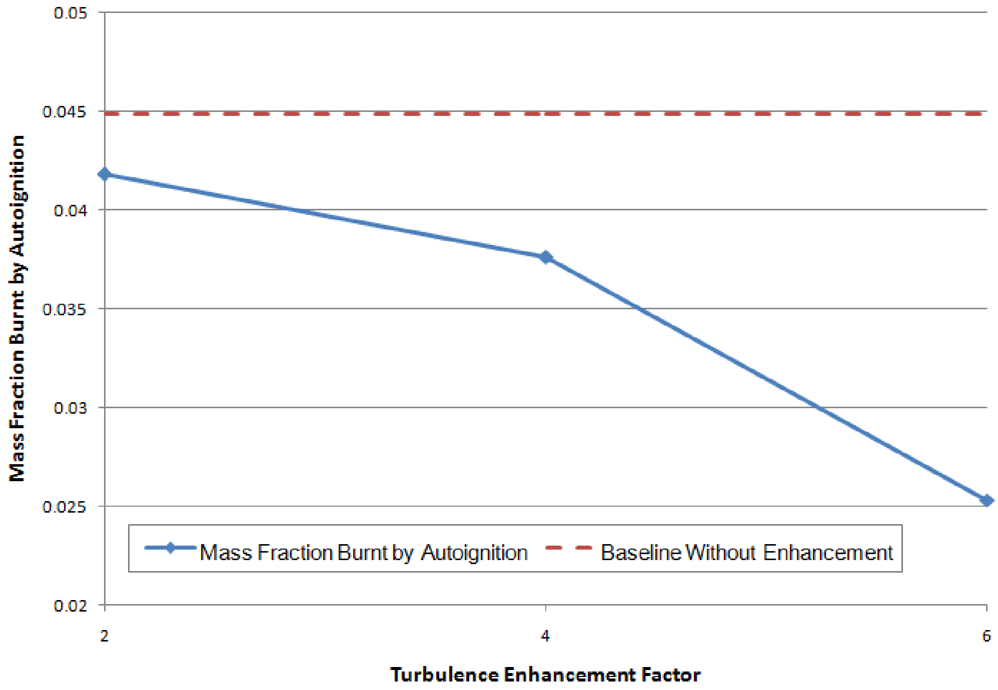

Fig. 7-6 Effects of turbulence intensity enhancement on mass fraction burnt by autoignition. Initial conditions are 373K, 3bar, stoichiometric mixture and ignition at 9° BTDC.

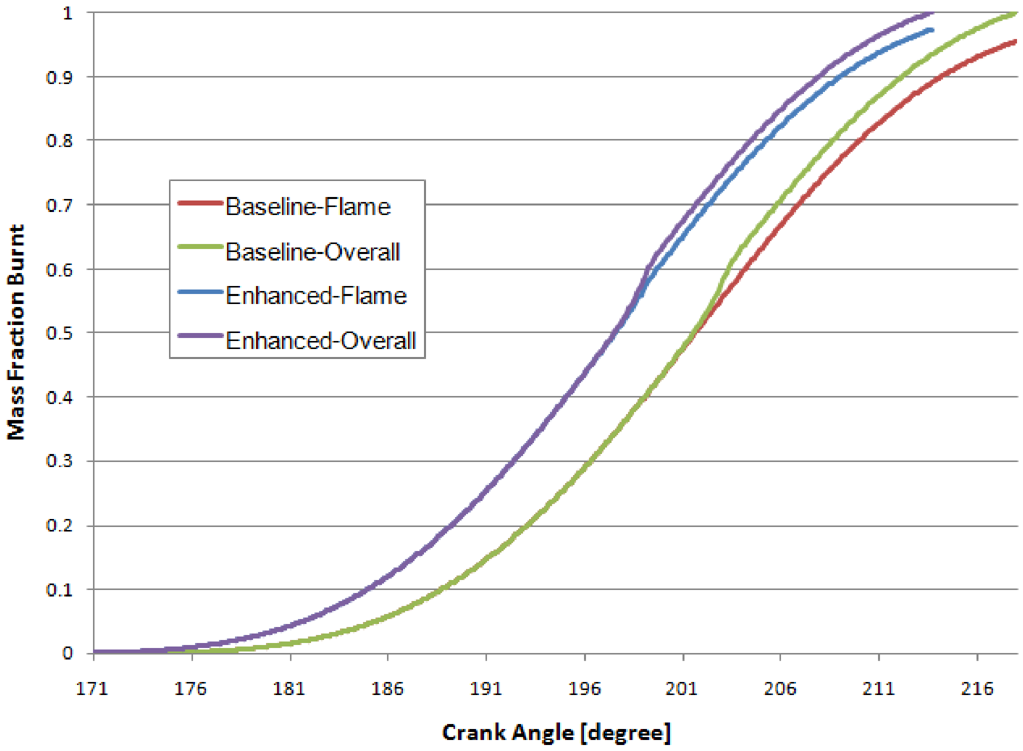

Fig. 7-7 Comparisons of mass fraction burnt by flame and overall combustion with baseline turbulence intensity and enhanced turbulence intensity (by a factor of 6).

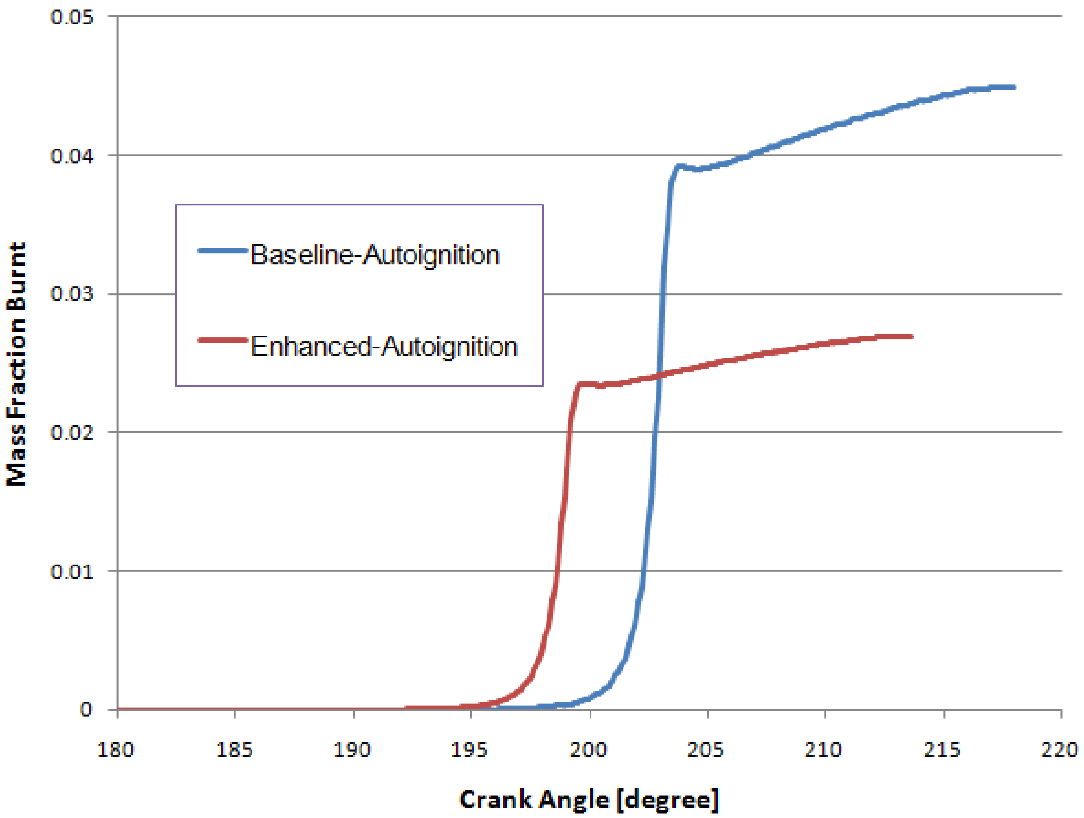

Fig. 7-8 Comparison of mass fraction burnt by autoignition with baseline turbulence intensity and enhanced turbulence intensity (by a factor of 6).

The combustion and autoignition processes with high intake pressure and enhanced turbulence intensity are illustrated in ***Fig. 7-7*** and ***7-8***. Mass fraction burnt by flame combustion under enhanced turbulence intensity is noticeably higher than non-enhanced baseline scenario, at the same crank angle after ignition. This is resultant from increased turbulent flame speed due to stronger turbulence intensity. Overall combustion duration has been shortened by approximately 8 crank angle degrees. In ***Fig. 7-8***, it can be seen that autoignition under enhanced turbulence intensity occurs approximately 4 crank angle degrees earlier than non-enhanced baseline scenario. Additionally, autoignition under enhanced turbulence intensity takes much less time to reach the maximum mass fraction burnt, indicating chain chemical reactions proceed with higher rates and under higher temperature. Although autoignition under enhanced turbulence intensity occurs at higher reaction rates, it ultimately burns less combustible mass, about 67% of non-enhanced baseline scenario. This is attributed to the fact that faster flame consumes more combustible mass before the time-dependent autoignition is fully developed and leaves less combustible mass to be burnt in autoignition. This phenomenon also explains why, under enhanced turbulence intensity, knock onset timing is advanced but knock intensity is somehow reduced.

7.4 Summary

Downsized and boosted spark ignition engines provide higher performance and lower fuel consumption and CO_2 emission. The benefit of such operating strategy is hugely limited by end gas autoignition and attendant knock. Traditional knock mitigation methods include retardation of spark timing and reduction of intake pressure, although effective, but these method results in compromises on engine performance and fuel consumption. A better knock mitigation method that minimise these compromises should be investigated.

In SI engines, knock is induced by autoignition of unburnt mixture ahead of the propagating flame. Chemically, autoignition is extremely temperature dependent and is slower that in-flame reactions. Autoignited mixtures need time to develop and gain strength to induce engine knock. Therefore, it is critical to control the time allowed for autoignition to develop to supress the occurrence of engine knock. At any known engine speed, this time allowed for autoignition to develop is dominated by the turbulent flame speed within the combustion chamber. As reviewed in Chapter Two, turbulent flame speed can be increased by enhanced turbulence intensity.

A knock mitigation strategy based on turbulence intensity enhancement has been investigated. Simulation results revealed that, by enhancing turbulence intensity, average flame speed during the combustion process can be increased to shorten the overall combustion duration. As the flame propagates faster, more combustible mass is consumed by the flame and leaves less combustible mass to be burnt by unburnt mixture autoignition, and thus knock intensity has been reduced. The drawback of such strategy is the advancement in knock onset timing, resultant from increased compression exerted by the faster propagating flame. Such compromise is acceptable in practical engine operation as it is the knock intensity that is more damaging to the engine.

Chapter Eight: Conclusions and Future Work

8.1 Concluding remarks

The current research study has been focused on the development, validation and application of two spark ignition engine models:

1. A naturally aspirated spark ignition engine combustion and flame propagation model.
2. A downsized boosted spark ignition engine knock model.

Both models are developed based on zero-dimensional multi-zone modelling philosophy, for the simulation of kinetically-driven combustion phenomenon within the flame and in the unburnt mixtures.

The major contributions of this research study is primarily made to establish a mathematical simulation model based on available physical, chemical, thermodynamic and fluid dynamic principles of combustion ,flame propagation and autoignition occur in spark ignition engines. The developed model is then solved by an in-house numerical solver. The aims of this research study is to establish better understanding of the transient turbulent flame propagation and its interaction with end gas autoignition and the attendant knock in spark ignition engines. The simulation model can be used as a diagnose tool for combustion and knock characteristics under realistic in-cylinder conditions.

Both in-flame combustion and end gas autoignition in spark ignition engines are chemical-kinetic-controlled. The difference is the ignition source where in-flame combustion is initiated by external energy input, i.e. electrical spark, and is maintained through mass diffusion and heat transfer. End gas autoignition, in contrary, is initiated by chemical reactions with heat release resultant from compression work by piston motion and flame propagation. Therefore, chemical kinetics modelling has been adopted to simulate both in-flame and autoignition combustion, which can be seen as processes of hydrocarbon oxidation occurring at different time scales and intensities.

Zero-dimensional, multi-zone engine modelling has been widely used as a functional simulation philosophy to study the combustion process in spark ignition engines. It has been regarded as a optimal balance between computational accuracy and costs. Combination of chemical kinetics models and zero-dimensional multi-zone thermodynamics model is then a effective and efficient method of modelling turbulent flame propagation and end gas autoignition phenomenon in spark ignition engines. Additional benefits of zero-dimensional multi-zone modelling are briefly listed below:

- Compared to single-zone models, multi-zone models account for temperature, pressure and composition gradient within the combustion chamber. It also enables the separation of a dedicated flame/burning zone to study the flame propagation process.
- Multi-zone models are capable of simulating mass and heat transfer between burning and unburnt zone, which is critical in flame propagation mechanism.
- Multi-zone models can be coupled with simplified mean turbulence models to significantly reduce computational costs, when detailed in-cylinder flow characteristics are not concerned.

In the development process of the model, some coding principles are bear in mind to make the model more efficient and user-friendly:

- The model has been written in programming language FORTRAN 77/90 to make the codes transferable between computers and different operation systems.
- The model has been constructed in a modular structure where a relatively

simple main program controls the data flow and calls for subroutines of different functions. It is therefore easier to turn some of the functions of the model on and off.

- A DVODE (Double-precision Variable-coefficient Ordinary Differential Equation) solver is applied to solve initial value problems for both stiff and non-stiff ODEs systems.

8.1.1 SI engine turbulent flame modelling

Turbulent flame propagation within spark ignition engines is closely related to combustion efficiency, fuel consumption, cyclic variation and abnormal combustion phenomenon. Previous research work on turbulent flame propagation under engine-like conditions is limited by its complexity and extremely random and transient nature. In the current research, turbulent flame propagation within spark ignition engines is assumed to fall into the wrinkle flamelet combustion regime. Therefore, the combustion process and the effects of turbulence on reacting laminar flamelets can be separately studied and modelled. The turbulent flame speed is then considered as a combination of laminar flame speeds and contribution from critical turbulence parameters, i.e. turbulence intensity.

The instantaneous turbulence intensity and other turbulence parameters at any given crank angles are evaluated using the rapid distortion theory with reference values at TDC position that are obtained experimentally.

Laminar flame speed is considered as a result of laminar burning velocity, flame stretch, flame instabilities and thermal expansion. Laminar burning velocity is a property of a fuel at given initial conditions, i.e. temperature, pressure and composition. Laminar burning velocity is chemically-controlled and therefore modelled using chemical kinetics mechanism. Such novel methodology has been firstly validated by modelling of spherical flames in constant volume combustion chamber, before being applied in spark ignition engine turbulent flame modelling.

The interaction between turbulence and laminar flame speed has been described using a established turbulence flame speed correlation. This correlation has been selected by extensive review on available correlations by the criterion that it best suits turbulence combustion under engine-like conditions which are characterised by higher turbulence levels and increased turbulent Reynolds Number.

Some model-specific assumptions are applied to suit the development of the model:

- The ignition process is neglected and a flame kernel is assumed to exist after the breakdown period. The kernel initially propagates at the rate of laminar flame speed under thermodynamic conditions at ignition. Pressure is assumed to be uniform on both sides of kernel. Adopted values for kernel size and breakdown period to be 1mm radius and 200$\boldsymbol{\mu s}$ respectively.
- The turbulent flame front is assumed to have a spherical shape and such shape is maintained throughout combustion. The instantaneous turbulent flame front is arbitrarily wrinkled by the small eddies in the turbulent flow. A mean flame front centre line is introduced to simplify the flame geometry, as depicted in ***Fig. 6-2***. The mean flame front has the same thickness as the instantaneous flame front, which is denoted as $\boldsymbol{\delta_T}$.
- The turbulent intensity within the combustion chamber is assumed to be spatially uniform. Additionally, the turbulence intensity is assumed to be a function of crank angle and its reference value at TDC, at a given engine speed.

Major contributions and findings of spark ignition engine turbulent flame modelling are listed below:

- Instantaneous laminar burning velocity increases during the flame propagation process, as a result of increased unburnt zone temperature. The increase rate of laminar flame speed is relatively low at initial stage of flame propagation. The rate increases suddenly and results in maximum laminar flame speed between 30 to 35° ATDC when the unburnt zone is compressed to a small fraction of its volume before ignition. The rate then starts to decrease towards the end of the flame propagation process. Such decrease has been attributed to pressure-sensitive chain termination reactions in the chemical kinetics model.

- Instantaneous turbulence flame speed increases with crank angle during the combustion phase. Richer mixtures have higher turbulence flame speed under simulated conditions ($0.8<\Phi<1.2$). Increase rates of turbulent flame speed are generally greater than those of laminar burning velocity at the same crank angle. This is attributed to contributions of turbulence intensity.

- Investigation of relation between turbulent and laminar flame speed, S_T/S_L, revealed that leaner laminar flames are more sensitive to turbulence intensity due to their relatively low flame speeds and thinner flame front. The effect of turbulence intensity has been found to decrease in the initial stage of combustion due to rapid decay. However, such effect starts to increase at around 200° CA as a result of strong compression of unburnt mixture by propagating flame.

8.1.2 Downsized boosted SI engine knock modelling

The current research also investigated the knock phenomenon in modern downsized boosted spark ignition engines. A modified Tanaka chemical kinetics model for gasoline has been applied to unburnt zone to simulate end gas autoignition. The purpose for modification is to make the model suitable for spark ignition combustion, as the original model was designed for HCCI combustion of gasoline. Reaction rates of key chain branching elementary reactions R6 and R18 in the original model have been amplified and validated to reproduce the characteristics of spark ignition combustion, which are higher burning rate and shorter ignition delay.

In order to simulate the effect of downsizing and boosting on combustion, intake pressure has been increased in the simulation model. The following knock characteristics have been revealed, at initial conditions of 373K, 1-3bar, stoichiometric mixture and ignition at 9° BTDC:

- Peak cylinder pressure has been found monotonically with increasing intake pressure. Peak cylinder pressure at 3 bar intake pressure is 53.8% and 208.5% higher than peak cylinder pressures recorded at 2bar and 1bar intake pressure, respectively.
- As intake pressure is increased, knock onset timing is advanced and knock intensity is amplified. This attributed to the increased unburnt zone temperature as a result of intake pressure increase.
- Autoignition at 1, 2 and 3bar intake pressure has been found to consume 1.10%, 1.37% and 4.49% of combustible charge inducted into the cylinder, respectively. This trend agrees with the fact that knock occurs earlier and has higher intensity when intake pressure is increased. End gas autoignition and attendant knock have effectively shortened the overall combustion duration.
- Average flame speed during the combustion phase has been proven to be influential in knock onset timing and intensity. Higher average flame speed causes earlier knock onset with higher intensity.
- Increased intake pressure can increase average flame speed and, theoretically, allows less time for time-dependent autoignition to occur and develop. However, such phenomenon is not depicted in the simulation results. This finding indicates that, in practical application, increasing intake pressure without optimisation of other engine operating parameters will increase flame speed and cylinder pressure and, therefore, improve engine performance, but also induce severe knock problem, making such operating strategy unfeasible.

A knock mitigation strategy that has minimum side effects on engine performance has been proposed. The strategy is based on the theory that when flame propagates faster and consumes more combustion mass, it leaves less time and combustible mass for end gas autoignition to develop and gain intensity. Previous attempts to manipulate in-cylinder turbulent flame speeds are concentrated in two areas: increase of intake temperature and increase of intake turbulence level. Increase of intake temperature is feasible in prevention of knock as autoignition is extremely temperature-sensitive. Therefore, a knock mitigation strategy based on increased turbulence intensity has been tested and following conclusions have been drawn:

- Turbulence intensity at ignition has noticeable effect on average flame speed during the combustion phase. Enhancements of turbulence intensity by a factor of 2, 4 and 6 resulted in 31%, 65% and 118% increase of average flame speed, respectively.
- The increase of average flame speed during the combustion phase shortens the combustion duration by up to 19.8%.
- When turbulence intensity is enhanced by a factor of 6, knock onset timing at 3bar intake pressure has been advanced by around 3° CA. However, knock intensity is reduced by 26% and mass fraction burnt by autoignition is reduced to 2.52% from 4.49% without enhancement.
- Detailed investigation of mass fraction burnt plots showed that, after turbulence intensity enhancement, the mass fraction burnt by flame propagation has increased at a given CA, while the mass fraction burnt by autoignition started to increase earlier but reached a lower maximum.

8.2 Future work

Based on the experience gained during the development of the models described in this thesis, together with knowledge gained from literature review on relevant topics, the following improvements are recommended for future researchers using these models:

- The heat transfer between the flame and the unburnt zone has been modelled using a semi-empirical correlation that was not originally designed for spark ignition engine combustion. Although the correlation contains parameters that can be tuned to match experimental results to validate the model, there is still a need for better systematic understanding and numerical expression of heat convection in the flame-unburnt interface.
- As recommended by a number of highly-regarded publications, the addition of a fourth zone, thermal boundary layer between unburnt zone and cylinder walls, will improve the model's ability of predicting emissions and heat transfer to cylinder walls. This is not particularly necessary for the current study as flame propagation and knock are the major concerns. However, as emissions are becoming more important in modern engine design, such addition is strongly recommended.
- The gasoline chemical kinetics model applied in the current models is a reduced mechanism. This is attributed to both the lack of a detailed gasoline kinetics mechanism and the lack of highly efficient numerical algorithm, such as parallel computing. The adoption of new numerical algorithm may involve major modifications on the code structure or even translation of the codes into other programming language.
- In terms of the model codes, the models developed are written in Windows Visual Studio 2010 using FORTRAN composer XE compiler. The interpretation and modification of the codes have to be conducted using the software package. This greatly limits the distribution and user-friendliness of the models. It is recommended that a GUI (Graphic User Interface) being developed for the models and subroutines in the models being transformed

into toolboxes, to allow end-users to take advantage of full or partial functionalities of the models.

References

Abraham, J., Williams, F. & Bracco, F., 1985. A discussion of turbulent flame structure in premixed charges. *SAE 850345*.

Aceves, S.M. et al., 2000. A multizone model for prediction of HCCI combustion and emissions. *SAE 2000-01-0327*.

Aditya Thallam Thattai, 2010. *A Validation Study For Turbulent Premixed Flame Propagation In Closed Vessels*. Delft University of Technology.

Akram, M., Kumar, S. & Saxena, P., 2013. Experimental and Computational Determination of Laminar Burning Velocity of Liquefied Petroleum Gas-Air Mixtures at Elevated Temperatures. *Journal of Engineering for Gas Turbines and Power*, 135(9), p.091501.

Aleiferis, P.G. & Rosati, M.F., 2012. Flame chemiluminescence and OH LIF imaging in a hydrogen-fuelled spark-ignition engine. *International Journal of Hydrogen Energy*, 37(2), pp.1797–1812.

Ali, A. et al., 2003. IMprovement in computational efficiency for HCCI engine modelling by using reduced mechanism and parallel computing. *Central State Section Meeting*.

Andrews, G. & Bradley, D., 1972b. The burning velocity of methane-air mixtures. *Combustion and Flame*, 19, pp.275–288.

Anon, 2013. Forte: CFD with real chemistry speeds accurate clean engine design.

Arrigoni, V. & Cornetti, G.M., 1974. High speed knock in SI engines. *SAE 741056*.

Assanis, D. & Heywood, J., 1986. Development and use of a computer simulation of the turbocompounded diesel system for engine performance and component heat transfer studies. *SAE 860329*.

Attard, W.P. et al., 2010. Combustion System Development and Analysis of a Downsized Highly Turbocharged PFI Small Engine. *SAE 2010-32-0093*.

Aung, K.T., Hassan, M.I. & Faeth, G.M., 1998. Effects of pressure and nitrogen dilution on flame/stretch interactions of laminar premixed H2/O2/N2 flames. *Combustion and Flame*, 112(1-2), pp.1–15.

Ball, J.K., Raine, R.R. & Stone, C.R., 1998. Combustion analysis and cycle-by-cycle variations in spark ignition engine combustion Part 1: An evaluation of combustion analysis routines by reference to model data. *Proceedings of the Institution of Mechanical Engineers, Part D: Journal of Automobile Engineering*, 212(5), pp.381–399.

Bechtold, J.K. & Matalon, M., 1987. Hydrodynamic and diffusion effects on the stability of spherically expanding flames. *Combustion and Flame*, 90, pp.77–90.

Bechtold, J.K. & Matalon, M., 2001. The dependence of the Markstein length on stoichiometry. *Combustion and Flame*, 127(1-2), pp.1906–1913.

Blasenbrey, T. & Maas, U., 2000. ILDMs of higher hydrocarbons and the hierarchy of chemical kinetics. *Proceedings of the Combustion Institute*, 28, pp.1623–1630.

Blunsdon, C.A. & Dent, J.C., 1994. The Simulation of Autoignition and Knock in a Spark Ignition Engine with Disk Geometry. *SAE 940524*.

Boivin, P. et al., 2011. An explicit reduced mechanism for H2H2–air combustion. *Proceedings of the Combustion Institute*, 33(1), pp.517–523.

Borgnakke, C., Arpaci, V.S. & Tabaczynski, R.J., 1980. A model for the instaneous heat transfer and turbulence in a spark ignition engine. *SAE 800287*.

Bradley, D. & Harper, C.M., 1994. The development of instabilities in laminar explosion flames. *Combustion and Flame*, 99(3-4), pp.562–572.

Bradley, D. et al., 1998. The Measurement of Laminar Burning Velocities and Markstein Numbers for Iso-octane–Air and Iso-octane–n-Heptane–Air Mixtures at Elevated Temperatures and Pressures in an Explosion Bomb. *Combustion and Flame*, 115(1-2), pp.126–144.

Bradley, D., 2000. Flame Propagation in a Tube: The Legacy of Henri Guenoche. *Combustion Science and Technology*, 158(1), pp.15–33.

Bradley, D., Gaskell, P. & Gu, X., 1996. Burning velocities, Markstein lengths, and flame quenching for spherical methane-air flames: a computational study. *Combustion and Flame*, 198, pp.176–198.

Bradley, D., Lau, a. K.C. & Lawes, M., 1992. Flame Stretch Rate as a Determinant of Turbulent Burning Velocity. *Philosophical Transactions of the Royal Society A: Mathematical, Physical and Engineering Sciences*, 338(1650), pp.359–387.

Bray, K.N.C., Champion, M. & Libby, P.A., 1994. *Turbulent Reacting Flows*, London: Academic Press.

Burke, M. et al., 2011. Comprehensive H2/O2 Kinetic Model for High Pressure Combustion. *Int. J. Chem. Kinect*, 44, p.444.

Burke, M.P. et al., 2009. Effect of cylindrical confinement on the determination of laminar flame speeds using outwardly propagating flames. *Combustion and Flame*, 156(4), pp.771–779.

Byun, J., 2011. *Laminar burning velocities and laminar flame speeds of multi-component fuel blends at elevated temperatures and pressures*. University of Texas at Austin.

C.K., W. & F.L., D., 1981. Simplified reaction mechanisms for the oxidation of hydrocarbon fuels in flames. *Combustion Science and Technology*, 27, pp.31–43.

Chander, S., & Ray, A. (2005). Flame impingement heat transfer: A review. *Energy Conversion and Management*, *46*(18-19), 2803–2837.

Cheng, R. & Oppenheim, A., 1984. Autoignition in methane-hydrogen mixtures. *Combustion and Flame*, 139, pp.125–139.

Chung, S.H. & Law, C.K., 1984. An invariant derivation of flame stretch. *Combsust. Flame*, 55, pp.123–125.

Curran, H. et al., 1998. A comprehensive modeling study of n-heptane oxidation. *Combustion and flame*, 2180(97).

Dahms, R.N. et al., 2011. Understanding ignition processes in spray-guided gasoline engines using high-speed imaging and the extended spark-ignition model SparkCIMM. Part A: Spark channel processes and the turbulent flame front propagation. *Combustion and Flame*, 158(11), pp.2229–2244.

Dahnz, C., Han, K.M. & Spicher, U., 2010. Investigations on Pre-ignition in Highly Supercharged SI Engines. *SAE International Journal of Engines*, 3(1), pp.214–224.

Damkohler, G., 1947. English translation NACA TM 1112. *Ze. Elektroch.*, 46, pp.601–652.

Daneshyar, H. & Hill, P., 1987. The structure of small-scale turbulence and its effect on combustion in spark ignition engines. *Progress in energy and combustion science*, 13. Davis, S.G. et al., 2003. work in progress paper A08. In *Proceedings of the Third Joint Meeting of the U. S. Sections of the Combustion Institute*. Chicago.

Douaud, A.M. & Eyzat, P., 1978. Four-Octane-Number Method for Predicting the Anti-Knock Behavior of Fuels and Engines. *SAE 780080*.

Dowdy, D. et al., 1991. The use of expanding spherical flames to determine burning velocities and stretch effects in hydrogen/air mixtures. *Symposium (International) on …*, pp.325–332.

E., H.J., 2007. *Principles of Chemical Kinetics* 2nd Editio., Burlington, Mass: Elsevier.

Eckert, P., Kong, S. & Reitz, R.D., 2003. Modeling Autoignition and Engine Knock Under Spark Ignition Conditions. *SAE 2003-01-0011*.

Ferguson, C. & Kirkpatrick, A.T., 2001. *Internal combustion engines:applied thermosciences* 2nd Editio., New York: Wiley.

Fernández-Galisteo, D. et al., 2009. One-step reduced kinetics for lean hydrogen–air deflagration. *Combustion and Flame*, 156(5), pp.985–996.

Filipi, Z. & Assanis, D.N., 1991. Quasi-Dimensional Computer Simulation of the Turbocharged Spark-Ignition Engine and its Use for 2- and 4-Valve Engine Matching Studies. *SAE 910075*.

Fiveland, S.B. & Assanis, D.N., 2001. Development of a Two-Zone HCCI Combustion Model Accounting for Boundary Layer Effects. *SAE 2001-01-1028*.

Floch, A. et al., Comparison of the Effects of Intake-Generated Swirl and Tumble on Turbulence Characteristics in a 4-Valve Engine Comparison of the Effects of Intake-Generated Swirl and Tumble on Turbulence Characteristics in a 4-Valve Engine. *SAE 952457*.

Fraser, N. et al., 2009. Challenges for increased efficiency through gasoline engine downsizing. *SAE 2009-01-1053*.

Friedfeldt, R. et al., 2012. Three-Cylinder Gasoline Engine With Direct Injection. *ATZautotechnology*, 12(2), pp.34–41.

Gerke, U., 2007. *Numerical analysis of mixture formation and combustion in a hydrogen direct-injection internal combustion engine*. Swiss Federal Institute of Technology Zurich.

Ghojel, J.I., 2010. Review of the development and applications of the Wiebe function: a tribute to the contribution of Ivan Wiebe to engine research. *International Journal of Engine Research*, 11(4), pp.297–312.

Gottgens J, Mauss F, P.N., 1992. Analytic approximations of burning velocities and flame thicknesses of lean hydrogen, methane, ethylene, ethane, acetylene, and propane flames. *Proc. Comb. Inst.*, 24, pp.129–135.

Groff, E., 1982. The cellular nature of confined spherical propane-air flames. *Combustion and Flame*, 62.

Groot, G., 2003. *Modelling of propagating spherical and cylindrical premixed flames*. Eindhoven University of Technology.

Gu, X.J. et al., 2000. Laminar burning velocity and Markstein lengths of methane–air mixtures. *Combustion and Flame*, 121(1-2), pp.41–58.

Gülder, Ö., 1982. Laminar burning velocities of methanol, ethanol and isooctane-air mixtures. *Symposium (international) on combustion*, pp.275–281.

Gülder, Ö., 1991. Turbulent premixed flame propagation models for different combustion regimes. *Symposium (International) on Combustion*, pp.743–750.

Hadler, J., 2009. Three-cylinder Engines from Volkswagen Present and Future. *ATZautotechnology*, 70(5), pp.4–8.

Hall, M.J. & Bracco, F. V, 1987. A study of velocities and turbulence intnesities measured in firing and motored engines. *SAE 870453*.

Hancock, D. et al., 2008. A New 3 Cylinder 1 . 2l Advanced Downsizing Technology Demonstrator Engine. *SAE 2008-01-0611*.

Herweg, R. & Maly, R., 1992. A fundamental model for flame kernel formation in SI engines. *SAE 922243*.

Heywood, J., 1988. *Internal Combustion Engine Fundamentals* Edition 1., New York: McGraw-Hill.

Heywood, J., 1994. Combustion and Its Modeling in Spark Ignition Engines. In *International Symposium COMODIA 94*.

Hu, E. et al., 2009. Experimental and numerical study on lean premixed methane–hydrogen–air flames at elevated pressures and temperatures. *International Journal of Hydrogen Energy*, 34(16), pp.6951–6960.

Hu, E. et al., 2009a. Experimental and numerical study on laminar burning velocities and flame instabilities of hydrogen–air mixtures at elevated pressures and temperatures. *International Journal of Hydrogen Energy*, 34(20), pp.8741–8755.

Hu, E. et al., 2009b. Experimental and numerical study on lean premixed methane–hydrogen–air flames at elevated pressures and temperatures. *International Journal of Hydrogen Energy*, 34(16), pp.6951–6960.

Hughes, K.J., Turaanyi, T. & Pilling, M.J., Leeds Methane Oxidation Mechanism.

Iida, S., Kusaka, J. & Daisho, Y., 2003. Numerical Study on Iso-Octane Homogeneous Charge Compression Ignition. *SAE 2003-01-1820*.

Iijima, T. & Takeno, T., 1986. Effects of temperature and pressure on burning velocity. *Combustion and Flame*, 65(1), pp.35–43.

Inoue, T., Inoue, Y. & Ishikawa, M., 2012. Abnormal Combustion in a Highly Boosted SI Engine - The Occurrence of Super Knock. *SAE 2012-01-1141*.

Iwashiro, Y., Tsurushima, T. & Nishijima, Y., 2002. Fuel consumption improvement and operation range expansion in HCCI by direct water injection. *SAE 2002-01-0105*.

Karlovitz, B. et al., 1953. Studies on Turbulent flames 1: A. Flame Propagation Across velocity gradients B. turbulence Measurement in flames. *4th Symposium (International) on Combustion*, p.613.

Keck, J.C., 1982. Turbulent flame structure and speed in spark-ignition engines. *Symposium (International) on Combustion*, 19(1), pp.1451–1466.

Kee, R. et al., 1996. *Chemkin III: a fortran chemical kinetics package for the analysis of gas-phase chemical and plasma kinetics.*,

Kelley, a. P. & Law, C.K., 2009. Nonlinear effects in the extraction of laminar flame speeds from expanding spherical flames. *Combustion and Flame*, 156(9), pp.1844–1851.

Kim, B. et al., In-cylinder turbulence measurements with a spark plug-in fiber LDV.

Kobayashi, H., Kawabata, Y. & Maruta, K., 1998. Experimental study on general correlation of turbulent burning velocity at high pressure. *Symposium (International) on …*, 27(1), pp.941–948.

Kong, S., Han, Z. & Reitz, R.D., 1995. The Development and Application of a Diesel Ignition and Combustion Model for Multidimensional Engine Simulation. *SAE 950278*.

Kong, S.C. & Reitz, R.D., 1993. Multidimensional modeling of desiel ignition and combustion using a multistep kinetcis model. *Journal of Engineering for Gas Turbines and Power*, 115, pp.781–789.

Konnov, A. a., 2008. Remaining uncertainties in the kinetic mechanism of hydrogen combustion. *Combustion and Flame*, 152(4), pp.507–528.

Kuo,K, K., 2005. *Principles of Combustion* 2nd Editio., New Jersey: John Wiley.

Kwon, O.. & Faeth, G.., 2001. Flame/stretch interactions of premixed hydrogen-fueled flames: measurements and predictions. *Combustion and Flame*, 124(4), pp.590–610.

LAKE, T. et al., 2004. Turbocharging concepts for downsized DI gasoline engines. *SAE 2004-01-0036*.

Law, C. et al., 2003. Development of comprehensive detailed and reduced reaction mechanisms for combustion modeling. *AIAA journal*, 41(9), pp.14–17.

Law, C., 2004. Effects of hydrocarbon substitution on atmospheric hydrogen–air flame propagation. *International Journal of Hydrogen Energy*, 29(8), pp.867–879

Lawes, M. et al., 2012. The turbulent burning velocity of iso-octane/air mixtures. *Combustion and Flame*, 159(5), pp.1949–1959.

Lee, J., Hwang, S. & Lim, J., 1998. A New Knock-Detection Method using Cylinder Pressure , Block Vibration and Sound Pressure Signals from a SI Engine. *SAE 981436*.

Lewis, B. & von Elbe, G., 1934. Determination of the Speed of Flames and the Temperature Distribution in a Spherical Bomb from Time-Pressure Explosion Records. *The Journal of Chemical Physics*, 2(5), p.283.

Li, G., Bo, T. & Chen, C., 2003. CFD Simulation of HCCI Combustion in a 2-stroke DI Gasoline Engine. *SAE 2003-01-1855*.

Li, J. et al., 2004. An updated comprehensive kinetic model of hydrogen combustion. *International Journal of Chemical Kinetics*, 36(10), pp.566–575.

Liang, L. & Reitz, R.D., 2006. Spark Ignition Engine Combustion Modeling Using a Level Set Method with Detailed Chemistry. *SAE 2006-01-0243*.

Liang, L., Stevens, J.G. & Farrell, J.T., 2009. A Dynamic Multi-Zone Partitioning Scheme for Solving Detailed Chemical Kinetics in Reactive Flow Computations. *Combustion Science and Technology*, 181(11), pp.1345–1371.

Libby, P.A. & Williams, F. a., 1982. Structure of laminar flamelets in premixed turbulent flames. *Combustion and Flame*, 44(1-3), pp.287–303.

Libby, P.A. & Williams, F.A., 1983. Strained Premixed Laminar Flames Under Nonadiabatic Conditions. *Combust. Sci. Tech.*, 31, pp.1–42.

Liu, F., Bao, X. & Liu, X., 2011. Stretch of Hydrogen-Air Outwardly Propagating Spherical Laminar Premixed Flames. *Chinese J. Combustion Sci. Technol.*, (17), p.3.

Liu, J. et al., 2006. Multi-dimensional Simulation of Air / Fuel Premixing and Stratified Combustion in a Gasoline Direct Injection Engine with Combustion Chamber Bowl Offset. *SAE 2006-32-0006*.

Liu, K., Burluka, a. a. & Sheppard, C.G.W., 2013. Turbulent flame and mass burning rate in a spark ignition engine. *Fuel*, 107, pp.202–208.

Liu, X. et al., 2013. A laminar flame speed correlation of hydrogen–methanol blends valid at engine-like conditions. *International Journal of Hydrogen Energy*, 38(35), pp.15500–15509.

Liu, Z., 2010. *Chemical Kinetics Modelling Study on Fuel Autoignition in Internal Combustion Engines*. Loughborough University.

Long, L. & Reitz, R.D., Spark Ignition Engine Combustion Modeling Using a Level Set Method with Detailed Chemistry. *SAE 2006-01-0241*.

Marinov, N.M., Westbrook, C.K. & Pitz, W.J., 1996. DETAILED AND GLOBAL CHEMICAL KINETICS MODEL FOR. *Transport phenomena in …*, (March).

Markstein, G.H., 1964. *Nonsteady Flame Propagation*, Pergamon.

Matalon, M., On flame stretch. *Combust. Sci. Tech.*, 1983(31), pp.169–181.

Metghalchi, M. & Keck, J.C., 1980. Laminar burning velocity of propane-air mixtures at high temperature and pressure. *Combustion and Flame*, 38, pp.143–154.

Metghalchi, M. & Keck, J.C., 1982. Burning velocities of mixtures of air with methanol, isooctane, and indolene at high pressure and temperature. *Combustion and Flame*, 48, pp.191–210.

Metghalchi, M. & Keck, J.C., 1982. Burning velocities of mixtures of air with methanol, isooctane, and indolene at high pressure and temperature. *Combustion and Flame*, 48, pp.191–210.

Miller, J. et al., 2013. Future Gasoline Engine Technology and the Effect on Thermal Management and Real World Fuel Consumption. *SAE 2013-01-0271*.

Milton, B.E. & Keck, J.C., 1984. Laminar burning velocities in stoichiometric hydrogen and hydrogen-hydrocarbon gas mixtures. *Combustion and Flame*, 58(1), pp.13–22.

Mueller, M.A. et al., 1999. Flow reactor studies and kinetic modeling of the H2/O2 reaction. *International Journal of Chemical Kinetics*, 31(2), pp.113–125.

Peters, N, 1991. Length scales in laminar and turbulent flames. *Progress in astronautics and aeronautics: Numerical approaches to combustion modeling*, 135, pp.155–182.

Negus, C.H., 1997. *An interactive chemical equilibrium solver for the personal computer*. Virginia Tech.

Conaire, M. et al., 2004. A comprehensive modeling study of hydrogen oxidation. *International Journal of Chemical Kinetics*, 36(11), pp.603–622.

Peters, N. & Smooke, M.D., 1985. Fluid dynamic-chemical interactions at the lean flammability limit. *Combustion and Flame*, 60(2), pp.171–182.

Peters, N., 2000. *Turbulent Combustion*, Cambridge: Cambridge University Press.

Peterson, B., Reuss, D.L. & Sick, V., 2014. On the ignition and flame development in a spray-guided direct-injection spark-ignition engine. *Combustion and Flame*, 161(1), pp.240–255.

Ponnusamy, S., Checkel, M.D. & Fleck, B.A., 2005. Maintaining Burning Velocity of Exhaust-Diluted Methane/Air Flames by Partial Fuel Reformation. *journal.ifrf.net*, (200506), pp.1–17.

Prucka, R.G. et al., 2010. Turbulence Intensity Calculation from Cylinder Pressure Data in a High Degree of Freedom Spark-Ignition Engine. *SAE 2010-01-0175*.

Puzinauskas, P. & Borgnakke, C., 1991. Evaluation and improvement of an unsteady heat transfer model for spark ignition engines. *SAE 910298*.

Ra, Y. & Reitz, R.D., 2008. A reduced chemical kinetic model for IC engine combustion simulations with primary reference fuels. *Combustion and Flame*, 155(4), pp.713–738.

Rahim, F. et al., 2002. Burning velocity measurements of methane-oxygen-argon mixtures and an application to extend methane-air burning velocity measurements. *International Journal of Engine Research*, 3(2), pp.81–92.

Rahim, F. et al., 2002. Burning velocity measurements of methane-oxygen-argon mixtures and an application to extend methane-air burning velocity measurements. *International Journal of Engine Research*, 3(2), pp.81–92.

Rakopoulos, C.D. & Michos, C.N., 2008. Development and validation of a multi-zone combustion model for performance and nitric oxide formation in syngas fueled spark ignition engine. *Energy Conversion and Management*, 49(10), pp.2924–2938.

Rousseau, S., Lemoult, B. & Tazerout, M., 1999. Combustion characterization of natural gas in a lean burn spark-ignition engine. *Proceedings of the Institution of Mechanical Engineers, Part D: Journal of Automobile Engineering*, 213(5), pp.481–489

Rozenchan, G. et al., 2002. Outward propagation, burning velocities, and chemical effects of methane flames up to 60 ATM. *Proceedings of the Combustion Institute*, 29(2), pp.1461–1470.

Saeed, K. & Stone, C.R., 2004. Measurements of the laminar burning velocity for mixtures of methanol and air from a constant-volume vessel using a multizone model. *Combustion and Flame*, 139(1-2), pp.152–166.

Schott, G.L. & Kinsey, J.L., 1958. Kinetic Studies of Hydroxyl Radicals in Shock Waves. II. Induction Times in the Hydrogen-Oxygen Reaction. *The Journal of Chemical Physics*, 29(5), p.1177.

Shaver, G. & Gerdes, J., 2003. Modeling for control of HCCI engines. *American Control …*, pp.4–9.

Shayler, P.J., Wisernan, M.W. & Co, F.M., 1990. Improving the Determination of Mass Fraction Burnt. *SAE Technical Paper 900351*.

Shudo, T., Nabetani, S. & Nakajima, Y., 2001. Analysis of the degree of constant volume and cooling loss in a spark ignition engine fuelled with hydrogen. *International Journal of Engine Research*, 2(1), pp.81–92.

Shy, S.S., Lin, W.J. & Wei, J.C., 2000. An experimental correlation of turbulent burning velocities for premixed turbulent methane-air combustion. *Proceedings of the Royal Society A: Mathematical, Physical and Engineering Sciences*, 456(2000), pp.1997–2019.

Simmie, J.M., 2003. Detailed chemical kinetic models for the combustion of hydrocarbon fuels. *Progress in Energy and Combustion Science*, 29(6), pp.599–634.

Simon, D.M. & Wong, E.L., 1953. Burning Velocity Measurement. *The Journal of Chemical Physics*, 21(5), p.936.

Slack, M., 1977. Rate coefficient for H+ O 2+ M= HO 2+ M evaluated from shock tube measurements of induction times. *Combustion and Flame*, 249(1977), pp.241–249.

Smith, G.P. et al., GRI-Mech 3.0. Available at: http://www.me.berkeley.edu/gri mech/.

Smith, G.P., 2002. *Diagnostics for Detailed Kinetic Modeling in Applied Combustion Diagnostics*, New York: Taylor and Francis.

Smooke, M.D. & Williams, F.A., 1995. A Numerical Investigation of Extinction and Ignition Limits in Laminar Nonpremixed Counterflowing Hydrogen-Air. , 80, pp.329–340.

Stone, C.R., 1987. Comparison of methods for the calculation of mass fraction burnt from engine pressure–time diagrams. *Proc. Inst. Mech. Eng.*, 201, pp.61–67.

Strohle, J. & Myhrvold, T., 2007. An evaluation of detailed reaction mechanisms for hydrogen combustion under gas turbine conditions. *International Journal of Hydrogen Energy*, 32(1), pp.125–135.

Sun, Z.-Y. et al., 2012. Research on cellular instabilities in outwardly propagating spherical hydrogen-air flames. *International Journal of Hydrogen Energy*, 37(9), pp.7889–7899.

Sung, C.J., Law, C.K. & Chen, J.-Y., 1998. An augmented reduced mechanism for methane oxidation with comprehensive global parametric validation. *Symposium (International) on Combustion*, 27(1), pp.295–304.

Tam, R. & Ludford, G.S.S., 1984. Comment on the Stretch-Resistant Flames of Seshadri and Peters. *Combust. Sci. Tech.*, 40, pp.303–305.

Tan, Z. & Reitz, R.D., 2003. Modeling Ignition and Combustion in Spark-ignition Engines Using a Level Set Method. *SAE 2003-01-0722*.

Tan, Z. & Reitz, R.D., 2006. An ignition and combustion model based on the level-set method for spark ignition engine multidimensional modeling. *Combustion and Flame*, 145(1-2), pp.1–15.

Tanaka, S., Ayala, F. & Keck, J., 2003. A reduced chemical kinetic model for HCCI combustion of primary reference fuels in a rapid compression machine. *Combustion and flame*, 133(4), pp.467–481.

Tang, C. et al., 2009. Effects of hydrogen addition on cellular instabilities of the spherically expanding propane flames. *International Journal of Hydrogen Energy*, 34(5), pp.2483–2487.

Taylor, A.M.K.P., 2008. Science review of internal combustion engines. *Energy Policy*, 36(12), pp.4657–4667.

Towers, J.M. & Hoekstra, R.., 1998. Engine knock, a renewed concern in motorsports-a literature review. *SAE 983026*.

Tseng, L., Ismail, M. & Faeth, G., 1993. Laminar burning velocities and Markstein numbers of hydrocarbonair flames. *Combustion and Flame*, 426, pp.410–426.

Verhelst, S. & Sheppard, C.G.W., 2009. Multi-zone thermodynamic modelling of spark-ignition engine combustion-an overview. *Energy Conversion and Management*, 50, pp.1326–1335.

Verhelst, S. et al., 2005. Laminar and unstable burning velocities and Markstein lengths of hydrogen–air mixtures at engine-like conditions. *Proceedings of the Combustion Institute*, 30(1), pp.209–216.

Verhelst, S. et al., 2011. A correlation for the laminar burning velocity for use in hydrogen spark ignition engine simulation. *International Journal of Hydrogen Energy*, 36(1), pp.957–974.

Vlachos, D., 1996. Reduction of detailed kinetic mechanisms for ignition and extinction of premixed hydrogen/air flames. *Chemical engineering science*, 51.

Vu, T.M. et al., 2011. Experimental study on cellular instabilities in hydrocarbon/hydrogen/carbon monoxide–air premixed flames. *International Journal of Hydrogen Energy*, 36(11), pp.6914–6924.

Walzer, P., 2001. Future Power Plants For Cars. *SAE 2001-01-3192*.

Warnatz, J., 1992. Resolution of gas phase and surface combustion chemistry into elementary reactions. *Symposium (International) on Combustion*, pp.553–579.

Westbrook, C.K. & Dryer, F.L., 1980. Prediction of laminar flame properties of methanol-air mixtures. *Combustion and Flame*, 37, pp.171–192.

Westbrook, C.K. & Dryer, F.L., 1984. Chemical kinetic modeling of hydrocarbon combustion. *Progress in Energy and Combustion Science*, 10(1), pp.1–57.

Williams, F.A., 1985. *Turbulent Combustion*, Philadelhpia: SIAM.

Wong, V.W. & Hoult, D.P., 1979. Rapid Distortion Theory Applied to Turbulent Combustion. *SAE 790357*, pp.1243–1262.

Worret, R. et al., Application of Different Cylinder Pressure Based Knock Detection Methods in Spark Ignition Engines Reprinted From : SI Engine Experiments. *SAE 2002-01-1668*.

Zhen, X. et al., 2012. The engine knock analysis - An overview. *Applied Energy*, 92, pp.628–636.

Zhen, X. et al., 2013. Study of knock in a high compression ratio spark-ignition methanol engine by multi-dimensional simulation. *Energy*, 50, pp.150–159.

Zheng, J., 2005. *study of homogeneous ignition and combustion processes in CI, SI, and HCCI engine systems*. Drexel University, PA, USA.

Zimont, V. & Polifke, W., 1998. An efficient computational model for premixed turbulent combustion at high Reynolds numbers based on a turbulent flame speed closure. *Journal of …*, 120(July 1998).

Zuo, B. & Symbols, G., 2001. Flame Acceleration Associated with the Darrieus-Landau Instability. , 2101, pp.2091–2101.

Appendix A: Modified Tanaka Chemical Kinetics Mechanism for Gasoline Combustion

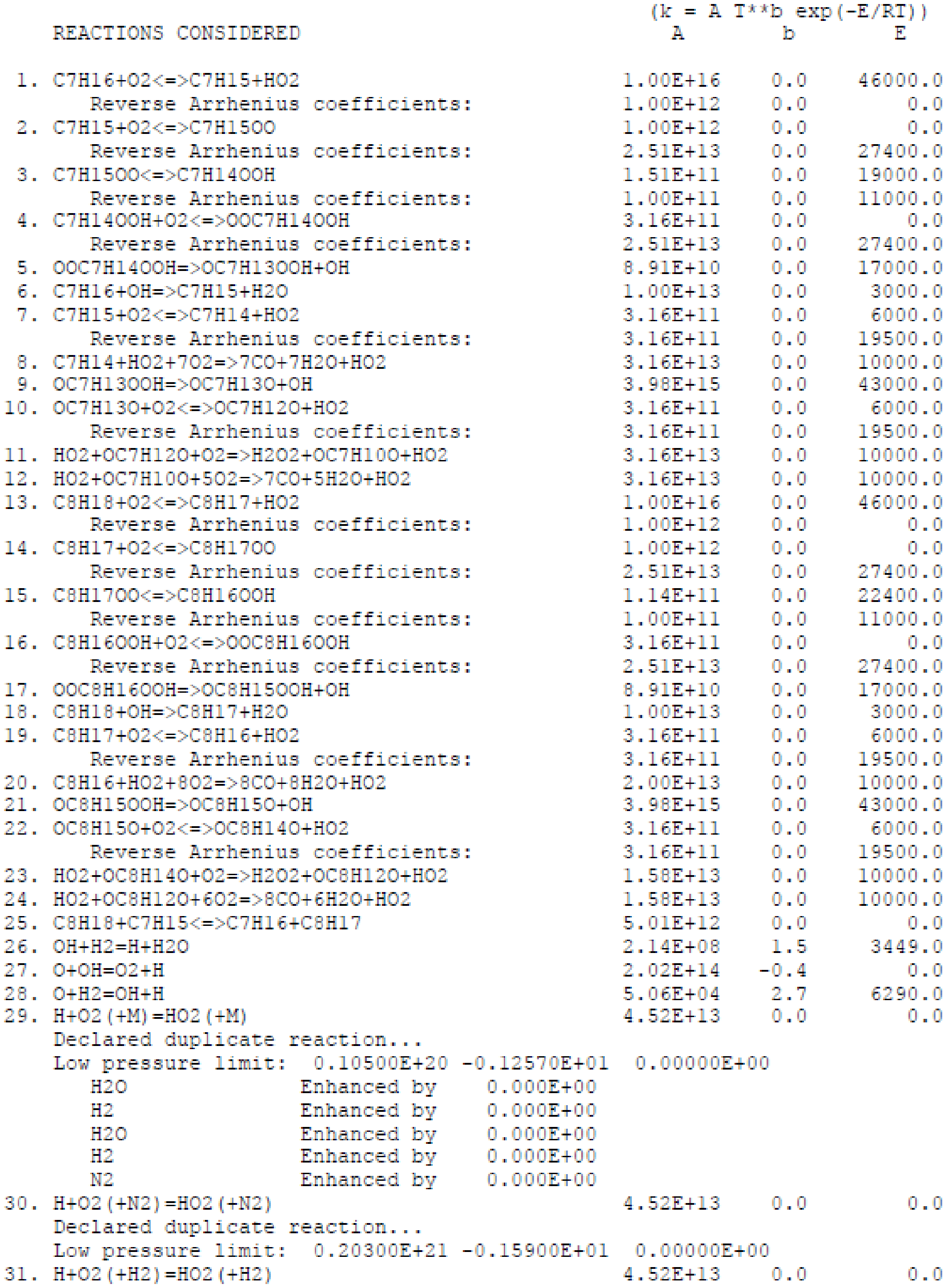

```
                                                      (k = A T**b exp(-E/RT))
   REACTIONS CONSIDERED                                  A         b         E

  1. C7H16+O2<=>C7H15+HO2                           1.00E+16   0.0    46000.0
        Reverse Arrhenius coefficients:             1.00E+12   0.0        0.0
  2. C7H15+O2<=>C7H15OO                             1.00E+12   0.0        0.0
        Reverse Arrhenius coefficients:             2.51E+13   0.0    27400.0
  3. C7H15OO<=>C7H14OOH                             1.51E+11   0.0    19000.0
        Reverse Arrhenius coefficients:             1.00E+11   0.0    11000.0
  4. C7H14OOH+O2<=>OOC7H14OOH                       3.16E+11   0.0        0.0
        Reverse Arrhenius coefficients:             2.51E+13   0.0    27400.0
  5. OOC7H14OOH=>OC7H13OOH+OH                       8.91E+10   0.0    17000.0
  6. C7H16+OH=>C7H15+H2O                            1.00E+13   0.0     3000.0
  7. C7H15+O2<=>C7H14+HO2                           3.16E+11   0.0     6000.0
        Reverse Arrhenius coefficients:             3.16E+11   0.0    19500.0
  8. C7H14+HO2+7O2=>7CO+7H2O+HO2                    3.16E+13   0.0    10000.0
  9. OC7H13OOH=>OC7H13O+OH                          3.98E+15   0.0    43000.0
 10. OC7H13O+O2<=>OC7H12O+HO2                       3.16E+11   0.0     6000.0
        Reverse Arrhenius coefficients:             3.16E+11   0.0    19500.0
 11. HO2+OC7H12O+O2=>H2O2+OC7H10O+HO2               3.16E+13   0.0    10000.0
 12. HO2+OC7H10O+5O2=>7CO+5H2O+HO2                  3.16E+13   0.0    10000.0
 13. C8H18+O2<=>C8H17+HO2                           1.00E+16   0.0    46000.0
        Reverse Arrhenius coefficients:             1.00E+12   0.0        0.0
 14. C8H17+O2<=>C8H17OO                             1.00E+12   0.0        0.0
        Reverse Arrhenius coefficients:             2.51E+13   0.0    27400.0
 15. C8H17OO<=>C8H16OOH                             1.14E+11   0.0    22400.0
        Reverse Arrhenius coefficients:             1.00E+11   0.0    11000.0
 16. C8H16OOH+O2<=>OOC8H16OOH                       3.16E+11   0.0        0.0
        Reverse Arrhenius coefficients:             2.51E+13   0.0    27400.0
 17. OOC8H16OOH=>OC8H15OOH+OH                       8.91E+10   0.0    17000.0
 18. C8H18+OH=>C8H17+H2O                            1.00E+13   0.0     3000.0
 19. C8H17+O2<=>C8H16+HO2                           3.16E+11   0.0     6000.0
        Reverse Arrhenius coefficients:             3.16E+11   0.0    19500.0
 20. C8H16+HO2+8O2=>8CO+8H2O+HO2                    2.00E+13   0.0    10000.0
 21. OC8H15OOH=>OC8H15O+OH                          3.98E+15   0.0    43000.0
 22. OC8H15O+O2<=>OC8H14O+HO2                       3.16E+11   0.0     6000.0
        Reverse Arrhenius coefficients:             3.16E+11   0.0    19500.0
 23. HO2+OC8H14O+O2=>H2O2+OC8H12O+HO2               1.58E+13   0.0    10000.0
 24. HO2+OC8H12O+6O2=>8CO+6H2O+HO2                  1.58E+13   0.0    10000.0
 25. C8H18+C7H15<=>C7H16+C8H17                      5.01E+12   0.0        0.0
 26. OH+H2=H+H2O                                    2.14E+08   1.5     3449.0
 27. O+OH=O2+H                                      2.02E+14  -0.4        0.0
 28. O+H2=OH+H                                      5.06E+04   2.7     6290.0
 29. H+O2(+M)=HO2(+M)                               4.52E+13   0.0        0.0
     Declared duplicate reaction...
     Low pressure limit:  0.10500E+20 -0.12570E+01  0.00000E+00
        H2O             Enhanced by    0.000E+00
        H2              Enhanced by    0.000E+00
        H2O             Enhanced by    0.000E+00
        H2              Enhanced by    0.000E+00
        N2              Enhanced by    0.000E+00
 30. H+O2(+N2)=HO2(+N2)                             4.52E+13   0.0        0.0
     Declared duplicate reaction...
     Low pressure limit:  0.20300E+21 -0.15900E+01  0.00000E+00
 31. H+O2(+H2)=HO2(+H2)                             4.52E+13   0.0        0.0
```

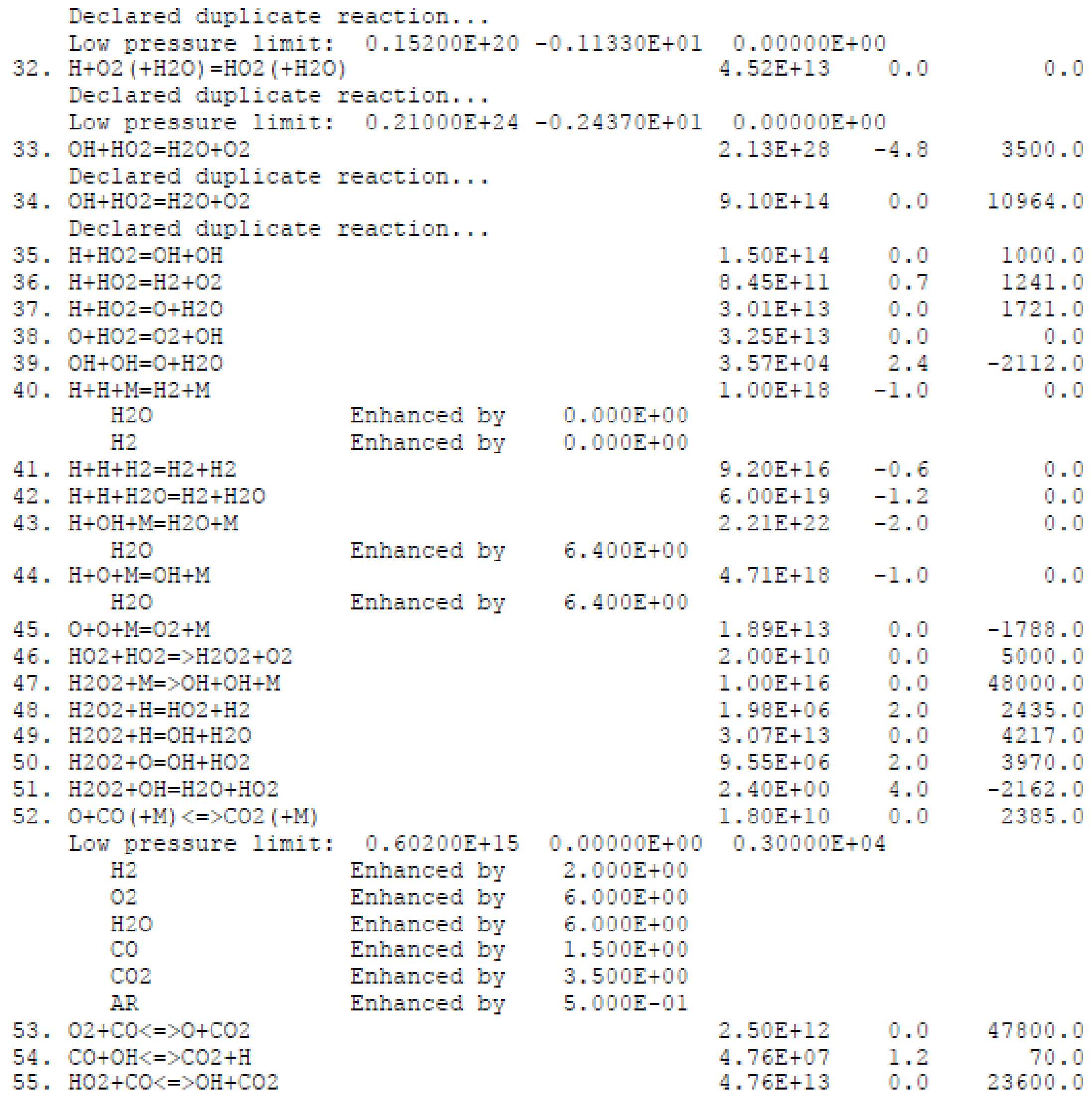

```
     Declared duplicate reaction...
     Low pressure limit:  0.15200E+20 -0.11330E+01  0.00000E+00
 32. H+O2(+H2O)=HO2(+H2O)                          4.52E+13    0.0         0.0
     Declared duplicate reaction...
     Low pressure limit:  0.21000E+24 -0.24370E+01  0.00000E+00
 33. OH+HO2=H2O+O2                                 2.13E+28   -4.8      3500.0
     Declared duplicate reaction...
 34. OH+HO2=H2O+O2                                 9.10E+14    0.0     10964.0
     Declared duplicate reaction...
 35. H+HO2=OH+OH                                   1.50E+14    0.0      1000.0
 36. H+HO2=H2+O2                                   8.45E+11    0.7      1241.0
 37. H+HO2=O+H2O                                   3.01E+13    0.0      1721.0
 38. O+HO2=O2+OH                                   3.25E+13    0.0         0.0
 39. OH+OH=O+H2O                                   3.57E+04    2.4     -2112.0
 40. H+H+M=H2+M                                    1.00E+18   -1.0         0.0
        H2O                Enhanced by    0.000E+00
        H2                 Enhanced by    0.000E+00
 41. H+H+H2=H2+H2                                  9.20E+16   -0.6         0.0
 42. H+H+H2O=H2+H2O                                6.00E+19   -1.2         0.0
 43. H+OH+M=H2O+M                                  2.21E+22   -2.0         0.0
        H2O                Enhanced by    6.400E+00
 44. H+O+M=OH+M                                    4.71E+18   -1.0         0.0
        H2O                Enhanced by    6.400E+00
 45. O+O+M=O2+M                                    1.89E+13    0.0     -1788.0
 46. HO2+HO2=>H2O2+O2                              2.00E+10    0.0      5000.0
 47. H2O2+M=>OH+OH+M                               1.00E+16    0.0     48000.0
 48. H2O2+H=HO2+H2                                 1.98E+06    2.0      2435.0
 49. H2O2+H=OH+H2O                                 3.07E+13    0.0      4217.0
 50. H2O2+O=OH+HO2                                 9.55E+06    2.0      3970.0
 51. H2O2+OH=H2O+HO2                               2.40E+00    4.0     -2162.0
 52. O+CO(+M)<=>CO2(+M)                            1.80E+10    0.0      2385.0
     Low pressure limit:  0.60200E+15  0.00000E+00  0.30000E+04
        H2                 Enhanced by    2.000E+00
        O2                 Enhanced by    6.000E+00
        H2O                Enhanced by    6.000E+00
        CO                 Enhanced by    1.500E+00
        CO2                Enhanced by    3.500E+00
        AR                 Enhanced by    5.000E-01
 53. O2+CO<=>O+CO2                                 2.50E+12    0.0     47800.0
 54. CO+OH<=>CO2+H                                 4.76E+07    1.2        70.0
 55. HO2+CO<=>OH+CO2                               4.76E+13    0.0     23600.0
```

NOTE: A unit - mole-cm-sec-K, E unit - cal/mole

Appendix B: Code Structure of Engine Flame Propagation and Knock Models